# Aqueous Processes across the Solar System: Isotopic Insights from Chondrites and Mars

Thesis by

Surjyendu Bhattacharjee

In Partial Fulfillment of the Requirements for
the degree of
Doctor of Philosophy

Caltech

CALIFORNIA INSTITUTE OF TECHNOLOGY
Pasadena, California

2026
(Defended September 24, 2025)

Surjyendu Bhattacharjee
ORCID: 0000-0002-3924-0357

# ACKNOWLEDGEMENTS

This dissertation marks the culmination of a long and rewarding journey, and I am profoundly grateful to everyone who made it possible.

I owe my deepest gratitude to my advisor, John Eiler, for his unwavering guidance, encouragement, and patience throughout this work. My many discussions with John have shaped not only this thesis but also my broader approach to science and research. I am also deeply thankful to Paul Asimow for guiding me to understand the formation of carbonate minerals through water–rock interactions, and teaching me the experimental, thermodynamic, and microanalytical techniques essential for this purpose. The unique scientific perspectives of both John and Paul have been a lasting source of inspiration. I also wish to thank William A. Goddard III for helping me explore the applications of quantum mechanical modeling to solid materials. Conversations with him motivated me to pursue a challenging class project that ultimately evolved into a thesis chapter and a published paper.

I am equally grateful to my committee members — George Rossman, Ken Farley, and Geoffrey Blake — for their thoughtful feedback and stimulating discussions at every stage of this work.

My sincere thanks go to my mentors and colleagues Ted Present, Uri Ryb, Issaku Kohl, and Damanveer Grewal, with whom I have worked closely over the years. Countless discussions and long hours in the lab with them have deepened my understanding of geochemical analysis and strengthened the scientific rigor of this research. Their dedication to science continues to inspire me.

I would also like to thank Chi Ma, Yunbin Guan, Nami Kitchen, Michael Mathuri, and Nathan Dalleska for their expert assistance with analytical instruments critical to generating the data presented here. I am grateful to Alex Sessions for generously sharing his lab space for my analytical work.

I extend my appreciation to my collaborators for their contributions, camaraderie, and the many discussions that made this research both productive and enjoyable. Special thanks to Clara Blättler for her guidance on Mg isotope analysis; Noriko Kita and John Valley for their insights on ion microprobe isotope ratio measurements; Maciej G. Sliwinski and Mokhles Azer for sharing magnesite standards; Avni S. Patel, Jie Cheng, Maija J. Raudsepp, and Sasha Wilson for synthesizing amorphous Mg-carbonates; and Greg Holk for providing the Rose Quartz standard.

I thank my former mentors, Peter Cawood, Priyadarshi Chowdhury, Sisir Mondal, Debajyoti Paul, and Nachiketa Rai for their guidance, which prepared me for this incredible journey.

This journey would not have been the same without the friendship and emotional support of my peers and friends, who made the highs and lows of graduate life more bearable — and often, truly enjoyable. My heartfelt thanks to Ruolin Deng, Ojashvi Rautela, Jonny Smith, Amogh Johri, Carl Swindle, Adriana Paez, Phelan Yu, Will Palfey, Shirui Peng, Krittanon Sirorattanakul, Abdallah Zaki, Korbinian Thalhammer, Amanda Bednarick, Hannah Dion-Kirschner, Justin Nghiem, Weiyi Liu, Noah Tashbook, Noam Lotem, Eran Funaro, Guannan Dong, Sarah Zeichner, Elliott Mueller, Simon Andren, Elizabeth Heiny, Amy E. Hofmann, Gabriella Weiss, Hao Xie, Yuanyuan He, Daniel Halford, Amrita Vyas, Damanveer Grewal, Jinping Hu, Shounak Dutta and many others for making this journey memorable. Special thanks to my friends in Santa Barbara — Tanmay Chavan, Aishwarya Ramesh, Neha Padwal, Ankit Kumar, Rahul Singh, Jinesh Jhonsa, Ramya Ragunathan, Harsh Shah, Colby Fronk, and others — who have been like family and brought joy to this experience. I'm also thankful to my friends beyond Pasadena — Soumendu Sarkar, Subhajit Roy, Sukalpa Chatterjee, Arkapratim Chatterjee, Rajdeep Mondal, Gargi Deshmukh, Garima Miglani, Akankshya Mishra, Asmita Basu, and others who have supported me in this journey.

I am deeply thankful to my family for their unwavering love and belief in me. My parents, Malabika and Mallinath, my in-laws Saroj and Sarmita, my sister Sutapa, my brother-in-law Subhanjan, and my sister-in-law Soumiki have always been there when I needed them. Their patience, encouragement, and sacrifices have been my greatest source of strength. My cousins and extended family — Ayan, Tinish, Partho, Soumee, Sritama, Shyamasree, Sreemoyee, Debayan, and many others — have filled my life with love and laughter, both essential for surviving graduate school.

Finally, I want to thank my partner, Rini, without whom this achievement would not have been possible. Her constant compassion, support, and understanding carried me through the most challenging times. I dedicate this work to her.

This research was supported in part by a Simons Foundation grant (No. 668346), a Caltech Center for Comparative Planetary Evolution grant awarded to Surjyendu Bhattacharjee and Ted Present, and by research grants to John Eiler from the Caltech Center for Comparative Planetary Evolution and the U.S. Department of Energy (No. DESC0016561).

# ABSTRACT

Since the birth of the solar system, volatiles have played a central role in shaping planetary environments and their habitability. They mediated the abiotic production of organic compounds, altered asteroidal bodies, and supplied liquid water and greenhouse gases to terrestrial planets, creating habitable conditions that are seen in the inner solar system. These cumulative processes ultimately set the stage for life's emergence on Earth. Despite decades of study, fundamental questions remain unresolved: the sources and distribution of volatiles across different reservoirs, their processing in the protoplanetary disk, and their operation on rocky planets. Progress has often been hindered by analytical limitations, necessitating the development of new approaches. This thesis addresses these gaps by investigating the origin and interaction of volatiles with rocks in two distinct solar system environments—prebiotic chemistry in the early solar system and water–rock interactions on early Mars.

The first part focuses on volatile-driven prebiotic chemistry, using oxygen isotope ratios in organic compounds as tracers. In Chapter 2, I employed quantum mechanical calculations to model how organics fractionate oxygen isotopes from different volatile sources ($H_2O$, CO, $CO_2$). These models predict distinct isotopic compositions for organic molecules depending on their source and formation mechanism. In Chapter 3, I developed a novel electrospray ionization Orbitrap mass spectrometry method to quantify oxygen-exchange kinetics between organics and water, constraining rate constants and activation energies. Carboxylic acids were found to exchange isotopes more slowly than other organic classes, making them promising candidates for triple oxygen isotope measurements. In Chapter 4, I applied this novel method to measure the isotopic compositions of select organic acids from a chondritic meteorite. The results revealed distinct formation pathways and fluid sources that contributed to prebiotic chemistry in the early solar system. This represents the first such triple oxygen isotope measurement of meteoritic organics and establishes a new framework for probing their origin.

The second part examines water–rock interactions on Mars and their role in planetary climate and habitability. In Chapter 5, I used quantum mechanical calculations to quantify carbon, oxygen, and magnesium isotope fractionations between hydrous and anhydrous Mg-carbonates and aqueous fluids. These results demonstrate that hydrous and anhydrous carbonates produce distinct Mg isotope signatures, reflecting different reaction pathways. In Chapter 6, I developed a robust in situ ion microprobe protocol for measuring Mg isotope ratios in carbonates, validated by extensive accuracy and precision testing. This method enables direct investigation of water–rock processes in planetary materials. Finally, in Chapter 7, I applied this technique to ALH84001 carbonates—the oldest known Martian carbonates, formed when Mars was potentially habitable. The isotopic data show that the early Martian carbon cycle was modulated by silicate weathering, linking climate regulation to surface–subsurface water cycling. These results indicate that Mars sustained episodic warm and aqueous environments and subsurface niches conducive to prebiotic chemistry far longer than previously thought.

Together, these studies introduce new analytical and computational tools and demonstrate their power in addressing fundamental questions about the role of volatiles in planetary evolution, prebiotic chemistry, and habitability across the solar system.

# PUBLISHED CONTENT AND CONTRIBUTIONS

Bhattacharjee S. and Eiler J. M. (2024) Oxygen isotope equilibria of O-bearing organic compounds based on first principle quantum mechanical models, and implications for their use in the study of extraterrestrial organics. In: *Geochim. Cosmochim. Acta* 380, 96–111. DOI: 10.1016/j.gca.2024.07.013.

S.B. conceptualized the project, performed the simulations, analyzed the results and wrote the manuscript.

Bhattacharjee S. and Eiler J. M. (2025). Constraining oxygen isotope exchange kinetics between organic compounds and water using electrospray ionization Orbitrap mass spectrometry, and implications for the oxygen isotopic compositions of meteoritic organics. In: *Geochim. Cosmochim. Acta* 404, 257–273. DOI: 10.1016/j.gca.2025.07.029.

S.B. conceptualized the project, performed the experiments, analyzed the samples, synthesized the results, and wrote the manuscript.

Bhattacharjee S., Patel A., Cheng J., Raudsepp M., Wilson S., Goddard W., Asimow P. and Eiler J. M. (2025). Constraining oxygen isotope exchange kinetics between organic compounds and water using electrospray ionization Orbitrap mass spectrometry, and implications for the oxygen isotopic compositions of meteoritic organics. In: *Geochim. Cosmochim. Acta*. DOI: 10.1016/j.gca.2025.09.026.

S.B. conceptualized the project, performed the experiments and simulations, analyzed the samples, synthesized the results, and wrote the manuscript.

Bhattacharjee S., Present T. M., Swindle C. R., Blättler C. L., Grewal D. S., Guan Y., Ma C., Asimow P. D., Valley J. W. and Eiler J. M. (2024) Tracking Near-Surface Aqueous Alteration Processes on Earth and Ancient Mars with Multiple Stable Isotopes in Magnesite. In: *LPI Contrib.* **3007**, 3531. BIBCODE: 2024LPICo3007.3531B

S.B. conceptualized the project, developed the analytical protocol, analyzed the samples, synthesized the results, and wrote the abstract.

# TABLE OF CONTENTS

# LIST OF ILLUSTRATIONS

# LIST OF ILLUSTRATIONS TABLES

# *Chapter 1*

# INTRODUCTION

## Volatiles and their role in the origin of Life

Unraveling the origin of life demands a primary understanding of the development of a habitable environment, i.e., what makes a planet habitable and facilitates the synthesis of molecular building blocks of life? Volatiles play an important role in modulating habitability on planetary and asteroidal scales. Following their production through the chemical evolution of the solar nebula, they have modulated the prebiotic synthesis of organic compounds that could facilitate the emergence of life in different solar system environments. These organic compounds are the main carriers of life-essential elements (C, N), contribute to the development of volatile inventory of rocky planets, and act as precursors to prebiotic molecules– factors that influence the emergence of life.

Rocky planets and asteroids in the solar system inherited volatiles such as liquid water and organic compounds from solar reservoirs. Their further processing or cycling between different reservoirs of a rocky planet helped in the development of the planetary atmosphere, hydrosphere, and ultimately, a biosphere that we see on Earth. Hence, it is critical to understand how volatiles modulate different processes in different environments across the solar system.

## Interactions of volatiles with rocks

The interactions of volatiles (liquid, vapor) and rocky reservoirs are called water-rock cycles. In the early solar system, volatile reservoirs mainly existed as gas (CO, water) and ice (water, methane, CO, $CO_2$). Advanced processing of the initial molecular cloud created segregated reservoirs of gas (CO) and water ice in the inner and outer solar system, respectively. These reservoirs, influenced by the radiation in the nebula, interacted with the rocks to produce organic compounds. These organic compounds can be imagined as the direct indicators of the nature of the volatiles they formed from, and sample diverse volatile reservoirs across the solar system.

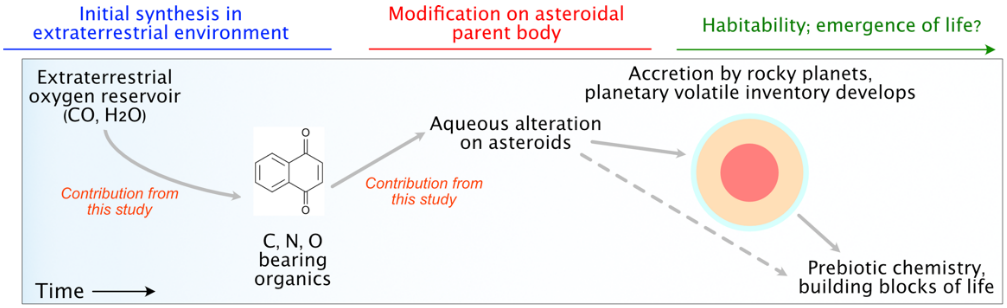

Figure 1.1: Role of volatiles in planetary evolution.

These organics were, in turn, delivered to planets along with volatiles such as ices during the planetary accretion. This planetary volatile reservoir is critical because its cycling could lead to the development of the atmosphere and the hydrosphere. This sets the stage for further near-surface water-rock cycling. There are two broad categories for planetary water-rock cycling: weathering and serpentinization. These processes hold the key to planetary habitability. There are at least two possible locations in the inner solar system where life could proliferate. Other than Earth, multiple lines of evidence suggest that Mars, one of the rocky planets in the inner solar system, was once habitable. Unlike Earth, it has preserved its ancient rock record due to the absence of tectonic processes. This presents an exclusive archive to study how water-cock cycles influence habitability in the non-terrestrial inner solar system environments.

I have explored both the origin of the early solar system organics and the water-rock cycles on Mars to comprehensively understand the essential roles that volatile played in shaping different environments. I discuss their details in two parts in my thesis.

## Part I: Origin of the oxygen-bearing organics in the solar system

Even after decades of research, it is unclear where and how organic compounds were formed in the early solar system and where their parental volatiles came from. These organics are found in carbonaceous chondrite meteorites. Investigations of the isotopic ratios of carbon

($\delta^{13}C$) and hydrogen ($\delta D$) have revealed multiple chemical pathways that possibly lead to their formation. However, these pathways are often not mutually exclusive. Because the carbon and hydrogen distribution in the solar system is complex, and organic synthesis processes fractionate them depending on the chemical reaction, it is difficult to use $\delta^{13}C$ and $\delta D$ to track the volatile sources of the organics in the asteroidal bodies.

However, stable isotopic compositions offer richer inventories of information than just bulk $\delta^{13}C$ and $\delta D$ that can provide significant further insights into these processes. The volatile reservoirs in the early solar system (ices and gases) had distinct triple oxygen isotopic composition ($\delta^{17}O$, $\delta^{18}O$), and organics should fractionate these isotopes depending on the thermodynamic conditions of the reaction. This gives us a different, and potentially more powerful approach to tracking the volatile reservoirs in the early solar system by measuring the triple oxygen isotopic compositions of organic compounds observed in the chondritic meteorites. However, such a measurement is challenging, given the small sample accounts and their presence as complex mixtures of compounds. Conventional isotope ratio mass spectrometry techniques are unable to mass resolve $^{17}O$-bearing isotopologues from neighboring $^{13}C$- and D-bearing ones, without the relatively arduous process of converting oxygen to $O_2$ (Ellis and Passey, 2023; Crocker et al., 2025), which can potentially modify oxygen isotope ratios. Moreover, how organics fractionate stable isotopes from their parental volatiles, and their propensity to undergo post-formational isotopic exchange with fluids, remains unknown. These unknowns warrant significant theoretical and methodological development, including predicting fractionation factors and developing a new analytical method, to facilitate this approach.

Here, I systematically address these unknowns. In Chapter 2, I constrain the triple oxygen isotopic fractionation between organic compounds and water or $CO/CO_2$, using quantum mechanical calculations. Using these fractionations, I predict the expected oxygen isotopic compositions of solar system organics, considering previously suggested formation mechanisms. I find that, various formation mechanisms should imprint organics with distinct compositions or trends in the triple oxygen isotope space. In Chapter 3, I experimentally document the kinetics of oxygen exchange between two classes of organic compounds and water. To do that, I develop a novel Orbitrap mass spectrometry-based method that can measure the oxygen isotopic ratio of these organics, even for small samples. I find that organics can be susceptible to exchange after formation if exposed to fluids in the long term. Finally, I measured the triple oxygen isotopic composition of organic acids extracted from CM chondrite Murchison using my new analytical method and present the results in Chapter 3. I find that organic acids have distinct triple oxygen isotopic compositions that suggest different volatile sources and different chemical processes that formed them. These insights advance the understanding of the origin of these compounds, with new insights into the early solar system evolution.

## Part II: Water-rock cycles on Mars

How the water-rock cycles occurred on Early Mars and facilitated its habitability remains unknown. There are two broad categories for planetary water-rock cycling: weathering and serpentinization. Serpentinization involves the reaction of water with olivine and pyroxene-rich rocks at elevated temperatures (typically ≥300 °C) to transform anhydrous silicates into phyllosilicate-carbonate assemblages, with magnetite and molecular hydrogen (Neal and Stanger, 1983; Tutolo and Tosca, 2023) as byproducts. Chemical weathering, by contrast, involves low-temperature (≤100 °C) reactions between near-surface aqueous fluids and silicate minerals, leaching and mobilizing cations that may subsequently precipitate in distant locations. The influence of these two processes on Martian habitability is profound. Serpentinization is associated with abiotic organic synthesis via Sabatier or Fischer-Tropsch reactions (Steele et al., 2022), which provide one of several possible pathways to the emergence of life. Serpentinization-generated molecular hydrogen, if outgassed at sufficiently high rates, can sustain a warm, habitable climate (Adams et al., 2025). Chemical weathering, on the other hand, serves to regulate long-term climate via $CO_2$ drawdown, leading to a negative feedback between surface temperature and the intensity of chemical weathering. The mineral products of serpentinization on Mars have been detected by the Mars 2020 Perseverance rover in the igneous Máaz formation on the Jezero Crater floor

(Tosca et al., 2025) and from orbit in terranes like Claritas Rise and the Nili Fossae (Ehlmann et al., 2010). The organic-phyllosilicate-carbonate assemblages in several of the Martian meteorites have also been interpreted as serpentinization products (*4*,*5*). Evidence for chemical weathering is limited to the orbital observation of various clay deposits on Martian terranes. The spectral observation of Fe-Mg clays overlain by Al-clays in these deposits suggests their production followed by chemical evolution through extensive chemical weathering (Ye and Michalski, 2022; Moore et al., 2025). How these processes cycle life-essential nutrients such as carbon, liquid water, and their role in the evolution of the Martian climate remains elusive.

Carbonate minerals are products of this water-rock cycling. These minerals have been observed on Mars. The isotopic compositions of their carbon, oxygen, and cations each reveal near-surface conditions and water-rock cycling that formed them. Particularly, their Mg isotopic compositions are useful indicators of the water-rock cycles that exported their cations and are widely used in a terrestrial context. Measurement of Mg isotopic compositions of Martian carbonates has the potential to highlight the water-rock cycles on Mars.

However, there are numerous challenges to conducting this investigation. The ways that different water-rock cycling mechanisms fractionate Mg isotopes in different carbonates is unknown. Pending Mars Sample Return, our only access to Martian carbonates is from Martian meteorites, where different generations of carbonates are present in minor (<1 weight %) quantities. Existing bulk-digestion isotope ratio measurements are unable to distinguish between Mg isotopic compositions of different carbonates and end up averaging them. These carbonates cannot possibly be mechanically isolated to conduct a clean bulk digestion analysis. This required the development of a method that can analyze Mg isotopic compositions in situ, in domains as small as 5 µm.

I address these questions systematically in the second part of my thesis. In Chapter 5, I use quantum mechanical calculations to predict fractionation of Mg, C and O isotopes between different hydrous and anhydrous carbonate minerals relevant to Mars. I find that weathering and serpentinization should impart distinct signatures on their product carbonates. Moreover, hydrous and anhydrous carbonates fractionate Mg isotopes differently. In Chapter 6, I present the development of a new ion microprobe-based technique to analyze Mg isotopic composition of carbonates *in situ*. I document natural and synthetic standards for this method and evaluate its accuracy and precision. Using these developments, I finally measured Mg isotopic composition of ~3.94 Ga carbonates from the Martian meteorite ALH84001, which is our only archive to near-surface conditions of early Mars. I find that under the evaporative early Martian conditions, hydromagnesite precipitated in the near-surface environments, with cations derived from the weathering of clays. This reveals modulation of weathering on the Martian carbon cycle, and how it could have possibly caused climatic transitions that created a favorable environment for the emergence of life. This significantly advances our understanding of early Martian habitability. The analytical method I develop here enables future studies on extraterrestrial carbonates such as those from asteroids Ryugu and Bennu and in samples returned from Mars in the future.

## References

Adams D., Scheucher M., Hu R., Ehlmann B. L., Thomas T. B., Wordsworth R., Scheller E., Lillis R., Smith K., Rauer H. and Yung Y. L. (2025) Episodic warm climates on early Mars primed by crustal hydration. *Nat. Geosci.* **18**, 133–139.

Crocker D. R., Sutherland K. M., Freudenberg B., Alonso K., Pearson A., Ward C. P. and Johnston D. T. (2025) Tracking Photo-Oxidation Reactions of Aquatic Organic Matter Using Triple Oxygen Isotopes. *ACS Earth Space Chem.* **9**, 1780–1790.

Ehlmann B. L., Mustard J. F. and Murchie S. L. (2010) Geologic setting of serpentine deposits on Mars. *Geophys. Res. Lett.* **37**, 2010GL042596.

Ellis N. M. and Passey B. H. (2023) A novel method for high-precision triple oxygen isotope analysis of diverse Earth materials using high temperature conversion–methanation–fluorination and isotope ratio mass spectrometry. *Chem. Geol.* **635**, 121616.

Lee M. R., Tomkinson T., Hallis L. J. and Mark D. F. (2015) Formation of iddingsite veins in the martian crust by centripetal replacement of olivine: Evidence from the nakhlite meteorite Lafayette. *Geochim. Cosmochim. Acta* **154**, 49–65.

Moore R. D., Goudge T. A., Klidaras A., Horgan B. H., Broz A., Wordsworth R. and Farrand W. H. (2025) Deep chemical weathering on ancient Mars landscapes driven by erosional and climatic patterns. *Nat. Astron.*, 1–9.

Neal C. and Stanger G. (1983) Hydrogen generation from mantle source rocks in Oman. *Earth Planet. Sci. Lett.* **66**, 315–320.

Steele A., Benning L. G., Wirth R., Schreiber A., Araki T., McCubbin F. M., Fries M. D., Nittler L. R., Wang J. and Hallis L. J. (2022) Organic synthesis associated with serpentinization and carbonation on early Mars. *Science* **375**, 172–177.

Tosca N. J., Tice M. M., Hurowitz J. A., Pedersen D. A. K., Henneke J., Mandon L., McCubbin F. M., Ross O., Tung P.-Y., Harrison R. J., Li A., Schmidt M. E., Kizovski T. V., Liu Y., Mayhew L., Jones M. W. M., Labrie J., Davidoff S., Allwood A. C., Beyssac O., Brown A., Cable M., Comellas J., Clark B. C., Galvin A. E., Horgan B., Heirwegh C. M., Nemere P., Orenstein B. J., Quantin-Nataf C., Royer C., Treiman A., Wade L. A., Wiens R. and Wright A. P. (2025) In situ evidence for serpentinization within the Máaz formation, Jezero crater, Mars. *Sci. Adv.* **11**, eadr8793.

Tutolo B. M. and Tosca N. J. (2023) Observational constraints on the process and products of Martian serpentinization. *Sci. Adv.* **9**, eadd8472.

Ye B. and Michalski J. R. (2022) Chemical weathering over hundreds of millions of years of greenhouse conditions on Mars. *Commun. Earth Environ.* **3**, 266.

# PART I

# ORIGIN OF THE OXYGEN-BEARING ORGANICS IN THE SOLAR SYSTEM

## *Chapter 2*

# OXYGEN ISOTOPE EQUILIBRIA OF O-BEARING ORGANIC COMPOUNDS BASED ON FIRST PRINCIPLE QUANTUM MECHANICAL MODELS

Surjyendu Bhattacharjee[1*], John M. Eiler[1]

[1]Division of Geological and Planetary Sciences, California Institute of Technology, Pasadena, CA-91125, USA

*Corresponding Author: sbhattac@caltech.edu

Bhattacharjee S. and Eiler J. M. (2024) Oxygen isotope equilibria of O-bearing organic compounds based on first principle quantum mechanical models, and implications for their use in the study of extraterrestrial organics. Geochim. Cosmochim. Acta 380, 96–111.

## Abstract

We report theoretically calculated equilibrium oxygen isotopic fractionation factors ($^{17}O/^{16}O$, $^{18}O/^{16}O$) between a set of representative O-bearing organic molecules and water, as well as site specific $^{13}C$, $^{15}N$ and $^{13}C$-$^{18}O$ equilibrium clumped isotopic anomalies in these compounds, all computed using density functional theory (DFT) methods combined with Urey-Bigeleisen-Mayer (UBM) calculations of reduced partition function ratios. We performed density functional theory (DFT) calculations with the B3LYP exchange correlation functional, and explored different basis sets, and treatments of solvation. After benchmarking results against prior theoretical and empirical studies, we conclude that B3LYP level of theory and aug-cc-pVTZ basis set with cluster solvation provides the most accurate treatment of this problem within the constraints of our approach. A representative set of O bearing organic compounds including aldehyde, ketones, amino acid and aromatic alcohol are predicted to be ~24 – 41 ‰ higher in $^{18}O/^{16}O$ relative to water with $\theta_{\text{compound – water}}$ varying in the range 0.522 – 0.526; and ~23 – 41 ‰ lower in $^{13}C/^{12}C$ and ~11 ‰ higher in $^{15}N/^{14}N$ relative to $CO_2$ and $N_2$, respectively (presuming equilibrium partitioning) at 273 K. This study is motivated by the study of soluble organic molecules found in carbonaceous chondrite meteorites, a significant fraction of which contain oxygen in their structure in the form of functional groups such as carbonyl, carboxylic acid, ester, ethers, and alcohol. These samples also contain oxygen-bearing macromolecular organic matter. We use the fractionation factors presented here to predict the triple oxygen isotope compositions of these organics, assuming equilibration with previously proposed early-solar-system volatile reservoirs and environments of organic synthesis.

## 2.1 Introduction

Oxygen bearing organic compounds are composed of molecules in which carbon and oxygen atoms are directly bonded, forming functional groups such as alcohol, aldehyde, ketone, carboxylic acid, ester, and ether. Oxygen bearing organic compounds participate in biochemical cycles in organisms (Ardawi and Newsholme, 1982; Bruss, 1997; VanItallie and Nufert, 2003), are components of biomass (West et al., 2008; Sacia et al., 2015; Liu et al., 2018), byproducts of petroleum refining processes (Hoffmann et al., 2016), present in industrial and automobile emissions (e.g., Kean et al., 2001; Ho et al., 2006; Correa & Arbilla, 2008; Kim et al., 2008; Seo & Baek, 2011), products of atmospheric photochemistry (e.g., Lary & Shallcross, 2000; Grannas et al., 2002; Liu et al., 2022), and are components of meteorites (Jungclaus et al., 1976; Aponte et al., 2019; Simkus et al., 2019). Carbonyl compounds, a subset of oxygen bearing organic compounds where carbon-oxygen double bonds are present, are widespread in natural and synthetic chemistry (e.g., King, 1970; Trost, 1978; Alabugin et al., 2019; Yuan et al., 2020; Foley & Waldmann, 2022), and are extensively used in polymer industry (e.g., Letsinger & Mahadevan, 1965; Nishikubo & Kameyama, 1993; Ley, 1997; Shi et al., 2012), fragrance synthesis (e.g., Villa et al., 2008; de Freitas et al., 2013; Vieira et al., 2012), and pharmaceutical applications (e.g., Ohta et al., 1987; Govindh et al., 2012; Rossi et al., 2018; Hossain et al., 2019).

Conditions and mechanisms of natural formation of these compounds is a field of active research. Analysis of the isotopic composition of oxygen (i.e., measurements of relative proportions of the three stable isotopes, $^{16}$O, $^{17}$O and $^{18}$O) in these compounds can potentially indicate source substrates (e.g., environmental water), pathway of formation (which dictates the O isotopic fractionation between substrate and product), and temperature of formation. However, there is relatively little prior data for oxygen isotope compositions of natural organic molecules, and particularly few prior studies that constrained proportions of all three isotopes (‘triple oxygen isotope measurement’). Oxygen isotope measurements of organic compounds face several analytical challenges, including separation of individual molecule analytes from complex mixtures and the fact that conventional gas source magnetic sector isotope ratio mass spectrometers lack sufficient mass resolution to resolve $^{13}$C from $^{17}$O peaks without the relatively arduous process of converting oxygen to $O_2$ (Ellis and Passey, 2023). The only substantial body of triple oxygen isotope data for natural organics has used the ion microprobe to conduct bulk (i.e., material average, as opposed to compound specific) measurements of kerogen and macromolecular organic material (Tartese et al., 2016a, 2016b, 2018). There is also limited prior research examining $^{18}O/^{16}O$ ratios of carbonyl compounds (Bramley et al., 1962; Vederas, 1980; O'Reilly and DeNiro, 1983). We are aware of no prior site-specific oxygen isotope measurements of natural organic molecules. However, the emergence of Orbitrap-enabled isotope ratio mass spectrometry could provide a means for broad exploration of oxygen isotopic compositions of organics, including compound-specific, site-specific and triple isotope measurement capabilities (Eiler et al., 2017; Hofmann et al., 2020; Mueller et al., 2021; Zeichner et al., 2022, 2023). The exceptionally high mass resolution of this approach permits direct observation of $^{17}O$ (and $^{18}O$) even in C-bearing molecules with no preparatory chemical transformation, analysis of fragment ions by this technique can constrain site-specific isotopic distributions, and Orbitrap instruments can be found on platforms designed for on-line chromatographic isolation of diverse volatile and soluble organic molecules.

The emergence of a platform for routine oxygen isotope measurements of organics creates a need for knowledge of isotopic fractionation factors involving oxygen-bearing organic compounds, as such data are essential to interpret oxygen isotopic signatures as constraints on substrates and formation mechanisms and conditions. In this study, we report theoretically calculated equilibrium triple oxygen isotopic fractionation factors (i.e., for both $^{17}O/^{16}O$ and $^{18}O/^{16}O$ ratios) between a set of representative O-bearing organic molecules (including representative aldehyde, ketone, amino acid, and aromatic alcohol) and water, as well as site-specific $^{13}C$, $^{15}N$ fractionations and $^{13}C$-$^{18}O$ equilibrium clumped isotopic anomalies in these compounds, using density functional theory (DFT) combined with the Urey-Bigeleisen-Mayer (UBM) model (Bigeleisen and Mayer, 1947; Urey, 1947). Prior similar studies conducted with this level of theory have demonstrated it provides a useful framework for the expected directions and magnitudes of isotope exchange equilibria (e.g., Wang et al., 2004; Schauble et al., 2006; Wang et al., 2009a, 2009b; Dennis et al., 2011; Wang et al., 2013; Piasecki et al., 2016a, 2016b; Xie et al., 2018; Dong et al., 2021; Zeichner et al., 2023). Nevertheless, future studies should refine the model predictions presented by comparison with additional experimental constraints and explore the relationships between partition function ratios we present and more complex, kinetically controlled chemical isotope effects (e.g., Watkins et al., 2017).

This work was conceived as a preparation for the laboratory study of oxygen isotope compositions of early solar system organic compounds. Formation of carbonyl compounds from the substrates available in the early solar system and the diverse mechanisms of prebiotic organic syntheses are expected to leave characteristic triple oxygen isotope signatures of the product organic compounds. The discussion section of this paper presents predictive models of expected O isotope compositions of select meteoritic organic compounds, for representative scenarios describing their possible origins and the oxygen reservoirs with which they interacted.

## 2.2 Methods

### 2.2.1 Calculation details

#### 2.2.1.1 Models of gas phase molecules

We used Density Functional Theory (DFT) to predict equilibrium structures of studied molecules and to obtaining the harmonic vibrational frequencies of unsubstituted and isotopically substituted species. Initial structures were prepared using the Avogadro chemical visualization package (Hanwell et al., 2012). These structures were energy minimized to obtain equilibrium geometries using DFT, assuming gas phase molecules *in vacuo,* using the B3LYP exchange correlation functional (Becke, 1993) and aug-cc-pVDZ (hereon, 'DZ') as well as aug-cc-pVTZ (hereon, 'TZ') basis sets (Woon and Dunning Jr, 1993). The B3LYP exchange correlation functional has been found to render accurate predictions of partition function ratios for compounds relevant to our study in different systems from previous studies, specifically for organic compounds (e.g., Rustad et al., 2008; Hill et al., 2014; Iron and Gropp, 2019; Boettger and Kubicki, 2021; Liu et al., 2022). Based on the findings of these prior studies, and the fact that B3LYP has been widely used for modelling organic compounds more generally, we decided this approach would provide the highest level of consistency with the recent literature. DFT calculations were done using the ENTOS Qcore simulation package (Manby et al., 2019) (with default criteria for geometry optimization convergence parameters). The optimized structure computed using B3LYP/aug-cc-pVDZ was used as the initial structure for the B3LYP/aug-cc-pVTZ computation. Harmonic vibrational frequencies for unsubstituted and isotopically substituted species for each molecule were computed using the optimized structure, at both B3LYP/aug-cc-pVDZ and B3LYP/aug-cc-pVTZ levels; frequencies calculated using aug-cc-pVTZ basis sets were used to calculate reported isotopic fractionations (see below), while those computed using aug-cc-pVDZ basis sets were used for cluster size analysis (see below) and benchmarking predicted O isotope fractionation against experimental data. All harmonic frequency calculations are done using ENTOS. Coulomb and exact exchange contribution to Fock matrix and energy is calculated using integral-direct approach (integral threshold was set at $10^{-12}$). The aug-cc-pVTZ basis set has been previously found to be sufficiently large for convergence of equilibrium energy and structures of small organic compounds (Rustad, 2009). Calculations at the B3LYP/aug-cc-pVTZ level are computationally expensive and not practically feasible for cluster size analysis, explicit solvation simulations (see section 2.1.3) or benchmarking studies described in this study. We have performed some of the benchmarking and cluster size analysis presented here using B3LYP/aug-cc-pVDZ level of theory (described in captions/legends of diagrams) and reported the preferred fractionation factors at B3LYP/aug-cc-pVTZ level. Any difference arising between ${}^{18}\beta$ of the same system calculated using aug-cc-pVDZ and aug-cc-pVTZ basis sets is attributed to basis set size (i.e., aug-cc-pVTZ is a larger basis set than aug-cc-pVDZ and is expected to render more accurate predictions). However, this difference is small (<1.4 ‰, see *the supplementary material section 1* for details), indicating that for small organic molecules, even the aug-cc-pVDZ basis set might have converged appropriately; this conclusion is similar to findings of Rustad (2009) (~1 ‰ difference for site specific ${}^{13}\beta$ in amino acids).

### 2.2.1.2 Models of solvated molecules assuming implicit solvation

Implicit solvation treats a solvent as a continuum media in which the solute is placed. We used the COSMO solvation model to account for solvation of molecules of interest by water. The dielectric constant of water was set at 80.4 (while settings for geometry optimization and vibrational frequency calculations used default implementations in

ENTOS), and models were calculated at B3LYP/aug-cc-pVDZ and B3LYP/aug-cc-pVTZ levels, with the D3 dispersion correction with zero damping (Grimme et al., 2010). Strict convergence criteria have been used to ensure close convergence to energy minima and to avoid producing model results that include imaginary frequencies. Geometry optimization for acetone with COSMO solvation was first done using ORCA (Neese et al., 2020) at B3LYP/aug-cc-pVTZ level using very tight optimization criteria for geometry optimization and tight criteria for self-consistent field for hessian matrix calculation. The optimized structure of acetone calculated using ORCA was further optimized using ENTOS before vibrational frequency calculation. Since a number of computational differences (e.g., B3LYP implementation, convergence criteria, grid settings etc.) can impact DFT calculations done using these two systems, we have additionally constrained the extent of such effects on calculated $^{18}\beta$. The difference between 1000ln($^{18}\beta$) of gas phase acetone calculated using ORCA and ENTOS at TZ level is less than 0.1 ‰. Organic compounds can have a variety of conformations that can influence isotope fractionation. Such effects have been observed previously for $^{13}C/^{12}C$ fractionations (Watts et al., 2011). However, the compounds modelled in this work are expected to have minimal conformational effects. We are not aware of any prior study that constrains the effect of conformation on $^{18}O/^{16}O$ fractionation involving organic compounds. A detailed investigation of this effect is beyond the scope of this work but remains to be constrained in future studies.

#### 2.2.1.3 Models of solvated molecules assuming cluster solvation and model for liquid water

Implicit solvation cannot accurately model solvation in aqueous systems, as it fails to simulate the hydrogen bonding network in the liquid and specific configurational effects associated with water-solute interactions (e.g., for phenol and alanine). To account for this, hydration has instead been described by adding water molecules around the molecule of interest (hereon, 'cluster solvation'). We specify clusters with a variable number of water molecules around a compound of interest. The structure of organic molecule - water clusters were adapted from lowest energy configurations found in previous studies (Parthasarathi et al., 2005; Chuchev and BelBruno, 2008; Mullin and Gordon, 2009; Shields et al., 2010; Vaquero et al., 2014; McNeill et al., 2020; Romero-Montalvo and DiLabio, 2021). These cluster structures are then geometry optimized multiple times at DZ and subsequently TZ levels of theory with convergence criteria mentioned in section 2.1.2, until an energy minimum is reached. After convergence, the structure of each cluster was again compared with that from prior studies to ensure consistency before vibrational frequency calculation. Vibrational frequencies are then calculated for those optimized geometries using convergence criteria mentioned in section 2.1.1. The model for liquid water was constructed using the same approach. Structures of clusters with up to 12 water molecules were adopted from previous studies (Shields et al., 2010; Walczak et al., 2011) and subjected to similar geometry optimization and vibrational frequency calculation scheme.

#### 2.2.1.4 Models of solvated molecules assuming explicit solvation

For benchmarking purposes, explicit solvation (where a molecule of interest is surrounded by water molecules, and the COSMO model is also applied to describe the broader solvation environment of that cluster) has been applied to phenol, acetone and alanine with 1-10 water molecules surrounding a molecule of interest, all computed at the DZ level, with geometry optimization convergence criteria and vibrational frequency calculation criteria mentioned in sections 2.1.2 and 2.1.3. We did not attempt explicit solvation at the TZ level, as it is computationally expensive. Instead, we calculate: (1) the difference between cluster and explicit solvation models for $^{18}$O reduced partition function ratios ($^{18}\beta$) calculated at the DZ level and (2) the difference between DZ and TZ level prediction for the $^{18}\beta$ value calculated for the same system, which we combine to estimate the difference between cluster and explicit models at TZ level (see *the supplementary material, section 1*).

#### 2.2.1.5 Comparison of solvation models

To test how different solvation models compare to one another, acetone has been modelled with implicit (TZ), explicit (DZ) and cluster (DZ, TZ) solvation models; and both phenol and alanine each modeled with both cluster and explicit (DZ) models. Initial geometries of an acetone – 2 water cluster are adapted from Romero-Montalvo & DiLabio (2021) (hereafter

Acetone – 2wERM) and Śmiechowski (2009) (hereafter Acetone – 2wM). The initial structure of an Alanine – 7 water cluster is adapted from (McNeill et al., 2020). That for a Phenol – 3 water cluster is adapted from Parthasarathi et al. (2005). All these structures are energy minimized and vibrational frequencies are obtained as described in previous sections.

### 2.2.1.6 Comparison of effects of incomplete basis sets (DZ vs TZ)

Conventionally, a finite size analysis for basis set effect is performed by calculating a specific $\beta$ factor using Hartree-Fock or post Hartree-Fock DFT methods with progressively larger basis sets (like aug-cc-pVDZ, aug-cc-pVTZ and so on to complete basis set limit) (e.g., Hill et al., 2014) to see the convergence of the $\beta$ factor with basis set size. Such detailed and computationally demanding calculations are beyond the scope of the present work. To test for basis set effect for convergence, calculations for several systems were performed with both DZ and TZ levels of theory and the results compared. See *the supplementary material section 1* for details. We do not go beyond TZ level as aug-cc-pVTZ basis set has been previously been found to be sufficiently large for convergence of $\beta$ factors for compounds that are similar to this study (Hill et al., 2014, 2020) and we also note good agreement between TZ-predicted fractionation factors with experimental data (see section 4.1). Finally, we found that difference between 1000ln($^{18}\beta$) at DZ and TZ calculations are small (~1 ‰ or less at 273 K).

### 2.2.2 Theory and terminology of partition function ratios

The unscaled harmonic vibrational frequencies calculated by the methods described above were used to compute partition function ratios (PFRs) using the model of Urey (1947) and Bigeleisen & Mayer (1947) (hereafter, UBM Model), which adopts the harmonic approximation:

$$\frac{Q'}{Q} = \left(\frac{m'}{m}\right)^{\frac{3r}{2}} \left(\frac{\sigma}{\sigma'}\right) \prod_{i=1}^{n} \left\{\frac{v_i'}{v_i} \frac{\exp\left(-0.5U_i'\right)}{\exp\left(-0.5U_i\right)} \frac{\left[1 - \exp\left(-U_i\right)\right]}{\left[1 - \exp\left(-U_i'\right)\right]}\right\}$$

where: $Q$ = Partition function for one isotopologue, ($Q'/Q$) = partition function ratio (PFR), $n$ = no. of normal modes of the system, $m$ = mass of the isotope being exchanged, $\sigma$ =

symmetry number of the system, $U = (h\nu/k_BT)$ where $\nu$ is the frequency of a normal mode, $h$ = Planck constant, $k_B$ = Boltzmann constant and $T$ = temperature at which the PFR is calculated. Values annotated with a prime symbol (') are for heavy-isotope substituted species, whereas those without a prime symbol are for the unsubstituted, or isotopically 'normal', species.

PFR's were then used to compute equilibrium isotope ratio fractionation factors between the compound of interest and an isolated atom of the element whose isotopic substitution is being considered. Such fractionations are referred to as 'reduced partition function ratios', RPFR values, or β factors. The β factor is defined as:

$$^{\mathrm{x}}\beta = \left[\left(\frac{Q'}{Q}\right)\left(\frac{m}{m'}\right)^{\frac{3r}{2}}\right]^{\frac{1}{r}}$$

Where x denotes the corresponding heavy isotope for which RPFR is calculated (e.g., x = 13, 15, 17, 18 for $^{13}$C, $^{15}$N, $^{17}$O, $^{18}$O respectively (see Chacko et al., 2001 for a relatively recent review). Equilibrium isotopic fractionations generally follow the transitive arithmetic property, thus isotopic fractionation factors between two molecules A and B, $\alpha_{\mathrm{A\text{-}B}}$, can be calculated as ratios of their respective β values:

$$^{\mathrm{x}}\alpha_{\mathrm{A-B}} = \frac{^{\mathrm{x}}\beta_{\mathrm{A}}}{^{\mathrm{x}}\beta_{\mathrm{B}}}$$

For triple oxygen isotope fractionation, the mass law for equilibrium isotopic fractionation between an atom in molecule A and isolated atom of that same element is denoted here as $k_{\mathrm{A-atom}}$ (equation from Cao and Liu, 2011) :

$$k_{\mathrm{A-atom}} = \frac{\ln(^{17}\beta_{\mathrm{A}})}{\ln(^{18}\beta_{\mathrm{A}})}$$

Finally, the mass law for triple isotope fractionation between two molecules A and B, $\theta_{\mathrm{A-B}}$, is derived from the respective α values as:

$$\theta_{\mathrm{A-B}} = \frac{\ln(^{17}\alpha_{\mathrm{A-B}})}{\ln(^{18}\alpha_{\mathrm{A-B}})}$$

For calculation of equilibrium clumped isotopic abundances, only adjacent C and O atoms are considered here (i.e., we assume for the sake of simplicity that thermodynamic preferences for or against non-adjacent heavy isotope clumping are negligible). We focus our attention on clumped isotope reactions in which two singly substituted reactants - a $^{13}C$ substituted species and a $^{18}O$ substituted species - react to form a $^{13}C$—$^{18}O$ clumped isotope species and an unsubstituted molecule as products. For example, such a reaction for Acetone would be:

$$H_3{}^{12}C—{}^{13}C^{16}O—{}^{12}CH_3 + H_3{}^{12}C—{}^{12}C^{18}O—CH_3 = H_3{}^{12}C—{}^{13}C^{18}O—{}^{12}CH_3 + H_3{}^{12}C—{}^{12}C^{16}O—{}^{12}CH_3$$

Following the formalism of Wang et al. (2004), the equilibrium constant ($K$) for such a reaction can be written as:

$$K = \frac{Q_{13-18}\,Q_{12-16}}{Q_{13-16}Q_{12-18}}$$

Where subscript 13 – 18 denotes a molecule with adjacent (bonded) $^{13}C$ and $^{18}O$ in it. This equation can be rearranged as:

$$K = \frac{\left({}^{Q_{13-18}}/_{Q_{12-16}}\right)}{\left({}^{Q_{13-16}}/_{Q_{12-16}}\right)\left({}^{Q_{12-18}}/_{Q_{12-16}}\right)}$$

Note that ($Q_{13\text{-}16}/Q_{12\text{-}16}$) is the PFR for $^{13}C$ substitution and ($Q_{12\text{-}18}/Q_{12\text{-}16}$) is that for $^{18}O$ substitution. Then we follow Wang et al. (2004) formalism to define the clumped isotopic anomaly, $\Delta_{13\text{-}18}$ (a measure of the enrichment relative to a stochastic proportion) as:

$$\Delta_{13-18}\ (‰) = -1000 \ln \frac{K}{K_\infty}$$

Where $K_\infty$ stands for the equilibrium constant at the stochastic limit (e.g., high temperature). Note that this definition of Δ value differs from that generally used to report clumped isotope analyses; these differences are insignificant when heavy-isotope abundances are in the natural terrestrial and solar-system range, but become significant (i.e., measurable) for highly isotope enriched materials.

For the molecules considered here, ${}^{x}\beta$, ${}^{x}\alpha_{A\text{–}B}$, $\theta_{A\text{–}B}$ and $\Delta_{13\text{–}18}$ are available as functions of temperature in the *data repository* (see data availability statement below). We present values for ${}^{x}\alpha_{A\text{–}B}$ values for ${}^{13}C/{}^{12}C$, ${}^{18}O/{}^{16}O$ and ${}^{15}N/{}^{14}N$ as fractionations between: 'A': the compound of interest ('A'); and 'B': gaseous $CO_2$ (for ${}^{13}C/{}^{12}C$), liquid water (for ${}^{18}O/{}^{16}O$), or gaseous $N_2$ (for ${}^{15}N/{}^{14}N$). $\theta_{A\text{–}B}$ values are reported as the mass law for triple oxygen isotope fractionation between molecule A and liquid water (e.g., $\theta_{A\text{–water}}$).

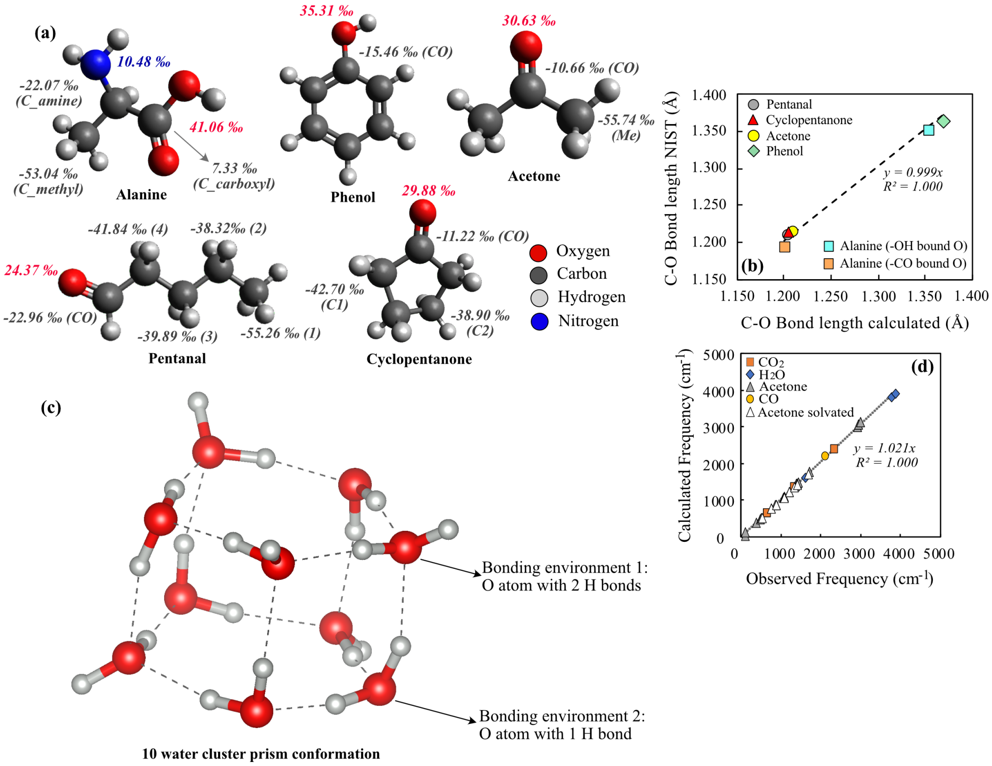

Figure 2.1: Structures of compounds and clusters modelled in this study. (a) Geometries of molecules considered in this study, annotated with the average position-specific fractionation factors (α values) for ${}^{13}C/{}^{12}C$ in gray (relative to gaseous $CO_2$), ${}^{18}O/{}^{16}O$ in red (relative to liquid water) and ${}^{15}N/{}^{14}N$ in blue (relative to $N_2$ gas) labelled by on the atoms. Names of sites are indicated in parentheses and correspond to fractionations presented in the *data repository*. (b) Comparison between gas phase C-O bond length calculated in this study and the same from NIST webbook for all the molecules modelled. (c) Structure of 10 water cluster used as best water model in this study. (d) Comparison between calculated and observed vibrational frequencies for molecules studied here (observed vibrational frequencies from Shimanouchi, 1973; Zhang et al., 1993; Chacko et al., 2001). Solid line represents best fit to the dataset.

## 2.3 Results

### 2.3.1 Bond lengths and geometries, and overview of isotopic fractionation factors

Equilibrium geometries of all solvated minimized structures are available in the *data repository*. Fig. 2.1a illustrates the geometries of solvated molecules considered in this study, annotated with the average position-specific fractionation factors (${}^{x}\alpha$ values) for ${}^{13}C/{}^{12}C$ (relative to gaseous $CO_2$), ${}^{18}O/{}^{16}O$ (relative to liquid water) and ${}^{15}N/{}^{14}N$ (relative to $N_2$ gas) labelled on the atoms. We have compared C-O bond lengths of the gas phase molecules calculated in this study at TZ level to experimental C—O bond length data

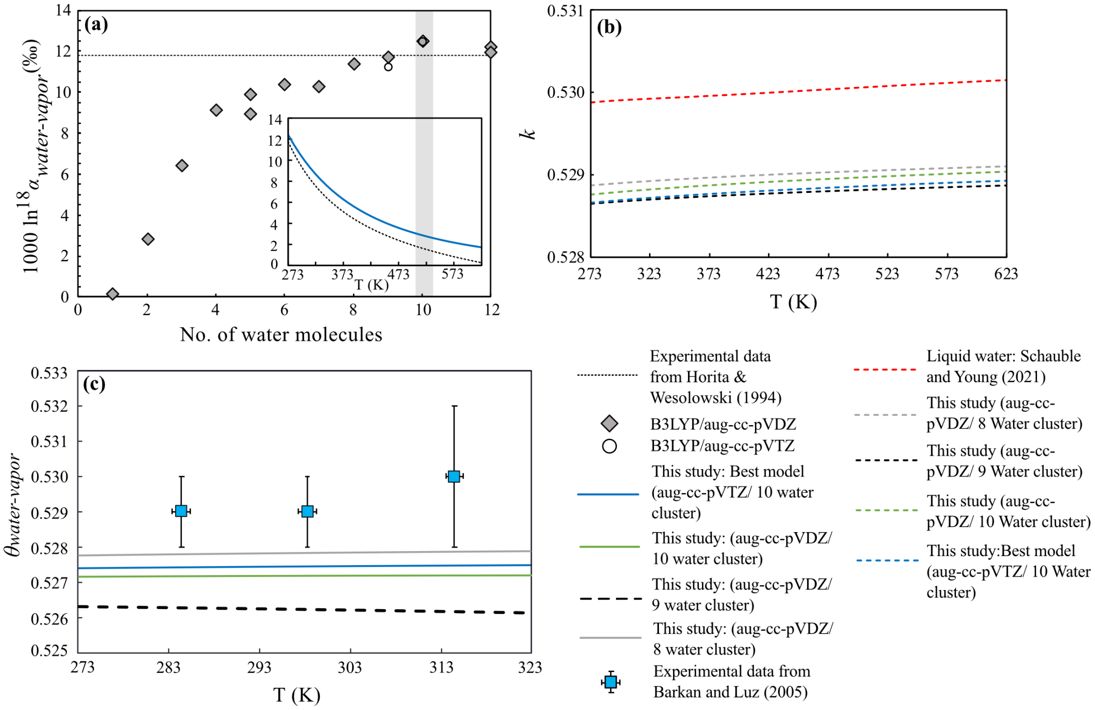

Figure 2.2: Cluster size analysis for water clusters. (a) Predicted ${}^{18}O/{}^{16}O$ fractionation between liquid water and water vapor (vapor pressure isotope effect; VPIE) with variable water cluster size at DZ (diamond) and TZ (circle) level at 273 K. Dotted line indicates experimental data from Horita & Wesolowski (1994). Shaded vertical bar indicates best model from this work. *Inset:* Comparison of experimentally determined temperature dependence of this VPIE (dotted line) with best model from this study (blue line). (b) Comparison of $k$ vs T relationship for various water clusters and comparison with calculations from Schauble & Young (2021). (c) Comparison between experimentally derived $\theta$ vs T relationship for this VPIE ( denoted as squares; after Barkan & Luz, 2005) and predictions from this study (solid and dashed lines)

available in Computational Chemistry Comparison and Benchmark DataBase (https://cccbdb.nist.gov/). Excellent agreement is noted for experimental and computed C—O bond lengths in gas phase (Fig. 2.1b). Calculated and experimentally observed vibrational frequencies agree well (Fig. 2.1d).

### 2.3.2 Cluster size analysis and Benchmarking for $CO_2$, water

We evaluated how many water molecules are necessary for RPFR values computed by cluster solvation models to converge to constant values as functions of numbers of explicit waters (following methods previously discussed by Zeebe, 2010). Water molecules are added, one by one, to a system containing a molecule of interest, and for each resulting geometry and energy minimization is done and harmonic vibrational frequencies and RPFR values are calculated. We refer to this analysis as *cluster size analysis*. In this work, this has been done for $^{18}\beta$ for water, $CO_2$, alanine and phenol at the DZ level. The cluster size analysis for water alone (Fig. 2.2a) is presented as the $^{18}O/^{16}O$ vapor pressure isotope effect (VPIE) in liquid-water — water-vapor system. This model, calculated at both the DZ and TZ levels of theory, converges on the experimentally measured value of 11.76 ‰ at 273 K (Horita & Wesolowski, 1994) when cluster size reaches 8 or more water molecules. The $k$ value for liquid water (i.e., the oxygen isotope mass exponent for its $^{18}O$ and $^{17}O$ RPFR's) also converge for water clusters in this size range (Fig. 2.2b). And, the calculated $\theta_{\text{liquid–vapor}}$ values (the mass exponent for the VPIE) for models containing 8 or more water molecules in a cluster are all close to experimental values across a range of temperatures (Barkan & Luz, 2005; though the 9 water cluster is noticeably anomalous). We conclude that the best liquid water model for our purposes contains 10 water molecules in a cluster.

Cluster size analysis for the $CO_2$-water cluster is conducted using the $^{18}O/^{16}O$ fractionation between $CO_2$ solvated in liquid water and $CO_2$ vapor, calculated at the DZ level (previously modelled by Rustad et al., 2008; Boettger and Kubicki, 2021). The convergence is much faster in this system (Fig. 2.3a) with $CO_2$ + 4 water cluster being closest to the experimental data (O'Neil and Adami, 1969; Vogel et al., 1970; Beck et al., 2005). Modelled temperature dependence of this fractionation (Fig. 2.3b) is also in agreement with experimental data.

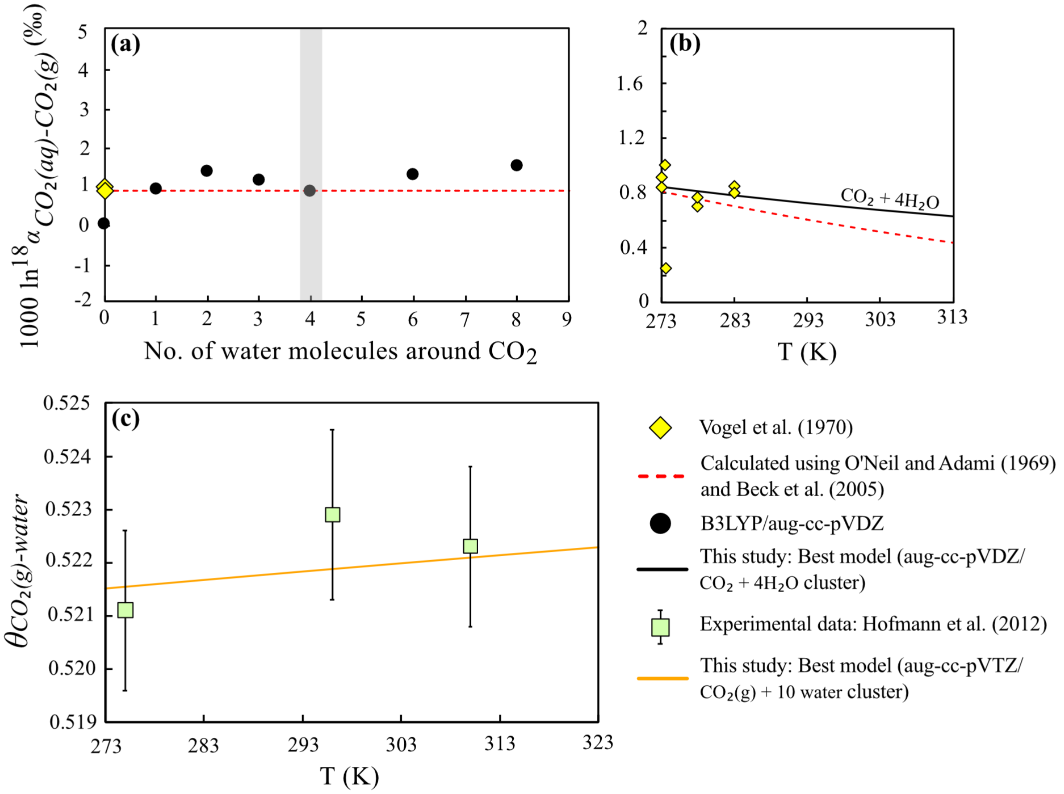

Figure 2.3: Cluster size analysis for $CO_2$ in water solvation isotope effect for $^{18}O/^{16}O$ fractionation between $CO_2$ solvated in water and gas phase $CO_2$ (solvation isotope effect; SIE) with cluster solvation at DZ level. (a) Predicted $^{18}O/^{16}O$ SIE effect for $CO_2 + nH_2O$ cluster at 273 K (solid circles); vertical shaded bar indicates best model from this study; dotted line indicates magnitude of $^{18}O/^{16}O$ SIE calculated from experimental data (O'Neil and Adami, 1969; Beck et al., 2005). (b) Comparison between experimentally derived temperature dependence of this $^{18}O/^{16}O$ SIE (yellow diamonds; Vogel et al., 1970) with best model ($CO_2 + 4H_2O$) from this study. (c) Comparison between experimentally derived $\theta$ vs T relationship for equilibrium $CO_2$(g) – liquid water $^{18}O/^{16}O$ fractionation (green squares; Hofmann et al., 2012) and prediction from best model of this study (orange line).

Finally, our model predictions of the mass law exponent for the oxygen isotope fractionation between gaseous $CO_2$ and liquid water (i.e., as represented by a 10-water-molecule cluster model) agree within experimental uncertainty with that reported by Hofmann et al. (2012) (Fig. 2.3c).

### 2.3.3 Cluster size analysis for alanine-water, phenol-water clusters

Alanine has two structurally distinct oxygen atoms: one in a C=O group and one in a C—O—H group (though they undergo rapid interconversion through proton transfer). Finite size analyses have been done for both the oxygen atoms in alanine solvated by clusters of water molecules, computed at DZ level at 273 K (Fig. 2.4a). $^{18}\beta$ for both oxygen sites approximately converge at 10 water molecules in the cluster, but variations in $^{18}\beta$ with number of water molecules are more pronounced for the C—O—H group. For phenol (Fig. 2.4b), this analysis has been done with 3, 4 and 8 water clusters at 273 K and all of them resulted in similar $^{18}\beta$. However, while calculating $^{18}\beta$ for phenol solvated by 8 water molecules (at TZ level of theory), one imaginary mode (~8 cm$^{-1}$) was observed. After an imaginary frequency was first noted, we re-adjusted the starting structure of 8 water cluster

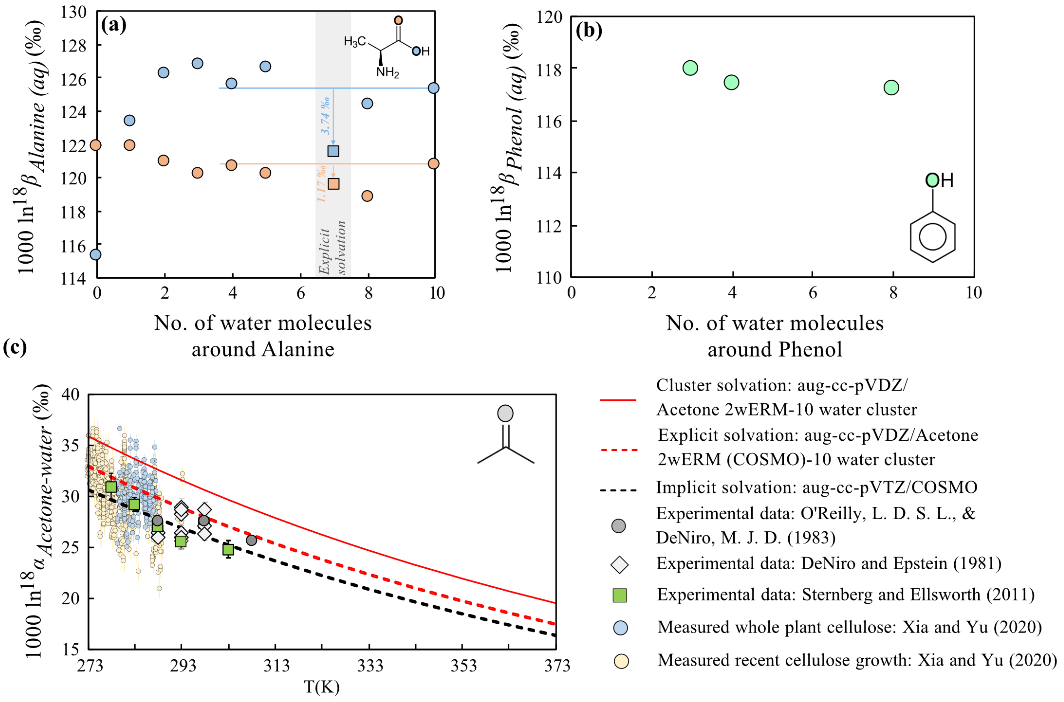

Figure 2.4: Cluster size analysis for different compounds. (a) $^{18}\beta$ of Alanine-water clusters at DZ level at 273 K. Orange circles indicate carbonyl oxygen and blue circles indicate -OH bound oxygen. Squares of same color indicate $^{18}\beta$ calculated with explicit solvation. Difference between explicit and cluster solvation is indicated with arrows and numbers. (b) $^{18}\beta$ of Phenol-water clusters at DZ level at 273 K. (c) Comparison of implicit, explicit and cluster solvation for acetone. Symbols indicate experimental data. See legend for details.

and performed geometry optimization. Even after repeating this procedure multiple times, we did not obtain a result that lacked the imaginary frequency. We have also tried moving the atom's position along the along the vector of vibration to overcome the imaginary mode. Even after moving the atom's position along the vector of vibration and consequent recalculation twice, the issue was not resolved. We then switched to a lower complexity model with 3 waters in the cluster, and the optimization concluded without any imaginary frequency. The $^{18}\beta$ and $k$ values calculated for 8 water cluster, ignoring the imaginary mode ('Truhlar's approach', Bursch et al., 2022), were negligibly different from that of 3 water clusters at 273 K (by 0.7 ‰ and 0.0007 respectively). We report the isotopic fractionation factors for phenol using 3 water cluster model at TZ level.

### 2.3.4 Comparison of solvation models and benchmarking with experimental data

Implicit, cluster and explicit solvation models were applied to acetone—water clusters to demonstrate the difference between different solvation models, and to benchmark those models against experimental data (DeNiro and Epstein, 1981; O'Reilly and DeNiro, 1983; Sternberg and Ellsworth, 2011; Xia and Yu, 2020); see Fig. 2.4c. Cluster solvation with two water molecules predicts higher acetone-water $^{18}O/^{16}O$ fractionation compared to calculation with implicit solvation for 2wERM and 2wM models. Both explicit solvation (Acetone 2wERM, DZ level) and implicit solvation (TZ level) yield acetone-water $^{18}O/^{16}O$ fractionations that are close to experimental data.

For alanine, explicit solvation predicts lower $^{18}\beta$ than cluster solvation (e.g., 3.74 ‰ lower for the C=O group and 1.17 ‰ lower for the C—O—H group, as compared to the 10-water cluster model, (Fig. 2.4a). Although the difference in $^{18}\beta$ between cluster and explicit solvation models is greater for C—O—H than C=O groups, their temperature dependence is similar (see the *supplementary material, Fig. S2.1)*. Finally, the difference in mass law between cluster and explicit models of these $^{18}\beta$ values (i.e., the change in $k$, or $\Delta k$) is greater for C—O—H than for C=O groups.

### 2.3.5 Synopsis of preferred predicted fractionation factors

The fractionation factors we consider most accurate, based on the level of theory and treatment of solvation used, are reported in Fig. 2.5 and Table 2.1. Preferred ${}^{18}\alpha_{\text{compound–water}}$ and $\theta_{\text{compound–water}}$ for acetone, cyclopentanone, pentanal are reported at TZ level including implicit solvation and that for alanine and phenol are reported at TZ level with cluster solvation. TZ-level fractionation factors are preferred because they are expected to be more precise as they suffer less from incomplete basis set effects. For ${}^{18}\alpha$ between various molecules of interest and water (Fig. 2.5a**),** alanine (molecular average ${}^{18}\beta$, formulated by averaging ${}^{18}\beta$ of C=O and C—O—H site, is used to calculate ${}^{18}\alpha_{\text{alanine–water}}$) is predicted to exhibit the highest enrichment in heavy oxygen isotopes relative to liquid water (33.8 ‰ at 303 K), phenol the second highest (29.4 ‰), Cyclopentanone and acetone sub-equal to each other and third highest (24.4 and 25.2 ‰, respectively), and pentanal the least enriched in ${}^{18}$O (20.4 ‰). The temperature dependence and mass laws ($\theta$ values) of these molecule-water fractionations are broadly similar to one another (Fig. 2.5b).

$\Delta_{13\text{-}18}$ values (Fig. 2.5c) are different for different functional groups: aldehyde (pentanal) is more enriched in ${}^{13}$C—${}^{18}$O bonding than ketones (acetone, cyclopentanone). While C=O bonds in alanine are similar to those of ketones (as expected, given their shared bond order), the ${}^{13}$C—${}^{18}$O clumping for C—O—H oxygen in alanine is much lower; because these two sites freely interconvert in alanine dissolved in water, the average of these two should be considered representative of the carboxyl group.

Molecular average ${}^{13}$C abundance relative to gaseous $CO_2$ is presented in Fig. 2.5d; all studied compounds are predicted to be 36.3 to 20.9 ‰ lower (at 303 K) in ${}^{13}$C/${}^{12}$C than $CO_2$, with an amplitude that decreases with increasing temperature. Alanine shows the least depletion (21.0 ‰), cyclopentanone showing the second least depletion (31.7 ‰) whereas pentanal and acetone sub-equally show the most depletion (35.3 and 36.3 ‰ respectively), all compared to $CO_2$(g) at 303 K.

Finally, we predict that isotopic equilibrium between gaseous $N_2$ and the $NH_2$ group in alanine concentrates $^{15}N$ in the latter, by 7.3 ‰ at 303 K (Fig. 2.5e).

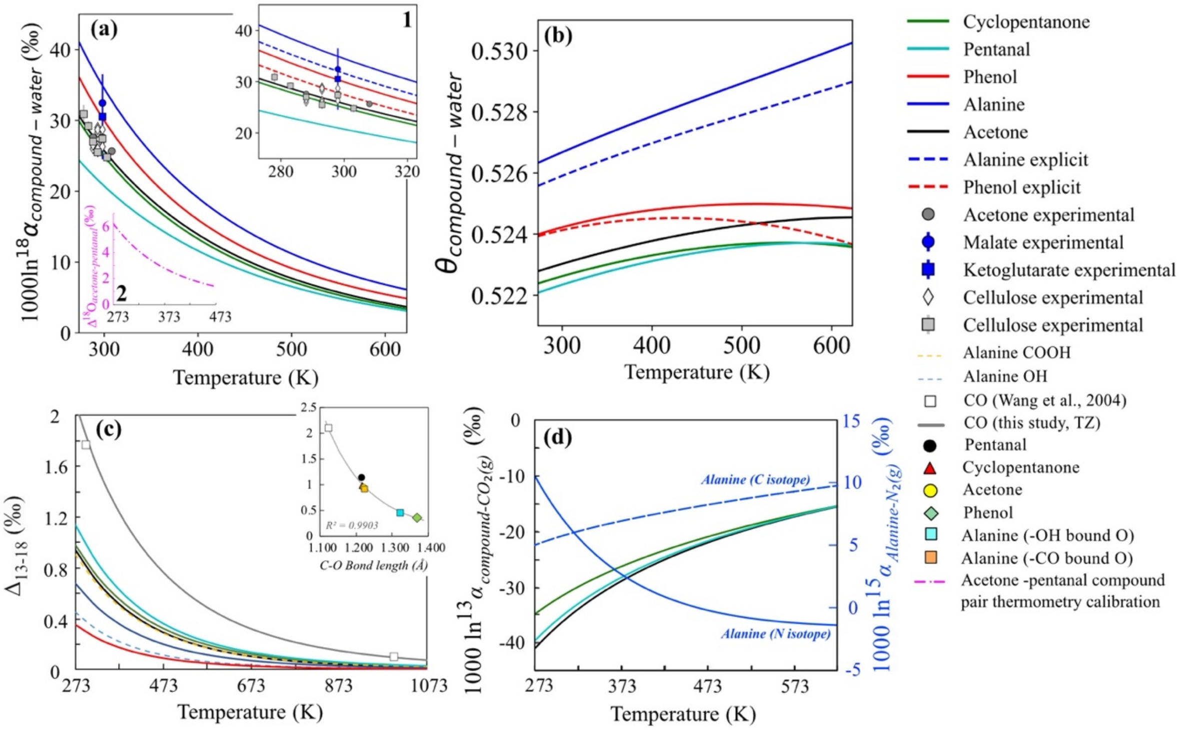

Figure 2.5: Final reported fractionation factors calculated at TZ level. (a) Temperature dependence of $^{18}O/^{16}O$ fractionation between compounds and liquid water. Inset 1 shows same fractionation at 273 - 323K with explicit solvation (DZ level) as dotted lines for alanine and phenol. Experimental data: 'Malate experimental' (blue circles, Blanchard & Cleland, 1980), 'ketoglutarate experimental' (blue squares, Rife & Cleland, 1980), 'cellulose experimental' (white diamonds; DeNiro & Epstein, 1981), cellulose experimental (gray squares; Sternberg & Ellsworth, 2011), acetone experimental (gray circles, O'Reilly & DeNiro, 1983). Inset 2 shows calibration of co-existing acetone - pentanal oxygen isotope thermometer over 273 K - 473 K, assuming they are in mutual equilibrium. (b) Mass laws for fractionations in (a); dotted lines indicate explicit solvation at DZ level for phenol and alanine. (c) Relationship between equilibrium $^{13}C$-$^{18}O$ clumped isotopic abundances and temperature involving solvated compounds investigated in this study at TZ level, inset shows correlation between equilibrium $^{13}C$-$^{18}O$ clumped isotopic abundances vs C-O bond lengths at 273 K. Dotted line indicates a best fit line with correlation coefficient shown in figure. (d) Molecular average $^{13}C/^{12}C$ fractionation vs. $CO_2$(g) and $^{15}N/^{14}N$ fractionation vs. $N_2$(g); unlabeled solid lines indicate $^{13}C/^{12}C$ fractionation between compounds and $CO_2$(g).

## 2.4 Discussion

### 2.4.1 Trends in fractionation and mass law: $^{13}$C, O, $^{13}$C-$^{18}$O

Our results indicate that the degree of enrichment in $^{18}$O in the oxygen bearing organic molecules examined in this study (assuming equilibrium with each other, water or some other common phase) follows the order: alanine > phenol > acetone ~ cyclopentanone > pentanal. This trend is broadly consistent with qualitative expectations based on bonding environment: Carboxylic acid groups should concentrate heavier oxygen isotopes more than the other compounds studied here as they have both a stiff C=O double bond (stiffer compared to C=O bond in ketones, characterized by higher C=O stretching frequency in alanine compared to acetone in gas phase) *and* extensive hydrogen bonding with aqueous solvents. Phenol has a lower order C—O bond (in the C—O—H group), on the other hand, but also participates in strong hydrogen bonding with solvating waters (Fennell and Dill, 2011), resulting in a RPFR that is lower than alanine but still higher than the relatively hydrophobic ketones and aldehydes. Ketones possess a C=O double bond but lack extensive hydrogen bonding with solvating water and hence concentrate heavy oxygen isotopes less than does alanine (in gas phase, in absence of any solvent interaction, alanine has higher $^{18}$O RPFR than acetone which in turn has a higher $^{18}$O RPFR than phenol — consistent with the discussion above). Aldehydes also have a C=O double bond but are also relatively hydrophobic. Moreover, their C=O bond always involves a terminal carbon that also possesses one C—C and one C—H bond; in contrast, the C=O double bond in ketones occurs in the interior of the molecule and the other bonds to the C atom in question are both C—C bonds, which provide a tighter bonding environment; this explains why ketones have higher $^{13}$C/$^{12}$C RPFRs as compared to aldehydes.

There is minimal prior experimental data for oxygen isotope fractionations involving exchange between organic molecules and water. However, the one available prior set of experiments on $^{18}$O/$^{16}$O fractionation between acetone and water (O'Reilly and DeNiro, 1983) agree well with our preferred model of this system (Fig. 2.5a inset; 5c). Moreover, cellulose in plants is hypothesized to reflect oxygen isotopic equilibrium between ketones and the growth medium water (as they form via hydration of ketone intermediate in synthetic pathways that lead to ketones being in isotopic exchange equilibrium with water); i.e., cellulose – water $^{18}O$ fractionations should approximate ketone – water oxygen isotope fractionation (DeNiro and Epstein, 1981; O'Reilly and DeNiro, 1983; Sternberg and Ellsworth, 2011). Plant culture experiments conducted at controlled temperatures, followed by determination of cellulose – water $^{18}O/^{16}O$ fractionation (DeNiro and Epstein, 1981; Sternberg and Ellsworth, 2011), exhibit fractionations that agree in magnitude, direction and temperature dependence with those we calculate for acetone – water and cyclopentanone – water. Measured cellulose – water $^{18}O/^{16}O$ fractionations for samples from natural plants (Xia and Yu, 2020) show a larger spread (Fig. 2.4c) but on average also match our experimental data. Prior experimental data for oxygen isotope fractionations between malate and water (Blanchard and Cleland, 1980) and ketoglutarate and water (Rife and Cleland, 1980) are similar to our calculated alanine – water $^{18}O/^{16}O$ equilibria, consistent with the approximation that the -COOH group in carboxylic acids generally have similar RPFR's and fractionations with respect to water. Finally, a prior theoretical study (Cleland, 1980) calculates a $^{18}O/^{16}O$ fractionation of 32.5‰ between isopropanol and water at 298 K; this approaches our phenol – water $^{18}O$ exchange prediction (30.4 ‰ at 298 K). The agreement noted between the predicted and experimentally constrained fractionation factors resulted from a complex combination of experimental (study design, isotopic measurements) and computational (effect of systematic errors, incomplete basis set, choice of solvation model, implementation of B3LYP functional, numerical errors, computational parameters, harmonic UBM model etc.) factors. Most of the computational effects expressed as error cancellation during fractionation factor calculation, which led to close match with experimental data.

To the best of our knowledge, no triple oxygen isotope exchange experiments (i.e., examining $^{17}O/^{16}O$ ratios as well as $^{18}O/^{16}O$ ratios) have been reported in systems containing oxygen-bearing organic molecules. However, our findings suggest a relationship between the chemical environment of organic-bound oxygen (i.e., the functional group hosting the oxygen atom) and calculated values of $\theta_{\text{compound–water}}$ (order of $\theta_{\text{compound–water}}$ : alanine > phenol > acetone ~ cyclopentanone > pentanal at 273 K), similar to previous modeling results of Cao & Liu (2011). According to general rules proposed by Cao & Liu (2011) concerning the relationship between $k$ values and T (see their section 4.5), the oxygen in a carbonyl group should have a lower $k$ than an oxygen in an -OH because the former involves a higher mass bonding partner than the latter (following Cao & Liu's rule 1, noting that the magnitude of this difference will also depend on the harmonic frequencies in the two compounds). Moreover, Cao & Liu (2011) would predict that -OH bound oxygen should have a flatter trend of *k* vs T, as compared with carbonyl oxygen (following their rule 2). Both of these predictions match the relationship of *k* vs T calculated in this study. These concepts also offer an interpretation of the relative differences among *k* values associated with oxygen isotope substitution in –OH groups in alanine and phenol. Phenol has higher frequencies of vibrational modes that are sensitive to O isotope substitutions (highest frequency shift upon $^{18}$O substitution noted at 3812 cm$^{-1}$ mode) compared to alanine (highest frequency shift upon $^{18}$O substitution noted at 1135 cm$^{-1}$ band). Hence, phenol has lower values of *k* compared to -OH in alanine, as suggested by Cao & Liu (2011). All mass laws calculated in this study approach the high temperature limit at higher temperatures, following rule 2 of Cao & Liu (2011).

All of the C=O-bearing compounds are predicted to be lower in $^{13}$C/$^{12}$C relative to $CO_2$(g) in isotopic equilibrium (Fig. 2.5d), reflecting the stiffer bonding environment for C in $CO_2$ compared to that in aldehydes and ketones. However, carbonyl carbon atoms are expected to be higher in $^{13}$C/$^{12}$C compared to methyl or aliphatic carbon (by 45‰ for acetone, 31.5‰ maximum for cyclopentanone and 32.6‰ maximum for pentanal at 273 K); thus, O bearing organics that conform to an equilibrium distribution of $^{13}$C among all carbon sites will generally exhibit pronounced site-specific isotopic variations. Similarly, aliphatic carbons in cyclopentanone are relatively enriched in $^{13}$C compared to methyl C in acetone, a difference that can be attributed to the greater proportion of relatively stiff C—C bonds in alkyl positions of cyclopentanone (two C—C bonds, compared to one C—C bond and 3 C—H bonds in methyl carbon). Overall, these results are consistent with previous findings of similar trends in site specific carbon isotope equilibria in amino acids (Rustad, 2009; McNeill et al., 2020;).

Variations in predicted $\Delta_{13\text{-}18}$ values at some reference temperature are also correlated with the functional group hosting the oxygen atom. More specifically, enrichment in proportions of $^{13}$C—$^{18}$O substituted C—O bonds correlates with the C—O bond length of the functional group (Fig. 2.5c inset). Results of this study can be used as a basis for thermometry from $^{13}C$—$^{18}O$ clumping in oxygen bearing organic compounds.

Finally, our finding that alanine is predicted to be higher in $^{15}N/^{14}N$ than $N_2(g)$ (at mutual equilibrium), owing to a combination of short N-H bond length (1.016 Å; this study) in alanine compared to $N_2$ (1.098 Å; Sutton & Bowen, 1958) as well as shift of higher frequency vibrational modes in alanine upon isotopic substitution by $^{15}N$.

### 2.4.2 Possible applications to early solar system organics

#### 2.4.2.1 Oxygen-bearing organic compounds in the early solar-system

Organic compounds are found in many carbonaceous chondrite meteorites. An early report of amino acids from the Murchison CM chondrite (Kvenvolden et al., 1971) dates back to 1970s. Subsequent studies have reported the presence in this and related samples of various organic compounds including alcohols (Sephton, 2002), monocarboxylic acids (Epstein et al., 1987), dicarboxylic acids (Pizzarello and Huang, 2002), carbonyl compounds (Simkus et al., 2019), sugars (Furukawa et al., 2019), polycyclic aromatic hydrocarbons (PAH), and nucleobases (Martins et al., 2008), and sulfur and nitrogen bearing hetero-compounds (Sephton, 2002), all accompanied by a larger fraction of macro-molecular, insoluble organic matter (IOM, Sephton et al., 1998; Alexander et al., 2022). Carbon and hydrogen isotope ratios of the solvent-extractable compounds and IOM are often (though not always) distinct from ratios typical of terrestrial organics.

Oxygen bearing organic compounds are a subset of the organics found in meteorites. Major structural types of these compounds include amino acids, mono- and dicarboxylic acids, alcohols and carbonyl compounds. IOM from carbonaceous chondrites also contains O, but with poorly known (and possibly poorly defined) chemical bonding environments. It should also be noted that O bearing organics have been detected astronomically in star forming environments (Charnley et al., 2001; Thi et al., 2004; Agúndez et al., 2008).

These O-bearing organic compounds in carbonaceous chondrites are generally interpreted to be prebiotic in nature, but several possible substrates, environments and mechanisms of origin are possible, including: Fischer-Tropsch-type chemistry of CO, $H_2$, $NH_3$ in the solar nebula or parent body interiors, perhaps with the aid of mineral catalysts

(Hayatsu and Anders, 1981); photochemistry, including ice-grain chemistry, in the interstellar medium (ISM) and molecular clouds (Agarwal et al., 1985; Singh et al., 2022); and aqueous syntheses on meteorite parent bodies (i.e., interiors of asteroids; Simkus et al., 2019). Experimental irradiation of methanol and other ices at ISM conditions produce organic compounds broadly similar to those found in extraterrestrial materials and settings but have not generated the great diversity and complexity of soluble organics found in carbonaceous meteorites, possibly suggesting that nebular or parent body processes are responsible for much of this diversity (though also plausibly simply a reflection of sensitivities and biases in spectroscopic observations of extra-solar-system settings). Finally, it should be noted that the aldehydes and ketones may also be consumed by prebiotic reactions such as Strecker synthesis in nebular and asteroidal environments (see Mejía et al., 2020; Singh et al., 2022 and references therein).

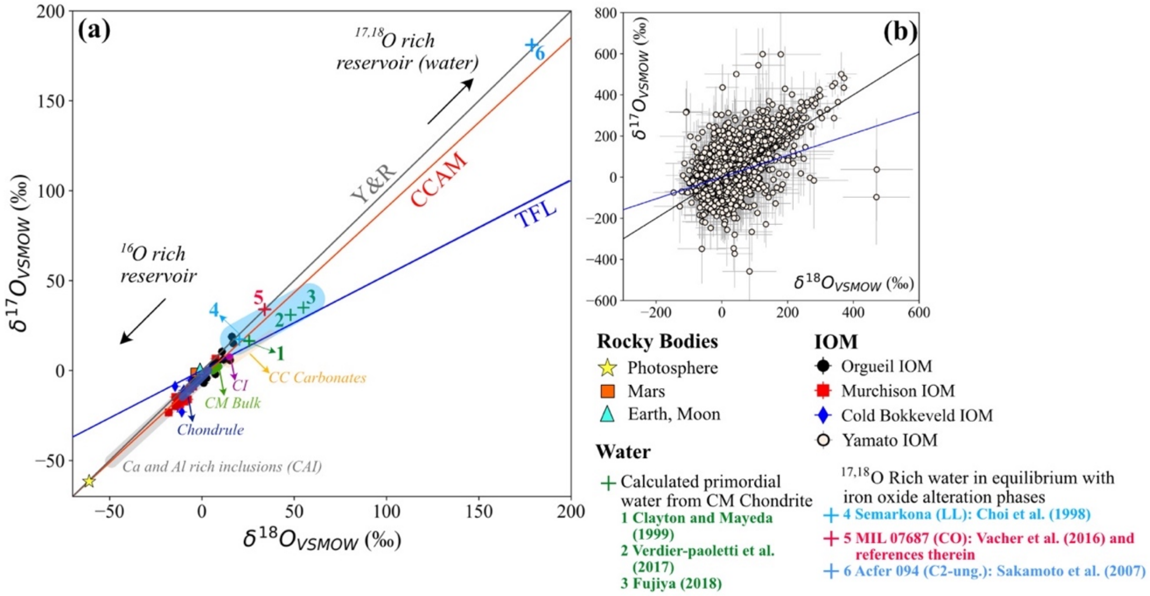

Figure 2.6: Triple oxygen isotopic composition of solar system components. (a) Rocky planets, solar photosphere (McKeegan and Leshin, 2001) and insoluble organic matter (IOM) measured from carbonaceous chondrites Orgueil, Murchison and Cold Bokkeveld (Tartèse et al., 2018). Fields of CAI, Chondrules, CI, CC Carbonates and CM bulk are after Tartèse et al. (2018). Blue fields and '+' symbols with numbers indicate isotopic composition of water (see legend for references). (b) Triple O isotopic composition of IOM from carbonaceous chondrite Yamato (Hashizume et al., 2011). TFL = Terrestrial fractionation line, CCAM = Carbonaceous chondrite anhydrous minerals, Y&R = slope 1 mixing line of Young and Russel (1998).

The three stable isotopes of oxygen - $^{16}O$, $^{17}O$, $^{18}O$ - form by different nucleosynthetic processes and are present in variable proportions in distinct extraterrestrial environments (i.e., interstellar medium ice or nebular gas). Moreover, chemical processing in the early solar system led to variations in oxygen isotope ratio among meteorites and various solar system bodies. These variations are generally classified as following either 'mass dependent' trends, where $^{17}O/^{16}O$ variations are approximately half of $^{18}O/^{16}O$ variations (more precisely, they follow a line with slope of ~0.52–0.53 in a plot of $\delta^{17}O$ vs. $\delta^{18}O$), or 'mass independent' trends, where $^{17}O/^{16}O$ and $^{18}O/^{16}O$ variations deviate from a mass-dependent trend. The terrestrial fractionation line, TFL, is a mass dependent trend that passes through the oxygen isotope composition of the bulk earth. Anhydrous minerals from carbonaceous chondrites closely conform to a pure mass independent oxygen isotope variation; the line of slope ~1 they define in a plot of $\delta^{17}O$ vs $\delta^{18}O$ plot is referred to as Carbonaceous Chondrites Anhydrous Material line, or CCAM). The $^{17}O$ anomaly ($\Delta^{17}O$ value) is a measure of a sample's departure from the TFL and is calculated as the difference between a material's $\delta^{17}O$ value, and the $\delta^{17}O$ value it would have if it conformed to the TFL at its $\delta^{18}O$ value.

The CCAM trend has been interpreted as a mixing line between oxygen from a $^{17}O$,$^{18}O$ rich reservoir of $H_2O$ that was generated photochemically in the early solar system or inherited from pre-solar compounds from or ISM or nebular ice (possibly due to photochmistry in a pre-solar-system setting) and a $^{16}O$ rich reservoir of CO that made up the majority of early solar system O (McKeegan and Leshin, 2001). Current models invoke CO self-shielding, or isotope selective photochemical dissociation of CO, in the early solar system to create $^{17}O$,$^{18}O$ rich water ice in the outer solar system (Clayton et al., 1973; Clayton, 2002; Lyons and Young, 2005). Such oxygen isotope compositions have been reported for alteration phases from the LL chondrite Semarkona (Choi et al., 1998), ungrouped carbonaceous chondrite Acfer 094 (Sakamoto et al., 2007) and estimated from CO chondrite MIL 07687 (Vacher et al., 2016 and references therein). Triple O isotopic composition of waters responsible for aqueous alteration of parent bodies of CM chondrites have also been calculated (Clayton & Mayeda, 1999; Verdier-Paoletti et al., 2017; Fujiya, 2018) and are modestly enriched in $^{17}O$ and $^{18}O$ relative to the bulk earth, plotting close to the intersection of the TFL and CCAM (Fig. 2.6a).

The O contained in organic compounds potentially constrains the role of early solar system oxygen reservoirs in organic synthesis. This O appears in several different kinds of molecular sites, including C=O double bonds (aldehydes, ketones), carboxylic acid groups, and OH sites in alcohols and sugars. These differ in their relative rates of O isotope exchange with water. Aldehyde and ketone compounds are generally thought to be less susceptible to O exchange with water compared to carboxylic acid or alcohols because of the doubly bonded O, making them preferred targets for measurements that aim to define their original triple oxygen isotope compositions (though it is important to note that there is little prior experimental data constraining quantitative rates of oxygen isotope exchange in such compounds). Although IOM does not conform to a well-defined chemical and structural type and its propensity to undergo isotopic exchange is not well known (generally macromolecules are thought to undergo slower oxygen isotope exchange with external water pool compared to functional groups such as carboxylic acid; see Wedeking & Hayes, 1983), it contains the only organic-associated O to have been previously measured for its O isotope composition pertaining to solar system materials (Hashizume et al., 2011; Tartèse et al., 2018;). These analyses of oxygen isotopes in IOM yield variable and somewhat ambiguous results; generally following the CCAM trend (Fig. 2.6).

We are aware of no previous measurements of triple oxygen isotopic compositions of individual organic molecules from meteoritic samples. Such measurements are challenging because of the low abundances of compounds of interest, and the inability of existing gas-source, sector, isotope ratio mass spectrometers to mass resolve $^{13}$C- and D- from $^{17}$O-bearing isotopologues. The advent of Orbitrap isotope ratio mass spectrometry (Eiler et al., 2017; Hofmann et al., 2020; Mueller et al., 2021; Zeichner et al., 2022, 2023) allows measurement of nano– to pico-molar quantities of individual organic molecules with sufficient mass resolution to resolve $^{13}$C- and D- from $^{17}$O isotopologues. This technology provides a plausible path to making precise analyses of triple O isotope compositions of carbonyl and other organic compounds extracted from carbonaceous chondrite meteorites. Csernica et al. (2023) demonstrated this possibility with a measurement of the $^{17}$O/$^{16}$O ratio of acetone using a Q Exactive Orbitrap mass spectrometer equipped with an ESI ion source. However, quantitative interpretation of such data will require constraints on the directions and amplitudes of oxygen isotope fractionations between O bearing organic molecules and other inorganic oxygen compounds (principally water). The quantum chemical calculations presented in preceding sections of this paper permit us to prepare for such measurements by predicting oxygen isotope compositions of meteoritic organic molecules, for several assumed formation scenarios.

#### 2.4.2.2 Predictions of possible O isotopic compositions of organic compounds in primitive meteorites

The O bearing organic compounds found in carbonaceous meteorites could have formed by any of several processes. Below we consider three of these mechanisms and the oxygen isotope signatures that might be expected to result:

(1) ***Formation from or equilibration with early solar system water reservoirs***. Oxygen bearing organics could form from inorganic and organic precursors during aqueous alteration of asteroid interiors. Simkus et al. (2019) proposed degradation of soluble amino acids and/or oxidation of IOM as potential mechanisms for forming carbonyl compounds during parent body alteration, based on compound-specific carbon isotopic compositions of aldehyde and ketones from the Murchison meteorite. And, oxygen-bearing organic compounds that were synthesized prior to parent body accretion (such as aldehydes that are observed in interstellar, nebular or disk settings; Gilmore et al., 1975; Hollis et al., 2004) could subsequently undergo oxygen isotope exchange with asteroidal pore waters. Timescales for such exchange are not known for the full range of compounds of interest and asteroid-interior conditions, but the few relevant published studies suggest full equilibration within days to weeks (Samuel and Silver, 1965; Greenzaid et al., 1968a, b). Thus, one of the more straightforward expectations is that organics found in meteorites or samples returned from aqueously altered primitive asteroids should have oxygen isotope compositions in equilibrium with their parent body waters at the temperatures of alteration.

We consider three families of compositions we might expect to find in extraterrestrial organics with such histories, each based on previous estimates of the oxygen isotope compositions of pore waters in the parent bodies of meteoritic and returned samples. The most common finding of prior studies of the aqueously altered and organic-rich

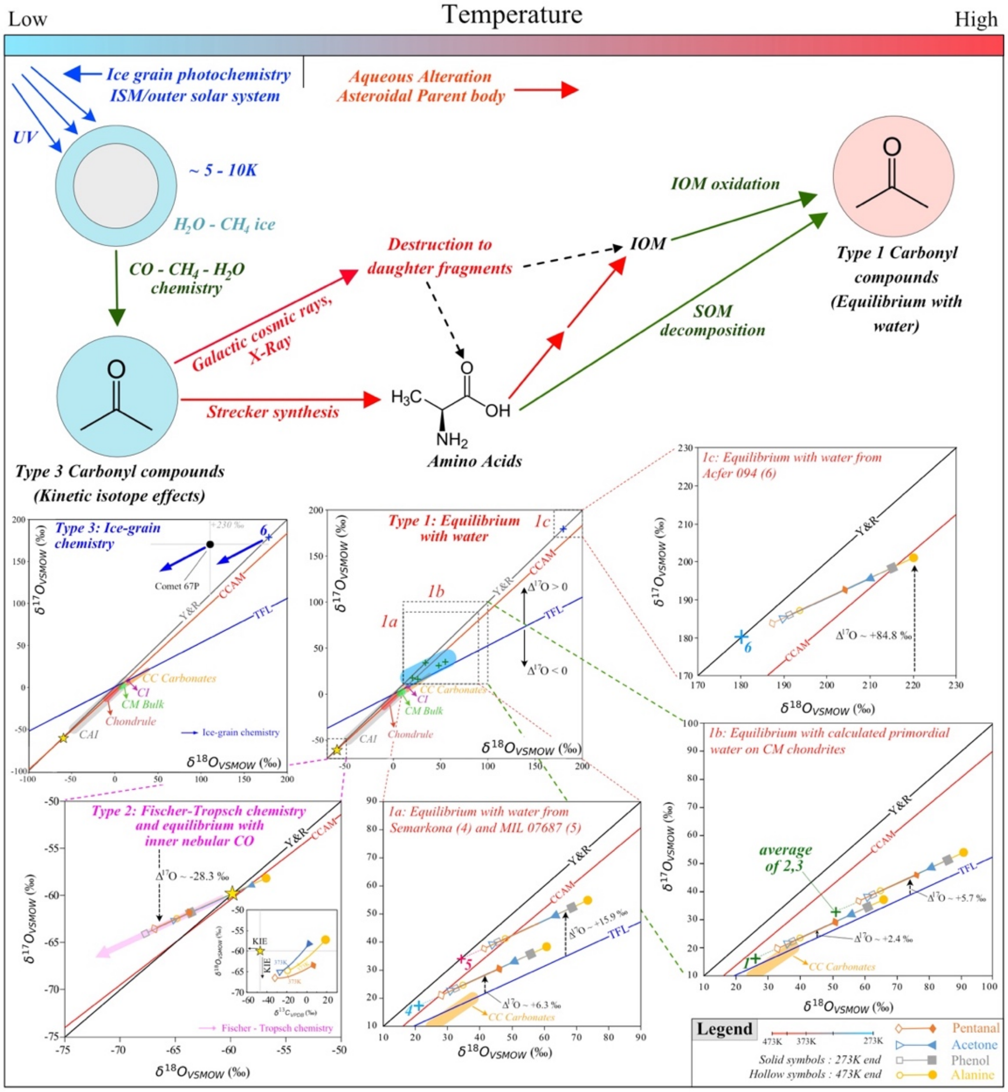

Figure 2.7: Probable mechanisms of formation of carbonyl compounds and resulting trends in triple isotopic space. Symbols and numerals for various water sources same as Fig. 2.6. Water sources and predicted equilibrium isotopic compositions of organic compounds are shown in boxes 1a-1c as linear trends in triple isotope space over a range of 273 K – 473 K. Solid and hollow symbols for any linear trend represent equilibrium composition of organics corresponding to 273 K and 473 K, respectively. As waters 2, 3 are very similar in isotopic composition, we have plotted the average $\delta^{17}O$, $\delta^{18}O$ of these two reservoirs and predicted trend of organics in equilibrium with this average composition in box 1b. Legend shows ideal anatomy of a trajectory with temperature tick marks and color-coded isotopic composition (blue end = more enriched, red end = less enriched; not to scale) for visual aid. For boxes where more than one fluid composition and corresponding organics are present (boxes 1a, 1b), a dotted line joining each fluid composition with the 473K end of corresponding

pentanal trajectory is shown. Dotted arrows indicate $^{17}O$ anomaly for organics formed from a specific fluid source. Triple O isotopic composition of organics in equilibrium with inner nebular CO or formed by FTT synthesis is shown in box 'Type 2', with inset showing the same in $\delta^{13}C$ - $\delta^{18}O$ space. Possible triple oxygen isotopic composition of organics formed as a product of ice-grain chemistry from water compositions similar to those inferred from comet 67P and Acfer 094 are shown in box 'Type 3'. SOM = soluble organic matter; IOM = insoluble organic matter.

carbonaceous chondrites (mostly CM, CI and CR chondrites) is that the initial water present on the parent bodies of said chondrites (calculated from oxygen isotopic compositions of hydrous silicate and carbonate alteration assemblages by mass balance approaches assuming closed system water rock reaction; Clayton and Mayeda, 1999; Verdier-Paoletti et al., 2017; Fujiya, 2018) plot close to the terrestrial fractionation line, with $\delta^{18}O$ values significantly higher than the carbonates and whole rock values of the hosts. Combination of these data with the equilibrium fraction factors presented in this study leads to predicted compositions of pentanal, acetone, phenol and alanine, as shown in box 1b of Fig. 2.7 (assuming molecule-water equilibration at temperatures between 273 and 473 K); these compositions would be appropriate for organics that formed before the alteration assemblages and did not subsequently undergo oxygen isotope exchange with more evolved waters. If the organics formed during or after the formation of the secondary alteration assemblages (i.e., from a water the alteration assemblages last equilibrated with, generally on or near the terrestrial fractionation line at $\delta^{18}O$ values below that of the whole-rock values of their hosts), they are expected to have $\delta^{17,18}O$ similar to the carbonates. Similar estimates for equilibrium with inferred parent body waters in the Semarkona, MIL 07687 and Acfer 094 meteorites (rare instances of samples containing aqueous alteration phases with strong $\Delta^{17}O$ enrichments; (Choi et al., 1998; Sakamoto et al., 2007; Vacher et al., 2016) are show in boxes 1a and 1c, respectively. Note that in all of these cases, oxygen isotope compositions of organics are predicted to fall to the right of the CCAM, near or above the terrestrial fractionation line. It is possible to constrain the temperature of formation or last equilibration of these compounds, and the oxygen isotopic composition of the water with which they equilibrated, using oxygen isotope thermometry of two or more co-existing compounds (assuming the two compounds attain mutual isotopic equilibrium at a given temperature with a water of given oxygen isotopic composition). One example of this approach is shown in Fig. 2.5a, inset 2, which illustrates the temperature dependence of the oxygen isotope difference between acetone and pentanal between 273 K and 473 K.

(2) ***Formation from volatiles in the pre-solar nebula and/or circumsolar disk***. If oxygen bearing organics formed from nebular volatiles by relatively high temperature Fischer – Tropsch type (FTT) reactions, they would inherit O atoms from CO of solar isotopic composition and thus should be relatively $^{16}$O enriched compared with the earth and most components of primitive meteorites (i.e., approaching the oxygen isotope composition of the sun, as established by the Genesis mission; (McKeegan et al., 2011). In case of FTT synthesis from a CO reservoir of solar composition, product organics would be expected to either directly inherit its isotopic composition ($\delta^{17,18}$O ~ −60 ‰), or be offset from that composition by a kinetic isotope effect associated with irreversible FTT reactions. To the best of our knowledge, there is no prior constraint on the magnitude or direction of such isotope effects, but if they follow common patterns of chemical-kinetic fractionations, they should lead to mass-dependent depletions in $^{18}$O and $^{17}$O, with amplitudes on the order of 10’s of per mil (pink arrow in Fig. 2.7, box 'Type 2'). If, instead, organics reached reversible oxygen isotope equilibrium with CO vapor (perhaps unexpected, given the limits in temperature at which organics can survive, but worth considering nonetheless), then these compounds will also be similar to or somewhat heavy-isotope depleted compared to solar oxygen isotope composition, reflecting the relatively high partition function ratio of CO as compared to $H_2O$ (this study; Schauble and Young, 2021). Carbon isotopic compositions of the organics might be used to distinguish whether organics formed by FTT synthesis or attained equilibrium with CO of solar composition. In case of FTT synthesis, organics are expected to inherit $\delta^{13}$C of CO or be offset to lower $\delta^{13}$C values due to kinetic isotope effect associated with the reaction (Lancet and Anders, 1970). Conversely, if they attained equilibrium with CO, they are expected to be 10's of per mil higher in $\delta^{13}$C than the CO (based on $^{13}$C RPFR of CO calculated in this study). Trajectories of organics in equilibrium with CO of solar composition (over 273 K – 473 K) is shown in inset of box 'Type 2', Fig. 2.7 along with directions of FTT reaction KIEs in $\delta^{13}$C (molecular average) - $\delta^{18}$O space, assuming CO of

solar photosphere has $\delta^{13}C = -48 \pm 7‰$ ($\delta^{13}C$ of CO in solar photosphere is not well constrained, this value is taken from a relatively recent prediction by Lyons et al., 2018).

(3) ***Formation by ice-grain chemistry in the interstellar medium. (ISM)***. The oxygen in the interstellar medium (ISM) is present as gas (dominantly CO) and as molecular ices (CO, $CO_2$, HCHO, $CH_3OH$, $H_2O$) (Loison et al., 2019). Irradiation of interstellar ice grains by UV photons, X-rays or galactic cosmic rays induces formation of complex organic compounds on ice surfaces and within icy mantles of grains (i.e., (Agarwal et al., 1985; Hodyss et al., 2009; de Marcellus et al., 2011; Almeida et al., 2014; Andrade et al., 2014; Abplanalp et al., 2016; Singh et al., 2022; Zhu et al., 2022). These are photoexcited, non-equilibrium reactions that involve radical intermediates. More specifically, radiolysis of $CH_4 - H_2O$ ice by galactic rays (Mejía et al., 2020) can lead to formation of CO and $CH_3CHO$ which can subsequently act as precursors for higher ketone/aldehyde synthesis (pathway 1). Alternatively, Singh et al. (2022) suggested that acetaldehyde forms when $CH_4$-CO ice is irradiated by galactic cosmic rays (at ~10 K) and acetone forms when $CH_4 - CH_3CHO$ ice is further irradiated with energetic electrons at ~5 K (pathway 2).

Telescopic measurements of $^{18}O/^{16}O$ from SO spectral lines of selected cold star-forming cores as well as cold molecular clouds indicate that these regions have higher $^{18}O$ abundance compared to solar system average (Loison et al., 2019). Similarly, $^{17}O$ is more abundant in gas phase of the local ISM compared to solar system average (Wilson, 1999). Being one of the most primordial materials, comets provide an important proxy to pre-solar volatile compositions. Water in the coma of comet 67P is enriched in $^{17}O$ and $^{18}O$ by 17 ± 6% (~170 ‰) and 11 ± 7% (~110 ‰) respectively relative to terrestrial values (Schroeder et al., 2019); although the uncertainties in these measurements are far larger than the isotopic variations and fractionations of interest to the study of most solar system materials, they are consistent with a composition on CCAM trend, at a position similar to the most extreme water compositions inferred from study of aqueously altered meteorites. Thus, a plausible initial guess regarding the oxygen isotope compositions of organics formed by reactions in pre-solar or outer solar system ices is that they are equal to those measured in water from comet

67P and inferred from aqueous alteration phases in the Acfer 094 meteorite, or offset from such compositions by kinetic isotope effects associated with ice grain reactions.

We are not aware of any prior constraints on the sizes, directions or mass laws of oxygen isotope kinetic effects associated with ice-grain reactions at astrochemically relevant conditions. However, a plausible first guess is that they are mass dependent and 'normal' in direction (favoring transfer of light isotopes from reactants to products); in this case, we would expect product organics to have oxygen isotope compositions that fall along the blue arrows in Fig. 2.7 box 'Type 3'.

Carbonyl compounds are relatively resistant to soft X-ray radiation under outer Oort cloud like conditions (Almeida et al., 2014), so they plausibly retain their isotopic compositions with minimal to no modification by radiation. At regions of high galactic cosmic ray activity (dense molecular cloud envelopes and cores; Andrade et al., 2014); these compounds are photochemically degraded and preservation of their isotopic signature would be less likely.

## 2.5 Summary and Conclusions

Here we present model calculations, made using density functional theory, of oxygen, carbon and nitrogen equilibrium isotope fractionations between solvated organic compounds and water, $CO_2$ and $N_2$, respectively, including the triple oxygen isotope exponent, as well as select equilibrium clumped isotope properties of these molecules. The organic-bound oxygen is found to be enriched in $^{18}O$ compared to the solvent water, with the degree of enrichment varying with the functional group hosting the oxygen. At 273 K, the equilibrium $^{18}O/^{16}O$ fractionation factor between the organic compounds we consider and water spans a 17 ‰ range: from 24.4 ‰ for pentanal, 29.9 ‰ and 30.6 ‰ for cyclopentanone and acetone respectively, 36.1 ‰ for phenol, to 41.1 ‰ for alanine; the triple oxygen isotope mass law associated with these fractionations at earth surface temperatures is in the range 0.522–0.526. Hydrogen bonding in the solvating network of water molecules plays a significant role in dictating the magnitude of this fractionation, with an amplitude that depends on the compound of interest. While these solvation effects are best described using a fully explicit solvation model, we demonstrate that carefully constructed cluster solvation models are sufficient to predict these fractionations within experimental uncertainty. However, the choice of different solvation models can affect the mass law of the oxygen isotope fractionations beyond analytical uncertainty. The organics we consider are also predicted to be depleted in $^{13}C$ relative to $CO_2$ (assuming mutual isotopic equilibrium) by 22.6 – 40.9 ‰ at 273 K, with the exact magnitude depending on abundance of different types of distinct carbon sites (e.g., $^{13}C$-poor methyl vs $^{13}C$-rich carbonyl carbon) in the compound of interest. Alanine is enriched in $^{15}N$ compared to $N_2$ in equilibrium (by 10.5 ‰ at 273 K); this fractionation reflects the shorter N-H bond length and relatively large shift of higher frequency vibrational modes upon $^{15}N$ substitution in alanine as compared to $N_2$. Enrichment of adjacent $^{13}C—^{18}O$ clumping relative to a stochastic distribution varies depending on functional groups (1.1 ‰ for pentanal, 0.9 ‰ and 1.0 ‰ for acetone and cyclopentanone respectively, 0.4 ‰ for phenol and 0.7 ‰ for alanine at 273 K) and correlates well with C—O bond length. Our predictions are in good agreement with findings of previous experimental and theoretical works.

We use these model results to make initial predictions of the triple oxygen isotopic compositions of organic molecules in the early solar system, assuming formation from or equilibrium with various hypothesized volatile reservoirs, in anticipation of compound-specific oxygen isotope measurements from primitive meteorites and samples returned from carbonaceous asteroids. The combination of mass independent isotopic differences between the abundant CO and $H_2O$ reservoirs (plausibly caused by 'self-shielding' effects) and isotope exchange reactions between those species and O-bearing organics leads to distinctive isotopic compositions that may be indicative of the environment and mode of organic synthesis and/or storage. Specifically, we predict that organics formed from or exposed to asteroidal pore waters will inherit the $\Delta^{17}O$ anomalies of those waters (which vary widely from broadly earth-like values to 10's of per mil mass independent enrichments), but in all cases will be displaced to the right of the CCAM, by 10's of per mil (varying with temperature and bonding environment of the oxygen atoms in question). Organics that formed from or (less plausibly) equilibrated with the CO that constituted the dominant gaseous oxygen reservoir in the early circum-solar disk, e.g., through Fischer-Tropsch type reactions, is expected to inherit the strongly $^{16}O$ enriched signature of solar O, possibly offset to lower $\delta^{17}$O and $\delta^{18}$O along a mass-dependent trend that passes through the solar composition (i.e., very low in $\Delta^{17}$O, and falling on or to the left of the CCAM). Finally, formation through reactions in pre-solar or molecular ice grains would be expected to produce organics that inherit the O isotope compositions of primitive waters perhaps resembling those measured for Comet 67P and estimated for the Acfer 094 meteorite, possibly offset to lower $\delta^{18}$O and $\delta^{17}$O compositions due to kinetic isotope effects associated with the ice grain reactions; thus, these organics should possess very high $\Delta^{17}$O values and fall on or to the left of the CCAM. Thus, the oxygen isotope compositions of early solar system organic molecules are expected to provide distinctive, high-amplitude signatures for their source substrates and environments of formation.

## Acknowledgements

SB acknowledges Roman Korol, Ojashvi Rautela, and Hao Xie for help with computational issues and Simon Andren, Alexander Meshoulam, Sarah Zeichner, Amy Hofmann, Laura Chimiak, and Noam Lotem for helpful discussions. This study is supported by Caltech Center for Comparative Planetary Evolution, United States Department of Energy (grant no.: DE-SC0016561) and Simons Foundation funding awarded to JME.

## Data availability

The *data repository* is available through CaltechDATA at https://doi.org/10.22002/5za3h-ckp07.

## 2.6 Supplementary Material

### 2.6.1 Factors influencing accuracy and precision of prediction

The choice of basis has a first order influence in calculation of vibrational frequency of a system. Larger basis set renders more accurate predictions but are also computationally demanding. To evaluate the effect of basis set size on calculation of $^{18}\beta$ and $k$; several systems have been investigated at both DZ and TZ level. Here we report two variables as measures of this difference:

$$\Delta^{18}O_{TZ\text{-}DZ} = 1000*\ln[{}^{18}\beta_{TZ}/{}^{18}\beta_{DZ}]$$

$$\Delta k_{TZ\text{-}DZ} = k_{TZ} - k_{DZ}$$

Generally, $\Delta^{18}O_{TZ\text{-}DZ}$ is small (<2 ‰) and within analytical uncertainty of previous experimental results for the systems investigated (Fig. S2.1b). $\Delta^{18}O_{TZ\text{-}DZ}$ values for C=O and C-O-H groups systematically differ from each other (1.23 ± 0.28 ‰ for C=O vs. 0.26 ± 0.38 ‰ for C-O-H at 273 K). The magnitude of this difference decreases as temperature increases. Average $\Delta k_{TZ\text{-}DZ}$ for all systems considered is indistinguishable from zero (Fig. S2.1d), within typical analytical uncertainties, and essentially constant with temperature.

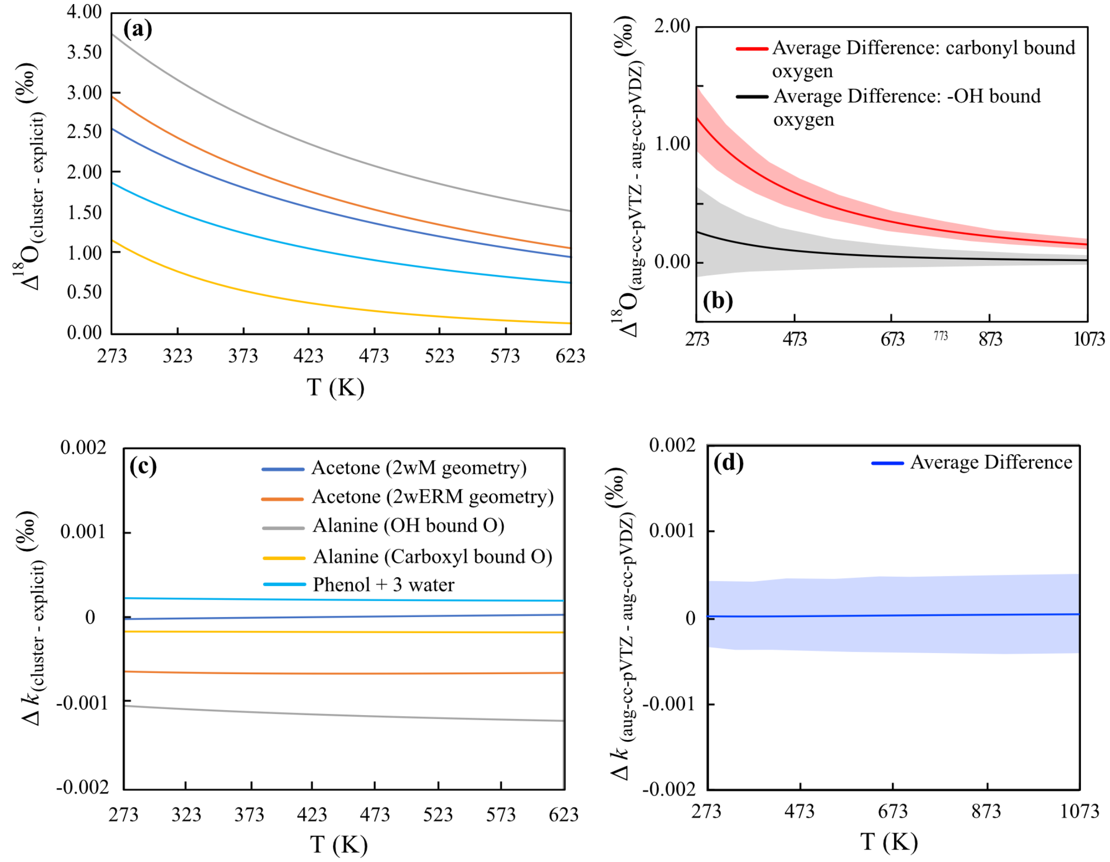

Figure S2.1: Difference in $^{18}O/^{16}O$ fractionation and mass laws for use of different basis sets and solvation models. (a) Difference in $^{18}O/^{16}O$ fractionation between cluster solvation and explicit solvation and its temperature dependence. (b) Difference in $^{18}O/^{16}O$ fractionation between calculations using DZ and TZ basis set (error envelope 1σ). (c) Difference in k between cluster and explicit solvation. (d) Difference in k between DZ and TZ basis set (error envelope 1σ).

Table 2.1: Fractionation factors and mass laws (TZ) calculated in this study.

| | **$1000 \ast \ln(^{18}\alpha)_{\text{compound - water}}$ (‰)** | | | | |
|---|---|---|---|---|---|
| **T (K)** | *Acetone* | *Cyclopentanone* | *Pentanal* | *Phenol (3w)* | *Alanine (10w)* |
| 273 | 30.63 | 29.88 | 24.37 | 36.12 | 41.06 |
| 323 | 22.21 | 21.46 | 18.09 | 25.71 | 29.88 |
| 373 | 16.34 | 15.66 | 13.55 | 18.77 | 22.23 |
| 423 | 12.13 | 11.55 | 10.18 | 13.97 | 16.81 |
| 473 | 9.03 | 8.55 | 7.65 | 10.56 | 12.87 |
| 523 | 6.73 | 6.32 | 5.72 | 8.08 | 9.96 |
| 573 | 5.00 | 4.66 | 4.25 | 6.24 | 7.78 |
| 623 | 3.68 | 3.39 | 3.12 | 4.86 | 6.11 |

| **T (K)** | **$\theta_{\text{compound-water}}$** | | | | |
|---|---|---|---|---|---|
| | *Acetone* | *Cyclopentanone* | *Pentanal* | *Phenol (3w)* | *Alanine (10w)* |
| 273 | 0.5228 | 0.5224 | 0.5221 | 0.5240 | 0.5263 |
| 323 | 0.5232 | 0.5228 | 0.5225 | 0.5244 | 0.5270 |
| 373 | 0.5236 | 0.5232 | 0.5229 | 0.5247 | 0.5276 |
| 423 | 0.5239 | 0.5234 | 0.5233 | 0.5249 | 0.5281 |
| 473 | 0.5242 | 0.5236 | 0.5235 | 0.5250 | 0.5286 |
| 523 | 0.5244 | 0.5237 | 0.5236 | 0.5250 | 0.5292 |
| 573 | 0.5245 | 0.5237 | 0.5237 | 0.5249 | 0.5297 |
| 623 | 0.5245 | 0.5236 | 0.5237 | 0.5248 | 0.5303 |

| | $1000^*\ln(^{13}\alpha)_{\text{compound-CO2}}$ (‰) | | | | $1000^*\ln(^{15}\alpha)_{\text{compound-N2}}$ (‰) |
|---|---|---|---|---|---|
| **T (K)** | *Acetone* | *Cyclopentanone* | *Pentanal* | *Alanine (10w)* | *Alanine (10w)* |
| 273 | -40.87 | -34.89 | -39.59 | -22.59 | 10.48 |
| 323 | -33.83 | -29.98 | -33.00 | -20.09 | 5.61 |
| 373 | -28.80 | -26.32 | -28.27 | -18.21 | 2.69 |
| 423 | -24.96 | -23.39 | -24.65 | -16.64 | 0.91 |
| 473 | -21.89 | -20.94 | -21.73 | -15.26 | -0.17 |
| 523 | -19.37 | -18.83 | -19.31 | -14.00 | -0.80 |
| 573 | -17.25 | -16.99 | -17.26 | -12.85 | -1.16 |
| 623 | -15.44 | -15.38 | -15.49 | -11.79 | -1.35 |

| | $\Delta_{13\text{-}18}$ (‰) | | | | | |
|---|---|---|---|---|---|---|
| **T (K)** | *Acetone* | *Cyclopentanone* | *Pentanal* | *Phenol (3w)* | *Alanine (10w)* | *CO* |
| 273 | 0.95 | 0.99 | 1.14 | 0.36 | 0.68 | 2.10 |
| 323 | 0.70 | 0.74 | 0.84 | 0.25 | 0.49 | 1.60 |
| 373 | 0.52 | 0.56 | 0.63 | 0.18 | 0.36 | 1.24 |
| 423 | 0.39 | 0.42 | 0.48 | 0.13 | 0.27 | 0.97 |
| 473 | 0.29 | 0.33 | 0.36 | 0.09 | 0.20 | 0.77 |
| 523 | 0.23 | 0.25 | 0.28 | 0.07 | 0.15 | 0.61 |
| 573 | 0.17 | 0.20 | 0.22 | 0.05 | 0.12 | 0.49 |
| 623 | 0.13 | 0.16 | 0.17 | 0.04 | 0.09 | 0.40 |

# BIBLIOGRAPHY

Abplanalp M. J., Gozem S., Krylov A. I., Shingledecker C. N., Herbst E. and Kaiser R. I. (2016) A study of interstellar aldehydes and enols as tracers of a cosmic ray-driven nonequilibrium synthesis of complex organic molecules. *Proceedings of the National Academy of Sciences* **113**, 7727–7732.

Agarwal V. K., Schutte W., Greenberg J. M., Ferris J. P., Briggs R., Connor S., Van de Bult C. and Baas F. (1985) Photochemical reactions in interstellar grains photolysis of CO, NH3, and H2O. *Origins of Life and Evolution of the Biosphere* **16**, 21–40.

Agúndez M., Cernicharo J. and Goicoechea J. R. (2008) Formation of simple organic molecules in inner T Tauri disks. *Astronomy & Astrophysics* **483**, 831–837.

Alabugin I. V., Gonzalez-Rodriguez E., Kawade R. K., Stepanov A. A. and Vasilevsky S. F. (2019) Alkynes as synthetic equivalents of ketones and aldehydes: a hidden entry into carbonyl chemistry. *Molecules* **24**, 1036.

Alexander C. M. O., Nilges M. J., Cody G. D. and Herd C. D. K. (2022) Are radicals responsible for the variable deuterium enrichments in chondritic insoluble organic material? *Geochimica et Cosmochimica Acta* **316**, 135–149.

Almeida G. C., Pilling S., Andrade D. P., Castro N. L. S., Mendoza E., Boechat-Roberty H. M. and Rocco M. L. M. (2014) Photodesorption and photostability of acetone ices: Relevance to solid phase astrochemistry. *The Journal of Physical Chemistry C* **118**, 6193–6200.

Andrade D. P., de Barros A. L., Ding J., Rothard H., Boduch P. and da Silveira E. F. (2014) Acetone degradation by cosmic rays in the solar neighbourhood and in the Galactic Centre. *Monthly Notices of the Royal Astronomical Society* **444**, 3792–3801.

Aponte J. C., Whitaker D., Powner M. W., Elsila J. E. and Dworkin J. P. (2019) Analyses of aliphatic aldehydes and ketones in carbonaceous chondrites. *ACS Earth and Space Chemistry* **3**, 463–472.

Ardawi M. S. M. and Newsholme E. A. (1982) Maximum activities of some enzymes of glycolysis, the tricarboxylic acid cycle and ketone-body and glutamine utilization pathways in lymphocytes of the rat. *Biochemical Journal* **208**, 743–748.

Barkan E. and Luz B. (2005) High precision measurements of 17O/16O and 18O/16O ratios in H2O. *Rapid Communications in Mass Spectrometry: An International Journal Devoted to the Rapid Dissemination of Up-to-the-Minute Research in Mass Spectrometry* **19**, 3737–3742.

Beck W. C., Grossman E. L. and Morse J. W. (2005) Experimental studies of oxygen isotope fractionation in the carbonic acid system at 15, 25, and 40 C. *Geochimica et Cosmochimica Acta* **69**, 3493–3503.

Becke A. D. (1993) Density-functional thermochemistry: III. The role of exact exchange. *J. Chem. Phys.* **98**, 5648–5652.

Bigeleisen J. and Mayer M. G. (1947) Calculation of equilibrium constants for isotopic exchange reactions. *The Journal of Chemical Physics* **15**, 261–267.

Blanchard J. S. and Cleland W. W. (1980) Use of isotope effects to deduce the chemical mechanism of fumarase. *Biochemistry* **19**, 4506–4513.

Boettger J. D. and Kubicki J. D. (2021) Equilibrium and kinetic isotopic fractionation in the CO2 hydration and hydroxylation reactions: Analysis of the role of hydrogen-bonding via quantum mechanical calculations. *Geochimica et Cosmochimica Acta* **292**, 37–63.

Bramley R., Figgis B. N. and Nyholm R. S. (1962) 13 C and 17 O nmr spectra of metal carbonyl compounds. *Transactions of the Faraday Society* **58**, 1893–1896.

Bruss M. L. (1997) Lipids and ketones. In *Clinical biochemistry of domestic animals* Elsevier. pp. 83–115.

Cao X. and Liu Y. (2011) Equilibrium mass-dependent fractionation relationships for triple oxygen isotopes. *Geochimica et Cosmochimica Acta* **75**, 7435–7445.

Chacko T., Cole D. R. and Horita J. (2001) Equilibrium oxygen, hydrogen and carbon isotope fractionation factors applicable to geologic systems. *Reviews in mineralogy and geochemistry* **43**, 1–81.

Charnley S. B., Ehrenfreund P. and Kuan Y.-J. (2001) Spectroscopic diagnostics of organic chemistry in the protostellar environment. *Spectrochimica Acta Part A: Molecular and Biomolecular Spectroscopy* **57**, 685–704.

Choi B.-G., McKeegan K. D., Krot A. N. and Wasson J. T. (1998) Extreme oxygen-isotope compositions in magnetite from unequilibrated ordinary chondrites. *Nature* **392**, 577–579.

Chuchev K. and BelBruno J. J. (2008) Computational treatment of the microsolvation of neutral and zwitterionic forms of alanine. *Journal of Molecular Structure: THEOCHEM* **850**, 111–120.

Clayton R. N. (2002) Self-shielding in the solar nebula. *Nature* **415**, 860–861.

Clayton R. N., Grossman L. and Mayeda T. K. (1973) A Component of Primitive Nuclear Composition in Carbonaceous Meteorites. *Science* **182**, 485–488.

Clayton R. N. and Mayeda T. K. (1999) Oxygen isotope studies of carbonaceous chondrites. *Geochimica et Cosmochimica Acta* **63**, 2089–2104.

Correa S. M. and Arbilla G. (2008) Carbonyl emissions in diesel and biodiesel exhaust. *Atmospheric environment* **42**, 769–775.

Csernica T., Bhattacharjee S. and Eiler J. (2023) Accuracy and precision of ESI-Orbitrap-IRMS observations of hours to tens of hours via reservoir injection. *International Journal of Mass Spectrometry* **490**, 117084.

de Freitas M. C., Vieira C. G., dos Santos E. N. and Gusevskaya E. V. (2013) Synthesis of Fragrance Compounds from Biorenewables: Tandem Hydroformylation–Acetalization of Bicyclic Monoterpenes. *ChemCatChem* **5**, 1884–1890.

DeNiro M. J. and Epstein S. (1981) Isotopic composition of cellulose from aquatic organisms. *Geochimica et Cosmochimica Acta* **45**, 1885–1894.

Dennis K. J., Affek H. P., Passey B. H., Schrag D. P. and Eiler J. M. (2011) Defining an absolute reference frame for 'clumped'isotope studies of CO2. *Geochimica et Cosmochimica Acta* **75**, 7117–7131.

Dong G., Xie H., Formolo M., Lawson M., Sessions A. and Eiler J. (2021) Clumped isotope effects of thermogenic methane formation: Insights from pyrolysis of hydrocarbons. *Geochimica et Cosmochimica Acta* **303**, 159–183.

Eiler J., Cesar J., Chimiak L., Dallas B., Grice K., Griep-Raming J., Juchelka D., Kitchen N., Lloyd M. and Makarov A. (2017) Analysis of molecular isotopic structures at high precision and accuracy by Orbitrap mass spectrometry. *International Journal of Mass Spectrometry* **422**, 126–142.

Ellis N. M. and Passey B. H. (2023) A novel method for high-precision triple oxygen isotope analysis of diverse Earth materials using high temperature conversion–methanation–fluorination and isotope ratio mass spectrometry. *Chemical Geology* **635**, 121616.

Epstein S., Krishnamurthy R. V., Cronin J. R., Pizzarello S. and Yuen G. U. (1987) Unusual stable isotope ratios in amino acid and carboxylic acid extracts from the Murchison meteorite. *Nature* **326**, 477–479.

Fennell C. J. and Dill K. A. (2011) Physical modeling of aqueous solvation. *Journal of statistical physics* **145**, 209–226.

Foley D. J. and Waldmann H. (2022) Ketones as strategic building blocks for the synthesis of natural product-inspired compounds. *Chemical Society Reviews* **51**, 4094–4120.

Fujiya W. (2018) Oxygen isotopic ratios of primordial water in carbonaceous chondrites. *Earth and Planetary Science Letters* **481**, 264–272.

Furukawa Y., Chikaraishi Y., Ohkouchi N., Ogawa N. O., Glavin D. P., Dworkin J. P., Abe C. and Nakamura T. (2019) Extraterrestrial ribose and other sugars in primitive meteorites. *Proceedings of the National Academy of Sciences* **116**, 24440–24445.

Gilmore W., Morris M., ZUCKERMAN B., TURNER B. and PALMER P. (1975) Observation of the 616-515 Transitions of Acetaldehyde in Sagittarius B2. *Reprints-National Radio Astronomy Observatory, Green Bank, W. Va: Series A.* **204**, 43–46.

Govindh B., Diwakar B. S. and Murthy Y. L. (2012) A brief review on synthesis & applications of [beta]-enamino carbonyl compounds. *Organic Communications* **5**, 105.

Grannas A. M., Shepson P. B., Guimbaud C., Sumner A. L., Albert M., Simpson W., Dominé F., Boudries H., Bottenheim J. and Beine H. J. (2002) A study of photochemical and physical processes affecting carbonyl compounds in the Arctic atmospheric boundary layer. *Atmospheric environment* **36**, 2733–2742.

Greenzaid P., Luz Z. and Samuel D. (1968a) Nmr study of reversible hydration of aliphatic aldehydes and ketones. Part 3.—Isotopic oxygen exchange of acetone. *Transactions of the Faraday Society* **64**, 2780–2786.

Greenzaid P., Luz Z. and Samuel D. (1968b) Nmr study of reversible hydration of aliphatic aldehydes and ketones. Part 4.—Isotopic oxygen exchange of cycloalkanones. *Transactions of the Faraday Society* **64**, 2787–2793.

Grimme S., Antony J., Ehrlich S. and Krieg H. (2010) A consistent and accurate ab initio parametrization of density functional dispersion correction (DFT-D) for the 94 elements H-Pu. *The Journal of chemical physics* **132**, 154104.

Hanwell M. D., Curtis D. E., Lonie D. C., Vandermeersch T., Zurek E. and Hutchison G. R. (2012) Avogadro: an advanced semantic chemical editor, visualization, and analysis platform. *J Cheminform* **4**, 17.

Hashizume K., Takahata N., Naraoka H. and Sano Y. (2011) Extreme oxygen isotope anomaly with a solar origin detected in meteoritic organics. *Nature Geoscience* **4**, 165–168.

Hayatsu R. and Anders E. (1981) Organic compounds in meteorites and their origins. In *Cosmo-and geochemistry* Springer. pp. 1–37.

Hill P. S., Schauble E. A. and Tripati A. (2020) Theoretical constraints on the effects of added cations on clumped, oxygen, and carbon isotope signatures of dissolved inorganic carbon species and minerals. *Geochimica et Cosmochimica Acta* **269**, 496–539.

Hill P. S., Tripati A. K. and Schauble E. A. (2014) Theoretical constraints on the effects of pH, salinity, and temperature on clumped isotope signatures of dissolved inorganic carbon species and precipitating carbonate minerals. *Geochimica et cosmochimica acta* **125**, 610–652.

Ho S. S. H., Yu J. Z., Chu K. W. and Yeung L. L. (2006) Carbonyl Emissions from Commercial Cooking Sources in Hong Kong. *Journal of the Air & Waste Management Association* **56**, 1091–1098.

Hodyss R., Johnson P. V., Stern J. V., Goguen J. D. and Kanik I. (2009) Photochemistry of methane–water ices. *Icarus* **200**, 338–342.

Hoffmann J., Jensen C. U. and Rosendahl L. A. (2016) Co-processing potential of HTL bio-crude at petroleum refineries–Part 1: Fractional distillation and characterization. *Fuel* **165**, 526–535.

Hofmann A. E., Chimiak L., Dallas B., Griep-Raming J., Juchelka D., Makarov A., Schwieters J. and Eiler J. M. (2020) Using Orbitrap mass spectrometry to assess the isotopic compositions of individual compounds in mixtures. *International Journal of Mass Spectrometry* **457**, 116410.

Hofmann M. E., Horváth B. and Pack A. (2012) Triple oxygen isotope equilibrium fractionation between carbon dioxide and water. *Earth and Planetary Science Letters* **319**, 159–164.

Hollis J. M., Jewell P. R., Lovas F. J., Remijan A. and Møllendal H. (2004) Green bank telescope detection of new interstellar aldehydes: propenal and propanal. *The Astrophysical Journal* **610**, L21.

Horita J. and Wesolowski D. J. (1994) Liquid-vapor fractionation of oxygen and hydrogen isotopes of water from the freezing to the critical temperature. *Geochimica et Cosmochimica Acta* **58**, 3425–3437.

Hossain M., Das U. and Dimmock J. R. (2019) Recent advances in α, β-unsaturated carbonyl compounds as mitochondrial toxins. *European Journal of Medicinal Chemistry* **183**, 111687.

Iron M. A. and Gropp J. (2019) Cost-effective density functional theory (DFT) calculations of equilibrium isotopic fractionation in large organic molecules. *Physical Chemistry Chemical Physics* **21**, 17555–17570.

Jungclaus G. A., Yuen G. U., Moore C. B. and Lawless J. G. (1976) Evidence for the presence of low molecular weight alcohols and carbonyl compounds in the Murchison meteorite. *Meteoritics* **11**, 231–237.

Kean A. J., Grosjean E., Grosjean D. and Harley R. A. (2001) On-Road Measurement of Carbonyls in California Light-Duty Vehicle Emissions. *Environ. Sci. Technol.* **35**, 4198–4204.

Kim K.-H., Hong Y.-J., Pal R., Jeon E.-C., Koo Y.-S. and Sunwoo Y. (2008) Investigation of carbonyl compounds in air from various industrial emission sources. *Chemosphere* **70**, 807–820.

King R. B. (1970) Applications of metal carbonyl anions in the synthesis of ususual organometallic compounds. *Acc. Chem. Res.* **3**, 417–427.

Kvenvolden K. A., Lawless J. G. and Ponnamperuma C. (1971) Nonprotein amino acids in the Murchison meteorite. *Proceedings of the National Academy of Sciences* **68**, 486–490.

Lancet M. S. and Anders E. (1970) Carbon Isotope Fractionation in the Fischer-Tropsch Synthesis and in Meteorites. *Science* **170**, 980–982.

Lary D. J. and Shallcross D. E. (2000) Central role of carbonyl compounds in atmospheric chemistry. *J. Geophys. Res.* **105**, 19771–19778.

Letsinger R. L. and Mahadevan V. (1965) Oligonucleotide Synthesis on a Polymer Support [1,2]. *J. Am. Chem. Soc.* **87**, 3526–3527.

Ley S. (1997) Polymer supported perruthenate (PSP): A new oxidant for clean organic synthesis. *Journal of the Chemical Society, Perkin Transactions 1*, 1907–1908.

Liu Q., Gao Y., Huang W., Ling Z., Wang Z. and Wang X. (2022) Carbonyl compounds in the atmosphere: A review of abundance, source and their contributions to O3 and SOA formation. *Atmospheric Research* **274**, 106184.

Liu Q., Zhang C., Shi N., Zhang X., Wang C. and Ma L. (2018) Production of renewable long-chained cycloalkanes from biomass-derived furfurals and cyclic ketones. *RSC advances* **8**, 13686–13696.

Loison J.-C., Wakelam V., Gratier P., Hickson K. M., Bacmann A., Agùndez M., Marcelino N., Cernicharo J., Guzman V. and Gerin M. (2019) Oxygen fractionation in dense molecular clouds. *Monthly Notices of the Royal Astronomical Society* **485**, 5777–5789.

Lyons J. R., Gharib-Nezhad E. and Ayres T. R. (2018) A light carbon isotope composition for the Sun. *Nature communications* **9**, 1–10.

Lyons J. R. and Young E. D. (2005) CO self-shielding as the origin of oxygen isotope anomalies in the early solar nebula. *Nature* **435**, 317–320.

Manby F., Miller T., Bygrave P., Ding F., Dresselhaus T., Batista-Romero F., Buccheri A., Bungey C., Lee S. and Meli R. (2019) entos: A quantum molecular simulation package.

de Marcellus P., Bertrand M., Nuevo M., Westall F. and Le Sergeant d'Hendecourt L. (2011) Prebiotic significance of extraterrestrial ice photochemistry: detection of hydantoin in organic residues. *Astrobiology* **11**, 847–854.

Martins Z., Botta O., Fogel M. L., Sephton M. A., Glavin D. P., Watson J. S., Dworkin J. P., Schwartz A. W. and Ehrenfreund P. (2008) Extraterrestrial nucleobases in the Murchison meteorite. *Earth and planetary science Letters* **270**, 130–136.

McKeegan K. D., Kallio A. P. A., Heber V. S., Jarzebinski G., Mao P. H., Coath C. D., Kunihiro T., Wiens R. C., Nordholt J. E., Moses R. W., Reisenfeld D. B., Jurewicz A. J. G. and Burnett D. S. (2011) The Oxygen Isotopic Composition of the Sun Inferred from Captured Solar Wind. *Science* **332**, 1528–1532.

McKeegan K. D. and Leshin L. A. (2001) Stable isotope variations in extraterrestrial materials. *Reviews in Mineralogy and Geochemistry* **43**, 279–318.

McNeill A. S., Dallas B. H., Eiler J. M., Bylaska E. J. and Dixon D. A. (2020) Reaction energetics and 13C fractionation of alanine transamination in the aqueous and gas phases. *The Journal of Physical Chemistry A* **124**, 2077–2089.

Mejía C., De Barros A. L. F., Rothard H., Boduch P. and Da Silveira E. F. (2020) Radiolysis of Ices by Cosmic-Rays: CH4 and H2O Ices Mixtures Irradiated by 40 MeV 58Ni11+ Ions. *The Astrophysical Journal* **894**, 132.

Mueller E. P., Sessions A. L., Sauer P. E., Weiss G. M. and Eiler J. M. (2021) Simultaneous, high-precision measurements of δ2H and δ13C in nanomole quantities of acetate using electrospray ionization-quadrupole-Orbitrap mass spectrometry. *Analytical Chemistry* **94**, 1092–1100.

Mullin J. M. and Gordon M. S. (2009) Alanine: Then There Was Water. *J. Phys. Chem. B* **113**, 8657–8669.

Neese F., Wennmohs F., Becker U. and Riplinger C. (2020) The ORCA quantum chemistry program package. *The Journal of chemical physics* **152**, 224108.

Nishikubo T. and Kameyama A. (1993) Addition reactions of cyclic ethers with various carbonyl compounds and their application for polymer synthesis. *Progress in polymer science* **18**, 963–995.

OHTA S., HAYAKAWA S., NISHIMURA K. and OKAMOTO M. (1987) Synthesis and application of imidazole derivatives. Synthesis of (1-methyl-1H-imidazol-2-yl) methanol derivatives and conversion into carbonyl compounds. *Chemical and pharmaceutical bulletin* **35**, 1058–1069.

O'Neil J. R. and Adami L. H. (1969) Oxygen isotope partition function ratio of water and the structure of liquid water. *The Journal of Physical Chemistry* **73**, 1553–1558.

O'Reilly L. da S. L. and DeNiro M. J. D. (1983) Biogeochemical implications of the isotopic equilibrium fractionation factor between the oxygen atoms of acetone and water. *Geochimica et Cosmochimica Acta* **47**, 2271–2274.

Parthasarathi R., Subramanian V. and Sathyamurthy N. (2005) Hydrogen bonding in phenol, water, and phenol- water clusters. *The Journal of Physical Chemistry A* **109**, 843–850.

Piasecki A., Sessions A., Lawson M., Ferreira A. A., Neto E. V. S. and Eiler J. M. (2016a) Analysis of the site-specific carbon isotope composition of propane by gas source isotope ratio mass spectrometer. *Geochimica et Cosmochimica Acta* **188**, 58–72.

Piasecki A., Sessions A., Peterson B. and Eiler J. (2016b) Prediction of equilibrium distributions of isotopologues for methane, ethane and propane using density functional theory. *Geochimica et Cosmochimica Acta* **190**, 1–12.

Pizzarello S. and Huang Y. (2002) Molecular and isotopic analyses of Tagish Lake alkyl dicarboxylic acids. *Meteoritics & Planetary Science* **37**, 687–696.

Rife J. E. and Cleland W. W. (1980) Kinetic mechanism of glutamate dehydrogenase. *Biochemistry* **19**, 2321–2328.

Romero-Montalvo E. and DiLabio G. A. (2021) Computational Study of Hydrogen Bond Interactions in Water Cluster–Organic Molecule Complexes. *The Journal of Physical Chemistry A* **125**, 3369–3377.

Rossi S., Puglisi A., Raimondi L. and Benaglia M. (2018) Synthesis of Alpha-trifluoromethylthio Carbonyl Compounds: A Survey of the Methods for the Direct Introduction of the $SCF_3$ Group on to Organic Molecules. *ChemCatChem* **10**, 2717–2733.

Rustad J. R. (2009) Ab initio calculation of the carbon isotope signatures of amino acids. *Organic geochemistry* **40**, 720–723.

Rustad J. R., Nelmes S. L., Jackson V. E. and Dixon D. A. (2008) Quantum-chemical calculations of carbon-isotope fractionation in CO2 (g), aqueous carbonate species, and carbonate minerals. *The Journal of Physical Chemistry A* **112**, 542–555.

Sacia E. R., Balakrishnan M., Deaner M. H., Goulas K. A., Toste F. D. and Bell A. T. (2015) Highly Selective Condensation of Biomass-Derived Methyl Ketones as a Source of Aviation Fuel. *ChemSusChem* **8**, 1726–1736.

Sakamoto N., Seto Y., Itoh S., Kuramoto K., Fujino K., Nagashima K., Krot A. N. and Yurimoto H. (2007) Remnants of the early solar system water enriched in heavy oxygen isotopes. *Science* **317**, 231–233.

Samuel D. and Silver B. L. (1965) Oxygen isotope exchange reactions of organic compounds. In *Advances in Physical Organic Chemistry* Elsevier. pp. 123–186.

Schauble E. A., Ghosh P. and Eiler J. M. (2006) Preferential formation of 13C–18O bonds in carbonate minerals, estimated using first-principles lattice dynamics. *Geochimica et Cosmochimica Acta* **70**, 2510–2529.

Schauble E. A. and Young E. D. (2021) Mass dependence of equilibrium oxygen isotope fractionation in carbonate, nitrate, oxide, perchlorate, phosphate, silicate, and sulfate minerals. *Reviews in Mineralogy and Geochemistry* **86**, 137–178.

Schroeder I. R., Altwegg K., Balsiger H., Berthelier J.-J., De Keyser J., Fiethe B., Fuselier S. A., Gasc S., Gombosi T. I. and Rubin M. (2019) 16O/18O ratio in water in the coma of comet 67P/Churyumov-Gerasimenko measured with the Rosetta/ROSINA double-focusing mass spectrometer. *Astronomy & Astrophysics* **630**, A29.

Seo Y.-K. and Baek S.-O. (2011) Characterization of carbonyl compounds in the ambient air of an industrial city in Korea. *Sensors* **11**, 949–963.

Sephton M. A. (2002) Organic compounds in carbonaceous meteorites. *Natural product reports* **19**, 292–311.

Shi M., Fu L., Hu X., Zuo L., Deng D., Chen J. and Chen H. (2012) Design and synthesis of carbonyl group modified conjugated polymers for photovoltaic application. *Polymer bulletin* **68**, 1867–1877.

Shields R. M., Temelso B., Archer K. A., Morrell T. E. and Shields G. C. (2010) Accurate predictions of water cluster formation,(H2O) n= 2- 10. *The Journal of Physical Chemistry A* **114**, 11725–11737.

Shimanouchi T. (1973) *Tables of molecular vibrational frequencies*., US Government Printing Office Washington, DC.

Simkus D. N., Aponte J. C., Hilts R. W., Elsila J. E. and Herd C. D. (2019) Compound-specific carbon isotope compositions of aldehydes and ketones in the Murchison meteorite. *Meteoritics & planetary science* **54**, 142–156.

Singh S. K., Kleimeier N. F., Eckhardt A. K. and Kaiser R. I. (2022) A Mechanistic Study on the Formation of Acetone (CH3COCH3), Propanal (CH3CH2CHO), Propylene Oxide (c-CH3CHOCH2) along with Their Propenol Enols (CH3CHCHOH/CH3C (OH) CH2) in Interstellar Analog Ices. *The Astrophysical Journal* **941**, 103.

Śmiechowski M. (2009) Theoretical study of the structure, energetics and vibrational frequencies of water–acetone and water–2-butanone complexes. *Chemical Physics Letters* **480**, 178–184.

Sternberg L. and Ellsworth P. F. V. (2011) Divergent biochemical fractionation, not convergent temperature, explains cellulose oxygen isotope enrichment across latitudes. *PloS one* **6**, e28040.

Sutton L. E. and Bowen H. J. M. (1958) *Tables of interatomic distances and configuration in molecules and ions*., Chemical Society, London.

Tartèse R., Chaussidon M., Gurenko A., Delarue F. and Robert F. (2018) Insights into the origin of carbonaceous chondrite organics from their triple oxygen isotope composition. *Proceedings of the National Academy of Sciences* **115**, 8535–8540.

Tartèse R., Chaussidon M., Gurenko A., Delarue F. and Robert F. (2016) Oxygen isotope analysis of fossil organic matter by secondary ion mass spectrometry. *Geochimica et Cosmochimica Acta* **182**, 24–39.

Tartese R., Chaussidon M., Gurenko A., Delarue F. and Robert F. (2016) Warm Archaean oceans reconstructed from oxygen isotope composition of early-life remnants. *Geochemical Perspectives Letters* **3**, 55.

Thi W.-F., Van Zadelhoff G.-J. and van Dishoeck E. F. (2004) Organic molecules in protoplanetary disks around T Tauri and Herbig Ae stars. *Astronomy & Astrophysics* **425**, 955–972.

Trost B. M. (1978) .alpha.-Sulfenylated carbonyl compounds in organic synthesis. *Chem. Rev.* **78**, 363–382.

Urey H. C. (1947) The thermodynamic properties of isotopic substances. *Journal of the Chemical Society (Resumed)*, 562–581.

Vacher L. G., Marrocchi Y., Verdier-Paoletti M. J., Villeneuve J. and Gounelle M. (2016) Inward radial mixing of interstellar water ices in the solar protoplanetary disk. *The Astrophysical journal letters* **827**, L1.

VanItallie T. B. and Nufert T. H. (2003) Ketones: metabolism's ugly duckling. *Nutrition reviews* **61**, 327–341.

Vaquero V., Sanz M. E., Peña I., Mata S., Cabezas C., López J. C. and Alonso J. L. (2014) Alanine water complexes. *The Journal of Physical Chemistry A* **118**, 2584–2590.

Vederas J. C. (1980) Structural dependence of oxygen-18 isotope shifts in carbon-13 NMR spectra. *J. Am. Chem. Soc.* **102**, 374–376.

Verdier-Paoletti M. J., Marrocchi Y., Avice G., Roskosz M., Gurenko A. and Gounelle M. (2017) Oxygen isotope constraints on the alteration temperatures of CM chondrites. *Earth and Planetary Science Letters* **458**, 273–281.

Vieira C. G., de Freitas M. C., dos Santos E. N. and Gusevskaya E. V. (2012) Synthesis of Fragrance Ingredients by Tandem Hydroformylation-Cyclization of Limonene Catalyzed by Rhodium Complexes and Pyridinium *p* -Toluenesulphonate. *ChemCatChem* **4**, 795–801.

Villa C., Trucchi B., Gambaro R. and Baldassari S. (2008) Green procedure for the preparation of scented alcohols from carbonyl compounds. *Intern J of Cosmetic Sci* **30**, 139–144.

Vogel J. C., Grootes P. M. and Mook W. G. (1970) Isotopic fractionation between gaseous and dissolved carbon dioxide. *Zeitschrift für Physik A Hadrons and nuclei* **230**, 225–238.

Walczak K., Friedrich J. and Dolg M. (2011) On basis set superposition error corrected stabilization energies for large n-body clusters. *The Journal of chemical physics* **135**.

Wang Y., Sessions A. L., Nielsen R. J. and Goddard III W. A. (2013) Equilibrium 2H/1H fractionation in organic molecules: III. Cyclic ketones and hydrocarbons. *Geochimica et Cosmochimica Acta* **107**, 82–95.

Wang Y., Sessions A. L., Nielsen R. J. and Goddard III W. A. (2009a) Equilibrium 2H/1H fractionations in organic molecules: I. Experimental calibration of ab initio calculations. *Geochimica et Cosmochimica Acta* **73**, 7060–7075.

Wang Y., Sessions A. L., Nielsen R. J. and Goddard III W. A. (2009b) Equilibrium 2H/1H fractionations in organic molecules. II: Linear alkanes, alkenes, ketones, carboxylic acids, esters, alcohols and ethers. *Geochimica et Cosmochimica Acta* **73**, 7076–7086.

Wang Z., Schauble E. A. and Eiler J. M. (2004) Equilibrium thermodynamics of multiply substituted isotopologues of molecular gases. *Geochimica et Cosmochimica Acta* **68**, 4779–4797.

Watkins J. M., DePaolo D. J. and Watson E. B. (2017) Kinetic fractionation of non-traditional stable isotopes by diffusion and crystal growth reactions. *Reviews in Mineralogy and Geochemistry* **82**, 85–125.

Watts H. D., Mohamed M. N. A. and Kubicki J. D. (2011) Comparison of Multistandard and TMS-Standard Calculated NMR Shifts for Coniferyl Alcohol and Application of the Multistandard Method to Lignin Dimers. *J. Phys. Chem. B* **115**, 1958–1970.

Wedeking K. W. and Hayes J. M. (1983) Exchange of oxygen isotopes between water and organic material. *Chemical geology* **41**, 357–370.

West R. M., Liu Z. Y., Peter M., Gärtner C. A. and Dumesic J. A. (2008) Carbon–carbon bond formation for biomass-derived furfurals and ketones by aldol condensation in a biphasic system. *Journal of Molecular Catalysis A: Chemical* **296**, 18–27.

Wilson T. L. (1999) Isotopes in the interstellar medium and circumstellar envelopes. *Reports on Progress in Physics* **62**, 143.

Woon D. E. and Dunning Jr T. H. (1993) Gaussian basis sets for use in correlated molecular calculations. III. The atoms aluminum through argon. *The Journal of chemical physics* **98**, 1358–1371.

Xia Z. and Yu Z. (2020) Temperature-dependent oxygen isotope fractionation in plant cellulose biosynthesis revealed by a global dataset of peat mosses. *Frontiers in Earth Science* **8**, 307.

Xie H., Ponton C., Formolo M. J., Lawson M., Peterson B. K., Lloyd M. K., Sessions A. L. and Eiler J. M. (2018) Position-specific hydrogen isotope equilibrium in propane. *Geochimica et Cosmochimica Acta* **238**, 193–207.

Young E. D. and Russell S. S. (1998) Oxygen Reservoirs in the Early Solar Nebula Inferred from an Allende CAI. *Science* **282**, 452–455.

Yuan Z., Liao J., Jiang H., Cao P. and Li Y. (2020) Aldehyde catalysis–from simple aldehydes to artificial enzymes. *RSC advances* **10**, 35433–35448.

Zeebe R. E. (2010) A new value for the stable oxygen isotope fractionation between dissolved sulfate ion and water. *Geochimica et Cosmochimica Acta* **74**, 818–828.

Zeichner S. S., Aponte J. C., Bhattacharjee S., Dong G., Hofmann A. E., Dworkin J. P., Glavin D. P., Elsila J. E., Graham H. V., Naraoka H., Takano Y., Tachibana S., Karp A. T., Grice K., Holman A. I., Freeman K. H., Yurimoto H., Nakamura T., Noguchi T., Okazaki R., Yabuta H., Sakamoto K., Yada T., Nishimura M., Nakato A., Miyazaki A., Yogata K., Abe M., Okada T., Usui T., Yoshikawa M., Saiki T., Tanaka Satoshi, Terui F., Nakazawa S., Watanabe S., Tsuda Y., Hamase K., Fukushima K., Aoki D., Hashiguchi M., Mita H., Chikaraishi Y., Ohkouchi N., Ogawa N. O., Sakai S., Parker E. T., McLain H. L., Orthous-Daunay F.-R., Vuitton V., Wolters C., Schmitt-Kopplin P., Hertkorn N., Thissen R., Ruf A., Isa J., Oba Y., Koga T., Yoshimura T., Araoka D., Sugahara H., Furusho A., Furukawa Y., Aoki J., Kano K., Nomura S. M., Sasaki K., Sato H., Yoshikawa T., Tanaka Satoru, Morita M., Onose M., Kabashima F., Fujishima K., Yamazaki T., Kimura Y. and Eiler J. M. (2023) Polycyclic aromatic hydrocarbons in samples of Ryugu formed in the interstellar medium. *Science* **382**, 1411–1416.

Zeichner S. S., Wilkes E. B., Hofmann A. E., Chimiak L., Sessions A. L., Makarov A. and Eiler J. M. (2022) Methods and limitations of stable isotope measurements via direct elution of chromatographic peaks using gas chromotography-Orbitrap mass spectrometry. *International Journal of Mass Spectrometry* **477**, 116848.

Zhang X. K., Lewars E. G., March R. E. and Parnis J. M. (1993) Vibrational spectrum of the acetone-water complex: a matrix isolation FTIR and theoretical study. *J. Phys. Chem.* **97**, 4320–4325.

Zhu C., Kleimeier N. F., Turner A. M., Singh S. K., Fortenberry R. C. and Kaiser R. I. (2022) Synthesis of methanediol [CH 2 (OH) 2]: The simplest geminal diol. *Proceedings of the National Academy of Sciences* **119**, e2111938119.

## *Chapter 3*

# CONSTRAINING OXYGEN ISOTOPE EXCHANGE KINETICS BETWEEN ORGANIC COMPOUNDS AND WATER USING ELECTROSPRAY IONIZATION ORBITRAP MASS SPECTROMETRY, AND IMPLICATIONS FOR THE OXYGEN ISOTOPIC COMPOSITIONS OF METEORITIC ORGANICS

Surjyendu Bhattacharjee[1*], John M. Eiler[1]

[1]Division of Geological and Planetary Sciences, California Institute of Technology, Pasadena, CA-91125, USA

*Corresponding Author: sbhattac@caltech.edu

Bhattacharjee S. and Eiler J. M. (2025). Constraining oxygen isotope exchange kinetics between organic compounds and water using electrospray ionization Orbitrap mass spectrometry, and implications for the oxygen isotopic compositions of meteoritic organics. Geochimica et Cosmochimica Acta 404, 257–273.

## Abstract

Oxygen isotopic composition of organic compounds is an important tracer of processes and environmental conditions, with applications ranging from prebiotic organic synthesis in the early solar system to paleoclimate reconstruction. To meaningfully interpret the oxygen isotopic signature of such molecules, we need to consider their rate of oxygen exchange with water, e.g., during aqueous alteration on asteroidal parent bodies or residence on the Earth. In this study, we experimentally constrained the kinetics of oxygen isotope exchange between water and ketones (acetone, cyclopentanone) or carboxylates (acetate, butyrate) near neutral pH between 274.7 – 373 K. We incubated them in $^{18}$O-rich water and measured their $^{18}O/^{16}O$ ratios after incubation using an electrospray ionization Orbitrap mass spectrometer. While ketones completely exchanged oxygen with water within hours, carboxylates achieved only up to 8% oxygen exchange after days of incubation. The time evolution of their $^{18}O/^{16}O$ were consistent with first order kinetics, with exchange rate constants of 1.99 (±0.1) × $10^{-4}$ $s^{-1}$ (acetone), 6.55 (±0.23) × $10^{-5}$ $s^{-1}$ (cyclopentanone), 3.9 (±0.1) × $10^{-8}$ $s^{-1}$ (acetate), 3.9 (±0.2) × $10^{-8}$ $s^{-1}$ (butyrate) at 298±1 K and activation energies of 14.47±0.43 kcal/mol (acetone), 20.35±1.47 kcal/mol (cyclopentanone), 3.53±0.26 kcal/mol (acetate), 2.81±0.43 kcal/mol (butyrate). Rapid exchange for ketones is explained by their hydration in aqueous media and implies that ketones extracted from meteorites should have completely re-equilibrated with the last water they were in contact with over periods of hours or more (possibly at asteroidal parent bodies, or by exposure to terrestrial meteoric or laboratory waters). Carboxylic acids are resistant to exchange due to electrostatic repulsion between the hydroxyl ion and carboxylate ion in basic media. Furthermore, we predict that significant oxygen isotopic exchange between meteoritic insoluble organic matter (IOM) and aqueous fluid is likely during aqueous alteration, based on rate constants reported in this study and previous studies and constraints on the bonding environments of oxygen in IOM.

## 3.1 Introduction

Oxygen bearing organic compounds are a class of organic molecules that contain one or more carbon—oxygen bonds (–C=O or –C–O–) in their structures. Carboxylic acids and carbonyl compounds (aldehydes and ketones) are subsets of this broader class. These compounds have been detected in a range of extraterrestrial environments through different approaches, including extraction from several carbonaceous chondrites (Aponte et al., 2011, 2019; Smith et al., 2014), observation in molecular clouds (Blair et al., 2008) and active protoplanetary disks (Liu et al., 2001; Marel et al., 2014; Favre et al., 2018), cometary ices (Bennett et al., 2010; Duvernay et al., 2014), as well as planetary atmospheres (Korablev et al., 1993). Additionally, such organic compounds constitute a fraction of terrestrial biomass (metabolic intermediates in organisms; DeNiro and Epstein, 1981; Ardawi and Newsholme, 1982; Fukao et al., 2004) and serve as proxies for paleoclimatic reconstructions (Silva et al., 2015; Labahn et al., 2022).

These compounds are suspected to be important components of prebiotic chemistry in early solar system, but their origins are not well understood. Experimental evidence indicates that aldehydes and ketones can form by galactic cosmic ray irradiation of water – carbon monoxide – alkane ices (Abplanalp and Kaiser, 2019; Singh et al., 2022) in conditions resembling the outer solar system or via ion-molecule reactions in the interstellar medium (Chimiak and Eiler, 2024). These compounds also can form at higher temperatures during aqueous alteration of meteorite parent bodies by oxidation of insoluble organic matter (Simkus et al., 2019), or from inner solar system volatile reservoirs via Fischer–Tropsch type reactions. Eventually, these compounds may react to form condensed organics that contribute to the refractory insoluble organic matter (IOM) pool in meteorites, either by exposure to elevated temperatures (>323 K) and basic pH conditions that enable the formose reaction or similar chemistry (Cody et al., 2011; Kebukawa and Cody, 2015), or by ionizing radiation in the inner protosolar nebula at temperatures up to 1000 K (Kuga et al., 2015). Carboxylic acids can form via oxidation of aldehydes or hydrolysis of cyanohydrin in solar nebula and/or asteroidal parent bodies of chondrites (Chimiak and Eiler, 2024).

Each of the aforementioned formation scenarios are expected to impart characteristic oxygen isotopic compositions ($^{18}O/^{16}O$ and $^{17}O/^{16}O$ ratios, or ‘triple oxygen isotope compositions') to the product compounds, due to large variations in the oxygen isotopic compositions of early solar system materials (see Bhattacharjee and Eiler, 2024 and references therein). Hence, studying triple oxygen isotopic compositions of these compounds extracted from carbonaceous chondrites and samples of primitive asteroids returned to Earth can potentially constrain the solar system volatile reservoir from which they formed. However, many carbonaceous chondrites, including most of those that are well studied for their organic chemistry, have experienced varying extents of aqueous alteration in asteroidal parent bodies. This gives rise to a possibility that these compounds underwent oxygen exchange with aqueous fluids during this process, losing any pristine isotopic signature and instead becoming a record of parent body fluids. Prior to study of meteoritic carbonyl compounds, their propensity to undergo oxygen exchange with water needs to be evaluated.

To evaluate the kinetics of this exchange, one must measure oxygen isotopic compositions of the carbonyl and carboxylic acids. For such measurements, previous studies (Samuel and Silver, 1965; Greenzaid et al., 1968a, b) used a nuclear magnetic resonance spectroscopy (NMR) based technique. While this allowed them to conveniently observe the exchange process in real time, it came at a cost of relatively high uncertainties (up to 15% error for NMR peak height for a single run, and comparable errors in reported rate constants). Furthermore, because these studies were conducted at only one temperature, they did not constrain activation energy and so could not be used to estimate exchange rate constants at other temperatures. Alternatively, oxygen isotopic compositions of these compounds can be measured using conventional gas–based isotope ratio mass spectrometry (IRMS) approaches. However, conventional approaches to such measurements require recovery of incubated compounds from water after exchange (which can be difficult due to their high solubilities) and subsequent conversion to CO (pyrolysis) or $O_2$ (fluorination) (e.g., Alexander et al., 2007; Wostbrock et al., 2020; Ellis and Passey, 2023). Since these conversions happen at high temperatures, trace amounts of water present in the recovered compounds will exchange vigorously and modify their isotopic signature during conversion. Complete quantitative yield during these conversions needs to be achieved as well. Furthermore, measuring $^{17}O/^{16}O$ of pyrolysis products (CO) is impossible using traditional magnetic sector mass spectrometers as they lack requisite mass resolution to resolve $^{13}$CO from C$^{17}$O peak.

Isotope ratio measurement using Orbitrap mass spectrometers (Orbitrap–IRMS technique) (Eiler et al., 2017) can potentially circumvent the analytical challenges mentioned above. Firstly, this technique enables measurements of isotopic compositions of analytes in liquid aqueous solvents, which reduces post–exchange processing time of samples to a few minutes and thus minimizes any exchange after an experiment; this approach also avoids challenging material recovery or chemical conversions. It is even possible to observe isotopic exchange in real time for up to tens of hours (Csernica et al., 2023). Secondly, Orbitrap–IRMS can achieve nominal mass resolution of up to 240,000 (measured at m/z of 200; as high as 500,000 on specialized instruments) which is sufficient to resolve $^{13}$C and $^{17}$O isotopologue peaks for many organic compounds. Thirdly, Orbitrap–IRMS allows simultaneous observation of several singly and multiply substituted isotopologues (e.g., $^{13}$C, $^{17}$O, $^{2}$H, $^{18}$O, $^{13}$C—$^{13}$C and $^{13}$C—$^{18}$O peaks) of these analytes, which allows us to observe isotopic variations for different elements, as well as multiply–substituted species, at the same time; only consuming nanomolar sample quantities for a measurement. All of these factors help constrain rate constants of isotopic exchange with high precision. Due to these and other advantages, the Orbitrap–IRMS technique, though relatively new, is increasingly being used to measure isotopic compositions of diverse organic and inorganic analytes (Eiler et al., 2017; Cesar et al., 2019; Hofmann et al., 2020; Neubauer et al., 2020; Chimiak et al., 2021; Hilkert et al., 2021; Mueller et al., 2021, 2024; Zeichner et al., 2022, 2023; Wilkes et al., 2022; Csernica et al., 2023; Weiss et al., 2023; Kantnerová et al., 2024; Hollenback and Jaisi, 2024).

In this work, we constrained the kinetics of oxygen exchange between water and acetone, cyclopentanone, acetate and butyrate individually at temperatures of 274.7 K – 373 K using the Orbitrap–IRMS technique. We quantify activation energies and pre–exponential factors for these exchanges from first–order rate constants across these temperatures. We then use these data to constrain models of expected oxygen isotopic compositions of terrestrial and extraterrestrial organic matter during burial diagenesis or meteorite parent body aqueous alteration processes, combining kinetics constrained in this study and previous works

(Samuel and Silver, 1965; Wedeking and Hayes, 1983). This is a proof–of–concept demonstration and a preparatory study for the future measurements of the oxygen isotopic compositions of meteoritic soluble organics.

## 3.2 Materials and methods

### 3.2.1 Materials

HPLC–Plus grade acetone (>99.9%, from Sigma Aldrich), analytical standard grade cyclopentanone (≥99.5%, acquired from Sigma Aldrich), standard grade sodium acetate (>99% acquired from Mallinckrodt Chemicals) and sodium butyrate (≥98%, acquired from Sigma Aldrich) were used as experimental starting materials in this study. LC–MS grade methanol (from Fischer Chemical) was used as solvent. $^{18}$O labelled water (10 atom% $^{18}$O, Sigma–Aldrich) was added to ultrapure (Milli–Q IQ 7000) deionized water (DIW, dispensed precisely in requisite volume from a Millipore water purification system) volumetrically (1.05 volume%) using adjustable, calibrated mechanical pipette (Eppendorf) or glass syringe (Hamilton) to prepare $^{18}$O rich waters ('heavy waters', or HWs) to be used in exchange experiments. Incubations for acetone and cyclopentanone were done in two separate sessions. Two batches of HW were made for acetone and cyclopentanone incubation experiments, to avoid modification of the $\delta^{18}$O of water during storage between sessions. HW used in the acetone experiments (HW_acetone) was first diluted (5 volume% in DIW) to prepare solution DS1_acetone which was further diluted (10 volume% in DIW) to prepare solution DS2_acetone. Similarly, HW for the cyclopentanone experiments (HW_cyclopentanone) was also diluted twice in DIW (5 volume% and 10 volume% successively) to prepare solution DS1_cyclopentanone and DS2_cyclopentanone. Uncertainty in volume mixing ratios were 0.6% or better. Acetate and butyrate incubations were done in a single session.

### 3.2.2 Exchange experiment

Analyte ketones were first mixed with HWs to prepare aqueous ketone solutions (12500 μM for acetone, 5000 μM for cyclopentanone). These starting solutions were immediately transferred to 2 mL GC vials (leaving no headspace to minimize volatilization), closed with screw top caps and inert teflon liners (Thermo Fischer Scientific), and sealed with Parafilm® M sealing film on the outside. Vials are shaken and subsequently incubated at controlled temperatures for variable durations. A 12–hour incubation for acetone at 298 K was additionally repeated in a 10 ml glass vial with aluminum crimp top and Teflon septa (no Parafilm® M sealing film applied) to evaluate experimental reproducibility.

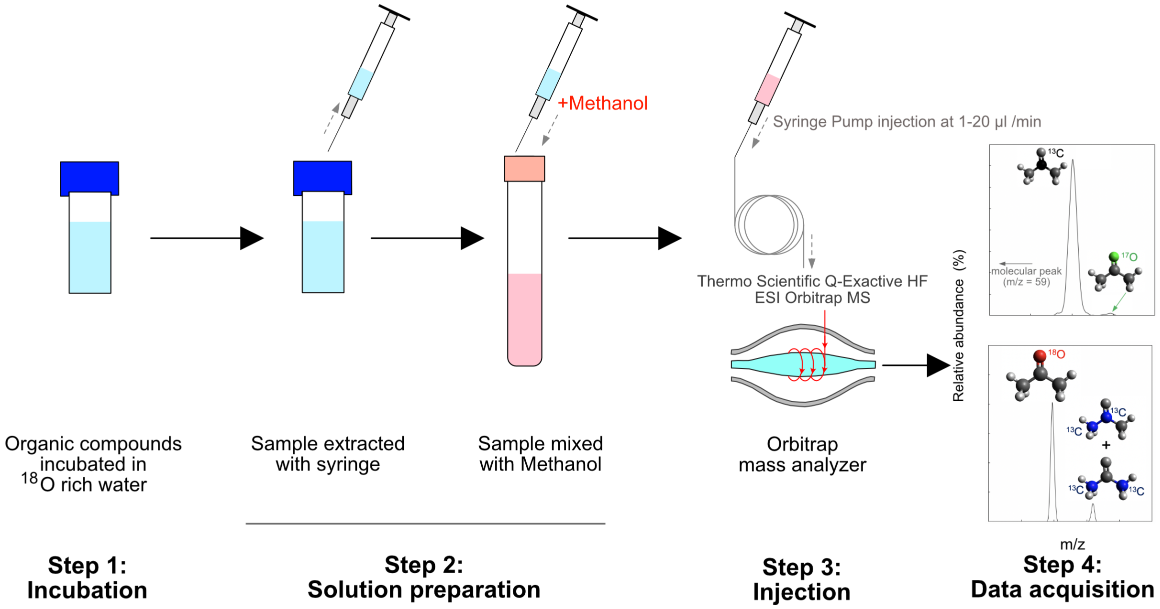

Figure 3.1: Outline of the oxygen isotope exchange experiment of this study. Schematic mass spectra for acetone are shown, for example.

Room temperature incubations were performed by partially submersing these vials in a thermostatted water bath held at 298±1 K. Cold incubations were performed by placing these vials in a refrigerator at 274.7±1 K. HWs used in preparation of aqueous ketone solutions for cold incubations were also kept overnight at 274.7±1 K to ensure thermal equilibrium of the starting solution. Following a similar procedure, 283±1 K incubations were performed in the cooled chamber of a Vanquish HPLC system. Warm incubations were performed in a thermostatted water bath held at 313±2 K (for cyclopentanone only).

After incubation, the vials were removed from the water bath or refrigerator. Solutions from these vials were mixed with methanol (1:9, v/v) to prepare a 1250 µM acetone analytical solution and a 500 µM cyclopentanone analytical solution for isotope ratio measurements. Details of the experimental protocol are outlined in Fig. 3.1. Solution preparation steps between removal of analytes from controlled environment and measurement took ~5–8 minutes at room temperature.

Carboxylic acids are known to undergo much slower oxygen exchange with water (Cohn and Urey, 1938; Roberts and Urey, 1939; Samuel and Silver, 1965; Redington, 1976). Given the possibility that these experiments might not reach exchange equilibrium in laboratory time scales under these conditions, we took a different approach from ketones. We prepared 500 μM stock solutions of carboxylate salts separately in DIW and HW_cyclopentanone and incubated them at different temperatures (thermostatted water baths at 298 K, 323 K, and oven at 373 K) for different durations as pairs, in 2 mL GC vials. Post experiment, solutions were diluted in methanol to prepare 50 μM solutions for isotope ratio measurements.

### 3.2.3 Analytical methods

#### 3.2.3.1 Isotopic composition of ketones and carboxylates

Analytical solutions were introduced to a Thermo Fisher Scientific Q–Exactive HF Orbitrap Mass Spectrometer equipped with an electrospray ionization (ESI) source (ESI–Orbitrap–MS) using a Hamilton 500 μL glass syringe and a syringe pump, in order to measure oxygen isotope ratios ($^{18}O/^{16}O$) of the ketones. Analytical conditions are listed in Table 3.1. Our protocol consumed at most 30 nmol analyte per measurement, calculated based on injection time, flow rate and analyte solution concentration stated in section 3.2.2. We estimated the timescale of complete oxygen exchange from previous studies (Greenzaid et al., 1968a, b) and verified it using trial experiments. Subsequently, we prepared fully equilibrated solutions of acetone and cyclopentanone by incubating acetone or cyclopentanone (as described in section 2.2) in respective HWs for 20 hours at room temperature. These fully equilibrated solutions were used for sample–standard bracketing (i.e., analytical sequence was A–B–A, where A = equilibrated solution, B = samples) over the course of each analytical session. Samples from 274.7 K and 298 K incubations of acetone were measured in session 1, those from 283 K incubations of acetone were measured in session 2, and all cyclopentanone experimental products were measured in session 3.

Carboxylates were measured following the protocol of Mueller et al. (2021) in a single session. 50 μM solutions were introduced to a Thermo Fisher Scientific Q–Exactive HF

Orbitrap Mass Spectrometer equipped with an electrospray ionization (ESI) source (ESI–Orbitrap–MS) using a Hamilton 500 μL glass syringe and a syringe pump, to measure oxygen isotope ratios ($^{18}O/^{16}O$) of the acetate and butyrate. Measurements of carboxylates incubated in HW were bracketed by carboxylates incubated in DIW (i.e., analytical sequence was A–B–A, where A = carboxylates incubated in DIW, B = carboxylates incubated in HW). This approach allows us to directly calculate the difference in oxygen isotopic compositions between HW- and DIW-incubated carboxylates at each step that can be used to evaluate *F* (eq. 9). Alternatively, if we used a freshly prepared standard solution for bracketing, then we needed to know the equilibrium oxygen isotope fractionation between carboxylates and water to calculate oxygen isotopic composition of carboxylates in equilibrium with water at each temperature (e.g., eqs. 5, 12) for rate constant calculation. To our knowledge, no study has examined the equilibrium oxygen isotope fractionation between acetate or butyrate and water at these temperatures. Assuming this fractionation is similar to other carboxylates could add uncertainty to the rate constant estimates.

After each measurement, intensities and corresponding noise values for each isotopologue ion peak in each Orbitrap scan were extracted from raw scan files using the IsoX data processing package and were subsequently processed with IsoXL (https://isoorbi.shinyapps.io/IsoXL/) to obtain $^{18}O/^{16}O$, relative standard error (hitherto 'analytical error',‰) and shot noise (SN) limit for a given analyte from each measurement. Refer to section 2.2.2 of Csernica et al. (2023) for a detailed description of data processing. Briefly, instrumental fractionation and drift were corrected using $^{18}O/^{16}O$ of bracketing standards, and resulting $^{18}O/^{16}O$ of samples were used to calculate δ–values:

$$\delta^{18}O_{sample} = [(^{18}O/^{16}O)_{sample}/(^{18}O/^{16}O)_{standard}) - 1]*1000.$$

Analytical errors of samples and standards were added in quadrature to calculate propagated analytical uncertainty for each measurement (reported in Tables 3.2, 3.3). For carboxylates, $\delta^{18}O_{HW-DIW}$ for a bracketed measurement was calculated as

$$\delta^{18}O_{HW-DIW} = [(^{18}O/^{16}O)_{HW}/(^{18}O/^{16}O)_{DIW}) - 1]*1000.$$

Each measurement has been filtered by two data–quality criteria post–processing:

(1) Measurements where analytical error is greater than twice that of SN limit have been discarded (Such measurements are unusual and inferred to suffer from instability in ionization conditions or other instrumental parameters; Eiler et al., 2017).

(2) Measurements where relative standard deviation (RSD) of the total ion current (TIC) is greater than 10% are discarded as they may suffer from unusually poor stability of sample flow or ion source conditions — problems that are particularly acute at low flow rate conditions (< 5 μL/min) used for all measurements in this study (Table 3.1).

Because our analytical protocol introduces the ketones in a solution of 9:1 methanol and water, the oxygen isotopic exchange between analytes and the water used in the injected solution at the ionization source or throughout a single measurement (30 minutes) must be evaluated and/or corrected for. We have constrained the extent of oxygen isotope exchange during these processes through a separate set of controlled experiments described in the ***supplementary information, section 2***. After 30 minutes of exchange, control solutions of both acetone and cyclopentanone were indistinguishable from the pre–exchange starting solution, within analytical uncertainties. We conclude that the effect of this exchange is negligible and can be safely ignored.

Additionally, we noted a small but significant change in TIC (up to 10%) between each measurement of cyclopentanone; we accounted for possible variation in instrumental bias in measured isotope ratios that might be associated with these changes by analyzing standard solutions of different concentrations and thus different observed TIC values (details in ***supplementary information***).

Solvent (9:1 methanol:DIW) blank contributions to measured $^{18}O/^{16}O$ of the studied ketones was found to be significant in case of acetone. The blank $^{18}O/^{16}O$ was measured over the entire analytical session and used to correct raw $^{18}O/^{16}O$ of samples; in this case, the fraction of blank present in a sample was calculated from the ratio of intensities of the monoisotopic peak of the blank to that of a sample. For most samples, blank corrections to $^{18}O/^{16}O$ ratio were 1–20‰, with two samples having 41–45‰ corrections (out of 600–700‰ raw signal; i.e. blank corrections represent ≤7.5% of measured isotopic differences). Blank contributions to the cyclopentanone monoisotopic peak were negligible and the $^{18}O$

substituted peak was not observed in the blank. No blank contributions were observed for molecular ion or M+2 peak for acetate and butyrate.

### 3.2.3.2 Isotopic composition of HWs

Oxygen isotopic compositions of DS2_acetone, Sol2_cyclopentanone and DIW were measured using a Picarro L2140i gas isotope analyzer in the Resnick Water and Environment Lab, California Institute of Technology. In–house standards spanning a range in $\delta^{18}O$ were used to construct a working calibration (see ***supplementary information***). The $^{18}O/^{16}O$ of DS2_acetone, Sol2_cyclopentanone and DIW were then used to calculate $\delta^{18}O$ of HWs used in the experiments, using volume mixing ratios. $\delta^{18}O$ of HW_acetone and HW_cyclopentanone were 601.1±0.2‰ and 531.7±0.2‰ respectively. Even though we used the same protocol for making heavy water, small human error in measuring the volume of $H_2{}^{18}O$ caused the two batches of water to have different $\delta^{18}O$.

### 3.2.4 Rate constants and Arrhenius parameters calculation

The isotopic exchange reactions observed in this study can be idealized as:

$$^{12}CH_3–^{12}C^{16}O–^{12}CH_3 + H_2{}^{18}O \rightleftharpoons {}^{12}CH_3–^{12}C^{18}O–^{12}CH_3 + H_2{}^{16}O \text{ (1a)}$$

$$(^{12}CH_2)_4{}^{12}C^{16}O + H_2{}^{18}O \rightleftharpoons (^{12}CH_2)_4{}^{12}C^{18}O + H_2{}^{16}O \text{ (1b)}$$

$$^{12}CH_3–^{12}C^{16}O_2H + H_2{}^{18}O \rightleftharpoons {}^{12}CH_3–^{12}C^{18}O^{16}OH + H_2{}^{16}O \text{ (2a)}$$

$$^{12}CH_3–(^{12}CH_2)_2–^{12}C^{16}O_2H + H_2{}^{18}O \rightleftharpoons {}^{12}CH_3–(^{12}CH_2)_2–^{12}C^{18}O^{16}OH + H_2{}^{16}O \text{ (2b)}$$

(note this treatment ignores possible solvation or other speciation effects). The $\delta^{18}O$ value of HW is expected to remain approximately constant throughout each incubation because it is present in great excess compared to acetone and/or cyclopentanone (e.g., mole fractions of acetone in incubation solutions are ~$2.3 \times 10^{-4}$). We have assumed a first–order rate law for the isotopic exchange process between organics and water, e.g.:

$$\frac{d}{dt}\, [^{12}CH_3–\, ^{12}C^{18}O–^{12}CH_3] = -k_{ex}\, [^{12}CH_3–\, ^{12}C^{18}O–^{12}CH_3] \text{ (3)}$$

where $k_{ex}$ indicates rate constant of isotopic exchange at a given temperature and $t$ denotes time. Equation 3 can be simplified and approximated to (for derivation of equations, see Passey and Henkes, 2012; Clog et al., 2015):

$$\frac{\delta^{18}\mathrm{O}_{\mathrm{organics,t}} - \delta^{18}\mathrm{O}_{\mathrm{organics,eq}}}{\delta^{18}\mathrm{O}_{\mathrm{organics,in}} - \delta^{18}\mathrm{O}_{\mathrm{organics,eq}}} = \mathrm{e}^{-k_{ex}t} \quad (4)$$

where subscripts 'eq', 'in' and 't' represent $\delta^{18}O$ values of organics at equilibrium, initial time and at time *t*, respectively. Furthermore, we define the reaction progress variable, *F,* as:

$$F = \frac{\delta^{18}\mathrm{O}_{\mathrm{organics,in}} - \delta^{18}\mathrm{O}_{\mathrm{organics,t}}}{\delta^{18}\mathrm{O}_{\mathrm{organics,in}} - \delta^{18}\mathrm{O}_{\mathrm{organics,eq}}} \quad (5)$$

which further simplifies eq 5 to:

$$\ln\,[1-F] = -k_{ex}t \quad (6)$$

The value of *F* has been calculated and documented in Tables 3.2, 3.3, 3.4. We have calculated rate constants for first order exchange at each temperature by fitting experimental data to equation (6) using linear regression, where $k_{\mathrm{ex}}$ is the only free parameter. The rate constants are tabulated in Tables 3.2, 3.3, along with errors associated with the fitting.

In cases where the rate constant ($k_{\mathrm{ex}}$) is constrained at two or more temperatures, we can estimate the pre–exponential factor ($A_0$) and activation energy ($E_a$) for exchange using the Arrhenius equation:

$$\mathrm{k_{ex}} = A_0 \,.\, \mathrm{e}^{\left(\frac{-E_a}{RT}\right)} \; (7)$$

or, alternatively,

$$\ln(k_{ex}) = \ln(A_0) - \frac{E_a}{RT} \; (8)$$

where *R* is ideal gas constant and *T* is temperature in Kelvin.

For carboxylates, the reaction progress variable *F* was calculated differently, because those incubations did not achieve exchange equilibrium like ketones. At each time point, the difference in $\delta^{18}O$ between carboxylates incubated in DIW and HW was measured. At equilibrium, this difference should be equal to the difference in $\delta^{18}O$ between DIW and HW. Hence, *F* is defined as:

$$F = \frac{\delta^{18}\mathrm{O}_{\mathrm{HW,t}} - \delta^{18}\mathrm{O}_{\mathrm{DIW,t}}}{\delta^{18}\mathrm{O}_{\mathrm{HW}} - \delta^{18}\mathrm{O}_{\mathrm{DIW}}} \quad (9)$$

## 3.3 Results

### 3.3.1 Time series of isotopic composition evolution

The experimental results are presented in Tables 3.2, 3.3, 3.4 and shown in Fig. 3.2, 3.3. Generally, we observed that $\delta^{18}O$ of the ketones evolved from initial to time–invariant (presumably fully equilibrated) values within tens of hours, and the exchange was faster at higher temperatures. Equilibrium in these experiments is identified by a state of time–invariant $\delta^{18}$O values for each ketone.

Acetone incubated at 298±1 K evolved from its initial oxygen isotope ratio to a value 613‰ higher after 4.5 hours, after which it remained time–invariant (and thus is inferred to have reached equilibrium). Cyclopentanone incubated under the same conditions evolved from its initial oxygen isotope ratio to a value 586‰ higher after 24 hours, after which it too remained time–invariant. Cyclopentanone incubated at 274.7±1 K evolved from its initial oxygen isotope ratio to a value 362‰ higher over 120 hours but had not reached a time–invariant plateau at that time and thus is inferred not to have fully equilibrated with its solvent water. Because our analysis of the rate constants for exchange depend in part on an estimate of the final equilibrium composition, we used prior theoretical calculations of the oxygen isotope fractionations between ketones and water to estimate the $\delta^{18}$O of cyclopentanone in equilibrium with HW at 274.7 K, using the following equation:

$$^{18}R_{\mathrm{eq\_274.7K}} = {}^{18}R_{\mathrm{eq\_298K}} * ({}^{18}\alpha_{\mathrm{cyclopentanone–water\_274.7K}} / {}^{18}\alpha_{\mathrm{cyclopentanone–water\_298K}}) \quad (10)$$

where $^{18}R$ = $^{18}$O/$^{16}$O, 'eq' indicates equilibrium and 'α' indicates equilibrium $^{18}$O/$^{16}$O fractionation between cyclopentanone and water at respective temperatures (from Bhattacharjee and Eiler, 2024). A similar approach for acetone incubated at 274.7±1 K indicates it reached close to equilibrium composition (~97% exchange) after 48 hours (~600‰ higher relative to starting composition). For incubations at 283 K, $\delta^{18}$O of acetone reached a time–invariant state after 24 hours of incubation (~541‰ higher relative to starting composition) while cyclopentanone attained that state after 96 hours (~588‰ higher relative to starting composition). Only cyclopentanone was incubated at 313 K, where its $\delta^{18}$O reached time invariant state after 9 hours (~582‰ higher relative to starting composition).

Carboxylates were much resilient to oxygen exchange with water. The $\delta^{18}$O difference between HW and DIW incubated acetate at the beginning of the experiment (t = 0) is 0‰. This difference reached a value of 20.6‰ after 10 days of incubation at 298 K (3.4% exchange). The highest extent of exchange was observed after incubation for 200 hours at 373 K (8.2% exchange). The extent of exchange for butyrate under similar conditions was even lower (6.8%) with a $\delta^{18}$O difference of 41.9‰. None of the acetate and butyrate exchange experiments attained time invariant isotopic equilibrium with water.

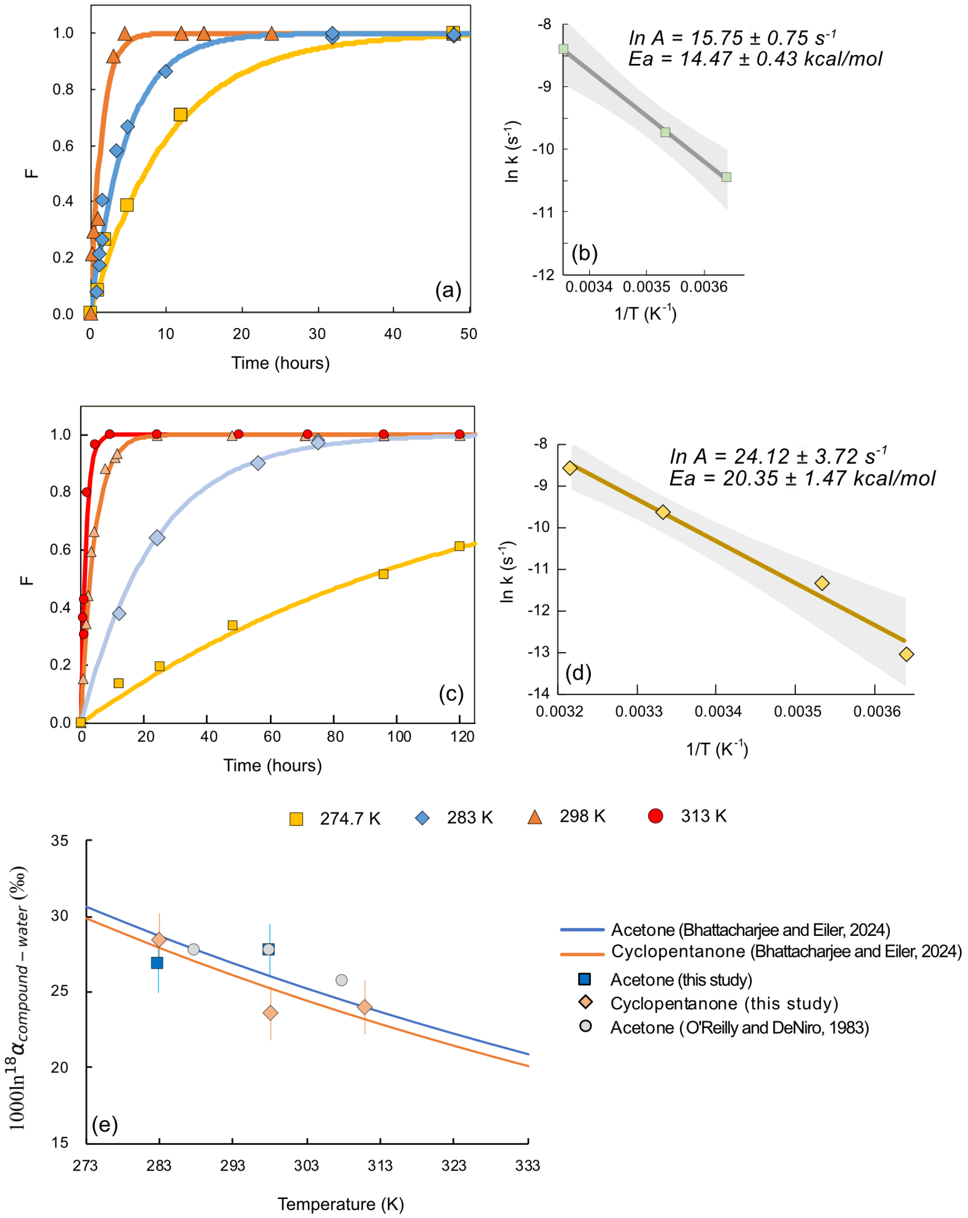

Figure 3.2: Results of oxygen isotope exchange experiments between ketones and water. (a) Plot of fraction of exchange vs time for acetone. (b) Plot of ln $k$ vs $1/T$ for acetone. (c) Plot of fraction of exchange vs time for cyclopentanone. (d) Plot of ln $k$ vs $1/T$ for cyclopentanone. For a and c, symbols indicate results of experiments from this study while solid curves indicate that obtained using equation 6 with rate constants calculated at each temperature. For b and d, solid lines represent best fits to the data and the shaded band shows the 95% confidence interval. (e) Comparison between equilibrium $^{18}$O/$^{16}$O fractionation between

water and acetone or cyclopentanone constrained in this study and previous works (O'Reilly and DeNiro, 1983; Bhattacharjee and Eiler, 2024). Error bars are 1SE.

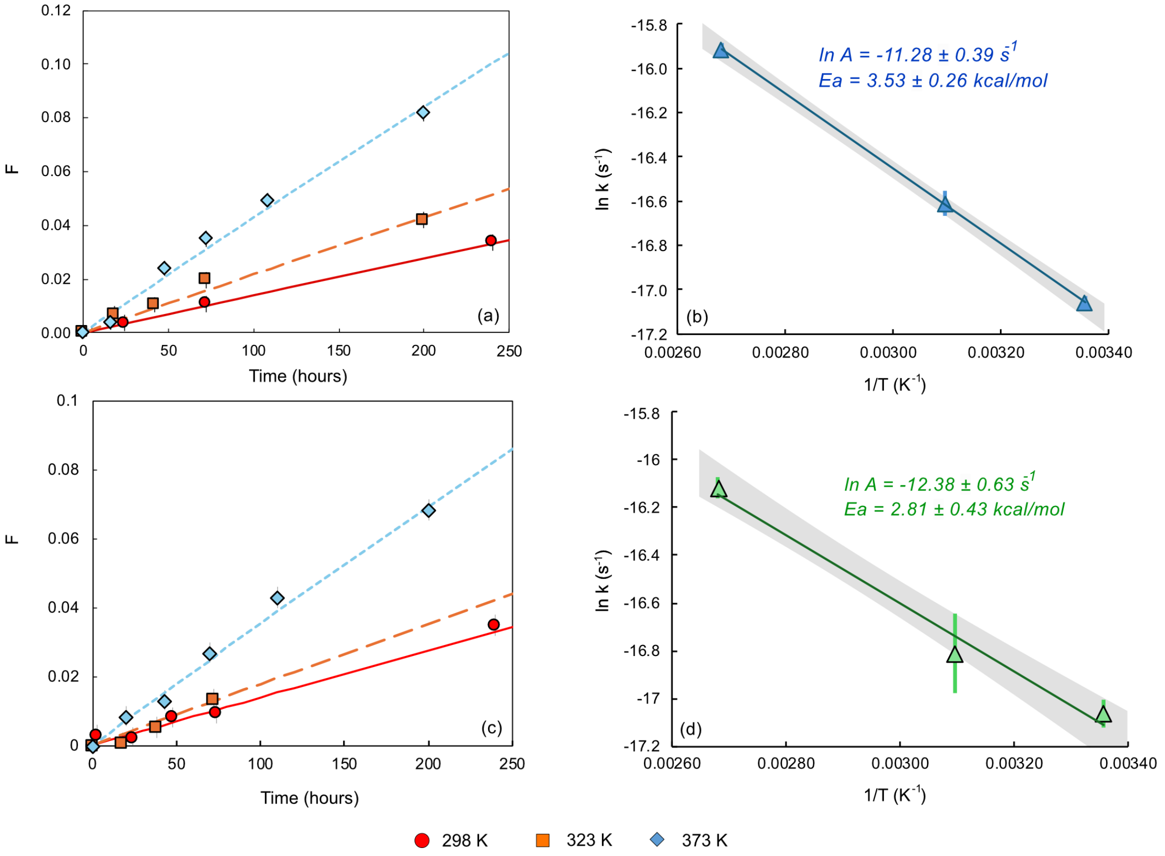

Figure 3.3: Results of oxygen isotope exchange experiments between carboxylates and water. (a) Plot of fraction of exchange vs time for acetate. (b) Plot of ln *k* vs 1/*T* for acetate. (c) Plot of fraction of exchange vs time for butyrate. (d) Plot of ln *k* vs 1/*T* for butyrate. For a and c, symbols indicate results of experiments from this study while lines indicate that obtained using equation 6 with rate constants calculated at each temperature. For b and d, solid lines represent best fits to the data and the shaded band shows the 95% confidence interval.

### 3.3.2 Rate Constants and Arrhenius parameters

Rate constants for both acetone and cyclopentanone exchange experiments define linear trends in ln($k_{ex}$) vs 1/$T$ space with $R^2 = 0.983$ or better (Fig. 3.2). Using slopes and intercepts of such linear trends, calculated activation energies for acetone–water and cyclopentanone–water oxygen isotope exchange are 13.78 (±1.2) kcal/mol and 20.35 (±1.47) kcal/mol, respectively, and values of ln($A_0$) were 14.75 (±2.1) $s^{-1}$ and 24.12 (±3.7) $s^{-1}$ respectively. Exchange rate constants for carboxylates were orders of magnitude slower than ketones. Rate constants for both acetate and butyrate exchange experiments also define linear trends in ln($k_{ex}$) vs 1/$T$ space with $R^2$ = 0.982 or better (Fig. 3.3). The calculated rate constants for acetate–water and butyrate–water oxygen isotope exchange are 3.53 (±0.26) kcal/mol and 2.81 (±0.43) kcal/mol, respectively, and values of ln($A_0$) were –11.28 (±0.39) $s^{-1}$ and –12.38 (±0.63) $s^{-1}$ respectively.

### 3. 3.3 Equilibrium $^{18}O/^{16}O$ fractionation between ketones and water

Since our experiments for ketones achieved equilibrium, we calculated equilibrium $^{18}O/^{16}O$ fractionations for acetone–water and cyclopentanone–water pairs. The results are summarized in Table 3.5. We obtained $1000\ln^{18}\alpha_{acetone-water}$ of 26.8±1.7‰ and 27.7±1.7‰ at 283 K and 298 K respectively, and $1000\ln^{18}\alpha_{cyclopentanone-water}$ of 28.4±1.7‰, 23.6±1.7‰ and 24.0±1.7‰ at 283 K, 298 K, and 311 K, respectively. These fractionation factors agree well with prior experimentally determined (O'Reilly and DeNiro, 1983) and quantum mechanics predicted fractionations (Bhattacharjee and Eiler, 2024), within analytical uncertainty (Fig. 3.2e).

## 3.4 Discussion

### 3.4.1 Mechanisms of isotopic exchange for various oxygen–bearing organic compounds

### 3.4.1.1 Ketones

The oxygen isotope exchange between water and ketones proceeds through reversible hydration of ketones via the formation of intermediate diol hydrates (Samuel and Silver, 1965; Greenzaid et al., 1968a; Wolfe et al., 1998). An example of acetone can be depicted as:

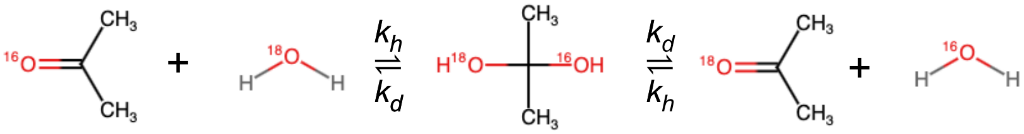

The equilibrium constant for hydration of acetone ($K = K_{hydration}$ = [diol]/[ketone] = $k_h/k_d$ where $k_h$ = rate constant of hydration and $k_d$ = rate constant of dehydration) has been determined to be $1.75 \times 10^{-3}$ at 298 K (Bell, 1966; Wiberg et al., 1994). Combining this constraint with the measured of rate constant of hydration ($k_h = 8.9 \times 10^{-6} - 2 \times 10^{-5}$; Greenzaid et al., 1968; Wolfe et al., 1998) yields a value of $k_d$ in the range $1.1 \times 10^{-2} - 5.1 \times 10^{-3}$. For cyclohexanone in water at 298 K ($K = 3.06 \times 10^{-2}$, $k_h = 7 \times 10^{-5}$; Greenzaid et al., 1968; Wiberg et al., 1994), $k_d = 2.3 \times 10^{-3}$. This analysis shows that the slowest step in the exchange reaction for the compounds studied here is the hydration of ketone compounds to form diol hydrate. For formaldehyde and acetaldehyde, $K > 1$, implying $k_h > k_d$. For these compounds, dehydration is the rate limiting step (Fig. 3.4d).

We did not attempt to constrain the variation in kinetics of oxygen exchange with pH. Acid or base catalysis for such exchanges has been established in prior studies (Greenzaid et al., 1968a, b), observed experimentally using nuclear magnetic resonance spectroscopy (NMR) based techniques. A compilation of previous experimental data shows the relationship between exchange rate constant and pH (Fig. 3.4) at 300 K, which suggests faster exchange at basic (pH > 7) or acidic (pH < 7) conditions, with base–catalyzed exchange between ketones and water being faster than acid–catalyzed exchange. This trend is also shown by sugar molecules (Fig. 3.4f), whose isotopic exchange with oxygen in water is dictated by their ring closure rate, hydration at the carbonyl site and mutarotation rate (Mega et al., 1990). However, previous experiments were done in the presence of ~1–10 mM phosphate buffer solution with greater concentration of ketones (1.4 M) and higher ionic strength solutions ($I = 0.1$) (Greenzaid et al., 1968a). All of these factors could have impacted the exchange rate constant since the buffers are also found to catalyze the reactions (Greenzaid et al., 1968a). Our results at 298 K, reflecting the rate of uncatalyzed exchange in water near neutral pH, agree well with prior findings for cyclopentanone (Fig. 3.4b). Our results for acetone at 298 K agree well with prior rate constant at pH = 6.7, which corresponds to the lowest buffer concentration for that pH in that study (Fig. 3.4a), but indicate ~6 times faster exchange compared to the prior rate constants measured at pH = 7 and relatively low buffer concentration (Greenzaid et al., 1968a).

Previous studies have reported catalytic rate constants for oxygen isotope exchange reactions between ketones and water (Greenzaid et al., 1968a, b), which depend on the mechanism of the reaction and the mode of catalysis (e.g., acid vs base catalysis). In acidic media, aldehydes and ketones experience two competing reaction paths. They can undergo either enolization or hydration. If enolized, the enol form converts back to keto form (no oxygen exchange) whereas if hydrated, the compound experiences oxygen exchange with water, as discussed earlier. Acid catalyzed enolization rate ($k_E$) and acid catalyzed oxygen

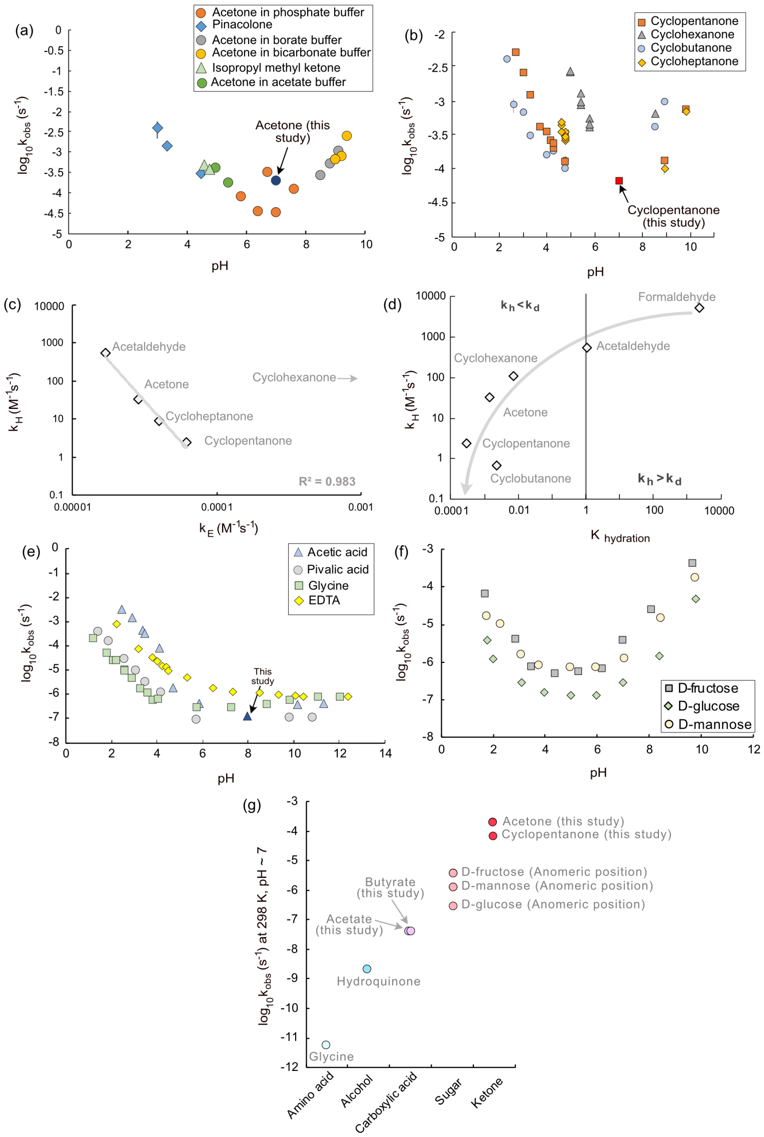

Figure 3.4: Control of pH and reaction mechanisms on oxygen exchange rate. (a) Variation of rate constant for oxygen exchange between acetone and water with pH at 300 K (Greenzaid et al., 1968a). (b) Variation of rate constant for oxygen exchange between cyclic ketones and water with pH at 300 K (Greenzaid et al., 1968b). (c) Variation of acid-catalyzed enolization rate ($k_E$) with acid-catalyzed oxygen exchange rate constant ($k_H$) (data from

Chiang et al., 1987, 1989; Keeffe et al., 1990). (d) Plot of acid-catalyzed oxygen exchange rate constant ($k_H$) between ketones or aldehydes and water against their hydration equilibrium constant, $K_{hydration}$ (data from Wiberg et al., 1994; Guthrie, 2000). Gray curve, indicating general trend, is only to guide the eye. (e) Variation of oxygen isotope exchange rate constants for different carboxylic acids with pH at 373 K (Cohn and Urey, 1938; Llewellyn and O'Connor, 1964; O'Connor and Llewellyn, 1965; Samuel and Silver, 1965; O'Connor, 1968; Redington, 1976; Murphy and Clay, 1979). (f) Variation of oxygen isotope exchange rate constants at the anomeric carbon position for different sugars with pH at 299 K (Mega et al., 1990). (g) Comparison of oxygen isotope exchange rate constants for various classes of oxygen-bearing organic compounds (Samuel and Silver, 1965; Murphy and Clay, 1979; Mega et al., 1990) at 298 K and pH~7.

exchange rate ($k_H$) for these compounds are negatively correlated (Fig. 3.4c), suggesting that compounds which prefer to form enols (higher $k_E$) have slower oxygen exchange rate (because the enolization pathway does not involve oxygen exchange) and vice versa. Cyclohexanone violates this trend by having significantly higher enolization rate ($k_E$ = 0.000238 $M^{-1}$ $s^{-1}$, Keeffe et al., 1990) than others, possibly due to greater stability of endocyclic double bonds in 6–membered rings compared to 5– or 7–membered rings. In summary, this demonstrates that oxygen exchange rates are influenced by hydration and enolization of aldehydes and ketones in acid media.

The ketone–water oxygen exchange reaction exhibits a significant energy barrier ranging from 13.7 to 20.4 kcal/mol. This illustrates the impact of hydration on the mechanism of the reaction. Acetone hydrates more quickly than cyclopentanone, suggesting it is energetically more advantageous to hydrate acetone, which helps promote the oxygen exchange. As a result, the activation energy for this exchange reaction in acetone is lower than that of cyclopentanone (Fig. 3.2).

#### 3.4.1.2 Carboxylic acids

The mechanism of oxygen exchange between carboxylic acid and water depends on pH conditions. Carboxylate salts dissolved in water reach a slightly alkaline pH (~7.5). Under these conditions, the exchange reaction is dictated by the hydroxide ion attack on the carboxylic group. However, due to electrostatic repulsions between both moieties, such an attack is unlikely (Llewellyn and O'Connor, 1964; O'Connor and Llewellyn, 1965; Samuel and Silver, 1965; O'Connor, 1968). Hence, the reaction becomes very slow (Samuel and

Silver, 1965) and leads to limited exchange. This is also reflected in similar values of pre–exponential factors ($\ln(A_0) = -11.28$ to $-12.38$), suggesting a small probability of successful collision that can lead to isotopic exchange between carboxylates and water. Such a negative pre–exponential factor is consistent with previous findings (Llewellyn and O'Connor, 1964), where $\ln(A_0)$ for acetic acid calculated using exchange rate constants for different temperatures at basic pH (~10.2) was found to be –16.98. Moreover, the rate constant becomes insensitive to pH at basic conditions (pH > 7) (Fig. 3.4e). However, at low pH, the exchange is acid–catalyzed and occurs much faster (Roberts and Urey, 1939; Llewellyn and O'Connor, 1964; O'Connor and Llewellyn, 1965; O'Connor, 1968; Redington, 1976), owing to rapid protonation of the carboxylates. In the region of pH ~ 1–6, the exchange rate constant decreases with increasing pH but remains insensitive to pH increase when pH > 6. Molecules with a carboxyl group (carboxylic acid; amino acid) show this general trend in $k_{ex}$ vs pH plot (Fig. 3.4e), indicating similarities in mechanisms of oxygen isotope exchange with water. The activation energy for oxygen exchange between carboxylic acid and water under slightly basic conditions is small (2.8 – 3.5 kcal/mol). This is in agreement with previous studies (5.3 kcal/mol for acetic acid at basic pH, combining the dataset of this study and Llewellyn and O'Connor, 1964; 13.1 kcal/mol for pivalic acid at basic pH, Llewellyn and O'Connor, 1964). This indicates that the energy barrier for carboxylic acid exchange is small, but the reaction is collisionally limited in basic media.

#### 3.4.1.3 Comparison of exchange rates for different oxygen–bearing functional groups

Exchange rate constants for different organic molecules at 298 K near neutral pH (~7) are presented in Figure 3.4g, combining results from this study and previous works (Llewellyn and O'Connor, 1964; O'Connor and Llewellyn, 1965; Samuel and Silver, 1965; O'Connor, 1968; Redington, 1976; Mega et al., 1990). Under these conditions, the order of exchange rate constants is ketone > sugar > carboxylic acid > alcohol > amino acid. This trend possibly reflects the control of the exchange mechanism and molecular structure on the rate constants, as discussed in the sections above.

### 3.4.2 Implications for environmental applications

#### 3.4.2.1 Implications for paleoclimate reconstruction using $^{18}O/^{16}O$ of plant cellulose

Our experimental results are relevant to applications of oxygen isotope geochemistry to reconstruct past climatic conditions using plant biomass archives, particularly cellulose. The $^{18}O/^{16}O$ ratio of plant cellulose is thought to reflect that of the water available to plants while they grow, offset by a biochemical fractionation that is similar to the equilibrium ketone–water fractionation at ambient temperatures (e.g., DeNiro and Epstein, 1981; Xia and Yu, 2020). Our results, combined with previous reports, enable us to revisit the applicability of this proxy to study the geological past.

Cellulose is a polysaccharide made of multiple sugar (glucose) units joined by glycosidic bonds. Sugar synthesis in plants involves many steps where oxygen exchange with fluid is fast due to involvement of carbonyl (aldehyde, ketone) intermediates (Greenzaid et al., 1968a, b; Viswanathan et al., 1982; O'Reilly and DeNiro, 1983), enzyme catalysis (e.g., aldolase, triose phosphate isomerase), heterotrophic sugar cycling (Waterhouse et al., 2013) via mechanisms like mutarotation, hydrolysis, and ring opening. Fast oxygen exchange between the anomeric positions of sugars and water in these steps (Rittenberg and Graff, 1958; Risley and Van Etten, 1980; Mega et al., 1990) suggests that the synthesized sugars should be in equilibrium with plant fluids. This signature is eventually recorded in cellulose when it is synthesized via polymerization of these sugars.

In the next step, cellulose exchanges oxygen with fluids post-synthesis. The extent of this exchange in a diagenetic subsurface environment governs the applicability of this proxy in deep time, and to our knowledge, no study constrained the kinetics of this exchange experimentally. Cellulose hosts oxygen in alcohol and ether groups (glycosidic bonds). Hollenback and Jaisi (2024) showed that in inositol phosphate (a sugar phosphate), oxygens that bridge phosphate and inositol (i.e., bridging oxygens) do not exchange with water at 358 K and pH ~ 6. We can approximate the exchangeability of glycosidic oxygens with that of the bridging oxygens and assume that they are essentially non-exchanging. Exchangeability of alcohols can vary significantly, depending on their structure. At pH ~ 0 and 398 K, the rate constant for oxygen exchange between neopentyl alcohol and water is $1.4 \times 10^{-8}\ s^{-1}$ (Samuel and Silver, 1965). Assuming kinetics is linear in $[H^+]$ (Wedeking and Hayes, 1983), half-life for this exchange at 398 K and pH ~ 5 is 0.16 Ma. Given their structural similarity, this can apply to the primary alcohol group in cellulose, whereas the exchangeability of secondary alcohols can be approximated by s-butyl alcohol (half-life of 3 years at 373 K and pH~5). These first-order estimates suggest that if cellulose is exposed to such conditions over geological time, its bulk isotopic signature can be completely modified, obliterating any signal associated with initial synthesis. However, cellulose from recent plant tissue, exposed to only near-surface temperatures, can retain its pristine signature and be useful for paleoclimate studies. Since the primary alcohol in cellulose is most resistant to oxygen exchange (~1.6 Ma for complete exchange), its site-specific oxygen isotope measurements can reveal valuable information on paleoclimate or plant metabolism (Waterhouse et al., 2013). This remains a tractable target for future studies.

#### 3.4.2.2 A theoretical framework to constrain oxygen exchange kinetics for macromolecules, and implications for lipid paleoclimate proxies

To understand oxygen isotopic compositions of macromolecules at large, we aim to construct a general model that can predict oxygen isotope exchange rates of macromolecules containing different oxygen–bearing functional groups, using the exchange rate constants for each of those individual functional groups from this study and previous works. This model can be applied to a variety of terrestrial and extraterrestrial problems, including chondritic organics and terrestrial paleoclimate proxies. For example, plant lipid biomarkers are important archives of paleoclimate, as their D/H and $^{18}O/^{16}O$ ratios record isotopic compositions of growth medium water, aridity, and temperature (Castañeda et al., 2010, 2016; Silva et al., 2015; Labahn et al., 2022). Their propensity to undergo isotopic exchange during burial diagenesis depends on the structure of the specific molecule in question, which differs in the functional groups hosting oxygen. However, the overall kinetics of oxygen isotope exchange of such molecules is poorly understood. In the following discussion, we construct and validate such a model using prior experimental data on algal biomass, and quantitatively estimate the propensity of lipids to undergo isotope exchange with water under conditions of burial diagenesis and early catagenesis.

Wedeking and Hayes (1983) attempted to constrain the oxygen isotope exchange kinetics of algal biomass at 353 K and pH 1 – 2. They noted incomplete isotopic exchange between bulk oxygen of the biomass and $^{18}$O rich water after incubation up to 100 hours. They interpreted these data as reflecting the exchangeability of two pools of oxygen in the biomass – 'exchangeable' and 'non–exchangeable' oxygen, which represent fast–exchanging and slow–exchanging oxygen sites in the molecular structure, respectively. Assuming the fast–exchanging pool has exchange kinetics similar to benzoic acid, they calculated ~30% of the total oxygen in the biomass is fast–exchanging. We revisit their experimental data (conducted at pH = 1) with rate constants reported in this study and previous works for a deeper understanding of such exchange in light of molecular structure. Assuming both the pools show first–order exchange kinetics, we describe the time evolution of bulk biomass $\delta^{18}$O using equations modified from Passey and Henkes (2012):

$$\delta^{18}O_{\mathrm{bulk(t)}} = (\delta^{18}O_{\mathrm{bulk(0)}} - \delta^{18}O_{\mathrm{bulk(eq)}})\,(f_{\mathrm{ex}}\exp(-k_{ex}.t) + f_{n\mathrm{ex}}\exp(-k_{nex}.t)) + \delta^{18}O_{\mathrm{bulk(eq)}} \quad (11)$$

where $\delta^{18}O_{\mathrm{bulk(t)}}$ = bulk biomass $\delta^{18}$O at time $t$, $\delta^{18}O_{\mathrm{bulk(0)}}$ = initial bulk biomass $\delta^{18}$O, $\delta^{18}O_{\mathrm{bulk(eq)}}$ = bulk biomass $\delta^{18}$O at equilibrium, $f_{\mathrm{ex}}$ = fraction of fast–exchanging oxygen pool in bulk biomass, $f_{n\mathrm{ex}}$ = fraction of slow–exchanging oxygen pool = 1–$f_{\mathrm{ex}}$, $k_{ex}$ = rate constant for oxygen isotope exchange for fast–exchanging oxygen pool, $k_{nex}$ = rate constant for oxygen isotope exchange for slow–exchanging oxygen pool. The estimation for equilibrium $\delta^{18}$O is given as:

$$\delta^{18}O_{\mathrm{bulk(eq)}} = f_{\mathrm{ex}}\,(\delta^{18}O_{\mathrm{water}} + 1000\ln{}^{18}\alpha_{\mathrm{ex–water\ at\ 353K}}) + f_{n\mathrm{ex}}\,(\delta^{18}O_{\mathrm{water}} + 1000\ln{}^{18}\alpha_{\mathrm{nex–water\ at\ 353K}}) \quad (12)$$

where $1000\ln{}^{18}\alpha_{\mathrm{ex–water\ at\ 353K}}$ presents equilibrium $^{18}$O/$^{16}$O fractionation between the fast–exchanging pool and water at 353 K and $1000\ln{}^{18}\alpha_{\mathrm{nex–water\ at\ 353K}}$ represents that for slow–exchanging pool and water. $1000\ln{}^{18}\alpha_{\mathrm{ex–water\ at\ 353K}}$, $1000\ln{}^{18}\alpha_{\mathrm{nex–water\ at\ 353K}}$ and $f_{\mathrm{ex}}$ ideally should vary depending on the choice of $k_{ex}$, $k_{nex}$ and functional groups comprising the fast–exchanging oxygen pool. For our initial fit to the prior experimental data, parameters were taken as follows (after Wedeking and Hayes, 1983):

$$1000\ln{}^{18}\alpha_{\mathrm{ex–water\ at\ 353K}} = 17‰$$

$$1000\ln{}^{18}\alpha_{\mathrm{nex–water\ at\ 353K}} = 0‰$$

$$k_{ex} = 2.33\mathrm{x}10^{-5}\ \mathrm{s}^{-1}$$

$\delta^{18}O_{\mathrm{bulk(0)}}$ and $\delta^{18}O_{\mathrm{bulk(t)}}$ = from original dataset while $f_{ex}$ was kept a free parameter. Comparison of the output of this model with prior data (Fig. 3.5c) yields best–fit values of $k_{nex} = 1.92 \times 10^{-7}$ s$^{-1}$ and $f_{ex} = 0.27$. Using this as an initial guess, we search for compounds which have similar k for oxygen isotope exchange at 353 K (Bender et al., 1956; Samuel and Silver, 1965; Murphy and Clay, 1979; Mega et al., 1990; Maxwell et al., 2018) to refine the model further. The possible candidates include hydroquinone, resorcinol, mesitoic acid. Exact $1000\ln^{18}\alpha_{\text{compound–water}}$(353 K) is unknown for these compounds. Hydroquinone, resorcinol are aromatic alcohol compounds and we assume that their $^{18}O/^{16}O$ fractionation behavior will be similar to that of phenol. Hence, for these three compounds, $1000\ln^{18}\alpha_{\text{compound–water}}$(353 K) is approximated to be 21‰ (Bhattacharjee and Eiler, 2024). Assuming an $^{18}O/^{16}O$ fractionation for mesiotic acid will be similar to benzoic acid, $1000\ln^{18}\alpha_{\text{compound–water}}$(353 K) = 17‰ is applied. Similarly, for the fast–exchanging pool ($f_{ex}$), cyclopentanone, benzoic acid, glycine, aspartic acid and D–mannose are taken as candidates; for benzoic acid, cyclopentanone and D–mannose, the $1000\ln^{18}\alpha_{\text{ex–water}}$(353 K) value is approximated to be 17‰ and the value for glycine and aspartic acid are assumed to be similar to alanine (25‰; Bhattacharjee and Eiler, 2024). Even though we carefully assigned the equilibrium fractionation factors, the model is relatively insensitive to the choice of these fractionation factors. For all data, we assumed the rate constant for oxygen isotope exchange is linear with [H$^+$] concentration (Wedeking and Hayes, 1983) to extrapolate rate constants from circum–neutral pH's to pH = 1.

Next, we explored different combinations of $k_{ex}$ and $k_{nex}$ to understand which combination best explains the experimental dataset of Wedeking and Hayes (1983) quantitatively (Fig. 3.5a,b). Specifically, we have used different pairs of $k_{ex}$ and $k_{nex}$ (Table 3.6) in equation (11) to determine which pair fits the experimental data best (i.e., highest $R^2$). Our analysis indicates that the best fit is achieved for $k_{ex}$ = benzoic acid and $k_{nex}$ = hydroquinone ($R^2$ = 0.9845) with $f_{ex}$ = 0.2417. The fit for this pair is shown in Figure 3.5c. From a structural standpoint, this finding is intuitively satisfying, as algal lipid biomass and kerogens are often dominated by carboxylic acids and esters and alcohol functional groups (Vandenbroucke and Largeau, 2007; Kumari et al., 2013). At 353 K and pH = 1, amino acids and ketones exchange too fast, and resorcinol and mesiotic acid too slowly, to be representative of algal biomass in this experiment. This analysis reveals the way in which molecular structure controls the kinetics of oxygen isotope exchange of macromolecular organic matter and validates our approach to predict oxygen isotope exchange rates for macromolecules. Extrapolating these findings to plausible diagenetic conditions (pH ~ 6.0; 353 K), we estimate it takes ~0.25 Ma for bulk biomass to undergo extensive oxygen isotope exchange with ambient water. This is an average exchange among all exchangeable positions, and some positions may exchange even faster (e.g., alkenones). This timescale is short concerning the durations and ages of many geological processes and materials.

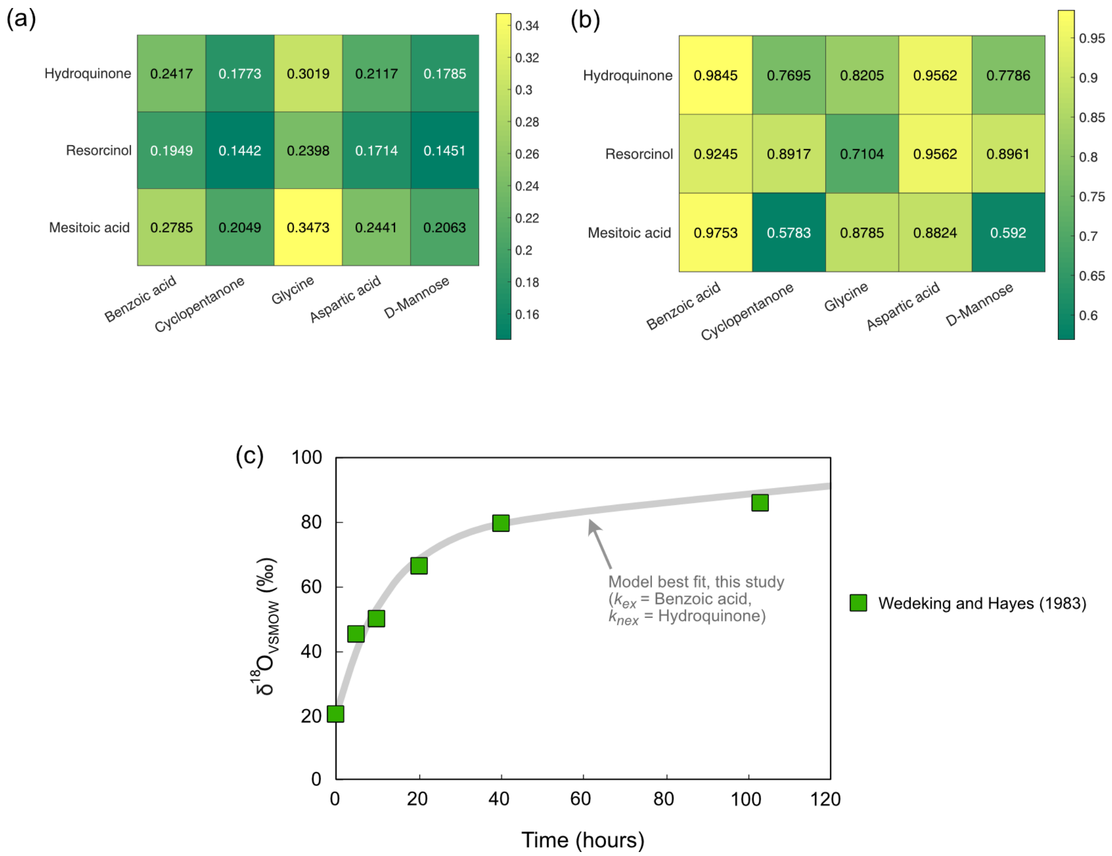

(a)

| | Benzoic acid | Cyclopentanone | Glycine | Aspartic acid | D-Mannose |
|---|---|---|---|---|---|
| Hydroquinone | 0.2417 | 0.1773 | 0.3019 | 0.2117 | 0.1785 |
| Resorcinol | 0.1949 | 0.1442 | 0.2398 | 0.1714 | 0.1451 |
| Mesitoic acid | 0.2785 | 0.2049 | 0.3473 | 0.2441 | 0.2063 |

(b)

| | Benzoic acid | Cyclopentanone | Glycine | Aspartic acid | D-Mannose |
|---|---|---|---|---|---|
| Hydroquinone | 0.9845 | 0.7695 | 0.8205 | 0.9562 | 0.7786 |
| Resorcinol | 0.9245 | 0.8917 | 0.7104 | 0.9562 | 0.8961 |
| Mesitoic acid | 0.9753 | 0.5783 | 0.8785 | 0.8824 | 0.592 |

Figure 3.5: Heatmaps for fraction of exchangeable oxygen (a) and regression $R^2$ values for different pairs (b). Experimental data of Wedeking and Hayes (1983) is plotted with the model best fit from our analysis (c).

### 3.4.3 Implications for oxygen isotopic compositions of meteoritic organics

Several oxygen–bearing organic compounds have been extracted from carbonaceous chondrite meteorites and measured for their abundances and carbon isotopic compositions (e.g., Jungclaus et al., 1976; Pizzarello and Huang, 2002; Sephton, 2002). Aponte et al.

(2019) reported up to ~150 nmol/g total ketone and 850 nmol/g total aldehyde contents from different CI, CV, CM and CR chondrites. The triple oxygen isotopic compositions of these compounds have not been previously measured, but our previous study predicted that they depend on the substrates and mechanisms of formation (Bhattacharjee and Eiler, 2024). Irrespective of their origin, these aldehydes and ketones may have partially or fully equilibrated with any water they may have come in contact with, such as during parent body alteration or terrestrial exposures; in fact, such exchange should be expected given the experimental evidence for rapid oxygen isotope exchange with water under laboratory conditions. Although carboxylic acids undergo slower oxygen exchange with water, they too are expected to completely equilibrate with aqueous alteration fluids given that the aqueous alteration persists for millions of years (Suttle et al., 2021; Lee et al., 2025).

During aqueous alteration of the parent bodies of carbonaceous chondrites, we estimate that the water–ketone oxygen isotope equilibration should be closely approached within several hours, given the high temperature (> 323 K) and basic (pH ~ 8+) fluid environment previously estimated based on petrologic and geochemical evidence (Zolensky et al., 1989; Ohnishi and Tomeoka, 2007; Suttle et al., 2021); this exchange may be significantly accelerated compared to laboratory experiments because base –catalyzed oxygen exchange happens even faster than that in neutral water (Greenzaid et al., 1968a, b). Thus, the oxygen isotope compositions of aldehydes and ketones in carbonaceous chondrites might be useful as tracers of the isotopic compositions of the fluids present on their asteroidal parent bodies. In contrast, compounds that are more resistant to oxygen exchange (e.g., ethers, aromatic alcohols, amino acids) should be more likely to retain the oxygen isotopic composition they had when synthesized, and hence have the potential to be proxies of early solar system volatile reservoirs and processes. Because isotopic exchange drives equilibrating systems toward mass dependent inter–compound isotopic fractionations, we would anticipate that any two materials subjected to equilibration with each other or some common phase would conform to mass dependent trends in plots of $\delta^{18}O$ vs. $\delta^{17}O$. Insoluble organic matter (IOM) is the organic residues of acid digestion of meteorites. Previous measurements of their triple oxygen isotopic compositions ($^{17}O/^{16}O$ and $^{18}O/^{16}O$) indicate that these materials are loosely consistent with a mass independent, slope ~1 line in a $\delta^{18}O$ vs. $\delta^{17}O$ plot, resembling the better defined slope–1 line defined by the 'carbonaceous chondrite anhydrous mineral' (CCAM) trend (Tartèse et al., 2018).

We expect that the kinetics of oxygen exchange between IOM and aqueous fluids will be influenced by their molecular structures, environmental temperature, and fluid pH, though we think it is imaginable that catalysis and the ability of fluids to perfuse IOM materials in the matrices of the CC's may also be controlling factors. Using a range of spectroscopic, electron microscopic as well as thermal and chemical degradation techniques, Derenne and Robert (2010) showed that most of the oxygen atoms in the IOM of CM chondrite Murchison are hosted by carboxylic acids and esters (69%) with the rest hosted by alcohol and ethers groups (33%). Long chain and aromatic alcohols and ethers are relatively resistant to oxygen isotope exchange even at high temperatures. Carboxylic acids are relatively resistant to isotopic exchange with water at basic conditions, but oxygen in ester groups undergoes oxygen exchange with ambient fluid by base–catalyzed hydrolysis (Samuel and Silver, 1965). Because a majority of the oxygen in IOM from the Murchison meteorite seems to be present as esters (Derenne and Robert, 2010), the rate of isotopic exchange between this IOM and water during aqueous alteration in Murchison's asteroidal parent body, which occurred at up to ~373 K and basic pH (Suttle et al., 2021; Clog et al., 2024), is predicted to be high. We assess the propensity of oxygen exchange between IOM and water below to interpret their oxygen isotopic composition.

First, we need to evaluate the temperature–dependent equilibrium $^{18}O/^{16}O$ fraction between IOM and water, which has not previously been investigated experimentally or computationally. Assuming the ether and alcohol groups fractionate $^{18}O/^{16}O$ similar to aromatic alcohols, and esters fractionate $^{18}O/^{16}O$ similar to carboxylic acids, we calculated the oxygen isotope fractionation between IOM and water that is a weighted average (weighted by their abundance in Murchison IOM, Derenne and Robert, 2010) of $^{18}O/^{16}O$ fractionations of individual functional groups (fractionations factors from Bhattacharjee and Eiler, 2024). Although the exact $^{18}O/^{16}O$ fractionation between IOM and water can vary slightly depending on its structure, our approximation is sufficient for a first–order exchangeability assessment. We find that IOM preferentially incorporates $^{18}O$ in its structure compared to water (Fig. 3.6a).

Next, we constrain oxygen exchange kinetics between IOM and water at circum–neutral pH, which have not been experimentally determined but can be constrained by the model discussed in section 4.2.2. Most alcohol and ether groups in IOM are connected to an aromatic ring (Derenne and Robert, 2010). We assume they exchange oxygen with water like hydroquinone, a structurally similar aromatic alcohol (Samuel and Silver, 1965). We further assume that carboxyl groups in IOM exchange oxygen with water like butyric acid, and the esters exchange like ethyl benzoate (an aromatic ester, which is structurally similar to ester groups in IOM, Samuel and Silver, 1965). Using equation 11 for four exchanging pools, we model the oxygen isotopic evolution of an IOM (initially $^{18}$O rich) in contact with relatively $^{16}$O rich water in CM chondrite parent bodies. We modelled two scenarios where IOM initially had a $\delta^{18}$O of 200‰ (similar to $^{18}$O rich cosmic symplectite in Acfer 094 ungrouped chondrite, Sakamoto et al., 2007) and 600‰ ($^{18}$O rich meteoritic organics reported in Hashizume et al., 2011). Murchison's asteroidal parent body experienced low temperature aqueous alteration (278 – 295 K) based on clumped isotope thermometry of carbonates (Clog et al., 2024), and $\delta^{18}$O of the fluid was calculated to be –5.2±1.8‰ and 2.3±1.2‰, respectively for 278 K and 295 K. For each initial $\delta^{18}O_{IOM}$, we calculated the time required for the IOM to reach complete oxygen isotopic equilibrium with fluid at the two temperatures and fluid compositions. Results clearly show that at these temperatures, most of IOM's oxygen sites would have equilibrated with parent body water within first 0.1 Ma of exposure to water (Fig. 3.6b)—a timescale much shorter than the durations of aqueous alteration of carbonaceous chondrites (0.2 – 8.0 Ma after CAIs; Suttle et al., 2021; Lee et al., 2025).

Consequently, the IOMs from CM chondrites are expected to be in oxygen isotopic equilibrium with fluids present in their asteroidal parent bodies. With progress of aqueous alteration, fluids in chondritic parent bodies become progressively $^{17,18}$O depleted due to isotopic exchange with $^{16}$O–rich primary oxides and silicates at elevated temperatures. As a result, their oxygen isotopic composition is defined by a linear trend in $\delta^{17}$O vs. $\delta^{18}$O space (Clayton and Mayeda, 1999; Clog et al., 2024). IOMs in equilibrium with end–member fluids of that linear trend ($\delta^{18}$O = –10‰ and 60‰, low and high $\delta^{18}$O waters, respectively) at temperatures of 278 – 430 K (alteration temperature range for Murchison and Cold

Bokkeveld CM chondrites; Clog et al., 2024) are expected to have compositions marked by red and blue circles in Fig. 3.6c, and occupy a region shown by the yellow field. Since exchange is a mass–dependent process, they are expected to conform to a slope ~0.53 line (TFL trend). Contrastingly, the measured $\delta^{17,18}$O of IOMs from Murchison and Cold Bokkeveld (Tartèse et al., 2018) CM chondrites are lower, barely overlap with the predicted trend and loosely conform to the CCAM line (Fig. 3.6c). This might suggest that the exchange in question might not have occurred. However, the measured $\delta^{17,18}$O have some contributions from $^{16}$O rich oxides included in the IOM (Tartèse et al., 2018), which can make them conform to CCAM trend.

Alexander et al. (2007) measured the $\delta^{18}$O of IOMs extracted from a wide collection of carbonaceous chondrites. If the IOMs indeed exchanged oxygen with aqueous alteration fluids, the $\delta^{18}$O of IOM from various carbonaceous chondrites should correlate with the $\delta^{18}$O of different aqueous alteration products (e.g., secondary carbonates, sulfates, matrix, etc.). Such correlations have not been observed in prior oxygen isotopic studies of IOM (Alexander et al., 2007; Tartèse et al., 2018; Chan et al., 2018). Here, we examine the genetic relationship between IOM and carbonates, an important aqueous alteration product. Protracted carbonate precipitation during aqueous alteration in the chondritic parent bodies results in the formation of diverse types of carbonates (calcite, dolomite, and breunnerite), which can record the nature of fluid-rock interactions, temperatures of formation and isotopic composition of carbonate precipitating fluids through their isotopic and geochemical compositions. Using carbonate clumped isotope thermometry, previous studies have constrained the temperatures of formation for carbonates from selected CM, CR and CI chondrites (Guo and Eiler, 2007; Clog et al., 2015) and the oxygen isotopic compositions of the fluids from which carbonates precipitated. Combining such temperatures and the oxygen isotopic composition of the carbonate forming fluids from those studies with the IOM–water oxygen isotope fractionation presented in this study (Fig. 3.6a), we have calculated the expected $\delta^{18}$O of IOMs in equilibrium with those carbonate forming fluids at carbonate formation temperatures. Calculated IOM $\delta^{18}$O values are plotted against $\delta^{18}$O of carbonate precipitating fluids in Fig. 3.6d as hollow symbols. These hollow symbols define a strong positive correlation between $\delta^{18}$O of fluids and calculated $\delta^{18}$O of IOMs (R=0.76, gray line

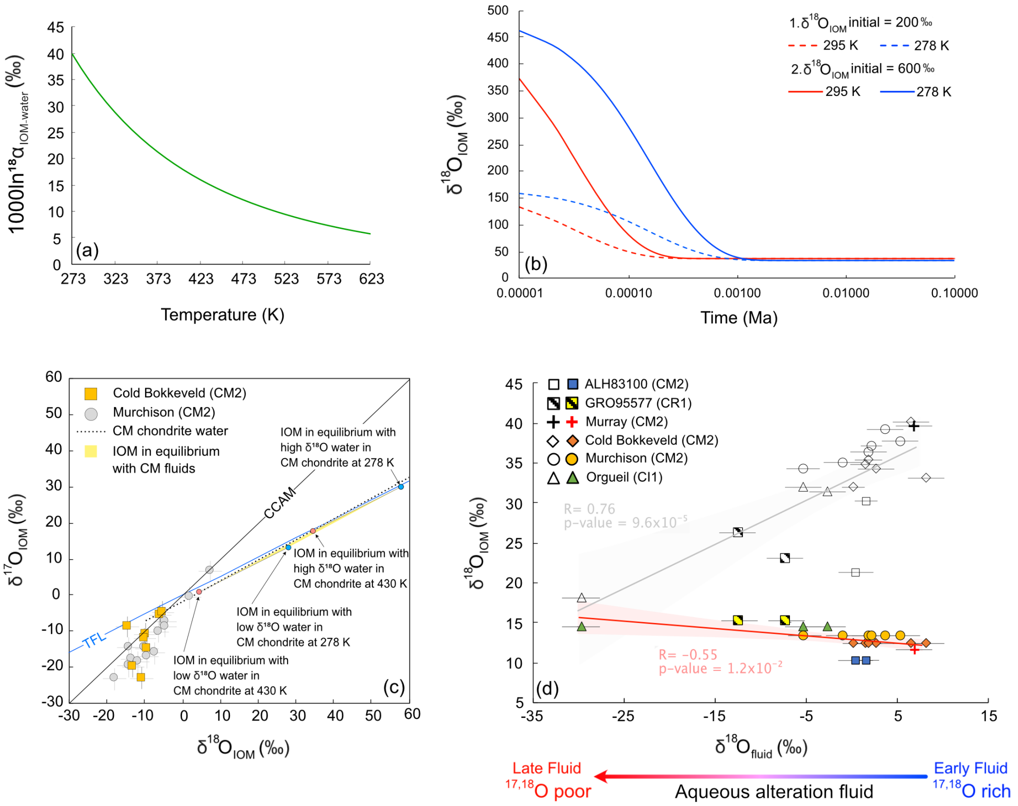

Figure 3.6: Interpretation of oxygen isotopic composition of meteoritic IOM (a) Equilibrium oxygen isotope fraction between Murchison IOM and water, calculated using compound specific fractionation factors from Bhattacharjee and Eiler (2024). (b). Model of oxygen isotopic evolution of Murchison IOM exposed to water for different durations at different temperatures. Two scenarios are modeled where IOM with initial $\delta^{18}$O values of 200‰ (Sakamoto et al., 2007) and 600‰ (Hashizume et al., 2011) are in contact with water with $\delta^{18}$O values of 2.3‰ at 295 K and –5.2‰ at 278 K (temperatures and $\delta^{18}$O of waters taken from Clog et al., 2015). Irrespective of the initial $\delta^{18}$O, IOM completely equilibrates with water within 0.1 Ma of exposure. (c) Triple oxygen isotopic composition of IOM from Cold Bokkeveld and Murchison CM chondrites (Tartèse et al., 2018), compared with that of IOM in equilibrium with low and high $\delta^{18}$O fluids in CM chondrite parent bodies at 278–430 K (Guo and Eiler, 2007; Clog et al., 2015). Measured $\delta^{17,18}$O of IOMs are lighter than equilibrium predictions, and conform to the CCAM trend rather than the terrestrial fractionation line (TFL) trend. (d) Trends in IOM $\delta^{18}$O vs fluid $\delta^{18}$O plot. Calculated $\delta^{18}$O of chondritic IOMs in equilibrium with carbonate-forming fluids at carbonate formation temperatures are shown by the hollow symbols. They display a positive correlation with $\delta^{18}$O fluid (gray line). Measured IOM $\delta^{18}$O from these chondrites are plotted as solid symbols, and show an inverse correlation with $\delta^{18}$O of carbonate precipitating fluid (red line). Shaded areas

show 95% confidence interval (data from Alexander et al., 2007; Guo and Eiler, 2007; Clog et al., 2015).

in Fig. 3.6d); as expected from mutual equilibrium. This suggests that if IOMs rapidly exchanged oxygen with aqueous alteration fluids (Fig. 3.6b) and completely equilibrated with them, then their $\delta^{18}O$ values should follow that of fluids and evolve from $^{17,18}O$ rich to $^{17,18}O$ poor compositions throughout alteration.

Alexander et al. (2007) measured the $\delta^{18}O$ of IOMs from these selected CM, CR and CI chondrites. The measured $\delta^{18}O$ of IOMs are plotted against the $\delta^{18}O$ of carbonate forming fluids as solid symbols in Fig. 3.6d. The measured $\delta^{18}O$ of IOMs do not positively correlate with $\delta^{18}O$ of carbonate forming fluids, but show a weak negative correlation ($R = -0.55$, red line in Fig. 3.6d), i.e., IOMs became slightly $^{18}O$ rich throughout aqueous alteration.. This suggests that oxygen isotopic compositions of IOMs and secondary minerals are decoupled and IOMs avoided oxygen exchange with alteration fluid, perhaps due to their hydrophobic and macromolecular nature (Danger et al., 2020, 2022), or were affected by post–alteration processes (e.g., Grewal et al., 2025a, b).

Given this observation, it is difficult to comprehend at present what the oxygen isotopic signature of IOMs represents. As calculations predict complete oxygen exchange between IOM and water while observation indicates a lack thereof, the only way to resolve this is by experimentally assessing the kinetics of oxygen exchange between bulk IOM and water at asteroidally relevant conditions, similar to those conducted before for hydrogen and nitrogen isotopes (Foustoukos and Cody, 2021). This remains a tractable target for future studies to constrain the origin and evolution of chondritic IOMs.

## 3.5 Summary and Conclusions

We have investigated the kinetics of oxygen isotopic exchange between $^{18}O$ rich water and ketones or carboxylates at 274.7 – 373 K and neutral pH using electrospray ionization Orbitrap mass spectrometry. Acetone and cyclopentanone showed complete exchange with water within 4.5 hours and 24 hours respectively at 298 K and circum–neutral pH, while acetate and butyrate achieved at most 8.2% exchange even after 10 days of incubation at 373 K. Both compounds show first order kinetics for the exchange over the range of temperature observed. The first order exchange rate constants for acetone were 2.75 (±0.21) × $10^{-5}$ $s^{-1}$ (274.7 K), 6.14 (±0.48) × $10^{-5}$ $s^{-1}$ (283 K), 1.99 (±0.16) × $10^{-4}$ $s^{-1}$ (298 K) while those for cyclopentanone were 2.19 (±0.15) × $10^{-6}$ $s^{-1}$ (274.7 K), 1.19 (±0.09) × $10^{-5}$ $s^{-1}$ (283 K), 6.55 (±0.23) × $10^{-5}$ $s^{-1}$ (298 K), 1.91 (±0.06) × $10^{-4}$ $s^{-1}$ (313 K). The first order exchange rate constants for acetate were 3.9 (±0.1) × $10^{-8}$ $s^{-1}$ (298 K), 6.1 (±0.3) × $10^{-8}$ $s^{-1}$ (323 K), 1.22 (±0.04) × $10^{-7}$ $s^{-1}$ (373 K) while those for butyrate were 3.9 (±0.1) × $10^{-8}$ $s^{-1}$ (298 K), 5.0 (±0.8) × $10^{-8}$ $s^{-1}$ (323 K), 1.0 (±0.04) × $10^{-7}$ $s^{-1}$ (373 K). These rate constants are consistent with previous reports of Greenzaid et al. (1968a, b) and Llewellyn and O'Connor (1964). The activation energies for such exchange for acetone and cyclopentanone are 14.47 (±0.43) kcal/mol and 20.35 (±1.47) kcal/mol, respectively. The exchange mechanism is driven by rapid hydration of ketone molecules in water. Activation energies of exchanges for acetate and butyrate are 3.53±0.26 kcal/mol and 2.81±0.43 kcal/mol, respectively, and the exchange mechanism is influenced by electrostatic repulsion between carboxylate and hydroxyl groups in slightly alkaline media. Extension of our observations to meteoritic organics suggest that aldehyde and ketone compounds reported from various carbonaceous chondrites should completely re–equilibrate with water during meteorite parent body aqueous alteration processes, making them tracers for the fluid composition in such environments (but also highly vulnerable to terrestrial, including laboratory, exchange) whereas carboxylic acids have a higher probability of preserving their oxygen isotopic composition associated with initial synthesis. Based on a newly constructed model, we predict that meteoritic insoluble organic matter should be susceptible to oxygen exchange with water during aqueous alteration and thermal metamorphic processes. If so, their oxygen isotopic composition should positively correlate with that of altering fluids in chondritic parent bodies. However, prior data indicates that such a correlation is absent, suggesting meteoritic IOM may be partially or completely protected from this exchange due to its macromolecular structure. Further experimental study is required to understand the oxygen isotopic composition of chondritic IOM.

## Acknowledgement

SB acknowledges Elliott Mueller and Gabriella Weiss for their help with Orbitrap measurements and Nami Kitchen, Makayla Betts, and Nathan Dalleska for their help with measurement of $^{18}O/^{16}O$ of water at Resnick Water and Environmental Lab, Caltech. This study was supported by a grant from Caltech Center for Comparative Planetary Evolution (grant no. 13520281) awarded to JME.

## Data availability

Data are available through CaltechDATA at https://doi.org/10.22002/efzgv–r2z41

## 3.6 Supplementary Material

### 3.6.1. Exchange at source the

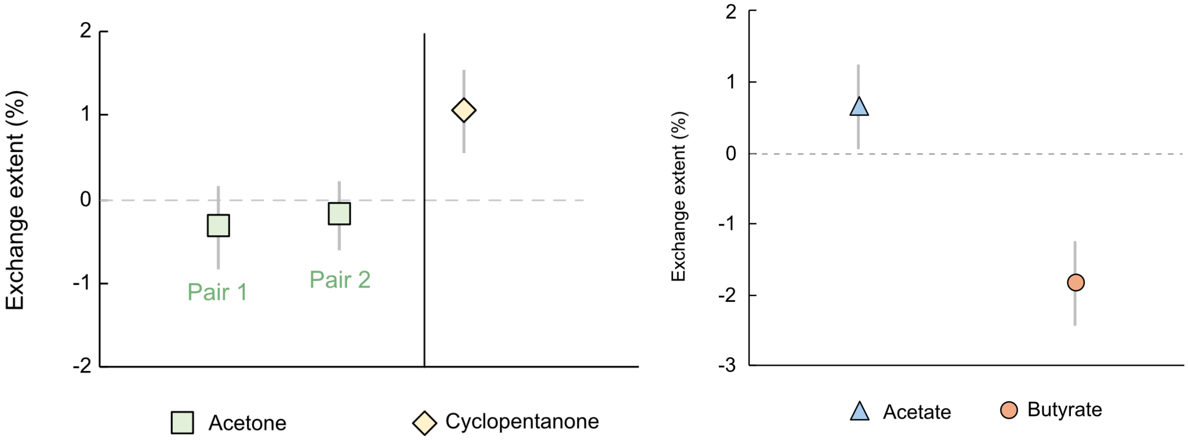

Figure S3.1: Extent of oxygen isotope exchange at the ionization source of Q-Exactive HF Orbitrap.

### 3.6.2. Exchange during measurement

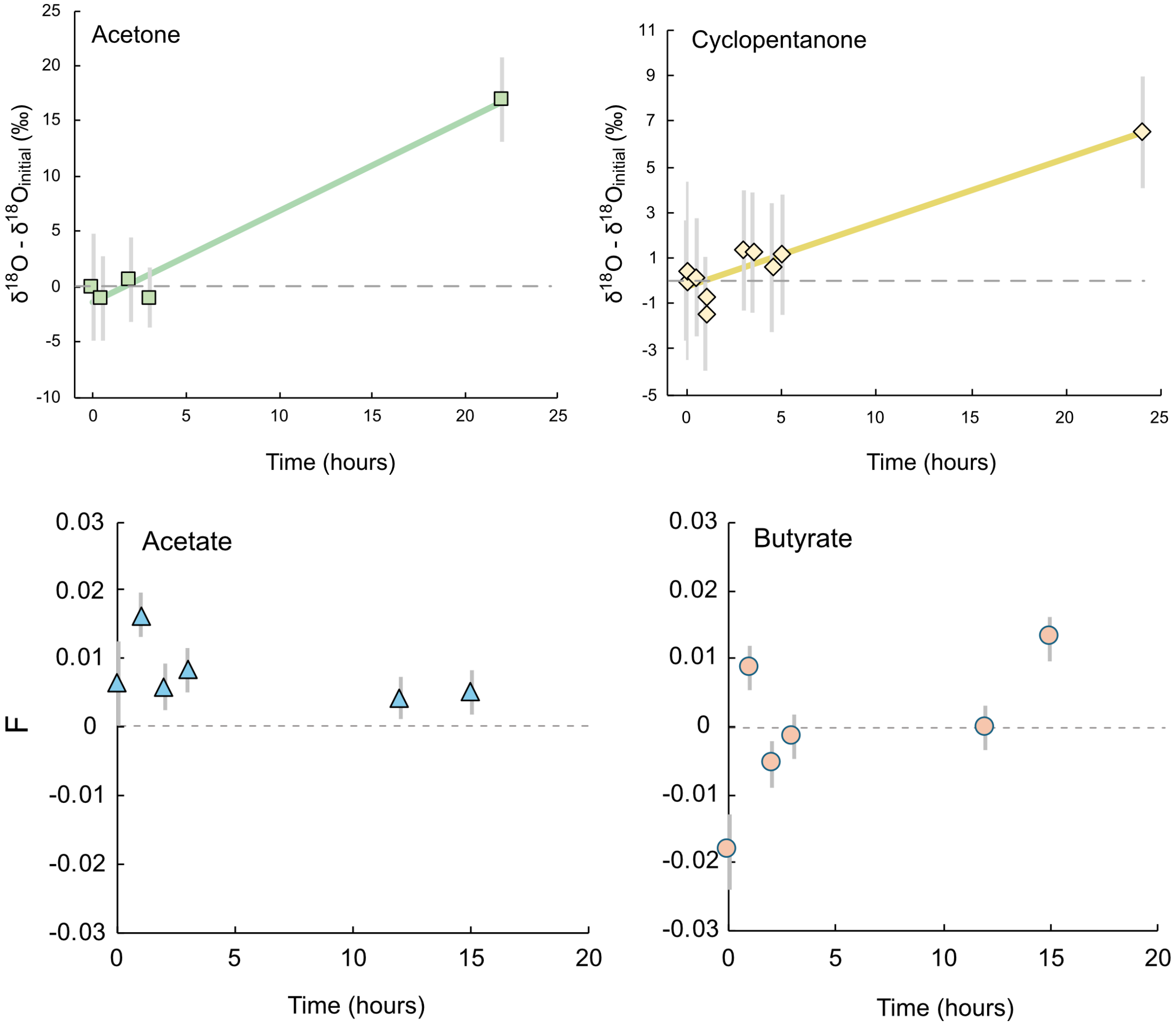

Figure S3.2: Oxygen isotope exchange over duration of $^{18}O/^{16}O$ measurement (30 minute) using Orbitrap IRMS for acetone (left panel) and cyclopentanone (right panel). For this experiment, standard acetone (1250 μM) or cyclopentanone (500 μM) in 9:1 (v/v) methanol + HW solvent incubated at room temperature for different time duration. Vertical axis shows increase $\delta^{18}O$ of acetone from starting solution and horizontal axis indicates duration of incubation for ketones and extent of exchange (F) for carboxylates (12 minutes). Horizontal dashed line indicates starting solution.

### 3.6.3. Correction schemes (variation with TIC intensity)

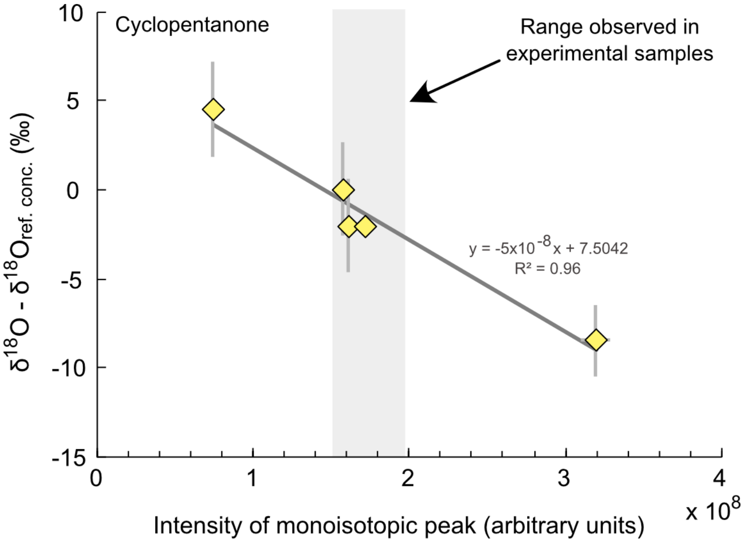

Figure S3.3: Effect of concentration on measured $\delta^{18}O$ of cyclopentanone. For this calibration, 200 µM, 500 µM and 1000 µM cyclopentanone solution (in 9:1 methanol + DIW) is made measured subsequently. The vertical axis represents deviation of $\delta^{18}O$ of cyclopentanone from that at a reference monoisotopic peak intensity (1.57x10$^8$ arbitrary units) and horizontal axis denotes intensity of monoisotopic peak (arbitrary units). Solid line represents best fit to the data. This relationship is used to make small (<3 ‰) correction to the dataset for varying intensity of monoisotopic peak during analytical session. Shaded region represents range of monoisotopic peak intensities of experimental samples.

### 3.6.4. Effect of flow rate on analytical precision and TIC stability

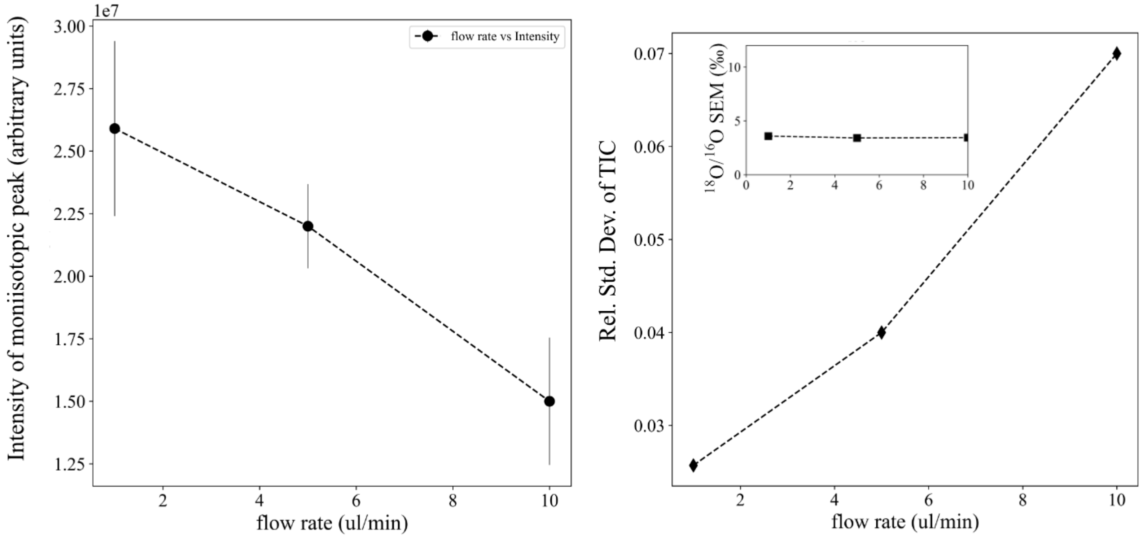

Figure S3.4: Effect of flow rate on intensity of monoisotopic peak (left panel) and TIC stability (right panel) for standard acetone (500 µM) in 9:1 methanol + DIW solution. TIC is more stable at lower flow rates. Right inset: variation of standard error of $^{18}O/^{16}O$ measurement with flow rate. Analytical precision is insensitive to flow rate. For data presented in this diagram, integration time was 15 minutes, no. of µscans was set at 10, AGC target was $2 \times 10^5$ and nominal mass resolution was set at 120,000.

### 3.6.5. Picarro calibration and water isotopic composition

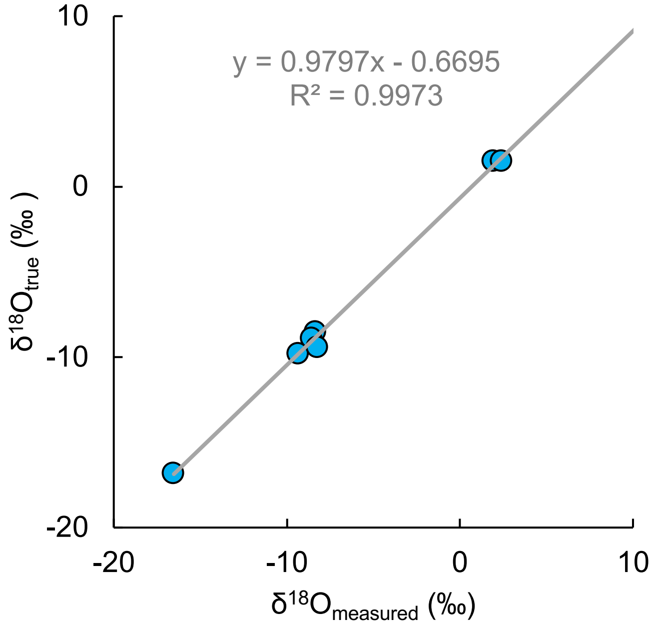

Figure S3.5: Calibration curve of Picarro L2140i for measuring $\delta^{18}$O of HWs using in-house standards.

Table S3.1 Isotopic composition of waters used in this study

| Sample Name | $\delta^{18}O_{VSMOW}$ (‰) | 1σ (‰) |
|---|---|---|
| DIW_1 | –11.18 | 0.1 |
| DS2_acetone | –8.13 | 0.2 |
| DS2_cyclopentanone | –8.47 | 0.1 |
| DIW_2 | –11.31 | 0.4 |
| | | |
| *Calculated* | | |
| DS1_cyclopentanone | 15.94 | 0.2 |
| DS1_acetone | 19.27 | 0.2 |
| | | |
| HW_cyclopentanone | 531.68 | 0.2 |
| HW_acetone | 601.06 | 0.2 |

Table 3.1: Instrument parameters for $^{18}O/^{16}O$ measurements using Orbitrap–IRMS.

| **Instrument parameters** | **Acetone** | **Cyclopentanone** | **Acetate** | **Butyrate** |
|---|---|---|---|---|
| Flow Rate (µL/min) | 1 | 1 | 20 | 20 |
| Polarity (+/-) | Positive | Positive | Negative | Negative |
| Spray Voltage (kV) | 4.5 | 4.1 | 3.7 | 3.7 |
| Sheath gas flow rate (arbitrary units) | 11 | 5 | 3 | 5 |
| Auxiliary gas flow rate (arbitrary units) | 0 | 1 | 2 | 0 |
| Sweep gas flow rate (arbitrary units) | 2 | 1 | 0 | 0 |
| Capillary temperature (°C) | 320 | 320 | 320 | 320 |
| S-lens RF level (arbitrary units) | 80 | 50 | 60 | 60 |
| Aux gas heater temperature (°C) | 80 | 100 | 80 | 80 |
| Analyzer temperature (°C) | 27.47 | 27.57 | 27.73 | 27.73 |
| Scan Range (*m/z*) | 57.0–63.0 | 84.0–88.0 | 58.0–62.0 | 86.0–90.0 |
| Molecular ion peak (*m/z*) | 59.04957 | 85.06497 | 59.01271 | 87.04404 |
| $^{18}O$ substituted M+2 peak (*m/z*) | 61.05379 | 87.06920 | 61.01696 | 89.04827 |
| Microscans | 2 | 2 | 1 | 1 |
| Automatic Gain Control (AGC) | 1 x $10^5$ | 1 x $10^5$ | 1 x 106 | 1 x $10^6$ |
| Nominal Mass Resolution (FWHM at m/z = 200) | 45,000 | 45,000 | 60,000 | 60,000 |
| Maximum Injection Time (ms) | 1000 | 1000 | 1000 | 1000 |
| TIC relative standard deviation (RSD) (%) | <0.1 | <0.1 | <0.1 | <0.1 |

Table 3.2: Oxygen isotope exchange data for acetone.

| **Session** | **Temp (K)** | **Time (hrs)** | **Blank contribution** | **Blank corrected $^{18}O/^{16}O$** | **1SE (‰)** | **$\delta^{18}O$ - $\delta^{18}O_{t0}$** | ***F*** | **1SE** | ***k* ($s^{-1}$)** | **1SE** |
|---|---|---|---|---|---|---|---|---|---|---|
| 1 | 274.7 | 0.001 | 0.05 | 0.00232471 | 1.78 | 0.00 | 0.00 | 0 | 0.00002747 | 0.00000214 |
| 1 | 274.7 | 1 | 0.05 | 0.00242668 | 1.72 | 50.86 | 0.08 | 0.004 | | |
| 1 | 274.7 | 2 | 0.06 | 0.00265153 | 1.61 | 163.00 | 0.26 | 0.004 | | |
| 1 | 274.7 | 5 | 0.06 | 0.00284531 | 1.63 | 259.65 | 0.42 | 0.004 | | |
| 1 | 274.7 | 12 | 0.06 | 0.00317047 | 1.50 | 421.82 | 0.68 | 0.004 | | |
| 1 | 274.7 | 48 | 0.07 | 0.00352727 | 1.43 | 599.78 | 0.97 | 0.004 | | |
| 1 | 298 | 0 | 0.05 | 0.00232117 | 1.78 | 0.00 | 0.00 | 0.000 | | |
| 1 | 298 | 0.25 | 0.05 | 0.00258875 | 1.65 | 133.46 | 0.22 | 0.004 | 0.00019981 | 0.00001558 |
| 1 | 298 | 0.5 | 0.06 | 0.00268034 | 1.65 | 179.14 | 0.29 | 0.004 | | |
| 1 | 298 | 1 | 0.05 | 0.00272657 | 1.64 | 202.19 | 0.33 | 0.004 | | |
| 1 | 298 | 3 | 0.05 | 0.00342181 | 1.42 | 548.95 | 0.90 | 0.004 | | |
| 1 | 298 | 4.5 | 0.06 | 0.00355031 | 1.44 | 613.04 | 1.00 | 0.004 | | |
| 1 | 298 | 12 | 0.06 | 0.00355035 | 1.42 | 613.06 | 1.00 | 0.004 | | |
| 1 | 298 | 12 | 0.05 | 0.00354570 | 1.41 | 610.74 | 1.00 | 0.004 | | |
| 1 | 298 | 15 | 0.06 | 0.00355555 | 1.42 | 615.65 | 1.00 | 0.004 | | |
| 1 | 298 | 15 | 0.06 | 0.00355006 | 1.45 | 612.91 | 1.00 | 0.004 | | |
| 1 | 298 | 24 | 0.06 | 0.00355059 | 1.45 | 613.18 | 1.00 | 0.004 | | |
| 1 | 298 | 48 | 0.06 | 0.00354731 | 1.45 | 611.54 | 1.00 | 0.004 | | |
| 2 | 283 | 0 | 0.09 | 0.00250070 | 1.72 | 0.00 | 0.00 | 0.000 | | |
| 2 | 283 | 0.5 | 0.09 | 0.00260400 | 1.71 | 51.52 | 0.10 | 0.005 | 0.00006144 | 0.00000479 |
| 2 | 283 | 1.25 | 0.10 | 0.00273185 | 1.71 | 115.29 | 0.21 | 0.005 | | |
| 2 | 283 | 1.5 | 0.12 | 0.00294643 | 1.59 | 222.31 | 0.41 | 0.005 | | |
| 2 | 283 | 5 | 0.17 | 0.00322743 | 1.56 | 362.46 | 0.67 | 0.005 | | |
| 2 | 283 | 5 | 0.12 | 0.00325976 | 1.80 | 378.58 | 0.70 | 0.005 | | |
| 2 | 283 | 3.5 | 0.16 | 0.00313111 | 1.62 | 314.42 | 0.58 | 0.005 | | |
| 2 | 283 | 10 | 0.13 | 0.00345255 | 1.49 | 474.74 | 0.88 | 0.005 | | |
| 2 | 283 | 32 | 0.06 | 0.00359194 | 1.46 | 544.26 | 1.01 | 0.005 | | |
| 2 | 283 | 32 | 0.06 | 0.00357953 | 1.42 | 538.07 | 1.00 | 0.005 | | |
| 2 | 283 | 48 | 0.07 | 0.00358339 | 1.24 | 540.00 | 1.00 | 0.005 | | |
| 1 | Blank (n=4) | | | 0.0022887 | 5.69 | | | | | |
| 2 | Blank (n=1) | | | 0.00239291 | 2.18 | | | | | |

Table 3.3: Oxygen isotope exchange data for cyclopentanone.

| **Session** | **Temp (K)** | **Time (hrs)** | **Corrected $^{18}O/^{16}O$** | **1SE (‰)** | **$\delta^{18}O$ - $\delta^{18}O_{t0}$** | **1SE (‰)** | ***F*** | **1SE** | ***k* ($s^{-1}$)** | **1SE** |
|---|---|---|---|---|---|---|---|---|---|---|
| 3 | 283 | 0 | 0.00224553 | 1.844 | 0.00 | 2.61 | 0.00 | 0.004 | 0.00001192 | 0.00000094 |
| 3 | 283 | 12 | 0.00270175 | 1.659 | 227.54 | 2.48 | 0.38 | 0.004 | | |
| 3 | 283 | 24 | 0.00301979 | 1.586 | 386.16 | 2.43 | 0.65 | 0.005 | | |
| 3 | 283 | 56 | 0.00332305 | 1.526 | 537.41 | 2.39 | 0.91 | 0.005 | | |
| 3 | 283 | 75 | 0.00341097 | 1.453 | 581.26 | 2.35 | 0.98 | 0.005 | | |
| 3 | 283 | 75 | 0.00340259 | 1.487 | 577.08 | 2.37 | 0.98 | 0.005 | | |
| 3 | 283 | 96 | 0.00342638 | 1.549 | 588.95 | 2.41 | 1.00 | 0.005 | | |
| 3 | 283 | 120 | 0.00342600 | 1.558 | 588.76 | 2.41 | 1.00 | 0.005 | | |
| 3 | 298 | 0 | 0.00224553 | 1.844 | 0.00 | 2.61 | 0.00 | 0.004 | 0.00006553 | 0.00000235 |
| 3 | 298 | 0.5 | 0.00242656 | 1.765 | 90.28 | 2.55 | 0.15 | 0.004 | | |
| 3 | 298 | 1.5 | 0.00265101 | 1.701 | 202.23 | 2.51 | 0.34 | 0.004 | | |
| 3 | 298 | 2.25 | 0.00276558 | 1.651 | 259.37 | 2.48 | 0.44 | 0.004 | | |
| 3 | 298 | 3 | 0.00294612 | 1.581 | 349.42 | 2.43 | 0.59 | 0.004 | | |
| 3 | 298 | 4 | 0.00302698 | 1.564 | 389.75 | 2.42 | 0.66 | 0.004 | | |
| 3 | 298 | 7.5 | 0.00328302 | 1.508 | 517.45 | 2.38 | 0.88 | 0.004 | | |
| 3 | 298 | 10.6 | 0.00332939 | 1.495 | 540.57 | 2.37 | 0.92 | 0.004 | | |
| 3 | 298 | 11.5 | 0.00334308 | 1.497 | 547.40 | 2.38 | 0.93 | 0.004 | | |
| 3 | 298 | 24 | 0.00341627 | 1.483 | 583.91 | 2.37 | 1.00 | 0.004 | | |
| 3 | 298 | 47.66 | 0.00341579 | 1.469 | 583.67 | 2.36 | 1.00 | 0.004 | | |
| 3 | 298 | 71 | 0.00342530 | 1.49 | 588.41 | 2.37 | 1.00 | 0.004 | | |
| 3 | 298 | 71 | 0.00341875 | 1.464 | 585.14 | 2.35 | 1.00 | 0.004 | | |
| 3 | 298 | 96 | 0.00342109 | 1.46 | 586.31 | 2.35 | 1.00 | 0.004 | | |
| 3 | 298 | 120 | 0.00341983 | 1.441 | 585.68 | 2.34 | 1.00 | 0.004 | | |
| 3 | 313 | 0 | 0.00224553 | 1.844 | 0.00 | 2.61 | 0.00 | 0.004 | 0.00019136 | 0.00000675 |
| 3 | 313 | 0.5 | 0.00267094 | 1.681 | 212.17 | 2.50 | 0.36 | 0.004 | | |
| 3 | 313 | 1 | 0.00274259 | 1.643 | 247.91 | 2.47 | 0.42 | 0.004 | | |
| 3 | 313 | 2 | 0.00317782 | 1.515 | 464.98 | 2.39 | 0.80 | 0.004 | | |
| 3 | 313 | 4.5 | 0.00337422 | 1.488 | 562.93 | 2.37 | 0.96 | 0.004 | | |
| 3 | 313 | 9 | 0.00341156 | 1.488 | 581.56 | 2.37 | 1.00 | 0.004 | | |
| 3 | 313 | 24 | 0.00343000 | 1.591 | 590.75 | 2.44 | 1.00 | 0.004 | | |
| 3 | 313 | 50 | 0.00340259 | 1.487 | 577.08 | 2.37 | 1.00 | 0.004 | | |
| 3 | 313 | 72 | 0.00341461 | 1.473 | 583.08 | 2.36 | 1.00 | 0.004 | | |
| 3 | 313 | 96 | 0.00341516 | 1.4 | 583.35 | 2.32 | 1.00 | 0.004 | | |
| 3 | 313 | 120 | 0.00342445 | 1.488 | 587.99 | 2.37 | 1.00 | 0.004 | | |
| 3 | 274.7 | 0 | 0.00224553 | 1.844 | 0.00 | 2.61 | 0.00 | 0.004 | 0.00000219 | 0.00000016 |
| 3 | 274.7 | 12 | 0.00240642 | 1.798 | 80.24 | 2.58 | 0.14 | 0.004 | | |
| 3 | 274.7 | 12 | 0.00240744 | 1.754 | 80.75 | 2.54 | 0.14 | 0.004 | | |
| 3 | 274.7 | 25 | 0.00247802 | 1.752 | 115.95 | 2.54 | 0.20 | 0.004 | | |
| 3 | 274.7 | 48 | 0.00264361 | 1.696 | 198.54 | 2.51 | 0.33 | 0.004 | | |
| 3 | 274.7 | 96 | 0.00285410 | 1.682 | 303.52 | 2.50 | 0.51 | 0.004 | | |
| 3 | 274.7 | 120 | 0.00297226 | 1.652 | 362.45 | 2.48 | 0.61 | 0.005 | | |

Table 3.4: Oxygen isotope exchange data for carboxylates.

| **Compound** | **Temp (K)** | **Time (hrs)** | **$\delta^{18}O_{HW}$ - $\delta^{18}O_{DIW}$ (‰)** | **1SE (‰)** | ***F*** | **1SE** | ***k* ($s^{-1}$)** | **1SE** |
|---|---|---|---|---|---|---|---|---|
| Acetate | 298 | 0 | 0.0 | 1.7 | 0.000 | 0.000 | 0.000000039 | 0.000000001 |
| | 298 | 5 | -0.5 | 2.7 | -0.001 | -0.004 | | |
| | 298 | 24 | 2.2 | 2.9 | 0.004 | 0.005 | | |
| | 298 | 72 | 6.6 | 3.0 | 0.011 | 0.005 | | |
| | 298 | 3 | -1.0 | 3.0 | -0.002 | 0.005 | | |
| | 298 | 240 | 20.6 | 3.3 | 0.034 | 0.005 | | |
| | 323 | 0 | 0.0 | 2.0 | 0.000 | 0.000 | 0.000000061 | 0.000000003 |
| | 323 | 18 | 4.2 | 2.8 | 0.007 | -0.005 | | |
| | 323 | 42 | 6.4 | 3.1 | 0.010 | 0.005 | | |
| | 323 | 72 | 12.0 | 1.6 | 0.020 | 0.003 | | |
| | 323 | 200 | 25.6 | 2.5 | 0.042 | 0.004 | | |
| | 373 | 0 | 0.0 | 3.8 | 0.000 | 0.000 | 0.000000122 | 0.000000004 |
| | 373 | 16 | 2.5 | 2.9 | 0.004 | 0.005 | | |
| | 373 | 48 | 14.7 | 3.1 | 0.024 | 0.005 | | |
| | 373 | 72 | 21.5 | 3.0 | 0.035 | 0.005 | | |
| | 373 | 108 | 30.1 | 3.0 | 0.049 | 0.005 | | |
| | 373 | 200 | 50.1 | 2.7 | 0.082 | 0.004 | | |
| Butyrate | 298 | 0 | 0.0 | 1.7 | 0.000 | 0.000 | 0.000000039 | 0.000000002 |
| | 298 | 5 | 3.4 | 2.0 | 0.000 | 0.003 | | |
| | 298 | 24 | 1.4 | 2.3 | 0.002 | 0.004 | | |
| | 298 | 48 | 5.0 | 2.2 | 0.008 | 0.004 | | |
| | 298 | 74 | 5.7 | 2.2 | 0.009 | 0.004 | | |
| | 298 | 3 | 1.9 | 2.2 | 0.003 | 0.000 | | |
| | 298 | 240 | 21.4 | 2.0 | 0.035 | 0.003 | | |
| | 323 | 0 | 0.0 | 2.0 | 0.000 | 0.000 | 0.000000050 | 0.000000008 |
| | 323 | 18 | 0.4 | 2.2 | 0.001 | 0.004 | | |
| | 323 | 38 | 3.2 | 2.6 | 0.005 | 0.004 | | |
| | 323 | 72 | 8.1 | 2.0 | 0.013 | 0.003 | | |
| | 373 | 0 | 0.0 | 2.0 | 0.000 | 0.000 | 0.000000100 | 0.000000004 |
| | 373 | 20 | 5.2 | 2.5 | 0.008 | 0.004 | | |
| | 373 | 43 | 8.0 | 2.3 | 0.013 | 0.004 | | |
| | 373 | 70 | 16.5 | 2.5 | 0.027 | 0.004 | | |
| | 373 | 110 | 26.3 | 2.0 | 0.043 | 0.003 | | |
| | 373 | 200 | 41.9 | 2.0 | 0.068 | 0.003 | | |

Table 3.5: Calculated equilibrium oxygen isotope fractionation between water and acetone or cyclopentanone from this study.

| Compound | Temp (K) | 1000ln$^{18}\alpha$ (‰) | 1SE (‰) |
|---|---|---|---|
| Acetone | 283 | 26.8 | 1.7 |
| | 298 | 27.7 | 1.7 |
| | | | |
| Cyclopentanone | 283 | 28.4 | 1.7 |
| | 298 | 23.6 | 1.7 |
| | 311 | 24.0 | 1.7 |

Table 3.6: Candidates for fast and slow exchanging component and their exchange rate constants.

| $f_{\text{nex}}$ | $k_{nex}$ (s$^{-1}$) | **Reference** | $f_{\text{ex}}$ | $k_{ex}$ (s$^{-1}$) | **Reference** |
|---|---|---|---|---|---|
| Hydroquinone | 2.41x10$^{-7}$ | Samuel and Silver (1965) | Benzoic Acid | 2.3341x10$^{-5}$ | Wedeking and Hayes (1983) |
| Resorcinol | 5.73 x10$^{-7}$ | Samuel and Silver (1965) | Cyclopentanone | 9.5141x10$^{-3}$ | This Study |
| Mesiotic Acid | 1.02 x10$^{-8}$ | Samuel and Silver (1965) | Glycine | 9.5241x10$^{-6}$ | Murphy and Clay (1979) |
| | | | Aspartic Acid | 4.1641x10$^{-5}$ | Murphy and Clay (1979) |
| | | | D-Mannose | 2.1141x10$^{-4}$ | Mega et al. (1990) |

# BIBLIOGRAPHY

Abplanalp M. J. and Kaiser R. I. (2019) On the formation of complex organic molecules in the interstellar medium: untangling the chemical complexity of carbon monoxide–hydrocarbon containing ice analogues exposed to ionizing radiation via a combined infrared and reflectron time-of-flight analysis. *Phys. Chem. Chem. Phys.* **21**, 16949–16980.

Alexander C. M. O., Bowden R., Fogel M. L. and Howard K. T. (2015) Carbonate abundances and isotopic compositions in chondrites. *Meteorit & Planetary Scien* **50**, 810–833.

Alexander C. O., Fogel M., Yabuta H. and Cody Gd. (2007) The origin and evolution of chondrites recorded in the elemental and isotopic compositions of their macromolecular organic matter. *Geochimica et Cosmochimica Acta* **71**, 4380–4403.

Aponte J. C., Alexandre M. R., Wang Y., Brearley A. J., Alexander C. M. and Huang Y. (2011) Effects of secondary alteration on the composition of free and IOM-derived monocarboxylic acids in carbonaceous chondrites. *Geochimica et Cosmochimica Acta* **75**, 2309–2323.

Aponte J. C., Whitaker D., Powner M. W., Elsila J. E. and Dworkin J. P. (2019) Analyses of aliphatic aldehydes and ketones in carbonaceous chondrites. *ACS Earth and Space Chemistry* **3**, 463–472.

Ardawi M. S. M. and Newsholme E. A. (1982) Maximum activities of some enzymes of glycolysis, the tricarboxylic acid cycle and ketone-body and glutamine utilization pathways in lymphocytes of the rat. *Biochemical Journal* **208**, 743–748.

Bell R. P. (1966) The reversible hydration of carbonyl compounds. In *Advances in physical organic chemistry* Elsevier. pp. 1–29.

Bender M. L., Stone R. R. and Dewey R. S. (1956) Kinetics of Isotopic Oxygen Exchange between Substituted Benzoic Acids and Water [1]. *J. Am. Chem. Soc.* **78**, 319–321.

Bennett C. J., Hama T., Kim Y. S., KAWASAkI M. and Kaiser R. I. (2010) Laboratory studies on the formation of formic acid (HCOOH) in interstellar and cometary ices. *The Astrophysical Journal* **727**, 27.

Bhattacharjee S. and Eiler J. M. (2024) Oxygen isotope equilibria of O-bearing organic compounds based on first principle quantum mechanical models, and implications for their use in the study of extraterrestrial organics. *Geochimica et Cosmochimica Acta* **380**, 96–111.

Blair S. K., Magnani L., Brand J. and Wouterloot J. G. A. (2008) Formaldehyde in the Far Outer Galaxy: Constraining the Outer Boundary of the Galactic Habitable Zone. *Astrobiology* **8**, 59–73.

Castañeda I. S., Schefuß E., Pätzold J., Sinninghe Damsté J. S., Weldeab S. and Schouten S. (2010) Millennial-scale sea surface temperature changes in the eastern Mediterranean (Nile River Delta region) over the last 27,000 years: EASTERN MEDITERRANEAN SST RECORDS. *Paleoceanography* **25**.

Castañeda I. S., Schouten S., Pätzold J., Lucassen F., Kasemann S., Kuhlmann H. and Schefuß E. (2016) Hydroclimate variability in the Nile River Basin during the past 28,000 years. *Earth and Planetary Science Letters* **438**, 47–56.

Cesar J., Eiler J., Dallas B., Chimiak L. and Grice K. (2019) Isotope heterogeneity in ethyltoluenes from Australian condensates, and their stable carbon site-specific isotope analysis. *Organic Geochemistry* **135**, 32–37.

Chan Q. H. S., Zolensky M. E., Kebukawa Y., Fries M., Ito M., Steele A., Rahman Z., Nakato A., Kilcoyne A. L. D., Suga H., Takahashi Y., Takeichi Y. and Mase K. (2018) Organic matter in extraterrestrial water-bearing salt crystals. *Sci. Adv.* **4**, eaao3521.

Chiang Y., Hojatti M., Keeffe J. R., Kresge A. J., Schepp N. P. and Wirz J. (1987) Vinyl alcohol. Generation and decay kinetics in aqueous solution and determination of the tautomerization equilibrium constant and acid dissociation constants of the aldehyde and enol forms. *J. Am. Chem. Soc.* **109**, 4000–4009.

Chiang Y., Kresge A. J. and Schepp N. P. (1989) Temperature coefficients of the rates of acid-catalyzed enolization of acetone and ketonization of its enol in aqueous and acetonitrile solutions. Comparison of thermodynamic parameters for the keto-enol equilibrium in solution with those in the gas phase. *J. Am. Chem. Soc.* **111**, 3977–3980.

Chimiak L. and Eiler J. (2024) Prebiotic synthesis on meteorite parent bodies: Insights from hydrogen and carbon isotope models. *Chemical Geology* **644**, 121828.

Chimiak L., Elsila J. E., Dallas B., Dworkin J. P., Aponte J. C., Sessions A. L. and Eiler J. M. (2021) Carbon isotope evidence for the substrates and mechanisms of prebiotic synthesis in the early solar system. *Geochimica et Cosmochimica Acta* **292**, 188–202.

Clayton R. N. and Mayeda T. K. (1999) Oxygen isotope studies of carbonaceous chondrites. *Geochimica et Cosmochimica Acta* **63**, 2089–2104.

Clog M., Lindgren P., Modestou S., McDonald A., Tait A., Donnelly T., Mark D. and Lee M. (2024) Clumped isotope and Δ17O measurements of carbonates in CM carbonaceous chondrites: New insights into parent body thermal and fluid evolution. *Geochimica et Cosmochimica Acta* **369**, 1–16.

Clog M., Stolper D. and Eiler J. M. (2015) Kinetics of CO2(g)–H2O(1) isotopic exchange, including mass 47 isotopologues. *Chemical Geology* **395**, 1–10.

Cody G. D., Heying E., Alexander C. M. O., Nittler L. R., Kilcoyne A. L. D., Sandford S. A. and Stroud R. M. (2011) Establishing a molecular relationship between chondritic and cometary organic solids. *Proceedings of the National Academy of Sciences* **108**, 19171–19176.

Cohn M. and Urey H. C. (1938) Oxygen Exchange Reactions of Organic Compounds and Water. *J. Am. Chem. Soc.* **60**, 679–687.

Csernica T., Bhattacharjee S. and Eiler J. (2023) Accuracy and precision of ESI-Orbitrap-IRMS observations of hours to tens of hours via reservoir injection. *International Journal of Mass Spectrometry* **490**, 117084.

Danger G., Ruf A., Javelle T., Maillard J., Vinogradoff V., Afonso C., Schmitz-Afonso I., Remusat L., Gabelica Z. and Schmitt-Kopplin P. (2022) The transition from soluble to insoluble organic matter in interstellar ice analogs and meteorites. *Astronomy & Astrophysics* **667**, A120.

Danger G., Ruf A., Maillard J., Hertzog J., Vinogradoff V., Schmitt-Kopplin P., Afonso C., Carrasco N., Schmitz-Afonso I. and d'Hendecourt L. L. S. (2020) Unprecedented molecular diversity revealed in meteoritic insoluble organic matter: the Paris Meteorite's case. *The Planetary Science Journal* **1**, 55.

DeNiro M. J. and Epstein S. (1981) Isotopic composition of cellulose from aquatic organisms. *Geochimica et Cosmochimica Acta* **45**, 1885–1894.

Derenne S. and Robert F. (2010) Model of molecular structure of the insoluble organic matter isolated from Murchison meteorite. *Meteorit & Planetary Scien* **45**, 1461–1475.

Duvernay F., Danger G., Theulé P., Chiavassa T. and Rimola A. (2014) FORMALDEHYDE CHEMISTRY IN COMETARY ICES: ON THE PROSPECTIVE DETECTION OF NH2CH2OH, HOCH2OH, AND POM BY THE ON-BOARD ROSINA INSTRUMENT OF THE ROSETTA MISSION. *ApJ* **791**, 75.

Eiler J., Cesar J., Chimiak L., Dallas B., Grice K., Griep-Raming J., Juchelka D., Kitchen N., Lloyd M. and Makarov A. (2017) Analysis of molecular isotopic structures at high precision and accuracy by Orbitrap mass spectrometry. *International Journal of Mass Spectrometry* **422**, 126–142.

Ellis N. M. and Passey B. H. (2023) A novel method for high-precision triple oxygen isotope analysis of diverse Earth materials using high temperature conversion–methanation–fluorination and isotope ratio mass spectrometry. *Chemical Geology* **635**, 121616.

Favre C., Fedele D., Semenov D., Parfenov S., Codella C., Ceccarelli C., Bergin E. A., Chapillon E., Testi L. and Hersant F. (2018) First detection of the simplest organic acid in a protoplanetary disk. *The Astrophysical Journal Letters* **862**, L2.

Foustoukos D. I. and Cody G. D. (2021) H and N systematics in thermally altered chondritic insoluble organic matter: An experimental study. *Geochimica et Cosmochimica Acta* **300**, 44–64.

Fujiya W., Hoppe P., Ushikubo T., Fukuda K., Lindgren P., Lee M. R., Koike M., Shirai K. and Sano Y. (2019) Migration of D-type asteroids from the outer Solar System inferred from carbonate in meteorites. *Nature Astronomy* **3**, 910–915.

Fujiya W., Sugiura N., Hotta H., Ichimura K. and Sano Y. (2012) Evidence for the late formation of hydrous asteroids from young meteoritic carbonates. *Nature communications* **3**, 627.

Fukao T., Lopaschuk G. D. and Mitchell G. A. (2004) Pathways and control of ketone body metabolism: on the fringe of lipid biochemistry. *Prostaglandins, leukotrienes and essential fatty acids* **70**, 243–251.

Greenzaid P., Luz Z. and Samuel D. (1968a) Nmr study of reversible hydration of aliphatic aldehydes and ketones. Part 3.—Isotopic oxygen exchange of acetone. *Transactions of the Faraday Society* **64**, 2780–2786.

Greenzaid P., Luz Z. and Samuel D. (1968b) Nmr study of reversible hydration of aliphatic aldehydes and ketones. Part 4.—Isotopic oxygen exchange of cycloalkanones. *Transactions of the Faraday Society* **64**, 2787–2793.

Grewal D. S., Bhattacharjee S., Mardaru G.-D. and Asimow P. D. (2025a) Tracing the origin of volatiles on Earth using nitrogen isotope ratios in iron meteorites. *Geochimica et Cosmochimica Acta* **388**, 34–47.

Grewal D. S., Bhattacharjee S., Zhang B., Nie N. X. and Miyazaki Y. (2025b) Enrichment of moderately volatile elements in first-generation planetesimals of the inner Solar System. *Sci. Adv.* **11**, eadq7848.

Guo W. and Eiler J. M. (2007) Temperatures of aqueous alteration and evidence for methane generation on the parent bodies of the CM chondrites. *Geochimica et Cosmochimica Acta* **71**, 5565–5575.

Guthrie J. P. (2000) Hydration of Carbonyl Compounds, an Analysis in Terms of Multidimensional Marcus Theory. *J. Am. Chem. Soc.* **122**, 5529–5538.

Hashizume K., Takahata N., Naraoka H. and Sano Y. (2011) Extreme oxygen isotope anomaly with a solar origin detected in meteoritic organics. *Nature Geoscience* **4**, 165–168.

Hilkert A., Bohlke J. K., Mroczkowski S. J., Fort K. L., Aizikov K., Wang X. T., Kopf S. H. and Neubauer C. (2021) Exploring the potential of electrospray-Orbitrap for stable isotope analysis using nitrate as a model. *Analytical Chemistry* **93**, 9139–9148.

Hofmann A. E., Chimiak L., Dallas B., Griep-Raming J., Juchelka D., Makarov A., Schwieters J. and Eiler J. M. (2020) Using Orbitrap mass spectrometry to assess the isotopic compositions of individual compounds in mixtures. *International Journal of Mass Spectrometry* **457**, 116410.

Hollenback A. J. and Jaisi D. P. (2024) Position-Specific Oxygen Isotope Analysis in Inositol Phosphates by Using Electrospray Ionization-Quadrupole-Orbitrap Mass Spectrometry. *J. Am. Soc. Mass Spectrom.* **35**, 2176–2186.

Jungclaus G. A., Yuen G. U., Moore C. B. and Lawless J. G. (1976) Evidence for the presence of low molecular weight alcohols and carbonyl compounds in the Murchison meteorite. *Meteoritics* **11**, 231–237.

Kantnerová K., Kuhlbusch N., Juchelka D., Hilkert A., Kopf S. and Neubauer C. (2024) A guide to precise measurements of isotope abundance by ESI-Orbitrap MS. *Nature Protocols*, 1–32.

Kebukawa Y. and Cody G. D. (2015) A kinetic study of the formation of organic solids from formaldehyde: Implications for the origin of extraterrestrial organic solids in primitive Solar System objects. *Icarus* **248**, 412–423.

Keeffe J. R., Kresge A. J. and Schepp N. P. (1990) Keto-enol equilibrium constants of simple monofunctional aldehydes and ketones in aqueous solution. *J. Am. Chem. Soc.* **112**, 4862–4868.

Korablev O. I., Ackerman M., Krasnopolsky V. A., Moroz V. I., Muller C., Rodin A. V. and Atreya S. K. (1993) Tentative identification of formaldehyde in the Martian atmosphere. *Planetary and Space Science* **41**, 441–451.

Kuga M., Marty B., Marrocchi Y. and Tissandier L. (2015) Synthesis of refractory organic matter in the ionized gas phase of the solar nebula. *Proceedings of the National Academy of Sciences* **112**, 7129–7134.

Kumari P., Kumar M., Reddy C. R. K. and Jha B. (2013) Algal lipids, fatty acids and sterols. In *Functional ingredients from algae for foods and nutraceuticals* Elsevier. pp. 87–134.

Labahn J., Bittner L., Hirschmann P., Roettig C.-B., Burghardt D., Glaser B., Marković S. B. and Zech M. (2022) 18 O analyses of bulk lipids as novel paleoclimate tool in loess research–a pilot study. *E&G Quaternary Science Journal* **71**, 83–90.

Lee M. R., Alexander C. M. O., Bischoff A., Brearley A. J., Dobrică E., Fujiya W., Le Guillou C., King A. J., Van Kooten E., Krot A. N., Leitner J., Marrocchi Y., Patzek M., Petaev M. I., Piani L., Pravdivtseva O., Remusat L., Telus M., Tsuchiyama A. and Vacher L. G. (2025) Low-Temperature Aqueous Alteration of Chondrites. *Space Sci Rev* **221**, 11.

Liu S.-Y., Mehringer D. M. and Snyder L. E. (2001) Observations of formic acid in hot molecular cores. *The Astrophysical Journal* **552**, 654.

Llewellyn D. R. and O'Connor C. (1964) 110. Tracer studies of carboxylic acids. Part I. Acetic and pivalic acid. *Journal of the Chemical Society (Resumed)*, 545–549.

Marel N. van der, Dishoeck E. F. van, Bruderer S. and Kempen T. A. van (2014) Warm formaldehyde in the Ophiuchus IRS 48 transitional disk. *A&A* **563**, A113.

Maxwell T. M., Silva L. C. R. and Horwath W. R. (2018) Predictable Oxygen Isotope Exchange Between Plant Lipids and Environmental Water: Implications for Ecosystem Water Balance Reconstruction. *JGR Biogeosciences* **123**, 2941–2954.

Mega T. L., Cortes S. and Van Etten R. L. (1990) The oxygen-18 isotope shift in carbon-13 nuclear magnetic resonance spectroscopy. 13. Oxygen exchange at the anomeric carbon of D-glucose, D-mannose, and D-fructose. *J. Org. Chem.* **55**, 522–528.

Mueller E. P., Panehal J., Meshoulam A., Song M., Hansen C. T., Warr O., Boettger J., Heuer V. B., Bach W. and Hinrichs K.-U. (2024) Isotopic evidence of acetate turnover in Precambrian continental fracture fluids. *Nature Communications* **15**, 9130.

Mueller E. P., Sessions A. L., Sauer P. E., Weiss G. M. and Eiler J. M. (2021) Simultaneous, high-precision measurements of δ2H and δ13C in nanomole quantities of acetate using electrospray ionization-quadrupole-Orbitrap mass spectrometry. *Analytical Chemistry* **94**, 1092–1100.

Murphy R. C. and Clay K. L. (1979) Synthesis and back exchange of18O labeled amino acids for use as internal standards with mass spectrometry. *Biol. Mass Spectrom.* **6**, 309–314.

Neubauer C., Crémière A., Wang X. T., Thiagarajan N., Sessions A. L., Adkins J. F., Dalleska N. F., Turchyn A. V., Clegg J. A. and Moradian A. (2020) Stable isotope analysis of intact oxyanions using electrospray quadrupole-orbitrap mass spectrometry. *Analytical Chemistry* **92**, 3077–3085.

Niles P. B., Zolotov M. Y. and Leshin L. A. (2009) Insights into the formation of Fe-and Mg-rich aqueous solutions on early Mars provided by the ALH 84001 carbonates. *Earth and Planetary Science Letters* **286**, 122–130.

de Obeso J. C., Santiago Ramos D. P., Higgins J. A. and Kelemen P. B. (2021) A Mg isotopic perspective on the mobility of magnesium during serpentinization and carbonation of the Oman ophiolite. *Journal of Geophysical Research: Solid Earth* **126**, e2020JB020237.

O'Connor C. (1968) Tracer studies of carboxylic acids—VI: Ethylenediaminetetraacetic acid. *Journal of Inorganic and Nuclear Chemistry* **30**, 2697–2708.

O'Connor C. and Llewellyn D. R. (1965) 484. Tracer studies in carboxylic acids. Part IV. Aminoacetic acid. *Journal of the Chemical Society (Resumed)*, 2669–2673.

Ohnishi I. and Tomeoka K. (2007) Hydrothermal alteration experiments of enstatite: Implications for aqueous alteration of carbonaceous chondrites. *Meteorit & Planetary Scien* **42**, 49–61.

O'Reilly L. da S. L. and DeNiro M. J. D. (1983) Biogeochemical implications of the isotopic equilibrium fractionation factor between the oxygen atoms of acetone and water. *Geochimica et Cosmochimica Acta* **47**, 2271–2274.

Passey B. H. and Henkes G. A. (2012) Carbonate clumped isotope bond reordering and geospeedometry. *Earth and Planetary Science Letters* **351**, 223–236.

Pizzarello S. and Huang Y. (2002) Molecular and isotopic analyses of Tagish Lake alkyl dicarboxylic acids. *Meteoritics & Planetary Science* **37**, 687–696.

Redington R. L. (1976) Kinetics of oxygen-18 exchange between carboxylic acids and water. *J. Phys. Chem.* **80**, 229–235.

Risley J. M. and Van Etten R. L. (1980) Oxygen-18 isotope effect in carbon-13 nuclear magnetic resonance spectroscopy. 2. The effect of structure. *J. Am. Chem. Soc.* **102**, 4609–4614.

Rittenberg D. and Graff C. (1958) A Comparison of the Rate of Mutarotation and $O^{18}$ Exchange of Glucose[1]. *J. Am. Chem. Soc.* **80**, 3370–3372.

Roberts I. and Urey H. C. (1939) Kinetics of the exchange of oxygen between benzoic acid and water. *Journal of the American Chemical Society* **61**, 2580–2584.

Sakamoto N., Seto Y., Itoh S., Kuramoto K., Fujino K., Nagashima K., Krot A. N. and Yurimoto H. (2007) Remnants of the early solar system water enriched in heavy oxygen isotopes. *Science* **317**, 231–233.

Samuel D. and Silver B. L. (1965) Oxygen isotope exchange reactions of organic compounds. In *Advances in Physical Organic Chemistry* Elsevier. pp. 123–186.

Scheller E. L., Swindle C., Grotzinger J., Barnhart H., Bhattacharjee S., Ehlmann B. L., Farley K., Fischer W. W., Greenberger R. and Ingalls M. (2021) Formation of Magnesium Carbonates on Earth and Implications for Mars. *Journal of Geophysical Research: Planets* **126**, e2021JE006828.

Sephton M. A. (2002) Organic compounds in carbonaceous meteorites. *Natural product reports* **19**, 292–311.

Silva L. C. R., Pedroso G., Doane T. A., Mukome F. N. D. and Horwath W. R. (2015) Beyond the cellulose: Oxygen isotope composition of plant lipids as a proxy for terrestrial water balance. *Geochem. Persp. Lett* **1**, 33–42.

Simkus D. N., Aponte J. C., Elsila J. E. and Dworkin J. P. (2020) Investigating the Alcohol Content of the Murchison Meteorite. In *Lunar and Planetary Science Conference* p. 2635.

Simkus D. N., Aponte J. C., Hilts R. W., Elsila J. E. and Herd C. D. (2019) Compound-specific carbon isotope compositions of aldehydes and ketones in the Murchison meteorite. *Meteoritics & planetary science* **54**, 142–156.

Singh S. K., Kleimeier N. F., Eckhardt A. K. and Kaiser R. I. (2022) A Mechanistic Study on the Formation of Acetone (CH3COCH3), Propanal (CH3CH2CHO), Propylene Oxide (c-CH3CHOCH2) along with Their Propenol Enols (CH3CHCHOH/CH3C (OH) CH2) in Interstellar Analog Ices. *The Astrophysical Journal* **941**, 103.

Smith K. E., Callahan M. P., Gerakines P. A., Dworkin J. P. and House C. H. (2014) Investigation of pyridine carboxylic acids in CM2 carbonaceous chondrites: Potential precursor molecules for ancient coenzymes. *Geochimica et Cosmochimica Acta* **136**, 1–12.

Suttle M. D., King A. J., Schofield P. F., Bates H. and Russell S. S. (2021) The aqueous alteration of CM chondrites, a review. *Geochimica et Cosmochimica Acta* **299**, 219–256.

Swindle C., Vasconcelos P., Dalleska N., Cardarelli E., Bhattacharjee S., Dimarco Z., Farley K. A. and Present T. (2025) Trace Element Compositions and Redox Shifts Preserved in Magnesites, Sediments and Soils from the Kunwarara Magnesite Mine. *Applied Geochemistry*, 106494.

Tartèse R., Chaussidon M., Gurenko A., Delarue F. and Robert F. (2018) Insights into the origin of carbonaceous chondrite organics from their triple oxygen isotope composition. *Proceedings of the National Academy of Sciences* **115**, 8535–8540.

Vandenbroucke M. and Largeau C. (2007) Kerogen origin, evolution and structure. *Organic geochemistry* **38**, 719–833.

Waterhouse J. S., Cheng S., Juchelka D., Loader N. J., McCarroll D., Switsur V. R. and Gautam L. (2013) Position-specific measurement of oxygen isotope ratios in cellulose: isotopic exchange during heterotrophic cellulose synthesis. *Geochimica et Cosmochimica Acta* **112**, 178–191.

Wedeking K. W. and Hayes J. M. (1983) Exchange of oxygen isotopes between water and organic material. *Chemical geology* **41**, 357–370.

Weiss G. M., Sessions A. L., Julien M., Csernica T., Yamada K., Gilbert A., Freeman K. H. and Eiler J. M. (2023) Analysis of intramolecular carbon isotope distributions in alanine by electrospray ionization Orbitrap mass spectrometry. *International Journal of Mass Spectrometry* **493**, 117128.

Wiberg K. B., Morgan K. M. and Maltz H. (1994) Thermochemistry of Carbonyl Reactions. 6. A Study of Hydration Equilibria. *J. Am. Chem. Soc.* **116**, 11067–11077.

Wilkes E. B., Sessions A. L., Zeichner S. S., Dallas B., Schubert B., Jahren A. H. and Eiler J. M. (2022) Position-specific carbon isotope analysis of serine by gas chromatography/Orbitrap mass spectrometry, and an application to plant metabolism. *Rapid Comm Mass Spectrometry* **36**, e9347.

Wolfe S., Shi Z., Yang K., Ro S., Weinberg N. and Kim C.-K. (1998) Hydration of the carbonyl group. Further evidence for a cooperative mechanism from experimental and theoretical studies of the hydrations of formaldehyde, acetaldehyde, acetone, and cyclohexanone. *Can. J. Chem.* **76**, 114–124.

Wostbrock J. A., Cano E. J. and Sharp Z. D. (2020) An internally consistent triple oxygen isotope calibration of standards for silicates, carbonates and air relative to VSMOW2 and SLAP2. *Chemical Geology* **533**, 119432.

Xia Z. and Yu Z. (2020) Temperature-dependent oxygen isotope fractionation in plant cellulose biosynthesis revealed by a global dataset of peat mosses. *Frontiers in Earth Science* **8**, 307.

Zeichner S. S., Aponte J. C., Bhattacharjee S., Dong G., Hofmann A. E., Dworkin J. P., Glavin D. P., Elsila J. E., Graham H. V., Naraoka H., Takano Y., Tachibana S., Karp A. T., Grice K., Holman A. I., Freeman K. H., Yurimoto H., Nakamura T., Noguchi T., Okazaki R., Yabuta H., Sakamoto K., Yada T., Nishimura M., Nakato A., Miyazaki A., Yogata K., Abe M., Okada T., Usui T., Yoshikawa M., Saiki T., Tanaka Satoshi, Terui F., Nakazawa S., Watanabe S., Tsuda Y., Hamase K., Fukushima K., Aoki D., Hashiguchi M., Mita H., Chikaraishi Y., Ohkouchi N., Ogawa N. O., Sakai S., Parker E. T., McLain H. L., Orthous-Daunay F.-R., Vuitton V., Wolters C., Schmitt-Kopplin P., Hertkorn N., Thissen R., Ruf A., Isa J., Oba Y., Koga T., Yoshimura T., Araoka D., Sugahara H., Furusho A., Furukawa Y., Aoki J., Kano K., Nomura S. M., Sasaki K., Sato H., Yoshikawa T., Tanaka Satoru, Morita M., Onose M., Kabashima F., Fujishima K., Yamazaki T., Kimura Y. and Eiler J. M. (2023)

Polycyclic aromatic hydrocarbons in samples of Ryugu formed in the interstellar medium. *Science* **382**, 1411–1416.

Zeichner S. S., Wilkes E. B., Hofmann A. E., Chimiak L., Sessions A. L., Makarov A. and Eiler J. M. (2022) Methods and limitations of stable isotope measurements via direct elution of chromatographic peaks using gas chromotography-Orbitrap mass spectrometry. *International Journal of Mass Spectrometry* **477**, 116848.

Zolensky M. E., Bourcier W. L. and Gooding J. L. (1989) Aqueous alteration on the hydrous asteroids: Results of EQ3/6 computer simulations. *Icarus* **78**, 411–425.

## Chapter 4

# TRIPLE OXYGEN ISOTOPIC COMPOSITION OF ORGANIC ACIDS FROM CM CHONDRITE MURCHISON TRACKS PRIMORDIAL VOLATILES IN THE SOLAR SYSTEM

Surjyendu Bhattacharjee[1*], Issaku E. Kohl[2] and John M. Eiler

[1]Division of Geological and Planetary Sciences, California Institute of Technology, Pasadena, CA-91125, USA

[2]Department of Geology & Geophysics, University of Utah, Salt Lake City, UT-84112, USA

*Corresponding Author: sbhattac@caltech.edu

## Abstract

Organic compounds detected in meteorites and active star-forming regions in the solar system suggest that abiotic organic synthesis was widespread in the early solar system. However, their connection to the primary volatiles (nebular gas, ices) in the solar system, and mechanisms of synthesis remains essentially unknown. Triple oxygen isotopic compositions ($^{17}O/^{16}O$, $^{18}O/^{16}O$) of organic compounds are characteristic of the volatile source and process they formed. However, without complicated chemical conversion, it is impossible to measure $^{17}O/^{16}O$ of carbon-bearing organic compounds using conventional gas source mass spectrometry methods due to their lack of requisite mass resolution. In this study, we report the first measurements of the triple oxygen isotopic compositions of organic acids (acetate, propionate, and glycolate) from CM chondrite Murchison, using novel Orbitrap Isotope Ratio Mass Spectrometry. While results for glycolate are pending a standard measurement, we find that propionate conforms to the primitive component mixing line, indicating inheritance of outer solar system ices without mass-dependent fractionation. Acetate, however, lies to the right of the primary component mixing line, indicating mass-dependent fractionation from a primary volatile that was present in a planetesimal-forming region. These two volatile reservoirs were genetically linked by the CO self-shielding process. Our study highlights the distinct organic formation processes in different parts of the early solar system, from volatiles that evolved via nebular processes.

## 4.1 Introduction

Volatiles play a critical role in dictating the chemical evolution of planetary bodies, and modulate their habitability (Rapin et al., 2023). However, the origin of volatiles that were accreted by different rocky reservoirs of the solar system is not fully understood. It is known that multiple volatile reservoirs exist in the inner and outer solar system (e.g., CO, ices) (Sakamoto et al., 2007; McKeegan et al., 2011; Bhattacharjee and Eiler, 2024). A series of complex physicochemical processes that led to the early solar system evolution is thought to have facilitated their formation (Choi et al., 1998; McKeegan and Leshin, 2001; Clayton, 2002). Details regarding the spectrum of the geochemical and isotopic compositions of those volatile reservoirs remain incomprehensible.

The three stable isotopes of oxygen - $^{16}O$, $^{17}O$, $^{18}O$ - form by different nucleosynthetic processes and are present in variable proportions in distinct extraterrestrial environments (i.e., interstellar medium ice or nebular gas). Moreover, chemical processing in the early solar system led to variations in oxygen isotope ratio among meteorites and various solar system bodies. These variations are generally classified as following either 'mass dependent' trends, where $^{17}O/^{16}O$ variations are approximately half of $^{18}O/^{16}O$ variations (more precisely, they follow a line with slope of ~0.52–0.53 in a plot of $\delta^{17}O$ vs. $\delta^{18}O$), or 'mass independent' trends, where $^{17}O/^{16}O$ and $^{18}O/^{16}O$ variations deviate from a mass-dependent trend. The terrestrial fractionation line, TFL, is a mass-dependent trend that passes through the oxygen isotope composition of the bulk Earth. Anhydrous minerals from carbonaceous chondrites closely conform to a pure mass independent oxygen isotope variation; the line of slope ~1 they define in a plot of $\delta^{17}O$ vs $\delta^{18}O$ plot is referred to as Carbonaceous Chondrites Anhydrous Material line, or CCAM). The $^{17}O$ anomaly ($\Delta^{17}O$ value) is a measure of a sample's departure from the TFL and is calculated as the difference between a material's $\delta^{17}O$ value, and the $\delta^{17}O$ value it would have if it conformed to the TFL at its $\delta^{18}O$ value.

The CCAM trend has been interpreted as a mixing line between oxygen from a $^{16}O$ rich reservoir of CO that made up the majority of early solar system oxygen and a $^{17}O$,$^{18}O$ rich reservoir of $H_2O$ that was generated photochemically in the early solar system or inherited from pre-solar compounds from interstellar medium (ISM) or nebular ice (possibly due to photochemistry in a pre-solar-system setting) (McKeegan and Leshin, 2001). Current models invoke CO self-shielding, or isotope selective photochemical dissociation of CO, in the early solar system to create $^{17}$O,$^{18}$O rich water ice in the outer solar system (Clayton et al., 1973; Clayton, 2002; Lyons and Young, 2005). Such oxygen isotope compositions have been reported for alteration phases from the LL chondrite Semarkona (Choi et al., 1998), ungrouped carbonaceous chondrite Acfer 094 (Sakamoto et al., 2007) and estimated from CO chondrite MIL 07687 (Vacher et al., 2016 and references therein). Triple O isotopic composition of waters responsible for aqueous alteration of parent bodies of CM chondrites (Clayton & Mayeda, 1999; Verdier-Paoletti et al., 2017; Fujiya, 2018) are modestly enriched in $^{17}$O and $^{18}$O relative to the bulk Earth.

Organic compounds are synthesized in the early nebular environments and on asteroids during their aqueous alteration. The oxygen contained in organic compounds potentially tracks the source of the volatile from which it formed. Two types of organics, soluble (SOM) and insoluble (IOM), are recovered from chondritic meteorites. Triple oxygen isotopic analysis of SOM has not been done to date. Limited triple oxygen isotope measurements from IOMs yield variable and somewhat ambiguous results, generally following the CCAM trend (Tartèse et al., 2018).

The oxygen isotopic composition of different chondritic components represent oxygen from different solar system reservoirs. While $^{16}$O-rich silicates inherit a nebular signature ($\Delta^{17}O << 0$), $^{17,18}$O-rich magnetite is thought to represent initial fluid accreted by a chondritic parent body ($\Delta^{17}O > 0$), and those of carbonates are thought to represent the oxygen isotopic variation of fluid in the chondritic parent body during aqueous alteration and thermal evolution, where $^{17,18}$O-rich fluid evolves by equilibration with $^{16}$O-rich silicates (McKeegan and Leshin, 2001; Guo and Eiler, 2007; Clog et al., 2015). The location of organics in this spectrum is unclear. In chapter 3, we showed that the oxygen in IOM did not equilibrate with carbonate-forming fluids (Bhattacharjee and Eiler, 2024), indicating their origin is unrelated to aqueous alteration processes (Alexander et al., 2007). However, given the lack of oxygen isotope data, there is little consensus about the formation and/or evolution of SOM in this context.

Different chemical processes preferentially facilitate the formation of SOMs with different oxygen-hosting functional groups from different volatile sources (Chimiak and

Eiler, 2024). Those SOMs are expected to have distinct oxygen isotopic compositions. On the other hand, IOM is a compositionally complex material with different oxygen-bearing functional groups. These groups, presumably formed via different chemical mechanisms, can be incorporated into the IOM at any stage of their synthesis (i.e., late aqueous alteration or early nebular processes) (Aponte et al., 2014a; Kuga et al., 2015; Foustoukos and Cody, 2021). Its oxygen isotope measurement reflects an average of all its oxygen-bearing functional groups. Interpreting the origin of the IOM is difficult from such a measurement. Hence, compound-specific triple oxygen isotopic composition analysis of SOMs holds the key to unraveling the diversity of volatiles involved in the organic synthesis in the early solar system.

However, analyzing triple oxygen isotopic composition of SOMs are met with severe analytical challenges. Unlike IOM, they cannot be measured *in situ* by ion microprobe due to their low abundance and unknown textural affinity. Their compound-specific analysis by conventional gas-source IRMS techniques is challenging because of the low abundances of compounds of interest, difficulty in separating them from complex meteoritic extracts, and the inability of existing gas-source magnetic sector isotope ratio mass spectrometers to mass resolve $^{13}$C- and D- from $^{17}$O-bearing isotopologues, without the relatively arduous process of converting oxygen to $O_2$ (Ellis and Passey, 2023; Crocker et al., 2025). These steps have the potential to modify the oxygen isotopic compositions of these compounds during analysis, if trace water is present.

The advent of Orbitrap isotope ratio mass spectrometry (Eiler et al., 2017; Hofmann et al., 2020; Hilkert et al., 2021; Mueller et al., 2021; Zeichner et al., 2022, 2023; Csernica et al., 2023; Hong et al., 2025) allows measurement of nano- to pico-molar quantities of individual organic molecules with sufficient mass resolution to resolve $^{13}$C- and D- from $^{17}$O-isotopologues. This technology provides a plausible path to making precise analyses of triple O isotope compositions of carbonyl and other organic compounds extracted from carbonaceous chondrite meteorites.

To this end, we present the first measurement of the triple oxygen isotopic composition of soluble organic acids from CM chondrite Murchison. Given their higher abundance compared to other SOMs and relative recalcitrance to oxygen exchange with fluid

(Bhattacharjee and Eiler, 2025), they are expected to retain their pristine signature associated with their initial synthesis.

## 4.2 Materials and methods

### 4.2.1 Organic acids extraction and characterization

A 1.6 g fragment of CM2 Murchison was acquired from the California Institute of Technology meteorite collection. This fragment had no visual signs of terrestrial mineralization or the presence of fusion crust. This fragment was ground to fine powder using an alumina mortar and pestle, pre-heated (1273 K) to remove adsorbed organic contaminants. Carboxylic acids were extracted from this powder following a previous protocol (Aponte et al., 2014a). A 0.1 N NaOH (excess to neutralize all anions) solution was made from analytical-grade NaOH (Sigma-Aldrich) and ultrapure (Milli–Q IQ 7000) deionized water (DIW, from a Millipore water purification system). The meteorite powder was suspended in 10 mL of this solution, sonicated for 30 min, and stirred at room temperature using a shaker for 2 h. Afterwards, the suspension was centrifuged, the aqueous layer was separated by decantation, and then frozen overnight. Given that glassware can retain adsorbed anions, which are impossible to remove even by high-temperature combustion, we used refractory HDPE tubes for the extraction process. A parallel procedural blank extraction was performed where the blank was treated identically to the sample and stored together in a flash freezer.

The extract contains a high amount of sulfate and phosphate, which can interfere with further organic acid characterization and isotopic analysis. Sulfate, carbonate, chloride and excess base was removed using a 2.5 cc Dionex OnGuard Ba/Ag/H cartridge following previous protocol (Mueller et al., 2024). The cartridge was pre-washed with >300 mL DIW overnight at a flow rate of 0.4 mL/min. Once conditioned, the sample was loaded into a 10 mL syringe, and passed through the cartridge at a flow rate of 0.2 mL/min. The effluents were collected in HDPE vials with pre-added 0.1 N NaOH in the requisite volume to titrate the solution to pH > 7, to prevent organic acid loss via volatilization. The first 6 mL effluent (the discard volume) was collected, stored separately, and not used for isotopic analysis. The last 4 mL (analytical fraction) was collected separately to be used for further characterization.

The procedural blank was treated identically to the sample. Each cartridge was used only once, after which it was discarded. This method has previously been observed not to generate significant organic acid blanks (Mueller et al., 2024). This protocol effectively removed almost all chloride and a majority of the sulfate from the solution.

The analytical fraction and discard volumes were characterized using a Thermo Dionex ion chromatography instrument with an AG-11HC column and a KOH gradient from 1 to 20 mM, following established protocols (Mueller et al., 2024). Based on the elution times of single compound standards, we characterized all the components of the solution. The procedural blank had contents identical to the DIW solvent, with negligible concentrations of organic acids.

We did not purify and collect the organic acid fraction using the IC because the collected fractions are aqueous solutions that cannot be directly introduced to the Orbitrap instruments. To have enough organic acids to make a precise triple oxygen isotope measurement, we need to collect ~8-10 fractions and evaporate the water. This means longer exposure to water at laboratory conditions, increasing the probability of oxygen isotope exchange with DIW. These compounds are severely lost during the evaporation step (Mueller et al., 2024). This loss is expected to be associated with oxygen isotopic composition modification by evaporative distillation. To avoid these complexitiess, we measured the oxygen isotopic composition of the acid directly from the analytical fraction.

### 4.2.2 Orbitrap isotope ratio mass spectrometry

After IC characterization, the analytical aqueous fraction was diluted in LC–MS grade methanol (Fischer Chemical) to yield a solution with a methanol:water ratio of 9:1. The isotopic compositions of acetate, propionate and glycolate in this sample solution were measured using Thermo Scientific Q-Exactive HF Electrospray Ionization Orbitrap Mass Spectrometer (Orbitrap MS) at the California Institute of Technology, using a dual syringe pump setup with 10 mL syringes. Measurements of samples were bracketed by standard measurements. The analytical conditions are recorded in Table 4.1.

A matrix-matched standard solution was prepared in 9:1 methanol-water solvent with all compounds that are present in the sample. To do this, a small amount of the sample solution was introduced to the Orbitrap MS, and its components and their signal intensity

(NL score, arbitrary units) were observed. The sample solution was found to contain sulfate, nitrate, chloride, acetate, propionate, butyrate, glycolate, oxalate, benzoate, and lactate. Na-salts of these anions were added in this order to a 9:1 methanol-water solvent, one by one. After each addition, the standard solution was observed in the Orbitrap MS for all the components' NL score. This process was repeated until the sample and standard solution achieved a satisfactory match (~10% or better) for all the components mentioned above. At this stage, the triple oxygen isotopic analysis was conducted. Every time after the syringes were refilled, the sample-standard matching was checked and adjusted, if required, to match all components. Solvent blank (NL-score of contaminant peaks present in the m/z of respective organic acids' monoisotopic peaks in the 9:1 methanol solvent) was negligible (<5%), and their corresponding isotopically substituted peaks were not observed.

We tested the accuracy of this method by analyzing isotopic compositions of organic acid standards in a synthetic Murchison-like solution using a matrix-matched solution and found that this method yields accurate results.

The oxygen isotopic compositions ($^{18}O/^{16}O$) of the standard organic acids were independently measured using a high temperature conversion elemental analyzer (TC/EA) coupled to a Finnigan Delta V+ at continuous flow mode at SIRFER, University of Utah (Table 4.2). $^{18}O/^{16}O$ measurement of glycolate is underway. Carbon isotope compositions ($^{13}C/^{12}C$) were measured using an Elementary Analyzer (EA) coupled to an Isotope Ratio Mass Spectrometer (IRMS) at the California Institute of Technology, using in-house organic compound standards (Mueller, 2024). Hydrogen isotopic compositions of these standards are from Mueller (2024).

After the analysis, data were reduced following previous guidelines (Csernica et al., 2023). Briefly, for each organic acid, the isotopic composition of each isotopic peak (e.g., $^{13}C$, $^{17}O$, D, $^{18}O$) was expressed relative to their bracketing standard, which was in turn converted to δ-values at international scales (VSMOW for O, H, and VPDB for C) using the independently characterized isotopic compositions of standards and reported in Table 4.3. Acquisition errors of samples were propagated in quadrature to bracketing standards and reported propagated uncertainty (1SE). We typically achieved propagated uncertainty (1SE) of ~2-6‰ for $\delta^{17}O$, ~0.8–4‰ for $\delta^{18}O$, ~0.3–1‰ for $\delta^{13}C$ and ~ 2–13‰ for δD.

## 4.3 Results

### 4.3.1 Isotopic compositions of organic acids

We measured the triple oxygen isotopic composition of acetate, propionate, and glycolate. They have $\delta^{18}O$ in the range ~23–58‰, $\delta^{17}O$ in the range ~19–45‰. The deviation of their $\delta^{17}O$ from that expected from a canonical mass-dependent fractionation relationship between $\delta^{18}O$–$\delta^{17}O$, denoted as $\Delta^{17}O$:

$$\Delta^{17}O = \delta^{17}O - 0.528 * \delta^{18}O \qquad (4.1)$$

is highly variable. Acetate is $^{17}O$ poor ($\Delta^{17}O = -11.7\pm2$‰), where propionate and glycolate are $^{17}O$ rich ($\Delta^{17}O = 19.2\pm5.7$‰ and 16.5±6.7‰). Note that for glycolate, $\delta^{18}O$ and $\delta^{17}O$ values cannot be calculated since the $^{18}O/^{16}O$ measurement of the standard is still underway. However, its $\Delta^{17}O$ can still be estimated from sample standard bracketing, given that all terrestrial materials have $\Delta^{17}O = 0$‰. Propionate roughly conforms to the CCAM line in $\delta^{18}O$–$\delta^{17}O$ plot, whereas acetate lies to the right of it (Fig. 4.1). Their $\delta^{13}C$ is in the range –34.3 to –1.5‰ and their $\delta D$ is in the range –157 to 631‰ (Table 4.3). Their $\delta^{13}C$ and $\delta D$ are in the range predicted by previous works (Fig. 4.2).

## 4.4 Discussion

### 4.4.1 Comparison with other Murchison oxygen reservoirs

Murchison hosts pristine silicate minerals and aqueous alteration products, with distinct oxygen isotopic compositions (Clayton and Mayeda, 1984). Silicates such as chondrules or CAIs are relatively $^{16}O$-rich and span a range of $\delta^{18}O = -16.5$‰ to 1‰ along the CCAM line. Spinel from CAIs is even $^{16}O$-rich, with $\delta^{18}O \sim -40$‰ and $\Delta^{17}O \sim -20$‰. Fine-grained matrix is relatively $^{16}O$ poor, with $\delta^{18}O = 12.6$‰ and $\Delta^{17}O = -1.96$‰. Organic acids from Murchison have much higher $\delta^{18}O$ than these constituents, but the $\Delta^{17}O$ of acetate overlaps with that of silicates.

Murchison experienced extended aqueous alteration that formed secondary phases such as sulfate and carbonates. Sulfates in Murchison have $\delta^{18}O = 9.5$‰ and $\Delta^{17}O = 0.8$‰

(Airieau et al., 2005). Carbonates have $\delta^{18}O = 28.4‰$ to $35.1‰$, and $\Delta^{17}O = -1.9‰$ to $2.5‰$ (Clayton and Mayeda, 1984; Guo and Eiler, 2007; Fujiya et al., 2015; Clog et al., 2024). Organic acids are $\delta^{18}O$ richer than these phases, and their $\Delta^{17}O$ are much higher or lower than carbonates and sulfates.

Finally, the oxygen reservoir constituted by macromolecular organic matter (IOM), with $\delta^{18}O = -18‰$ to $7.5‰$ and $\Delta^{17}O = -12.1‰$ to $2.7‰$ (Tartèse et al., 2018). Organic acids measured in this study have higher $\delta^{18}O$ than this pool. While propionate has much higher $\Delta^{17}O$ than IOM, acetate $\Delta^{17}O$ shows an overlap with that of the IOM. These comparisons are presented in Fig. 4.1.

### 4.4.2 Sources and mechanisms of organic acid formation

Since organic acids are expected to acquire $\Delta^{17}O$ from their fluid source, the $\Delta^{17}O$ of organic acids is an indicator of the fluid that formed them. Assuming those fluids were located on the CCAM line and formed by a mixture of nebular volatiles and outer solar system ices, we can estimate the $\delta^{18}O$ of fluids that were involved in organosynthesis by connecting the $\delta^{18}O$ of organic acids to the CCAM line via a horizontal line in Fig. 4.1. This suggests that acetate formed from a fluid with $\delta^{18}O \sim -24‰$, $\Delta^{17}O = -11.7‰$.

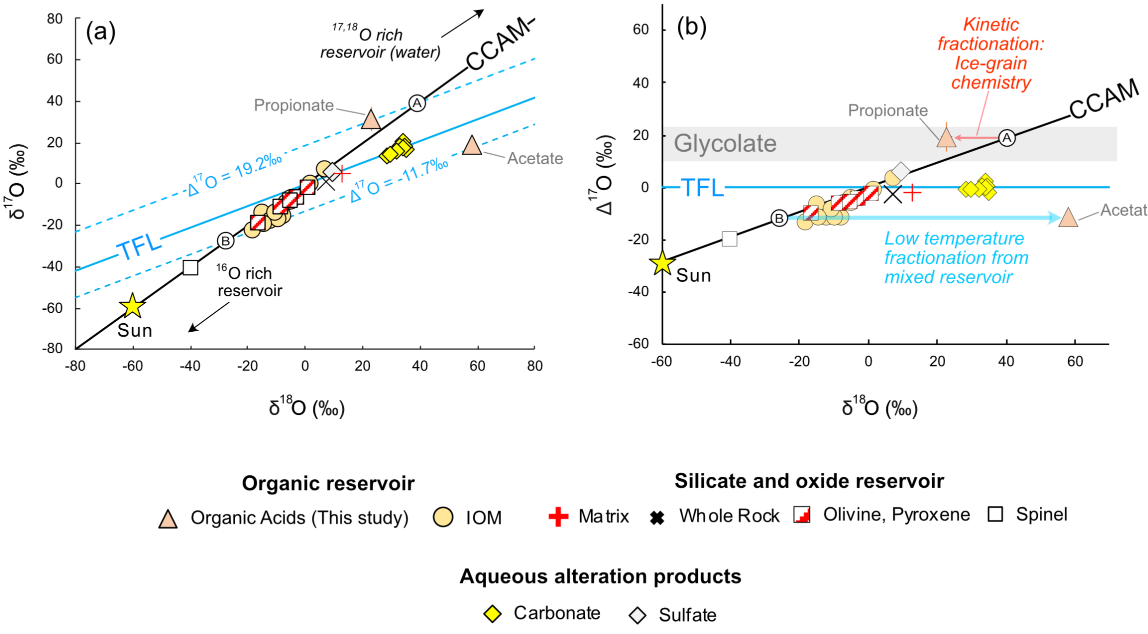

Figure 4.1: Triple oxygen isotopic composition of organic acids (this study) and other oxygen reservoirs in Murchison plotted in (a) $\delta^{18}O$–$\delta^{17}O$ space. Contours of $\Delta^{17}O$ corresponding to acetate and propionate are shown. Circles marked as A and B are the intersections of these

contours with CCAM line, their potential fluid source. The terrestrial fractionation line (TFL) has $\Delta^{17}O=0$. (b) Organic acids and other Murchison components in $\delta^{18}O$–$\Delta^{17}O$ space. $\Delta^{17}O$ of glycolate highlighted by gray field. In this space, $\Delta^{17}O$ contours are horizontal lines parallel to TFL, and mass-dependent fractionations move along these lines. The measured isotopic composition of acetate can be explained by an equilibrium low-temperature mass-dependent fractionation from fluid B, where acetate fractionated $^{17,18}O$ from fluid. On the contrary, the measured propionate composition can be explained by formation from fluid A, via a normal kinetic isotope effect, where propionate fractionates $^{16}O$ relative to fluid. (Data for different oxygen reservoirs from: Clayton and Mayeda, 1984; McKeegan et al., 2011; Fujiya et al., 2015; Tartèse et al., 2018).

If acetate exchanged with fluids in Murchison's parent body during aqueous alteration, it would have $\Delta^{17}O$ comparable to carbonate or sulfate, which is not the case (Fig. 4.1). This suggests that acetate retained its pristine composition associated with primordial synthesis. One can argue that acetate formed at the end of aqueous alteration phases, where fluid evolved to $^{16}O$-rich composition by exchange with silicates, at sub-zero temperatures. This is the case for late-stage carbonate formation in CI chondrites (Guo, 2008). The aqueous alteration history of Murchison is well constrained (e.g., Suttle et al., 2021; Lee et al., 2025). Their aqueous alteration occurred at 278–295 K, and fluids had $\Delta^{17}O$ of –1.9‰ or higher (Clayton and Mayeda, 1984; Fujiya et al., 2015; Clog et al., 2015). As such, we don't find evidence for sub-zero temperature, $^{16}O$-rich fluids from late-stage aqueous alteration that can explain the $\delta^{18}O$ of acetate. The $\Delta^{17}O$–$\delta^{18}O$ of carbonates suggests that fluid $\Delta^{17}O$ evolution was limited at the aqueous alteration stage, most likely buffered by matrix minerals. Here, $\delta^{17,18}O$ of fluid should evolve along a mass-dependent line, where fluid $\Delta^{17}O$ would stay constant at ~ –1.9‰ (i.e., at or near $\Delta^{17}O$ of matrix) as the exchange proceeds. Hence, aqueous alteration does not explain the composition of the acetate. Moreover, the acetate-forming fluid cannot be explained by formation from a fluid that equilibrated with olivine and pyroxene at low temperatures, because in this scenario, the fluids would have $\delta^{18}O$ ~ 15–21‰ lower (Schauble and Young, 2021) than olivine and pyroxene ($\delta^{18}O$ ~ –24‰ at $\Delta^{17}O$ = –11.7‰). In that case, we require about ~100‰ $^{18}O/^{16}O$ fractionation between acetate and fluid to explain the measured composition, which seems incomprehensible in this context.

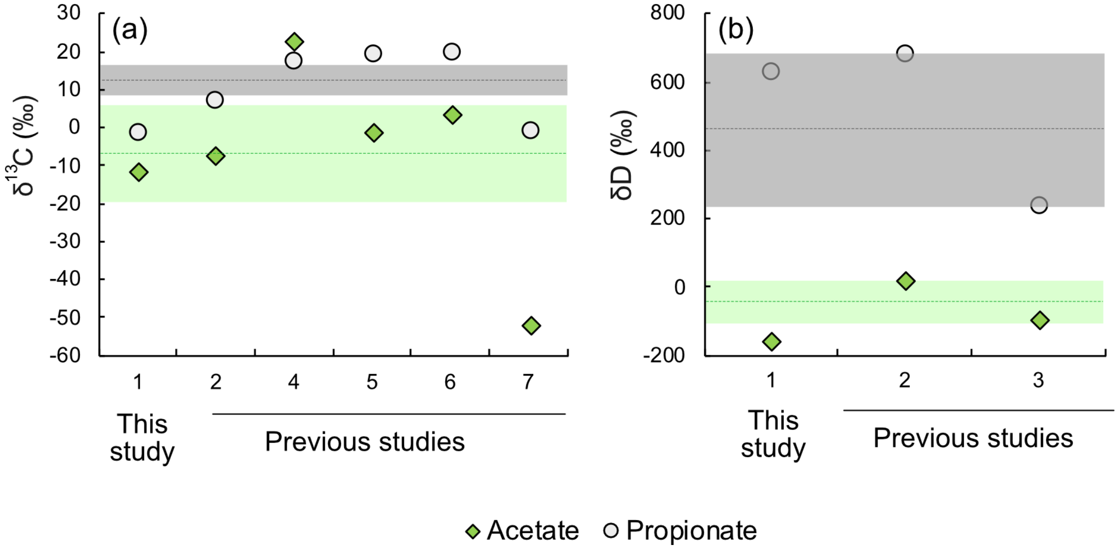

Figure 4.2: Comparison of (a) δ13C and (b) δD of acetate and propionate measured in this study and previous works. The green dotted line in each plot indicates the average acetate composition of previous studies, and the gray dotted line indicates that for propionate. Green and gray shaded bar indicates 1SE of the previous data for acetate and propionate, respectively. Previous data from: 2– Huang et al. (2005), 3– Aponte et al. (2014), 4– Yuen et al. (1984), 5,6– Mimura et al. (2024), 7– Aponte et al. (2019).

Acetate has $\Delta^{17}$O that overlaps with silicates and IOM from Murchison. However, silicates form at elevated temperatures, which are far outside the stability field of organics, excluding their co-synthesis as a possibility. Silicate and organic synthesis were likely spatio-temporally distinct from each other. However, the $\Delta^{17}$O similarity between silicates, IOM, and acetate may indicate a common origin of the fluid.

Acetate is offset from the CCAM line by ~82‰ at constant $\Delta^{17}$O. This large offset suggests a low-temperature mass-dependent fractionation from a $^{16}$O-rich fluid. Extrapolation the oxygen isotope fractionation behavior of alanine down to 233 K (Bhattacharjee and Eiler, 2024), we observe that organic acids should be fractionated from fluid by 55‰, much smaller than the requisite range. This suggests that additional mechanisms of isotope fractionation are needed to explain the acetate composition. The most plausible scenario is that acetate formed from a fluid that condensed as ice at sub-zero temperatures in a protoplanetary disk environment, and acetate formed from this ice, via mass-dependent chemistry. In this case, the fluid precursor to the ice first forms via mixing or primordial volatile components (e.g., nebular gas and ices), having $\delta^{18}O$ = –24‰, $\Delta^{17}O$ = –11.7‰. Next, ice condenses from this fluid in equilibrium at ~233 K, with $\delta^{18}O$ of ~1‰ (equilibrium $^{18}O/^{16}O$ fractionation makes the ice higher in δ18O than fluid by 25‰ at 233K; Ellehoj et al., 2013). Next, acetate forms from or equilibrates with this fluid at 233K, resulting in an isotopic composition ($\delta^{18}O$ = –56‰, $\Delta^{17}O$ = –11.7‰) that can explain our acetate measurement. This seems to be the only explanation that can explain the isotopic composition of the acetate parsimoniously.

Propionate conforms to the CCAM line within analytical uncertainty. This indicates that they inherited the isotopic composition of their fluid without any mass-dependent fractionation and did not exchange with asteroidal fluid during aqueous alteration. Following the discussion in Chapter 2, the only scenario that can explain their isotopic composition ($\delta^{18}O$ = –22.8‰, $\Delta^{17}O$ = 19.2‰) is formation by ice-grain chemistry in the interstellar medium (ISM) or outer disk. In this case, the reaction proceeded with a normal kinetic isotope effect, and propionate was offset to lighter $\delta^{17,18}O$ from the CCAM line following a mass-dependent trend. Extrapolation to CCAM source along a mass-dependent line suggests that the propionate-forming ice should have $\delta^{18}O$ = 40.7‰, $\Delta^{17}O$ = 19.2‰. This fluid composition is consistent with the calculated isotopic composition of ISM ice ($\delta^{18}O$ = 34‰, $\Delta^{17}O$ = 16‰) signature from CO chondrite MIL 07687 (Vacher et al., 2016).

### 4.4.3 Implications for early solar system evolution

The isotopic compositions of organic acids provide a window into the early solar system processes. The oxygen isotopic evolution of volatiles in the early solar system is best explained by the photochemical self-shielding of carbon monoxide (Clayton, 2002; Lyons and Young, 2005). In protoplanetary disk, rare isotopologues of CO (e.g., $C^{17}O$, $C^{18}O$) are completely dissociated by ultraviolet radiation to create C and $^{17,18}O$ atoms. Oxygen atoms immediately combine with $H_2$ to form water and condense $^{17,18}O$-rich ice in the outer disk region. Due to high abundance, $C^{16}O$ survives complete photochemical dissociation and dominates the inner disk region volatile inventory. $^{17,18}O$-rich ice signature from carbonaceous chondrites ($\Delta^{17}O$ = 16–90‰, Bhattacharjee and Eiler, 2024 and references therein) and determination of nebular CO by Genesis Mission ($\Delta^{17}O$ = –30‰, McKeegan et al., 2011) testify to self-shielding in the protoplanetary disk.

Given that their $\Delta^{17}O$ is highly different, it is implausible that both acetate and propionate formed from the same fluids on the CM chondrite parent asteroid after its accretion. Instead, they seem to represent two distinct provenances. Propionate formed in the $^{17,18}O$ rich ices (possible products of the CO self-shielding process) in the outer solar system (outwards of the water snow line) via ice-grain chemistry, and later got accreted in the CM parent asteroid. Propionate seems to have formed earlier than acetate as well as CM chondrite parent body, given its $\Delta^{17}O$ is significantly higher than both.

On the other hand, acetate formed by fractionation from a reservoir that evolved by mixing of $^{17,18}O$-rich and $^{16}O$-rich volatiles. It is possible that such a reservoir existed at the asteroid-forming region, where the influx of high $\Delta^{17}O$ volatiles in CO-dominated areas (e.g., Choi et al., 1998) (or migration of water snow line) caused this mixing. This reservoir possibly condensed onto the CM chondrite parent asteroid, and acetate formed after this condensation. This fluid also seems to have influenced the oxygen isotopic composition of silicates and facilitated IOM production. As such, this points to a dynamic environment in the early solar system. A plausible location for this process to occur is the outer disk midplane, where continual IOM production continues (Lawrence et al., 2025). At or near this line, nebular volatiles can mix with $^{17,18}O$-rich ice to generate fluids that form the IOM. If this fluid crosses the snow line vertically, it will condense with IOM onto the CM chondrite parent body. Low-temperature fractionation of acetate from this fluid can explain its oxygen isotopic composition. Thus, isotopic compositions of organic acids track those of their parental fluids and hint at distinct locations of organic acid formation in the early solar system.

## 4.5 Conclusion

The isotopic compositions of organic acids from CM chondrite Murchison provide new insights into volatile reservoirs and chemical processes in the early solar system. We find that soluble organic acids can retain pristine isotopic signatures despite subsequent aqueous alteration on meteorite parent bodies. Acetate and propionate display distinct $\Delta^{17}O$ signatures, indicating that they did not share a common fluid origin or formation environment. Instead, they represent separate provenances: propionate likely formed in

$^{17,18}$O-rich ices through ice-grain chemistry in the outer solar system, while acetate reflects mass-dependent fractionation from a mixed volatile reservoir closer to the asteroid-forming region. The study supports CO self-shielding as a fundamental driver of oxygen isotope diversity in nebular volatiles. Importantly, the results point to multiple spatially distinct settings where prebiotic chemistry took place. Ultimately, these findings demonstrate that isotopic studies of meteoritic organics are key to reconstructing the pathways that shaped planetary building blocks and early habitability potential.

### Acknowledgement

SB acknowledges Elliott Mueller, Simon Andren, Noam Lotem, Nami Kitchen, Michael Mathuri, Nathan Dalleska, and Alex Sessions for their help with analytical techniques and insightful discussions. This study was supported by a grant from the Caltech Center for Comparative Planetary Evolution (grant no. 13520281) awarded to JME.

### Data availability

All data are reported in tabulated format in this chapter.

Table 4.1: Analytical conditions used in this study.

| **Instrument parameters** | **Acetate** | **Propionate** | **Glycolate** |
|---|---|---|---|
| Flow Rate (µL/min) | 20 | 20 | 20 |
| Polarity (+/-) | Negative | Negative | Negative |
| Spray Voltage (kV) | 3.5 | 3.5 | 3.5 |
| Sheath gas flow rate (arbitrary units) | 3 | 3 | 3 |
| Auxiliary gas flow rate (arbitrary units) | 1 | 0 | 0 |
| Sweep gas flow rate (arbitrary units) | 0 | 0 | 0 |
| Capillary temperature (°C) | 320 | 320 | 320 |
| S-lens RF level (arbitrary units) | 55 | 55 | 55 |
| Aux gas heater temperature (°C) | 100 | 100 | 100 |
| Analyzer temperature (°C) | 27.73 | 27.73 | 27.57 |
| | | | |
| Scan Range (*m/z*) | 58.0–62.0 | 70.5–78.5 | 70.5–78.5 |
| Molecular ion peak (*m/z*) | 59.01271 | 73.02846 | 75.00772 |
| Microscans | 6 | 6 | 6 |
| Automatic Gain Control (AGC) | $2 \times 10^5$ | $2 \times 10^5$ | $2 \times 10^5$ |
| Nominal Mass Resolution (FWHM at m/z = 200) | 120,000 | 240,000 | 240,000 |
| Maximum Injection Time (ms) | 1000 | 1000 | 1000 |
| TIC relative standard deviation (RSD) (%) | <0.1 | <0.1 | <0.1 |

Table 4.2: Isotopic compositions of standards used in this study (errors 1SE).

| | **$\delta^{13}C_{VPDB}$ (‰)** | ± | **$\delta^{18}O_{VSMOW}$ (‰)** | ± | **$\delta D_{VSMOW}$ (‰)** | ± |
|---|---|---|---|---|---|---|
| AcJME | –17.8 | 0.3 | 23.2 | 0.1 | –127 | 1.9 |
| Prop | –35.7 | 0.2 | 24.1 | 0.1 | –110 | 1.5 |
| But | –30.7 | 0.0 | 25.2 | 0.1 | –113 | 1 |
| Gly | –43.0 | 0.2 | | | | |

Table 4.3: Isotopic compositions of Murchison organic acids measured using Orbitrap IRMS.

| | **$\delta^{17}O_{VSMOW}$ (‰)** | ± | **$\delta^{18}O_{VSMOW}$ (‰)** | ± | **$\Delta^{17}O$ (‰)** | ± |
|---|---|---|---|---|---|---|
| Acetate | 19.1 | 2.0 | 58.2 | 0.8 | –11.7 | 2.0 |
| Propionate | 31.3 | 5.7 | 22.8 | 1.6 | 19.2 | 5.7 |
| Glycolate | | | | | 16.5 | 6.7 |

| | **$\delta^{13}C_{VPDB}$ (‰)** | ± | **$\delta D_{VSMOW}$ (‰)** | ± |
|---|---|---|---|---|
| Acetate | –11.7 | 0.3 | –157.3 | 2.3 |
| Propionate | –1.5 | 0.6 | 631.4 | 13.3 |
| Glycolate | –34.3 | 1.0 | | |

# BIBLIOGRAPHY

Airieau S. A., Farquhar J., Thiemens M. H., Leshin L. A., Bao H. and Young E. (2005) Planetesimal sulfate and aqueous alteration in CM and CI carbonaceous chondrites. *Geochimica et Cosmochimica Acta* **69**, 4167–4172.

Alexander C. O., Fogel M., Yabuta H. and Cody Gd. (2007) The origin and evolution of chondrites recorded in the elemental and isotopic compositions of their macromolecular organic matter. *Geochimica et Cosmochimica Acta* **71**, 4380–4403.

Aponte J. C., Tarozo R., Alexandre M. R., Alexander C. M., Charnley S. B., Hallmann C., Summons R. E. and Huang Y. (2014a) Chirality of meteoritic free and IOM-derived monocarboxylic acids and implications for prebiotic organic synthesis. *Geochimica et Cosmochimica Acta* **131**, 1–12.

Aponte J. C., Tarozo R., Alexandre M. R., Alexander C. M. O., Charnley S. B., Hallmann C., Summons R. E. and Huang Y. (2014b) Chirality of meteoritic free and IOM-derived monocarboxylic acids and implications for prebiotic organic synthesis. *Geochimica et Cosmochimica Acta* **131**, 1–12.

Aponte J. C., Woodward H. K., Abreu N. M., Elsila J. E. and Dworkin J. P. (2019) Molecular distribution,$^{13}$ C-isotope, and enantiomeric compositions of carbonaceous chondrite monocarboxylic acids. *Meteorit & Planetary Scien* **54**, 415–430.

Bhattacharjee S. and Eiler J. M. (2025) Constraining oxygen isotope exchange kinetics between organic compounds and water using electrospray ionization Orbitrap mass spectrometry, and implications for the oxygen isotopic compositions of meteoritic organics. *Geochimica et Cosmochimica Acta*.

Bhattacharjee S. and Eiler J. M. (2024) Oxygen isotope equilibria of O-bearing organic compounds based on first principle quantum mechanical models, and implications for their use in the study of extraterrestrial organics. *Geochimica et Cosmochimica Acta* **380**, 96–111.

Chimiak L. and Eiler J. (2024) Prebiotic synthesis on meteorite parent bodies: Insights from hydrogen and carbon isotope models. *Chemical Geology* **644**, 121828.

Choi B.-G., McKeegan K. D., Krot A. N. and Wasson J. T. (1998) Extreme oxygen-isotope compositions in magnetite from unequilibrated ordinary chondrites. *Nature* **392**, 577–579.

Clayton R. N. (2002) Self-shielding in the solar nebula. *Nature* **415**, 860–861.

Clayton R. N., Grossman L. and Mayeda T. K. (1973) A Component of Primitive Nuclear Composition in Carbonaceous Meteorites. *Science* **182**, 485–488.

Clayton R. N. and Mayeda T. K. (1999) Oxygen isotope studies of carbonaceous chondrites. *Geochimica et Cosmochimica Acta* **63**, 2089–2104.

Clayton R. N. and Mayeda T. K. (1984) The oxygen isotope record in Murchison and other carbonaceous chondrites. *Earth and Planetary Science Letters* **67**, 151–161.

Clog M., Lindgren P., Modestou S., McDonald A., Tait A., Donnelly T., Mark D. and Lee M. (2024) Clumped isotope and Δ17O measurements of carbonates in CM carbonaceous chondrites: New insights into parent body thermal and fluid evolution. *Geochimica et Cosmochimica Acta* **369**, 1–16.

Clog M., Stolper D. and Eiler J. M. (2015) Kinetics of CO2(g)–H2O(1) isotopic exchange, including mass 47 isotopologues. *Chemical Geology* **395**, 1–10.

Crocker D. R., Sutherland K. M., Freudenberg B., Alonso K., Pearson A., Ward C. P. and Johnston D. T. (2025) Tracking Photo-Oxidation Reactions of Aquatic Organic Matter Using Triple Oxygen Isotopes. *ACS Earth Space Chem.* **9**, 1780–1790.

Csernica T., Bhattacharjee S. and Eiler J. (2023) Accuracy and precision of ESI-Orbitrap-IRMS observations of hours to tens of hours via reservoir injection. *International Journal of Mass Spectrometry* **490**, 117084.

Eiler J., Cesar J., Chimiak L., Dallas B., Grice K., Griep-Raming J., Juchelka D., Kitchen N., Lloyd M. and Makarov A. (2017) Analysis of molecular isotopic structures at high precision and accuracy by Orbitrap mass spectrometry. *International Journal of Mass Spectrometry* **422**, 126–142.

Ellehoj M. D., Steen-Larsen H. C., Johnsen S. J. and Madsen M. B. (2013) Ice-vapor equilibrium fractionation factor of hydrogen and oxygen isotopes: Experimental investigations and implications for stable water isotope studies. *Rapid Comm Mass Spectrometry* **27**, 2149–2158.

Ellis N. M. and Passey B. H. (2023) A novel method for high-precision triple oxygen isotope analysis of diverse Earth materials using high temperature conversion–methanation–fluorination and isotope ratio mass spectrometry. *Chemical Geology* **635**, 121616.

Foustoukos D. I. and Cody G. D. (2021) H and N systematics in thermally altered chondritic insoluble organic matter: An experimental study. *Geochimica et Cosmochimica Acta* **300**, 44–64.

Fujiya W. (2018) Oxygen isotopic ratios of primordial water in carbonaceous chondrites. *Earth and Planetary Science Letters* **481**, 264–272.

Fujiya W., Sugiura N., Marrocchi Y., Takahata N., Hoppe P., Shirai K., Sano Y. and Hiyagon H. (2015) Comprehensive study of carbon and oxygen isotopic compositions, trace element abundances, and cathodoluminescence intensities of calcite in the Murchison CM chondrite. *Geochimica et Cosmochimica Acta* **161**, 101–117.

Guo W. (2008) *Carbonate clumped isotope thermometry: application to carbonaceous chondrites & effects of kinetic isotope fractionation.*, California Institute of Technology.

Guo W. and Eiler J. M. (2007) Temperatures of aqueous alteration and evidence for methane generation on the parent bodies of the CM chondrites. *Geochimica et Cosmochimica Acta* **71**, 5565–5575.

Hilkert A., Bohlke J. K., Mroczkowski S. J., Fort K. L., Aizikov K., Wang X. T., Kopf S. H. and Neubauer C. (2021) Exploring the potential of electrospray-Orbitrap for stable isotope analysis using nitrate as a model. *Analytical Chemistry* **93**, 9139–9148.

Hofmann A. E., Chimiak L., Dallas B., Griep-Raming J., Juchelka D., Makarov A., Schwieters J. and Eiler J. M. (2020) Using Orbitrap mass spectrometry to assess the isotopic compositions of individual compounds in mixtures. *International Journal of Mass Spectrometry* **457**, 116410.

Hong Y., Zhu L., Crocker D. R., Liu T., Wang Z., Wei Z., Yu C., Wei Y., Yan H., Johnston D. T., Kohl I. E., Peng Y., Hilkert A., Neubauer C. and Hattori S. (2025) Triple Oxygen Isotope Analysis of Methanesulfonate Using the SO3– Fragment in ESI-Orbitrap-MS. *Anal. Chem.* **97**, 14339–14348.

Huang Y., Wang Y., Alexandre M. R., Lee T., Rose-Petruck C., Fuller M. and Pizzarello S. (2005) Molecular and compound-specific isotopic characterization of monocarboxylic acids in carbonaceous meteorites. *Geochimica et Cosmochimica Acta* **69**, 1073–1084.

Kuga M., Marty B., Marrocchi Y. and Tissandier L. (2015) Synthesis of refractory organic matter in the ionized gas phase of the solar nebula. *Proceedings of the National Academy of Sciences* **112**, 7129–7134.

Lawrence W. M., Blake G. A. and Eiler J. (2025) Carbon and oxygen isotope evidence for a protoplanetary disk origin of organic solids in meteorites. *Proc. Natl. Acad. Sci. U.S.A.* **122**, e2423345122.

Lee M. R., Alexander C. M. O., Bischoff A., Brearley A. J., Dobrică E., Fujiya W., Le Guillou C., King A. J., Van Kooten E., Krot A. N., Leitner J., Marrocchi Y., Patzek M., Petaev M. I., Piani L., Pravdivtseva O., Remusat L., Telus M., Tsuchiyama A. and Vacher L. G. (2025) Low-Temperature Aqueous Alteration of Chondrites. *Space Sci Rev* **221**, 11.

Lyons J. R. and Young E. D. (2005) CO self-shielding as the origin of oxygen isotope anomalies in the early solar nebula. *Nature* **435**, 317–320.

McKeegan K. D., Kallio A. P. A., Heber V. S., Jarzebinski G., Mao P. H., Coath C. D., Kunihiro T., Wiens R. C., Nordholt J. E., Moses R. W., Reisenfeld D. B., Jurewicz A. J. G. and Burnett D. S. (2011) The Oxygen Isotopic Composition of the Sun Inferred from Captured Solar Wind. *Science* **332**, 1528–1532.

McKeegan K. D. and Leshin L. A. (2001) Stable isotope variations in extraterrestrial materials. *Reviews in Mineralogy and Geochemistry* **43**, 279–318.

Mimura K., Yamada R., Maejima N., Kawamura K., Kunwar B. and Hashiguchi M. (2024) Analysis of Monocarboxylic Acids in the Murchison Meteorite by Sequential Extraction. *ACS Earth Space Chem.* **8**, 1313–1323.

Mueller E. P. (2024) Carbon Currencies: Isotopic Constraints on the Biogeochemistry of Organic Acids. phd, California Institute of Technology.

Mueller E. P., Panehal J., Meshoulam A., Song M., Hansen C. T., Warr O., Boettger J., Heuer V. B., Bach W. and Hinrichs K.-U. (2024) Isotopic evidence of acetate turnover in Precambrian continental fracture fluids. *Nature Communications* **15**, 9130.

Mueller E. P., Sessions A. L., Sauer P. E., Weiss G. M. and Eiler J. M. (2021) Simultaneous, high-precision measurements of δ2H and δ13C in nanomole quantities of acetate using electrospray ionization-quadrupole-Orbitrap mass spectrometry. *Analytical Chemistry* **94**, 1092–1100.

Rapin W., Dromart G., Clark B. C., Schieber J., Kite E. S., Kah L. C., Thompson L. M., Gasnault O., Lasue J. and Meslin P.-Y. (2023) Sustained wet–dry cycling on early Mars. *Nature* **620**, 299–302.

Sakamoto N., Seto Y., Itoh S., Kuramoto K., Fujino K., Nagashima K., Krot A. N. and Yurimoto H. (2007) Remnants of the early solar system water enriched in heavy oxygen isotopes. *Science* **317**, 231–233.

Schauble E. A. and Young E. D. (2021) Mass dependence of equilibrium oxygen isotope fractionation in carbonate, nitrate, oxide, perchlorate, phosphate, silicate, and sulfate minerals. *Reviews in Mineralogy and Geochemistry* **86**, 137–178.

Suttle M. D., King A. J., Schofield P. F., Bates H. and Russell S. S. (2021) The aqueous alteration of CM chondrites, a review. *Geochimica et Cosmochimica Acta* **299**, 219–256.

Tartèse R., Chaussidon M., Gurenko A., Delarue F. and Robert F. (2018) Insights into the origin of carbonaceous chondrite organics from their triple oxygen isotope composition. *Proceedings of the National Academy of Sciences* **115**, 8535–8540.

Vacher L. G., Marrocchi Y., Verdier-Paoletti M. J., Villeneuve J. and Gounelle M. (2016) Inward radial mixing of interstellar water ices in the solar protoplanetary disk. *The Astrophysical journal letters* **827**, L1.

Verdier-Paoletti M. J., Marrocchi Y., Avice G., Roskosz M., Gurenko A. and Gounelle M. (2017) Oxygen isotope constraints on the alteration temperatures of CM chondrites. *Earth and Planetary Science Letters* **458**, 273–281.

Yuen G., Blair N., Des Marais D. J. and Chang S. (1984) Carbon isotope composition of low molecular weight hydrocarbons and monocarboxylic acids from Murchison meteorite. *Nature* **307**, 252–254.

Zeichner S. S., Aponte J. C., Bhattacharjee S., Dong G., Hofmann A. E., Dworkin J. P., Glavin D. P., Elsila J. E., Graham H. V., Naraoka H., Takano Y., Tachibana S., Karp A. T., Grice K., Holman A. I., Freeman K. H., Yurimoto H., Nakamura T., Noguchi T., Okazaki R., Yabuta H., Sakamoto K., Yada T., Nishimura M., Nakato A., Miyazaki A., Yogata K., Abe M., Okada T., Usui T., Yoshikawa M., Saiki T., Tanaka Satoshi, Terui F., Nakazawa S., Watanabe S., Tsuda Y., Hamase K., Fukushima K., Aoki D., Hashiguchi M., Mita H., Chikaraishi Y., Ohkouchi N., Ogawa N. O., Sakai S., Parker E. T., McLain H. L., Orthous-Daunay F.-R., Vuitton V., Wolters C., Schmitt-Kopplin P., Hertkorn N., Thissen R., Ruf A., Isa J., Oba Y., Koga T., Yoshimura T., Araoka D., Sugahara H., Furusho A., Furukawa Y., Aoki J., Kano K., Nomura S. M., Sasaki K., Sato H., Yoshikawa T., Tanaka Satoru, Morita M., Onose M., Kabashima F., Fujishima K., Yamazaki T., Kimura Y. and Eiler J. M. (2023) Polycyclic aromatic hydrocarbons in samples of Ryugu formed in the interstellar medium. *Science* **382**, 1411–1416.

Zeichner S. S., Wilkes E. B., Hofmann A. E., Chimiak L., Sessions A. L., Makarov A. and Eiler J. M. (2022) Methods and limitations of stable isotope measurements via direct elution of chromatographic peaks using gas chromotography-Orbitrap mass spectrometry. *International Journal of Mass Spectrometry* **477**, 116848.

# PART II

## WATER-ROCK CYCLES ON MARS

## Chapter 5

# EQUILIBRIUM CARBON, MAGNESIUM AND POSITION-SPECIFIC OXYGEN ISOTOPE FRACTIONATIONS IN THE MAGNESIUM CARBONATE – WATER – CARBON DIOXIDE SYSTEM BASED ON QUANTUM MECHANICAL CALCULATIONS AND LABORATORY PRECIPITATION EXPERIMENTS

Surjyendu Bhattacharjee[1], Avni S. Patel[2], Jie Cheng[2], Maija J. Raudsepp[2], Sasha Wilson[2], William A. Goddard III[3,4], Paul D. Asimow[1] and John M. Eiler[1]

[1]Division of Geological and Planetary Sciences, California Institute of Technology, 1200 E. California Blvd., Pasadena, California 91125, USA

[2]Department of Earth and Atmospheric Sciences, University of Alberta, 116 St & 85 Ave., Edmonton, AB T6G 2R3, CA

[3]Division of Chemistry and Chemical Engineering, California Institute of Technology, 1200 E. California Blvd., Pasadena, California 91125, USA

[4]Materials and Process Simulation Center, California Institute of Technology, 1200 E. California Blvd., Pasadena, California 91125, USA

*Corresponding Author: sbhattac@caltech.edu

Bhattacharjee S., Patel A., Cheng J., Raudsepp M., Wilson S., Goddard W., Asimow P. and Eiler J. M. (2025). Constraining oxygen isotope exchange kinetics between organic compounds and water using electrospray ionization Orbitrap mass spectrometry, and implications for the oxygen isotopic compositions of meteoritic organics. Geochimica et Cosmochimica Acta.

## Abstract

Mg-carbonate minerals form in and help constrain our understanding of low-temperature surface processes in terrestrial environments and on Mars and the parent bodies of some primitive meteorites. Knowledge of isotopic fractionations among Mg-carbonates, water, and $CO_2$ can contribute to interpretation of the environmental significance of natural magnesium carbonate minerals, but we presently lack a comprehensive body of experimentally calibrated fractionations among these phases. In this study, we use quantum mechanics (density functional theory) to evaluate equilibrium mineral-fluid fractionation factors for C, O, and Mg isotopes, including selected site-specific fractionations, for a series of hydrous and anhydrous Mg-carbonate minerals and amorphous magnesium carbonate (AMC). We also revisit the existing calibrations for the temperature-dependent abundance of multiply-substituted ('clumped') species for hydrous Mg-carbonates. Because magnesite (anhydrous $MgCO_3$) precipitation is kinetically hindered under laboratory conditions in the temperature range of interest, we use measurements of the isotope effects associated with AMC precipitation to assess the accuracy of our calculations. Using these fractionation factors, we predict $^{26}Mg/^{24}Mg$ of magnesite detected on Mars. These results can be used to investigate the formation of Mg-carbonates and the compositions of their coexisting fluids in numerous natural settings.

## 5.1 Introduction

Magnesite ($MgCO_3$) is a carbonate mineral found in numerous natural terrestrial settings (del Real et al., 2016; Scheller et al., 2021; Swindle et al., 2025). Because of its potential to preserve information about the conditions of its formation, it is an important archive for paleoenvironmental studies, especially in environments with elevated pH, Mg-saturated and Ca-depleted solutions, and evaporative conditions. In laboratory experiments, precipitation of magnesite from low-temperature aqueous solutions is suggested to occur through dissolution-reprecipitation of precursor minerals like amorphous magnesium carbonate (AMC), nesquehonite ($MgCO_3 \cdot 3H_2O$) (Stephan and MacGillavry, 1972), and hydromagnesite [$Mg_5(CO_3)_4(OH)_2 \cdot 4H_2O$] (Tanaka et al., 2019), facilitated by temperature–pH cycling (Hobbs and Xu, 2020) and elevated relative humidity (Patel et al., 2024). In natural terrestrial environments, magnesite forms in playas and lakes at low temperature under evaporative conditions (Zedef et al., 2000; Power et al., 2019; Lin et al., 2023; Raudsepp et al., 2023); potentially from an amorphous precursor by a non-classical crystallization pathway (Raudsepp et al., 2022, 2024). It also is found as veins and stockworks in listvenites and weathered serpentinite horizons (Oskierski et al., 2013; Falk and Kelemen, 2015; Quesnel et al., 2016; Azer et al., 2019; de Obeso et al., 2021), where arguably it may be a high temperature product of hydrothermal alteration or a low temperature product of meteoric water infiltration and weathering. Magnesite in the Martian meteorite ALH84001 was also shown to have formed in a low temperature evaporative condition (e.g., Valley et al., 1997; Leshin et al., 1998; Mcsween Jr & Harvey, 1998; Warren, 1998; Eiler et al., 2002; Halevy et al., 2011). Finally, magnesite has been detected on the Martian surface from orbital remote sensing (Ehlmann et al., 2008) and by the Mars 2020 Perseverance rover (Farley et al., 2022), where it is associated with an olivine–pyroxene assemblage and has been attributed to aqueous alteration and serpentinization (Scheller et al., 2022; Steele et al., 2022). Occurrences of 'breunnerite' (Fe–bearing magnesite) have been reported from aqueously altered carbonaceous chondrites such as CM2 QUE 93005 (Lee et al., 2012), CM2 LON 94101 (Lindgren et al., 2013), CI Orgueil (Hoppe et al., 2007), CH/CB Isheyevo (Bonal et al., 2010), C2-ungrouped Tagish lake (Grady et al., 2002; Guo, 2008; Fujiya et al., 2013) and asteroids such as Ryugu and Bennu (Kaplan et al., 2020; Yoshimura et al., 2024). This material usually forms at a late stage of aqueous alteration of carbonaceous chondrites on asteroidal parent bodies (Fujiya et al., 2013), and its isotopic relationship with other phases is a valuable proxy to alteration processes in asteroidal parent bodies (Alexander et al., 2015; Bhattacharjee and Eiler, 2025).

A major limitation in the study of magnesite and its formation environments is the lack of experimentally derived $^{13}C/^{12}C$ and $^{18}O/^{16}O$ fractionation factors in the magnesite–$H_2O$–$CO_2$ system. Estimates of these fractionation factors have been reported in the literature based on empirical, semi-empirical, or theoretical calculations (see section 4.3 for detailed discussion) but none are experimentally verified, since low temperature (<40°C) equilibrium precipitation of magnesite in the laboratory is kinetically inhibited (and, to-date, never achieved except using compounds such as carboxylated microspheres to overcome the dehydration barrier of hydrated $Mg^{2+}$ ions; Power et al., 2017). The existing estimates for $^{13}C/^{12}C$ and $^{18}O/^{16}O$ fractionation factors between magnesite and $CO_2$ or $H_2O$, respectively, span a range of ~8 ‰ at constant temperature. Furthermore, little is known about C–O–Mg isotope fractionations involving hydrous Mg-carbonates (e.g., AMC, nesquehonite, dypingite [$Mg_5(CO_3)_4(OH)_2$•$5H_2O$], lansfordite ($MgCO_3$•$5H_2O$), hydromagnesite) — thought to be important precursors for magnesite formation in some natural environments.

In this study, we used the density functional theory (DFT) and molecular dynamics (DFT–MD) description of quantum mechanics (QM) to numerically simulate the structures, vibrational dynamics, and isotopic ($^{13}C/^{12}C$, $^{18}O/^{16}O$ and $^{26}Mg/^{24}Mg$) fractionation behavior in the carbonate – water – $CO_2$ system, including position-specific isotope effects and multiple substitutions. We consider amorphous magnesium carbonate (AMC), nesquehonite, lansfordite, hydromagnesite, magnesite, ikaite and aqueous fluids, as well as dolomite — a structurally and chemically similar phase that is relatively well studied. The calculations are benchmarked against the experimentally constrained fractionation factors involving dolomite and new measurements of isotopic fractionation and isotopic clumping in synthetic AMC samples. Using these fractionation factors, we predict $^{26}Mg/^{24}Mg$ of magnesite detected on Mars for various formation scenarios.

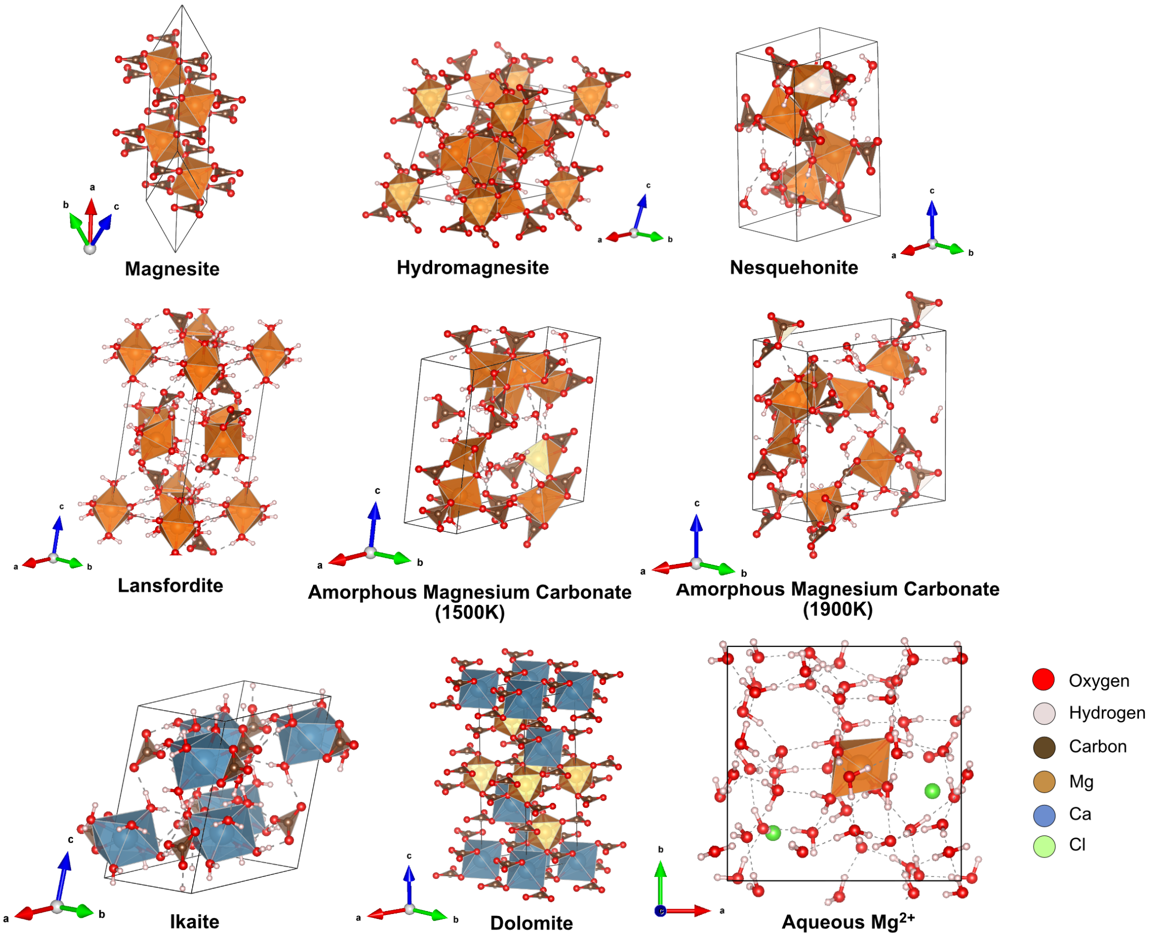

Figure 5.1: Structures of carbonate minerals and aqueous species used for fractionation factor calculations.

## 5.2 Methods

### 5.2.1 Reduced Partition Function Ratio Calculation

The equation for calculation of the partition function ratio (PFR) for minerals in the model of Bigeleisen & Mayer (1947) (hereafter, BM Model), using the harmonic approximation, is given as (see equation 11 of Chacko et al., 2001):

$$\frac{Q'}{Q} = \prod_{i=1}^{3n} \left\{ \frac{\exp(-0.5U_i')}{\exp(-0.5U_i)} \, \frac{[1 - \exp(-U_i)]}{[1 - \exp(-U_i')]} \right\} \qquad (1)$$

where $Q$ = Partition function for one isotopologue; ($Q'/Q$) = partition function ratio (PFR); $3n$ = total number of vibrational modes in a system with $n$ atoms in the unit cell (for linear and non-linear molecules, this is replaced by 3*n*-5 and 3*n*-6 which are the number of vibrational modes in those systems, respectively); and $U_i = (h\nu_i/k_BT)$, where $h$ = Planck constant, $\nu_i$ = vibrational frequency of a mode, $k_B$ = Boltzmann constant, and $T$ = temperature at which the PFR is calculated. Primed symbols indicate corresponding properties of heavy isotope substituted species.

Fractionations are conceptualized as enrichment of ratio of heavy to light isotopes in the compound of interest relative to an isolated gas atom (β-factor or RPFR) (Chacko et al., 2001):

$$^{x}\beta = \left[\left(\frac{Q'}{Q}\right)\left(\frac{m}{m'}\right)^{\frac{3r}{2}}\right]^{\frac{1}{r}} \tag{2}$$

where $x$ denotes the corresponding heavy isotope for which the RPFR is calculated (e.g., $x$ = 13, 17, 18, 26 for $^{13}$C, $^{17}$O, $^{18}$O and $^{26}$Mg respectively), $m$ = mass of the isotope, and $r$ denotes the number of atoms substituted with a heavy isotope. From the high temperature product rule (Chacko et al., 2001 and references therein), we know:

$$\prod_{i=1}^{3n}\left(\frac{\nu_i}{\nu'_i}\right)^{g_i} = \left(\frac{m'}{m}\right)^{\frac{3r}{2}} \tag{3}$$

where $g_i$ = degeneracy of a vibrational mode. Substituting this expression into equation (2), we get the equation for RPFR of minerals in the high temperature approximation, which was used to calculate RPFRs in this study:

$$^{x}\beta = \left[\left(\frac{Q'}{Q}\right)\prod_{i=1}^{3n}\left(\frac{\nu_i}{\nu'_i}\right)^{g_i}\right]^{\frac{1}{r}} = \left[\prod_{i=1}^{3n}\left\{\left(\frac{\nu_i}{\nu'_i}\right)^{g_i}\frac{exp(-0.5U'_i)}{exp(-0.5U_i)}\,\frac{[1-exp(-U_i)]}{[1-exp(-U'_i)]}\right\}\right]^{\frac{1}{r}} \tag{4}$$

The isotopic fractionation factor (α) between two compounds A and B is defined as:

$$^{x}\alpha_{\mathrm{A-B}} = \frac{^{x}\beta_{\mathrm{A}}}{^{x}\beta_{\mathrm{B}}}. \tag{5}$$

The mass law for triple oxygen fractionation between an oxygen atom in compound A and an isolated oxygen atom is defined as $k_{A-atom}$ (equation from Cao and Liu, 2011):

$$k_{\mathrm{A-atom}} = \frac{\ln(^{17}\beta_{\mathrm{A}})}{\ln(^{18}\beta_{\mathrm{A}})} \tag{6}$$

and the mass law for triple isotope fractionation between two compounds A and B is

$$\theta_{\mathrm{A-B}} = \frac{\ln(^{17}\alpha_{\mathrm{A-B}})}{\ln(^{18}\alpha_{\mathrm{A-B}})}. \tag{7}$$

### 5.2.2 Computational Details and Settings

#### 5.2.2.1 Model of AMC and crystalline carbonates

Starting estimates of crystal structures of dolomite [$CaMg(CO_3)_2$], ikaite ($CaCO_3{\bullet}6H_2O$), magnesite ($MgCO_3$), hydromagnesite [$Mg_5(CO_3)_4(OH)_2{\bullet}4H_2O$], lansfordite ($MgCO_3{\bullet}5H_2O$) and nesquehonite ($MgCO_3{\bullet}3H_2O$) are taken from the American Mineralogist Crystal Structure Database (https://rruff.geo.arizona.edu/AMS/amcsd.php) (Downs and Hall-Wallace, 2003). Experimental crystal structures and unit cell parameters of these carbonates in the database are sourced as follows: dolomite = Steinfink and Sans (1959); ikaite = Hesse et al. (1983); magnesite = Ross (1997); hydromagnesite = Akao & Iwai (1977); lansfordite = Liu et al. (1990), nesquehonite = Stephan & MacGillavry (1972). These structures were optimized with the London dispersion-corrected (Grimme et al., 2010) Perdew-Burke-Ernzerhof functional (Perdew et al., 1996) (PBE-D3) level of DFT and the Projector Augmented Wave (PAW) (Blöchl, 1994) with pseudopotentials method (Kresse and Joubert, 1999). An energy cutoff of 500 eV was used along with a 3x3x3 Monkhorst–Pack k–point mesh (Monkhorst and Pack, 1976) to sample the Brillouin zone. Carbonate mineral structures (***Fig 5.1***) were relaxed, allowing cell dimensions, shape and size to change freely until total free energy of the system met a strict convergence criterion for self-consistent field (SCF) energy ($10^{-7}$ eV) and atomic forces were converged to <0.001 eV/Å.

We simulated AMC with QM based molecular dynamics (DFT–MD) using the Vienna *Ab initio* Simulation Package (VASP) (Kresse and Furthmüller, 1996; Hafner, 2008). The Brillouin zone was sampled with a 1x1x2 k–point grid. We applied a London dispersion-corrected (Grimme et al., 2010) Perdew-Burke-Ernzerhof functional (Perdew et al., 1996) (PBE-D3), the Projector Augmented Wave (PAW) method (Blöchl, 1994), an energy cutoff of 500 eV, a step size of 1 fs, and a Nosé-Hoover thermostat (for NVT ensembles) or a Langevin thermostat (for NPT ensembles). We began with the structure of nesquehonite given by the American Mineralogist Crystal Structure Database; one water was removed from each $MgCO_3$ unit to obtain a structure corresponding to $MgCO_3{\bullet}2H_2O$ (to match with structural formula of synthesized AMC, which – based on thermogravimetric analysis – contains two moles of water per formula unit, see section 2.3.1 and the supplementary material). This structure was relaxed at 0 K, allowing cell shape, dimensions and volume to vary freely. The resulting structure was then subjected to a progressive stepwise heating - quenching schedule as outlined in Table 5.1. The unit cell was subjected to heating and equilibration up to 300 K to get the equilibrium crystal structure and atomic velocities (steps 1 to 6, Table 5.1). Next, a 2x1x1 supercell was again relaxed, allowing cell shape, dimensions and volume to vary freely (step 7, Table 5.1). The resulting structure was heated to 1500 K, quenched to 298 K and equilibrated as outlined in steps 8-13 (Table 5.1), resulting in the final structure we term 'AMC_1500'. For simulating the AMC structure at 1900 K, the sequence was similar except at steps 9 to 11, where it was heated up to 1900 K and quenched to 298 K, yielding the 'AMC_1900' structure. To obtain the vibrational spectra of both simulated AMC structures, we applied the 2PT analysis (Lin et al., 2003) to NVT trajectories of length 22 ps (for AMC_1900) and 19 ps (for AMC_1500). Finally, both of these structures were optimized at PBE–D3 level using the same convergence criteria as for crystalline carbonate minerals.

### 5.2.2.2 Model of Fluid Species

All oxygen isotope fractionations are expressed relative to liquid water. The β-factor of liquid water is calculated following the procedure of Schauble & Young (2021) by multiplying the β-factor of gas phase $H_2O$ by the experimentally-derived vapor pressure isotope effect of water (Horita and Wesolowski, 1994). Water clusters (constructed by including 2 to 6 water molecules in the same cell) overestimate $^{18}\alpha_{\text{liquid – vapor}}$ for water but they predict a triple oxygen isotope fractionation mass law (θ) that compares well with experimental data (Barkan and Luz, 2005). Using the 2 water-cluster predicted θ and the experimental $^{18}\alpha_{\text{liquid – vapor}}$ yields $^{17}\alpha_{\text{liquid – vapor}}$. Then $^{17}\beta_{\text{liquid}}$ is calculated by multiplying $^{17}\beta_{\text{vapor}}$ by $^{17}\alpha_{\text{liquid – vapor}}$. Finally, $k_{\text{liquid water}}$ is calculated from $^{17}\beta_{\text{liquid}}$ and $^{18}\beta_{\text{liquid}}$. The structures of water clusters and their predicted triple oxygen isotope mass law for the vapor pressure isotope effect of water are presented in supplementary material.

$^{13}C/^{12}C$ fractionations in carbonate system is conventionally expressed relative to $CO_2$(g), and we have followed the same practice (Golyshev et al., 1981; Aharon, 1988; Chacko et al., 1991; Romanek et al., 1992; Deines, 2004; Schauble et al., 2006a; Rustad et al., 2008; Horita, 2014; del Real et al., 2016). A conversion of the reported fractionation factors relative to dissolved $CO_2$ or $CO_2$(aq) can be easily done using $CO_2$(aq) - $CO_2$(g) $^{13}C/^{12}C$ fractionations of (Vogel et al., 1970).Starting structures of $H_2O$ and $CO_2$ were modified after Bhattacharjee and Eiler (2024). These structures were optimized as isolated molecules in enlarged cells to minimize intermolecular interactions to aptly model them as gas phase molecules.

$^{26}Mg/^{24}Mg$ fractionation in the carbonate-fluid system is expressed relative to aqueous $Mg^{2+}$ or $Mg(H_2O)_6^{2+}$. The potential energy surface of aqueous $Mg^{2+}$ is extremely complex. Therefore, to determine the RPFR of aqueous $Mg^{2+}$, it is recommended to calculate a series of RPFRs based on multiple configurations extracted from an MD simulations to obtain a reliable average value (Rustad et al., 2010). The best treatment of the solvated aqueous $Mg^{2+}$ system is found in Wang et al. (2019) who simulated the structure of aqueous $Mg^{2+}$ with up to 70 water molecules using DFT–MD. They reported that a system with 50 water molecules adequately describe the solvation of aqueous $Mg^{2+}$. We have taken their structure of aqueous $Mg^{2+}$ solvated by 50 water molecules ($Mg[H_2O]_{50}{}^{2+}$) and optimized it at PBE-D3 level. Subsequently, we calculated aqueous $Mg^{2+}$ RPFRs following snapshot method (Wang et al., 2019). From a 26 ps DFT–MD trajectory (performed with 1 fs time step), we extracted $Mg[H_2O]_{50}{}^{2+}$ structures (snapshots) at 1 ps interval from 5 ps onwards (first 5 ps were allowed for the system to equilibrate). Each snapshot was optimized at PBE-D3 level, and vibrational frequencies were calculated for the entire system (Wang et al., 2019) as well as inner $Mg^{2+}$ solvation shell (Domagal-Goldman and Kubicki, 2008; Rustad et al., 2010; Gao et al., 2018).

### 5.2.2.3 Vibrational Frequency Calculation

Harmonic vibrational frequencies of optimized structures were calculated in VASP, using a 3x3x3 Monkhorst-Pack k-point mesh (Monkhorst and Pack, 1976) (for Brillouin zone integration), the PBE-D3 functional, and the Projector Augmented Wave (PAW) (Blöchl, 1994) with pseudopotentials method (Kresse and Joubert, 1999). Phonon modes were calculated for the optimized structures by the Finite Difference (FD) method. For reduced partition function ratio (RPFR) calculations, substituting all atoms of an element by a heavy isotope in a cell (all-substitution approach) can cause an anomalous triple isotope fractionation mass law, whereas substituting one atom at a time can be time consuming, and some substitutions can lead to symmetry-breaking, yielding an inaccurate reduced partition function ratio (□-factor) (see supplementary material for details). Incorporation of water of hydration in Mg-carbonates results in originally equivalent C and O sites to exhibit non-equivalent effects at the microscopic bonding scales and in DFT calculations. Additionally, we cannot calculate position specific isotope effects using the all-substitution approach.

To ameliorate these issues, we used a 'Selective Dynamics' function to calculate position-specific equilibrium isotope effects. 'Selective Dynamics' is a means to sample all different bonding environments in a crystal structure, one at a time. Using selective dynamics on a bonding environment (e.g., one carbonate group or water molecule in hydrated carbonate structure), one atom at a time was substituted by heavier isotopes for all C and O in that bonding environment for vibrational frequency calculation. We repeated this process multiple times until all different types of C or O bonding environments in each carbonate mineral cell or AMC were sampled (e.g., multiple carbonate groups or waters of hydration). Ultimately, we expressed fractionations for a specific bonding environment by averaging RPFRs for all atoms of C or O in that specific bonding environment within a carbonate mineral cell or AMC. For $^{26}$Mg/$^{24}$Mg fractionation, using selective dynamics and sampling each Mg bonding environment is inefficient. Rather, all Mg atoms in a cell could safely be substituted for RPFR calculation. For benchmarking purposes, C and O isotope RPFRs were also determined for magnesite using the conventional Density Functional Perturbation Theory (DFPT) method.

For calculations involving solid materials and minerals, the PBE functional has been the most frequently used in studies of stable isotope fractionation (Schauble et al., 2006; Méheut et al., 2007; Schauble and Young, 2021). Higher levels of theory, such as B3LYP, may be more accurate but are computationally demanding for plane wave calculations using VASP. Density functional perturbation theory (DFPT) has been widely used for calculating vibrational frequencies in minerals (Schauble et al., 2006; Méheut et al., 2007; Schauble, 2011; Schauble and Young, 2021). In the implementation in the version of VASP (version 5.4.4) used in this study, the selective dynamics function is incompatible with DFPT but can be used instead with the Finite Difference (FD) method to model position specific isotope effects efficiently without concerns about cell symmetry or the need to substitute multiple atoms at the same time. To demonstrate this functionality, we calculated $^{13}\beta$, $^{18}\beta$ and $k$ (see section 2.2) for magnesite using both DFPT and FD/selective dynamics for comparison.

Previous studies reported that for large aqueous $Mg^{2+}$ clusters, the high-temperature product approximation can fail (i.e., left- and right-hand terms of equation 3 may not equate), and β-values might not converge to unity at high temperatures. There are two solutions to this problem:

(1) Calculating $^{26}Mg/^{24}Mg$ RPFR from vibrational frequencies of the entire cluster with product of frequency ratios (equation 4) instead of isotopic mass ratio. This ensures convergence of calculated β-values to unity at high temperatures (Domagal-Goldman and Kubicki, 2008).

(2) Calculating $^{26}Mg/^{24}Mg$ RPFR from vibrational frequencies of only the inner solvation shell of aqueous $Mg^{2+}$ clusters (i.e., by fixing outer solvation shell water molecules in their equilibrium positions). In this system, left- and right-hand terms of equation 3 show good agreement (Rustad et al., 2010).

We have calculated aqueous $Mg^{2+}$ RPFRs following both recommendations. For each time snapshot extracted from DFT–MD, we calculated vibrational frequencies for the entire $Mg[H_2O]_{50}{}^{2+}$ cluster as well as $Mg^{2+}$ with fixed outer solvation shell water molecules. RPFRs calculated from those two sets of vibrational frequencies converge to identical values at 298 K (supplementary material, Fig. S5.6).

#### 5.2.2.4 Frequency scaling factor

The Perdew-Burke-Ernzerhof functional (Perdew et al., 1996) systematically underestimates the phonon frequencies. RPFRs calculated using such frequencies using harmonic BM equation can be inaccurate. An empirical correction for this effect is commonly applied (Schauble et al., 2006b; Méheut et al., 2007, 2009; Blanchard et al., 2009; Schauble, 2011; Schauble and Young, 2021) by scaling the phonon frequencies to the fundamental frequencies. Since fundamental frequencies for minerals generally deviate from harmonic frequencies in the same direction as anharmonic zero-point energy correction, but to a greater extent, scaling to fundamental frequencies can cause over-correction of anharmonic zero-point energy (Schauble and Young, 2021). A full anharmonic effect correction for minerals is simply not possible due to their structural complexities. Previous studies have either scaled their phonon frequencies (Schauble et al., 2006b; Méheut et al., 2007, 2009; Blanchard et al., 2009; Schauble, 2011; Schauble and Young, 2021) or avoided scaling (Wang et al., 2017, 2019; Rabin et al., 2023) for RPFR calculation. We report both scaled and unscaled fractionation factors. A scaling factor of 1.0324, derived by comparing modeled frequencies against measured vibrational frequencies (by Raman, infrared and neutron scattering techniques) of isotopically unsubstituted species modeled in this study, is used to scale vibrational frequencies before RPFR calculation, following recommendations of Schauble & Young (2021). We prefer the scaled versions because they compare well to benchmarking (section 3.2). We also present the difference between scaled and unscaled versions of select fractionations in supplementary material. Both scaled and unscaled versions of all reported fractionation factors are reported in the online data repository and supplementary material.

### 5.2.3 Analytical and Experimental Methods

#### 5.2.3.1 Amorphous magnesium carbonate (AMC) Synthesis

Amorphous magnesium carbonate (AMC) was synthesized following a modified version of the procedure from Purgstaller et al. (2019) at University of Alberta. Freshly prepared stock solutions of 250 mM $MgCl_2 \cdot 6H_2O$ (ACS, Sigma Aldrich) and 250 mM $Na_2CO_3$ (ACS, Sigma Aldrich) were made with the same discrete sample of de-ionized water (MilliQ: 18.2 MΩ·cm and 20 ± 0.5 °C). A volume of 25 mL of each stock solution was dispensed into a 50 mL Falcon tube and the temperature of the solutions was equilibrated in a water bath (303 K and 313 K) or in a low-temperature incubator (283 K and 293 K) for at least 30 minutes. The temperature of the water bath, or air within the incubator, was monitored prior to and during synthesis with a Traceable Total-Range Thermometer (Fisherbrand) in addition to using these devices' built–in thermometers. All syntheses were carried out in duplicate.

For water bath syntheses (303 K and 313 K), solutions were mixed by rapidly pouring the 25 mL magnesium chloride solution into the 25 mL sodium carbonate solution, capping the Falcon tube and mixing while holding the Falcon tube in the water bath. Precipitation of AMC was almost instantaneous. Falcon tubes were centrifuged at 7000 rcf (relative centrifugal force) for 4 minutes to separate solids from the liquid phase. The supernatant was poured into a new Falcon tube and filtered through a 0.22 μm syringe filter into 10 mL Labco Exetainer vials with zero headspace in preparation for isotopic analysis. The remaining filtered supernatant was used for pH measurement. The AMC solids were washed with 45 mL of de-ionized water (using the same reservoir of water used for the synthesis; ~294 K) to remove NaCl, centrifuged at 7000 rcf for 2 minutes, and the solution poured off. AMC solids were washed a final time with 100% ethanol, centrifuged at 7000 rcf for 2 minutes and then air dried (~288 K, 3% relative humidity) overnight.

For low-temperature incubator syntheses (283 K and 293 K), 25 mL volumes of each stock were equilibrated in 50 mL Falcon tubes in a Fisherbrand Isotemp BOD Refrigerated Incubator for at least 1 hour. De-ionized water and ethanol used for washing were temperature-equilibrated alongside stock solutions to avoid post synthetic isotopic exchange with water and/or ethanol during washing. Solutions were quickly mixed following the procedure above and then solids were separated by vacuum filtration (0.22 µm filter) in the incubator. The solids were washed in the vacuum filter with 50 mL of Milli-Q water and then 50 mL of 100% ethanol. The temperature of the initial filtrate was measured and then quickly dispensed into 10 mL Labco Exetainer vials with zero headspace in preparation for isotopic analysis. The filtrates from both the 283 K and 293 K syntheses yielded additional precipitation of AMC as the filtrate warmed to room temperature owing to retrograde solubility of carbonate phases. As such, care was taken to record both the synthesis temperature and the final temperature of the supernatant when filtration was complete. AMC samples and water used for synthesis were shipped to Caltech with a desiccant (drierite) to prevent crystallization. The atomic-level structure of AMC was characterized using Fourier-transform infrared (FTIR) spectroscopy at University of Alberta. Amorphous nature of the synthetic AMC samples were confirmed by X-Ray diffraction (XRD) analysis at University of Alberta (see supplementary material).

### 5.2.3.2 Stable and Clumped Isotopic Analysis

Isotopic analysis of AMC and $Na_2CO_3$ at California Institute of Technology used the method described in Ghosh et al. (2006), Guo et al. (2009), Huntington et al. (2009), and Lloyd et al. (2017). Briefly, 10 mg of carbonate powder is digested offline in 15 mL phosphoric acid at 363 K. The evolved $CO_2$ is purified using a dry ice-ethanol slush trap and a dry ice–pentane slush to remove water and $SO_2$, respectively. Clean $CO_2$ is collected in a liquid nitrogen trap, flame sealed in glass tubes, and introduced to a Thermo MAT 253 dual inlet isotope ratio mass spectrometer by way of an automated gas handling and purification system, which removes traces of water and organic compounds by passing the $CO_2$ through dry ice-ethanol traps and a Porapaq resin-packed GC column. After purification, the $CO_2$ is transferred to the dual inlet bellows of the mass spectrometer and measured for masses 44 – 49 using faraday cups, normalized by bracketed observations of a reference working gas (Oztech). Clumped isotope analysis is calculated in the absolute reference frame using measurements of heated and 298 K equilibrated gases (Dennis et al., 2011) and reported on the carbon dioxide equilibrium scale (CDES) of Bonifacie et al. (2017) for AMC samples. CIT Carrara and TV04 standards were analyzed throughout the session to assess reference frame stability through each analytical session. An acid fractionation correction of 0.092 ‰ for $\Delta_{47}$ at 298 K was applied to the standards. An $^{18}O/^{16}O$ acid digestion fractionation factor of 9.42 ‰ (Sharma et al., 2002) is used to correct AMC data. All C and O isotope compositions are reported on VPDB and VSMOW scales respectively.

Oxygen isotope analysis of water used a Picarro L2140i gas isotope analyzer in the Resnick Water and Environment Lab, California Institute of Technology. In-house standards spanning a range in $\delta^{18}O$ were used to construct a working calibration.

### 5.2.3.3 Isotope effect calculation for AMC precipitation

The oxygen isotope effect of AMC precipitation under the conditions of our synthesis experiments was calculated as the difference between $\delta^{18}O$ of AMC and the water collected after synthesis. The carbon isotope effect is calculated using the following mass balance equations:

$$\delta^{13}C_{\mathrm{total}} = (X_{\mathrm{AMC}} \,.\, \delta^{13}C_{\mathrm{AMC}}) + (X_{\mathrm{DIC}} \,.\, \delta^{13}C_{\mathrm{DIC}}), \qquad (8)$$

where $\delta^{13}C_{\mathrm{total}}$ is the C isotopic composition of the bulk system, which equals the $\delta^{13}C$ of starting $Na_2CO_3$ — the only C source used in synthesis, $\delta^{13}C_{\mathrm{AMC}}$ is the measured C isotope composition of AMC, $X_{\mathrm{AMC}}$ is the mass fraction of $Na_2CO_3$ precipitated as AMC, and $X_{\mathrm{DIC}}$ is the mass fraction of $Na_2CO_3$ existing as $X_{\mathrm{DIC}} = (1 - X_{\mathrm{AMC}})$. Equation (8) is solved for $\delta^{13}C_{\mathrm{DIC}}$ and then

$$1000\ln{}^{13}\alpha_{\mathrm{AMC-CO2(g)}} = (\delta^{13}C_{\mathrm{AMC}} - \delta^{13}C_{\mathrm{DIC}}) + \Delta^{13}C_{\mathrm{DIC-CO2(g)}} \qquad (9)$$

where $\Delta^{13}C_{\mathrm{DIC-CO2(g)}}$ is the pH–dependent equilibrium C isotope fractionation between DIC and $CO_2(g)$ (Zeebe and Wolf–Gladrow, 2001; Zeebe, 2010).

## 5.3 Results

### 5.3.1 Structure of AMC and carbonate minerals

The structure of AMC from MD simulations is presented in terms of its radial distribution function (RDF), $g(r)$, which is a measure of both short- and long-range atomic ordering. Relative to the starting structure derived from nesquehonite (see section 2.1.1), both AMC_1500 (Fig 5.2, left pane) and AMC_1900 (Fig 5.2, right pane) show significantly decreased long-range atomic correlation, revealed by loss of periodic long–range structure in their RDF curves. The large peaks at 0.99 Å and 1.29 Å are due to O—H bonds in water and C—O bonds in carbonates, respectively. Furthermore, the partial RDFs for Mg—Mg, Mg—C and Mg—O pairs in both AMC structures show differences from the starting material. This confirms the amorphous nature of the simulated AMC structures. The predicted vibrational bands of the model structures match the FTIR spectrum (Fig 5.3) of synthetic AMC, and the scaling of model spectral frequencies to experimental frequencies are, within error, linear for each material (Fig 5.4). Since both AMC structures show amorphous nature, we focused on AMC_1500 only for RPFR calculations.

Unit cell parameters and volumes calculated in this study for crystalline carbonate minerals are presented in Table 5.2 along with the mean absolute difference (MAD, %) from experimentally determined unit cell dimension, angles, and volume data. MAD for unit cell dimensions ($a$, $b$, $c$), angles ($\alpha$, $\beta$, $\gamma$) and cell volume are 1.21, 0.74, 1.31, 0.18, 0.77, 0.18 and 1.95 %, respectively.

### 5.3.2 Benchmarking Calculations

#### 5.3.2.1 Fractionations in Dolomite – water – $CO_2$(g) and $CO_2$(g) – water system

Predicted $^{13}C/^{12}C$ and $^{18}O/^{16}O$ fractionation factors in the dolomite–water–$CO_2$ system are compared against available experimental data from Horita (2014) and references therein. Within the temperature range of interest, the modeled $^{13}C/^{12}C$ and $^{18}O/^{16}O$ fractionation behavior from this study is within ~2 ‰ (for $^{18}O/^{16}O$) and ~3.5 ‰ (for $^{13}C/^{12}C$) of experimental data (Fig. 5.5a,b). For comparison, dolomite – water $^{18}O$ fractionation factors predicted by Schauble & Young (2021) with harmonic and anharmonic liquid water models are also shown in Fig 5.5a. Our model yields results similar to the model of Schauble &

Young (2021) that incorporated anharmonicity corrections for liquid water, while their model with no such corrections is significantly closer to the experimental data.

$^{18}O/^{16}O$ fractionation between $CO_2$(g) and liquid water has been extensively studied experimentally (Bottinga and Craig, 1968; Brenninkmeijer et al., 1983; Hofmann et al., 2012). Our prediction for $^{18}O/^{16}O$ fractionation in this system is presented in Fig 5.5e, which shows that our prediction is within ~1 ‰ of experimental data.

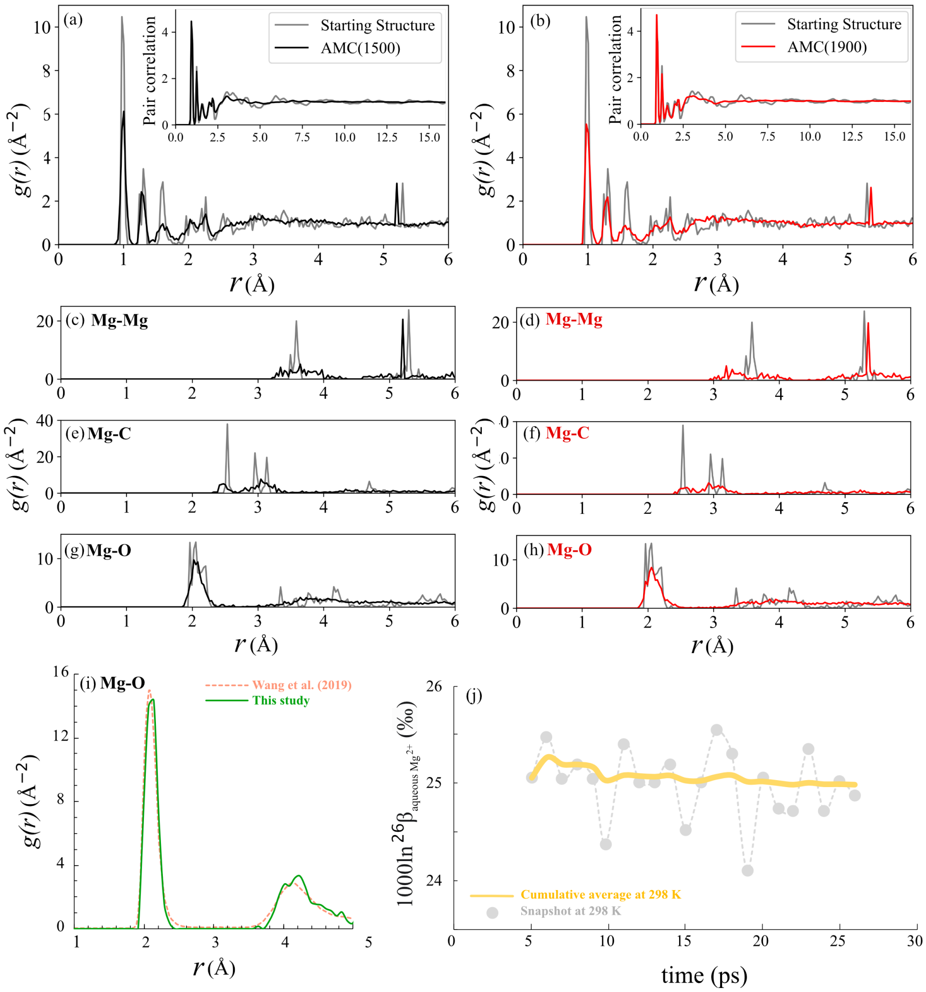

Figure 5.2: Radial distribution functions (RDF) (Inset: Pair correlation function), as well as pairwise Mg–Mg, Mg–C, Mg–O partial RDFs in simulated AMC structures compared with crystalline starting material (gray curves).(a,c,e,g): AMC_1500; (b,d,f,h): AMC_1900. (i) Comparison of Mg–O partial RDF for aqueous $Mg^{2+}$ from this study and Wang et al. (2019). (j) Convergence of $\ln^{26}\beta$ (‰) at 298 K for aqueous $Mg^{2+}$ from snapshot method. Time

averaged cumulative RFFR is shown by thick yellow solid line, whereas gray circles indicate $\ln^{26}\beta$ (‰) at each time point.

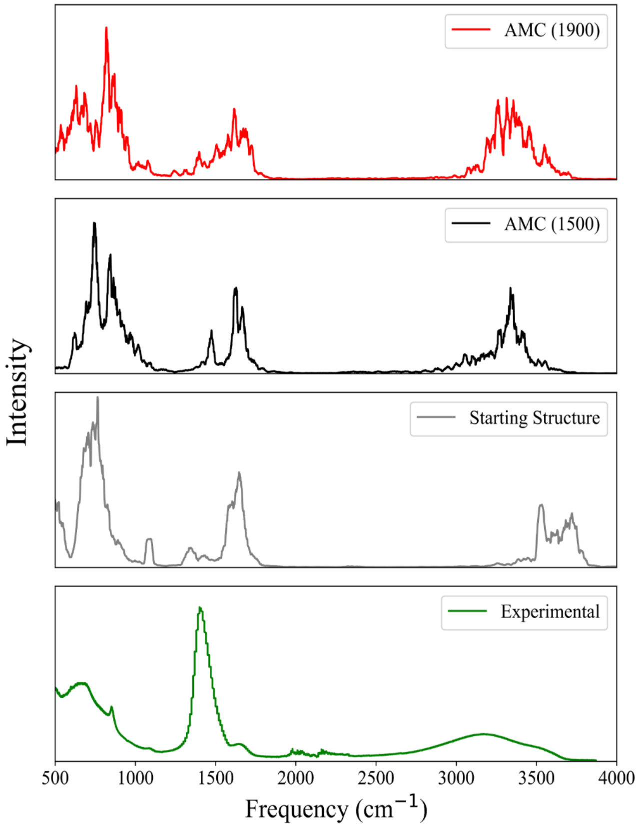

Figure 5.3: Predicted vibrational spectra from 2PT calculations (Lin et al., 2003) of simulated AMC structures and crystalline starting material (before scaling), compared with our experimental Fourier transform infrared (FTIR) spectrum of synthetic AMC.

#### 5.3.2.2 Benchmarking for mass law for triple oxygen isotope fractionation

We examined the accuracy of the modeled triple oxygen isotope fractionation mass law by comparing it to the experimentally determined mass law in the $CO_2$(g) – water system (Hofmann et al., 2012) and the vapor pressure isotope effect of water (Barkan & Luz, 2005). In both cases, predictions are closely consistent with experimental data (Fig. 5.5c,d).

### 5.3.3 Isotope effect during AMC precipitation

Measured stable and clumped isotopic abundances of AMC and parental water are presented in the data repository. AMC concentrated $^{13}C$ relative to the starting $Na_2CO_3$ reagent at all synthesis temperatures. Parental water $\delta^{18}O$ remained virtually the same in AMC syntheses at all temperatures, and $1000\ln^{18}\alpha_{AMC\text{–}water}$ increases monotonically with synthesis temperature; albeit the net magnitude of this increase from 283 K to 313 K is small (~1.9 ‰). The $\Delta_{47ARF}$ of synthetic AMC samples are invariant with temperature, and are conforming to equilibrium for other carbonate minerals, within 2σ of calibration error, except at 283 K.

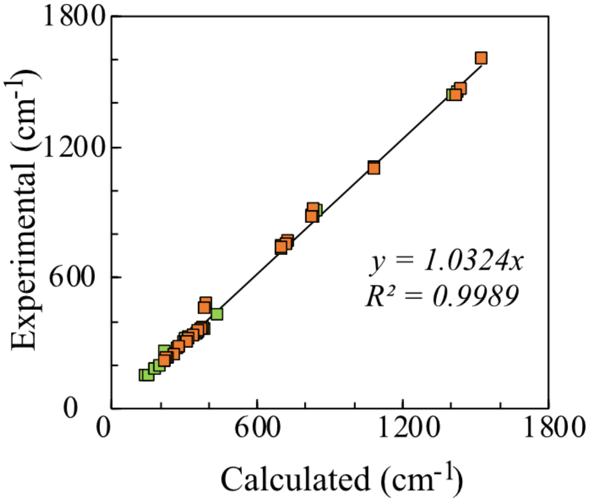

Figure 5.4: Universal scaling factor used in this study, by comparing observed and calculated vibrational frequencies.

### 5.3.4 Isotopic fractionation factors in the carbonate–water–$CO_2$ system

Final predicted equilibrium carbon and oxygen fractionation factors for various carbonate mineral–water pairs are reported in the data repository. At 273 K, the $^{18}O/^{16}O$ fractionation between carbonate and water spans a range of ~37.2 - 43.7 ‰ for different carbonates, and the $^{13}C/^{12}C$ fractionation between carbonate and $CO_2$ spans a range of ~11.6 - 16.4 ‰, which in all cases are larger than the corresponding fractionations in the dolomite – water and dolomite – $CO_2$(g) systems. The temperature–dependence of $^{13}C/^{12}C$ and $^{18}O/^{16}O$ fractionations between minerals and $CO_2$(g) or water are similar. The mass law for triple oxygen isotope fractionation between carbonate-bound oxygen and external water is similar for all carbonates (0.5255 - 0.5258 at 273 K) except lansfordite (0.5235 at 273 K). Oxygen isotope fractionations between structural and external water are variable between different carbonate minerals but the mass law for this fractionation is nearly the same for all minerals considered and similar to the mass law for the vapor pressure isotope effect of water. The Mg isotope fractionation is reported vs. aqueous $Mg^{2+}$, showing variable magnitudes and directions in different carbonate minerals. Hydrated carbonates like nesquehonite and hydromagnesite preferentially incorporate $^{26}$Mg relative to $^{24}$Mg ($\Delta^{26}$Mg$_{\text{carbonate–aqueous Mg}}$ = 0.6 to 1.3 ‰ at 273 K). AMC does not fractionate Mg isotopes relative to aqueous Mg ($\Delta^{26}$Mg$_{\text{carbonate–aqueous Mg}}$ = 0.0 ‰ at 273 K). Magnesite preferentially incorporates $^{24}$Mg ($\Delta^{26}$Mg$_{\text{carbonate–aqueous Mg}}$ = –2.6 ‰ at 273 K). Lansfordite, despite being a hydrous carbonate, also prefers $^{24}$Mg ($\Delta^{26}$Mg$_{\text{carbonate–aqueous–Mg}}$ = –1.4 ‰ at 273 K). The measured clumped isotopic compositions of synthetic AMC are rather insensitive to synthesis temperatures, with average $\Delta_{47\text{CDES}}$ ~0.56±0.2‰; a comparison with temperature-dependent clumped isotopic composition of other carbonate phases is presented in Figure 5.8g.

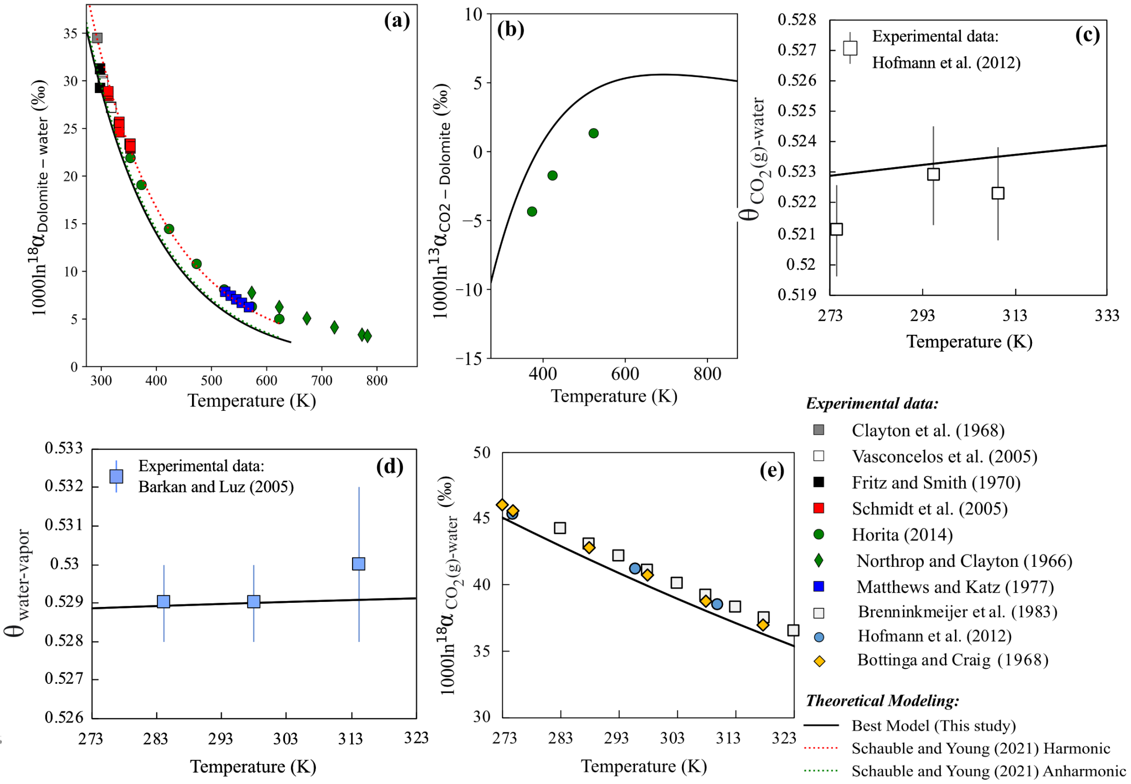

Figure 5.5: Benchmarking calculations. (a) Dolomite–water oxygen isotope fractionation (Experimental data: Northrop and Clayton, 1966; Clayton and Jones, 1968; Fritz and Smith, 1970; Matthews and Katz, 1977; Schmidt et al., 2005; Vasconcelos et al., 2005; Horita, 2014). (b) $CO_2$ – dolomite C isotope fractionation. Experimental data for (a), (b) are from Horita (2014) and references therein. (c) Triple oxygen isotope fractionation mass law for $CO_2$ – water system; experimental data from Hofmann et al. (2012). (d) Triple oxygen isotope fractionation mass law for vapor pressure isotope effect of water; experimental data from Barkan & Luz (2005). (e) $^{18}$O/$^{16}$O fractionation in $CO_2$(g) - water system (Experimental data: Bottinga and Craig, 1968; Brenninkmeijer et al., 1983; Hofmann et al., 2012).

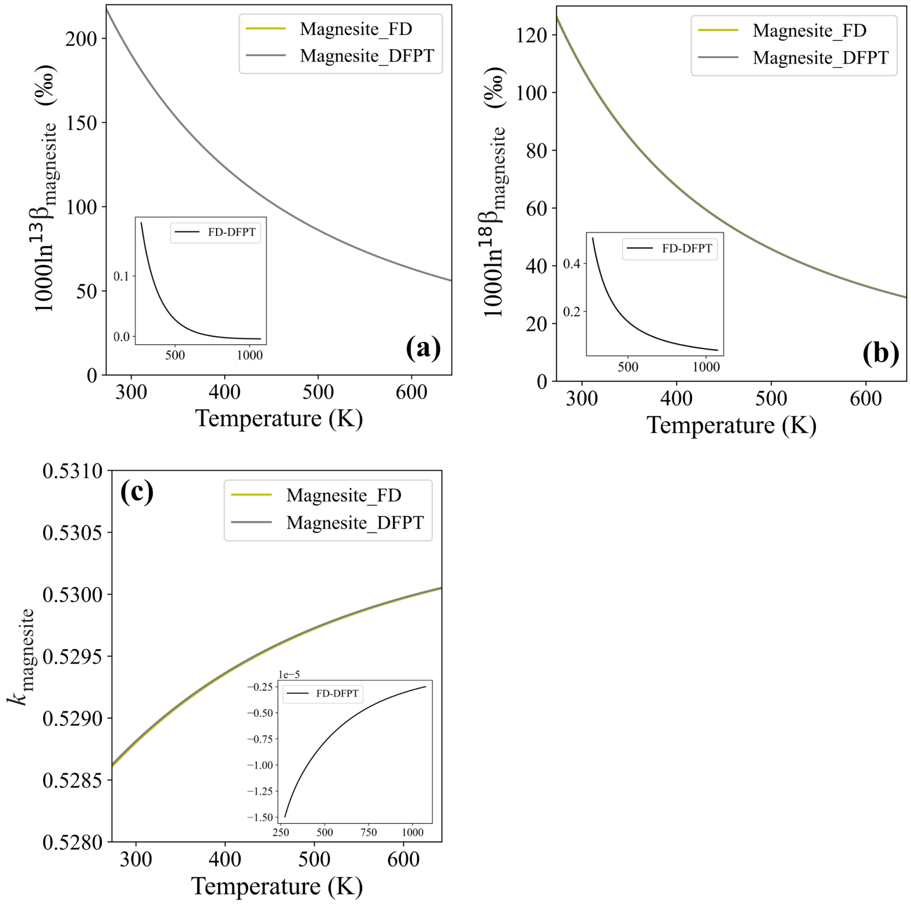

Figure 5.6: Comparison of $^{13}\beta$, $^{18}\beta$, $k$ derived from quantum mechanics using DFPT and FD methods (inset: residuals).

## 5.4 Discussion

### 5.4.1 Factors impacting calculation of RPFRs

The most important source of potential error in our calculations is the choice of vibrational frequency scaling factors, which stems from the limitations of the computational methods used (e.g., DFT functional used, cutoff energy applied). The discussion in Schauble & Young (2021) indicates that uniform or mineral specific scaling factors may be used. However, scaling different species by different scaling factors can also introduce potential non-systematic errors in the predicted RPFRs, which might not cancel out during fractionation factor calculation. In our study, we applied a universal scaling factor of 1.0324 (Fig. 5.4).

The accuracy of this approach is confirmed by our benchmarking of *k* and β (Fig.5. 7) against independent calculations performed using similar or different levels of theory. The scaling factor calculated in this study (1.0324) compares well with that calculated by Schauble et al. (2006) for anhydrous carbonates (1.0331). The effect of scaling is further explored in supplementary material with magnesite-water-$CO_2$ system. At 273 K, the differences between scaled and unscaled fractionation factors are small (~3 ‰, ~1.5 ‰ and ~0.07 ‰ for $^{18}O/^{16}O$, $^{13}C/^{12}C$ and $^{26}Mg/^{24}Mg$ fractionations respectively). The difference between scaled and unscaled $^{18}\alpha_{structural\ -\ external\ water}$ in ikaite is 1.1‰ at 273 K. While we prefer scaled fractionation factors in this study as they compare well with experimental data, all corresponding unscaled fractionation factors are also reported in the online data repository and supplementary material.

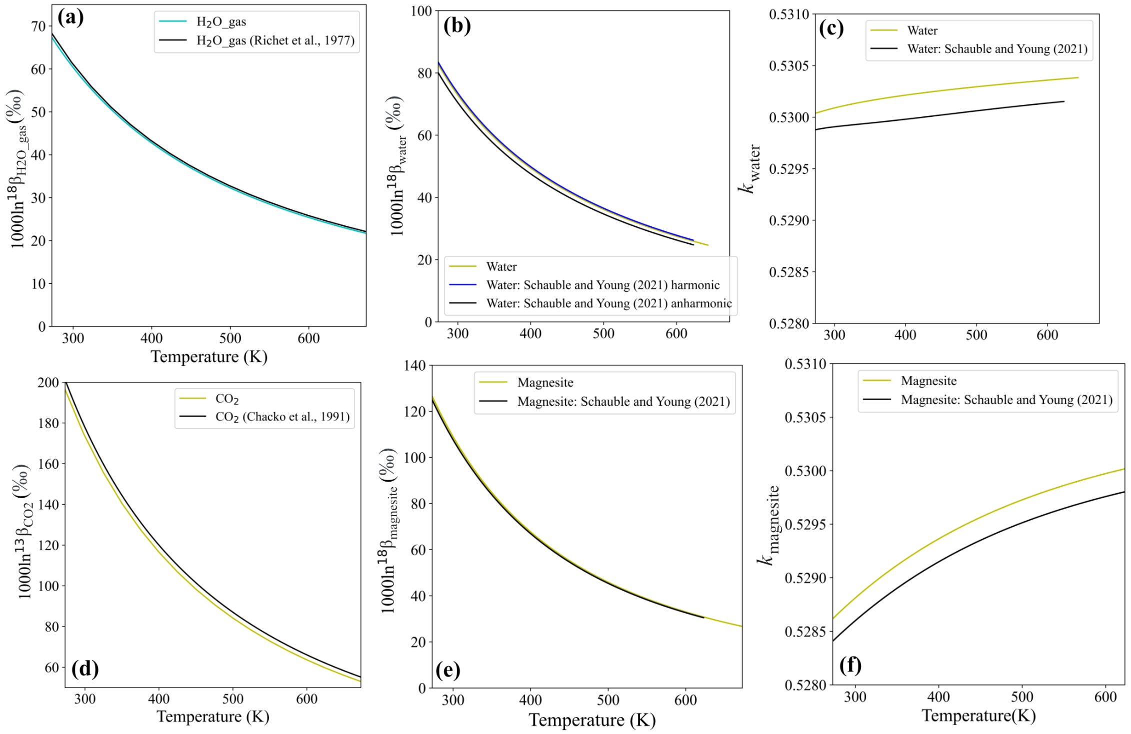

Figure 5.7: Comparison between *k* and β–factors (for minerals, molecules and complexes) calculated from quantum mechanics in this study and those calculated in other studies. $H_2O$ gas $^{18}\beta$: Richet et al. (1977); $CO_2$ gas $^{13}\beta$: Chacko et al. (1991); $^{18}\beta_{magnesite}$, $k_{magnesite}$, $^{18}\beta_{water}$, $k_{water}$: Schauble & Young (2021).

The robustness of calculated RPFRs is further demonstrated by the match of magnesite–water Mg isotope fractionation factors (Fig. 5.8f) and of the triple O isotope exponent compared to experimental data for the vapor pressure isotope effect of water (Fig. 5.5d) (Barkan and Luz, 2005) and triple oxygen isotope fractionation in the $CO_2$–water system (Fig. 5c,e) (Bottinga and Craig, 1968; Brenninkmeijer et al., 1983; Hofmann et al., 2012). Comparison of $^{13}\beta$, $^{18}\beta$ and $k$ for magnesite calculated using both DFPT and FD/selective dynamics approaches demonstrate that they are closely similar (Fig. 5.6), indicating that no systematic difference was introduced by using FD/selective dynamics compared to more conventional DFPT approach.

Explicit corrections for vibrational anharmonicity beyond scaling have not been included in this study. Inclusion of these corrections can cause small (~3 ‰) differences in calculated $1000\ln^{18}\beta$ for water (Schauble and Young, 2021) at 298 K. Our results for water (Fig. 5.7b) resemble the harmonic water model of Schauble & Young (2021). Other effects like nuclear field shift fractionation (Schauble and Young, 2021) and diagonal Born-Oppenheimer corrections (Zhang and Liu, 2018) seem to be small in our temperature range of interest and hence have not been accounted for.

Aqueous $Mg^{2+}$ RPFR is sensitive to the size and configuration of the solvated cluster (Domagal-Goldman and Kubicki, 2008; Rustad et al., 2010; Schauble, 2011; Pinilla et al., 2015; Schott et al., 2016; Gao et al., 2018; Wang et al., 2019). As the best treatment of this system at PBE level is done by Wang et al. (2019), we calculated our aqueous $Mg^{2+}$ RPFRs following their methodology and starting cluster structure. Following initial structural optimization and DFT–MD, our aqueous $Mg^{2+}$ system structurally converged to that of Wang et al. (2019), indicated by the close agreement of the radial distribution function of Mg–O atom pairs (Fig. 5.2i) between two studies. RPFRs calculated by the two approaches described in section 2.2.3 converged to identical values at 298 K (supplementary material, Fig. S6). Additionally, both sets of β-values converged to unity at high temperature. For the fixed outer solvation shell system, left- and right-hand terms of equation 3 agree well (to ~0.1 ‰). We select RPFRs calculated with fixed outer solvation shell system as our preferred model for describing aqueous $Mg^{2+}$ behavior (Fig. 5.2j) as it fulfills all the criteria for calculation robustness laid out in previous studies.

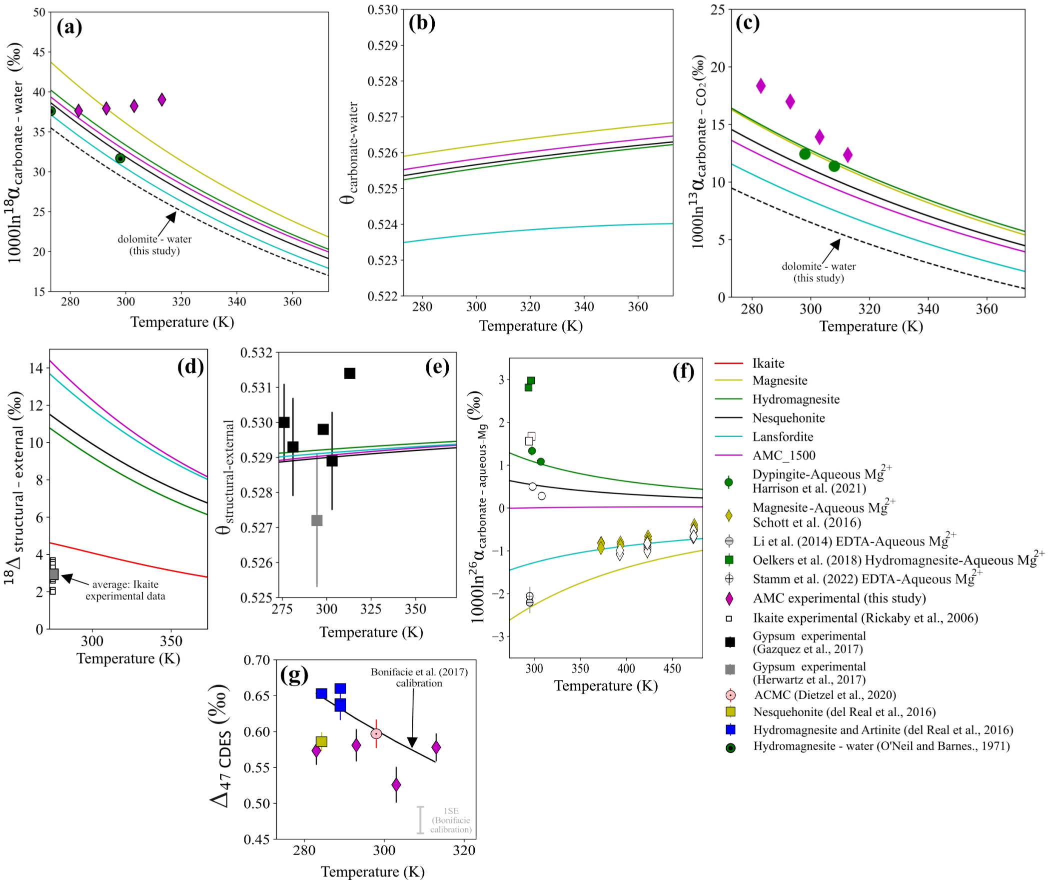

Figure 5.8: Isotope fractionation predictions and comparison with experimental data. (a) Carbonate–water $^{18}O/^{16}O$ fractionation (experimental hydromagnesite–water oxygen isotope fractionation from O'Neil & Barnes, 1971). AMC data is plotted assuming complete resetting of their $\delta^{18}O$ post-precipitation at 288 K. (b) Triple O isotope fractionation mass law for carbonate–water O isotope fractionation. (c) Carbonate–$CO_2$(g) $^{13}C/^{12}C$ fractionation (dypingite–$CO_{2(g)}$ $^{13}C/^{12}C$ fractionation from Harrison et al., 2021). (d) $^{18}O/^{16}O$ fractionation between structurally bound water in hydrous carbonates and water in external environment (experimental $^{18}O/^{16}O$ fractionation between structural water of ikaite and external water; from Rickaby et al., 2006). (e) Triple O isotope fractionation mass law for fractionation in (d) (experimental data in gypsum system from Gázquez et al., 2017; Herwartz et al., 2017). (f) $^{26}Mg/^{24}Mg$ fractionation between carbonate minerals and aqueous $Mg^{2+}$ (experimental data: Li et al., 2014; Schott et al., 2016; Oelkers et al., 2018; Harrison et al., 2021; Stamm et al., 2022). Experimental data are corrected with $^{26}Mg/^{24}Mg$ fractionation factors reported by Schott et al. (2016) (solid symbols) and Gao et al. (2018) (hollow symbols). (g) Clumped isotopic composition ($\Delta_{47}$) of synthetic AMC. Solid line: universal clumped isotope calibration (del Real et al., 2016). Hydromagnesite, artinite, nesquehonite (Dietzel et al., 2020) and amorphous calcium magnesium carbonate (ACMC) (Dietzel et al., 2020) follow the calibration line closely.

### 5.4.2 Structure of AMC

Although the AMC simulated numerically in this study is clearly amorphous, as shown by its RDF and partial atomic correlations (Fig. 5.2), we are limited by computational time from extending our stepwise heating-quenching technique to a larger cell that might give us more robust constraints on its structure and properties. White et al. (2014) numerically simulated AMC ($MgCO_3{\bullet}3D_2O$) by heating a larger system (448 atoms) directly at 1500 K for 10,000 steps of 1 fs each. Such a large system is supposed to undergo randomization to a greater extent. The simulated RDF in that study (their Fig. 4b) was validated against an X–ray scattering based pair distribution function (PDF). The RDF of AMC calculated here agrees well with White et al. (2014), in terms of both position and relative intensity of the correlation peaks, except that this previous study shows a stronger Mg—O bond compared to our study, most likely due to better sampling of the coordination environments in the larger system.

The AMC structure simulated in our study shows that water molecules form extensive hydrogen bonding networks both among themselves and with oxygens from the carbonate units, in addition to coordinating $Mg^{2+}$. This agrees with findings of Jensen et al. (2020), who attributed such behavior to the small ionic radius and coordination number of $Mg^{2+}$. As in their study, $Mg^{2+}$ cations in AMC_1500 and AMC_1900 are present in 4-, 5- and 6-fold co-ordinations, with 6-fold being dominant. Both simulated and synthetic AMC in this study contain OH groups in their structure (see supplementary material), in agreement with findings of Jensen et al. (2018). Mg in both the simulated AMC structures show strong preference for monodentate carbonate ligands, similar to observations of Prange et al. (2023).

The match between experimental FTIR spectra and the theoretical vibrational spectrum confirms that vibrational properties are well represented in the simulated structure, though we have not conducted a group theory analysis to identify which simulated bands might not be IR-active.

The calculated densities of AMC_1500 and AMC_1900 are 1.98 g cm$^{-3}$, 2.04 g cm$^{-3}$, respectively, which compare to 2.05 g cm$^{-3}$ for synthetic amorphous mesoporous magnesium carbonate (Åhlén et al., 2019).

### 5.4.3 Comparison of predicted fractionation factors with previous studies

The scarcity of experimental data in the investigated system makes it challenging to assess accuracy of our predictions, beyond the benchmarking discussed above. Experimentally evaluated $^{18}O/^{16}O$ fractionations between synthetic hydromagnesite and water at 273 K and 298 K (O'Neil and Barnes, 1971) are ~3 ‰ lower than the theoretical prediction presented in this study. $^{13}C/^{12}C$ fractionations established experimentally between dypingite and $CO_2$ at 298 K and 308 K (Harrison et al., 2021) are within ~0.6 ‰ of the predicted hydromagnesite fractionation curve (Fig. 5.8c). Although dypingite is a polytypic and polysomatic variant of hydromagnesite, dypingite is hydrated to a greater extent, which may contribute to differences in fractionation factors between the two phases. We are aware of no other previous experimental report of $^{13}C/^{12}C$ and $^{18}O/^{16}O$ fractionation in the magnesium carbonate – $CO_2$ – water system that can be used for comparison.

In this study, we synthesized AMC at 283, 293, 303 and 313 K to experimentally define the temperature dependence of the equilibrium carbonate–water $^{18}\alpha$ and the clumped isotope composition. We find that for both of these parameters (Figs. 5.8a,g), the experimental results appear to be essentially the same at all temperatures. Lucarelli et al. (2023) also reported a similar behavior of amorphous carbonates precipitated at 283 - 333 K. Yet clumped isotopic composition is known to be temperature sensitive, and it is known that the temperature recorded by the isotopic clumping of amorphous calcium magnesium carbonate precursor is preserved during transformation to Mg-calcite at constant temperature (Dietzel et al., 2020).

One possible explanation of our experimental findings is the presence of kinetic isotope effects (KIE) during the very fast experimental precipitation of AMC. The magnitude of the $^{18}O/^{16}O$ KIE in the calcite–water system in a pH range similar to our study (9.5 - 10.1) at the kinetic limit (Devriendt et al., 2017) is at most 10 ‰ (i.e., calcite is at most 10 ‰ enriched in $^{18}O$ compared to the water) at 313 K, which is much lower than the ~39 ‰ fractionation we observe in the AMC – water system at 313 K, implying that most of the observed fractionation is not simply a KIE.

The other possibility is that some resetting of the $\delta^{18}O$ and $\Delta_{47}$ of our precipitates happened post-synthesis, such as exchange between carbonate-bound and water-bound oxygen atoms. Given the highly hydrous nature of AMC (ratio of carbonate oxygen to hydration oxygen = 3:2) and its lack of crystallinity, this is plausible. This might have occurred during air drying overnight at ~288 K, during shipping, or during storage prior to analysis, and may have been accompanied by dehydration. If we assume that all the analyses reflect complete exchange at 288 K then they plot close to our theoretically predicted fractionation behavior for AMC_1500 at this temperature.

The most likely explanation is that this stems from an isotopic disequilibrium between DIC and water during precipitation. We have equilibrated the pre-precipitation AMC stock solution for 30 mins - 1 hour at respective temperatures of precipitation. This might be inadequate for DIC species and water to reach oxygen and clumped isotope equilibrium. Lucarelli et al. (2023) precipitated amorphous carbonates in disequilibrium and observed a similar effect, where $^{18}\alpha_{\text{AMC-water}}$ and clumped isotopic composition of AMC precipitated at different temperatures (283 - 333 K) remained temperature invariant. We attribute our measured $^{18}\alpha_{\text{AMC-water}}$ and clumped isotopic composition to such a disequilibrium effect that did not allow us achieve equilibrium. In that case, our dataset may not be useful for constraining equilibrium.

Even though these effects cumulatively impacted our AMC analyses, it should be noted that as AMC transforms to crystalline carbonates in solutions, this disequilibrium signature is erased, and the crystalline phases precipitate in near equilibrium conditions at laboratory scale. During further residence in the solution, crystalline phases undergo isotopic exchange with fluid and reach equilibrium (Mavromatis et al., 2017; Dietzel et al., 2020; Harrison et al., 2021; Lucarelli et al., 2023).

Structural water strongly concentrates $^{18}O$ relative to free water (Fig. 5.8d), which is intuitive given the short Mg–$O_{\text{water}}$ bond lengths in hydrous magnesium carbonates. Comparison of modeled ikaite–water $^{18}O$ fractionation with experimental data (Rickaby et al., 2006) shows that our predictions are higher by ~1.5 ‰, suggesting that predictions for hydrated Mg-carbonates are likely off by a similar amount. Predicted mass laws for this fractionation are relatively temperature insensitive, very much like that for the vapor pressure isotope effect of water (Barkan and Luz, 2005). The mass law for $^{18}O/^{16}O$ vs. $^{17}O/^{16}O$ fractionation between lattice and external water of hydrated carbonates has not been experimentally studied, so we compare predictions with experimental data in the gypsum

($CaSO_4 \cdot 2H_2O$) system (Gázquez et al., 2017; Herwartz et al., 2017), finding that they agree well (Fig. 5.8e).

Previous experimental studies have quantified the extent of $^{26}Mg/^{24}Mg$ fractionation in magnesite – aqueous Mg (Pearce et al., 2012; Schott et al., 2016), hydromagnesite – aqueous Mg (Oelkers et al., 2018) and dypingite – aqueous Mg (Harrison et al., 2021) systems over a range of temperatures (298 K to 473 K). In these experiments, the general approach is to measure a fractionation between the solid precipitate and bulk fluid. This measurement is then corrected using knowledge of relative proportions of Mg–bearing complexes in the fluid along with theoretically estimated $^{26}Mg/^{24}Mg$ fractionation factors between these complexes (e.g., Schott et al., 2016; Gao et al., 2018), yielding an estimate of the $^{26}Mg/^{24}Mg$ fractionation between solid and aqueous $Mg^{2+}$ ions. This typically takes the form (modified from Gao et al., 2018):

$$\Delta^{26}Mg_{\text{solid–aqueous } Mg^{2+}} = \Delta^{26}Mg_{\text{solid–bulk fluid}} \text{ (measured)} + \Delta^{26}Mg_{\text{bulk fluid–aqueous } Mg^{2+}} \text{ (calculated)} \quad (10)$$

Gao et al. (2018) modeled the $^{26}Mg/^{24}Mg$ fractionation between different aqueous complexes as large solvated clusters (up to 36 water molecules in a cluster), which is expected to render more accurate estimates compared to the ones proposed by Schott et al. (2016) (up to 18 water molecules in a cluster) by accounting for more of the long–range solvent–solute interactions. We consider corrections to the experimental $^{26}Mg/^{24}Mg$ fractionation data using both Schott et al. (2016) and Gao et al. (2018) (Fig. 5.8f, solid and hollow symbols, respectively). For $^{26}Mg/^{24}Mg$ fractionation between carbonates and aqueous $Mg^{2+}$ ion, our predictions generally are in good agreement with experimental results (Fig. 5.8f). The most significant finding is that hydromagnesite and magnesite have opposite directions of Mg isotope fractionation, which is consistent with Mg isotope data for coexisting hydromagnesite and magnesite in natural settings (Mavromatis et al., 2021).

A number of $^{13}C/^{12}C$ and $^{18}O/^{16}O$ fractionation factors are found in the literature for the magnesite–water–$CO_2$ system (del Real et al., 2016) and a review is presented in Fig. 5.9. For oxygen (Fig. 5.9a), Aharon (1988) proposed fractionation factors based on extrapolation of relationships between fractionation factor and ionic radius for alkaline earth carbonates, including and excluding dolomite. Zheng (1999) proposed fractionations based on a semi-empirical increment method. Both of these methods are semi-empirical and lack theoretical justification. Chacko & Deines (2008) proposed $^{13}C/^{12}C$ and $^{18}O/^{16}O$ fractionations involving magnesite by combining the RPFR of magnesite (derived from experimental vibrational frequencies of carbonate minerals) with the RPFR for liquid water calculated by Rosenbaum (1997). Schauble & Young (2021) predicted fractionation factors using DFT-based RPFR calculations for both magnesite and water, hoping to eliminate systematic errors between experiment and calculation in previous works. The results of our study resemble the magnesite–water fractionation computed by Schauble & Young (2021) using anharmonic water model.

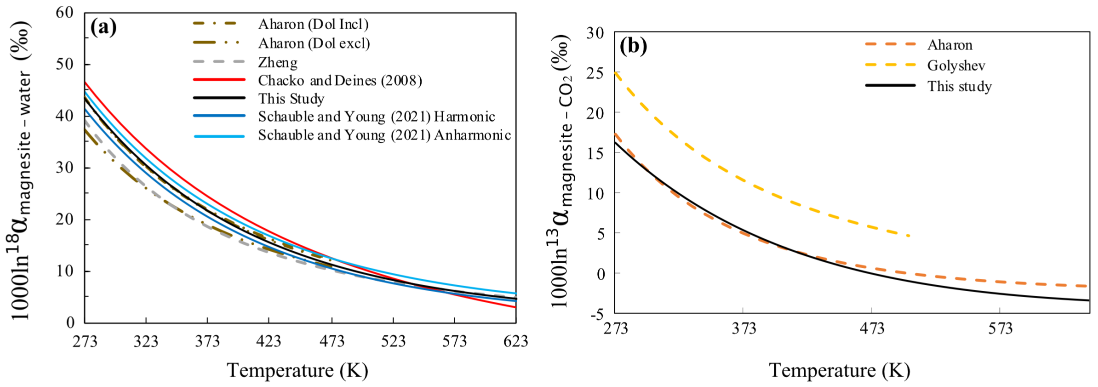

Figure 5.9: Compilation of isotope fractionation curves in magnesite–water–$CO_2$ system. (a) Temperature dependency of $^{18}O/^{16}O$ fractionation between magnesite and water. DFT based prediction from Chacko & Deines (2008) and Schauble & Young (2021) using their harmonic and anharmonic water models. (b) Temperature dependency of $^{13}C/^{12}C$ fractionation between magnesite and $CO_{2(g)}$. Solid lines indicate our Quantum Mechanics (DFT) based predictions where broken lines indicate semi–empirical or empirical calibrations. Legend keywords and their reference: Aharon (Dol Incl), Aharon (Dol Excl), Aharon = Aharon (1988); Zheng = Zheng (1999); Golyshev = Golyshev (1981).

For carbon isotopes (Fig. 5.9b), Aharon (1988) used the extrapolation method described earlier to predict magnesite–$CO_2$ fractionation. Golyshev et al. (1981) used experimental vibrational frequencies of carbonate minerals to predict this fractionation but their results may be affected by the incompleteness of the IR–active set of vibrational frequencies for carbonates. The $^{13}C$ RPFR for magnesite was calculated by Schauble et al. (2006) and estimated from experimental vibrational frequencies by Deines (2004). Both these studies needed to combine their results with an independently calculated $CO_2$ RPFR (Chacko et al. 1991) to predict the isotopic fractionation. Because differences between computational methods can introduce ~2–3 ‰ inaccuracies, we do not use these two results for comparison. Here, we calculated the RPFRs for both magnesite and $CO_2$ using the same level of theory, expecting that systematic errors arising from calculation methods will largely cancel out. Our prediction agrees with that of Aharon (1988).

### 5.4.4 Factors and mechanisms controlling fractionation behavior

Among the various carbonate minerals studied, we observe that the magnitudes of carbon and oxygen isotopic fractionation factors show negative correlations with the mineral water content (Fig. 5.10) and positive correlations with the density of the minerals. This can be understood in terms of dehydration-driven mineral maturation. As these minerals transform and their water content decreases, their densities increase, leading to increase in $^{13}C/^{12}C$ and $^{18}O/^{16}O$ fractionation as density increase leads to more compact bonding environments in carbonate structure. $^{13}C/^{12}C$ fractionation in these minerals is indicated by the C—O bond length within the carbonate groups. In lansfordite, the carbonate units are almost isolated, the $Mg^{2+}$ ions being mostly coordinated by water. As water content decreases, $Mg^{2+}$ progressively moves into $MgO_6$ octahedra that share $CO_3^{2-}$ units between them (i.e., all O atoms in $CO_3^{2-}$ units become coordinated to $MgO_6$ octahedra). This favors shorter C—O bonds, a tighter bonding environment for the C atom, and increasing $^{13}\beta$. Once all the carbonate units are fully shared, however, this increase comes to a halt (no net increase from hydromagnesite to magnesite). AMC plots off this trend because it lacks a well-defined crystal structure and so deviates from the correlation between composition and extent of $CO_3^{2-}$ sharing between $MgO_6$ octahedra that characterizes the crystalline phases ($CO_3^{2-}$ units in AMC are mostly isolated or partially shared between octahedra, with a few fully shared between octahedra).

$^{18}O/^{16}O$ fractionation is controlled by both C—O and Mg—O bonding. As dehydration proceeds, carbonate oxygens bond to $Mg^{2+}$, increasing the stiffness of the O bonding environment and causing a net trend of increasing $^{18}\beta$. In this case, AMC plots right on this trend, perhaps coincidentally because AMC has 4- and 5-coordinated Mg polyhedra with tighter O bonding environments.

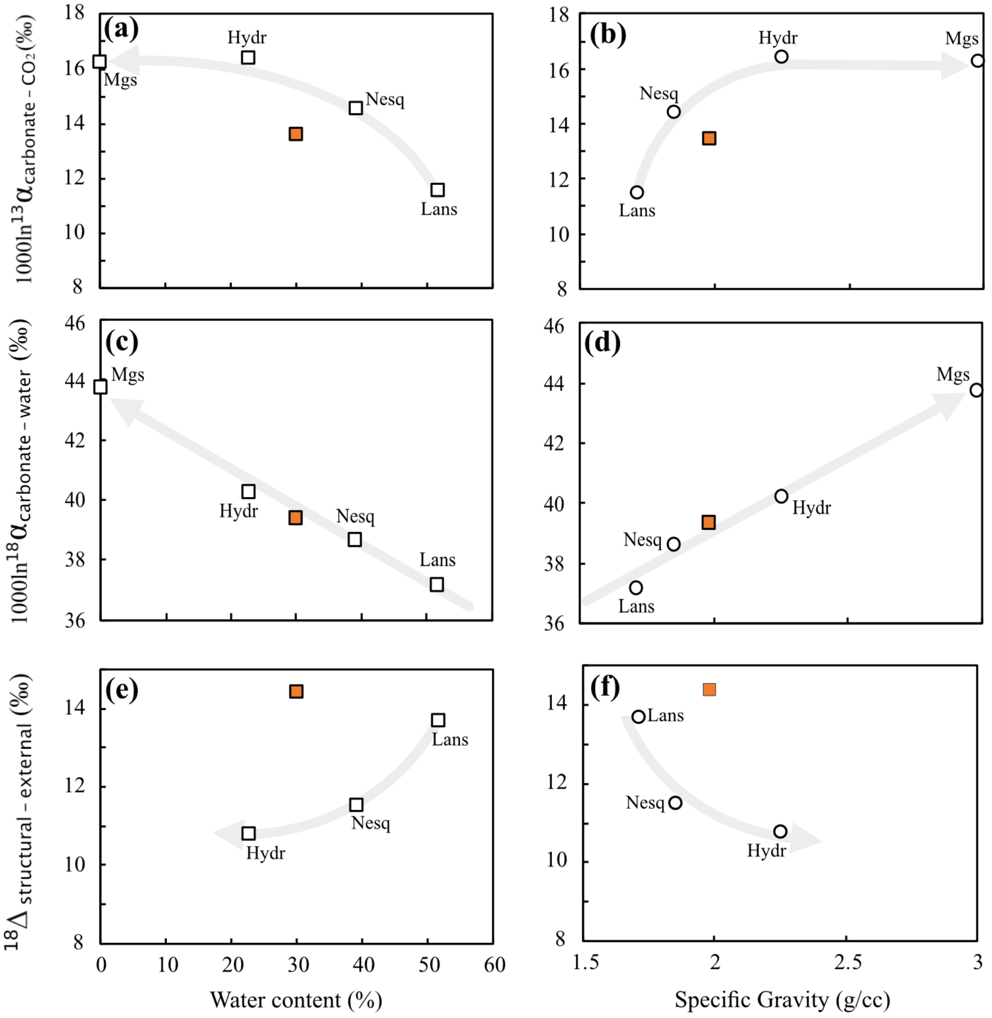

Figure 5.10: Co–variance of $^{13}\beta$, $^{18}\beta$, $^{18}\Delta_{\text{structural – external water}}$ of carbonate minerals with water content (weight %) of mineral (a.c,e) and specific gravity of mineral (b,d,f). Abbreviations: Mgs = magnesite; Hydr = hydromagnesite, Nesq = nesquehonite, Lans = lansfordite. Orange square symbol represents AMC_1500. Grey arrows are to guide the eye.

The $^{18}O/^{16}O$ fractionation between structural and external water has the opposite behavior to the total mineral–external water fractionation. It is positively correlated with mineral water content (Fig 5.10e). In mineral phases with higher water contents, additional stability is achieved via an extensive intermolecular hydrogen bonding network. This stability increases $^{18}\beta$. As water content drops, this bonding is lost, resulting in lower $^{18}\beta$s. AMC falls off this trend as AMC has localized hydrogen–bonded water clusters that cannot form at low water content in an ordered structure, creating tighter bonding environments and higher $^{18}\beta$.

### 5.4.5 Implications for formation of Martian carbonates

The fractionation factor predictions presented in this study help us form a framework to understand the formation mechanism of magnesite in both terrestrial and extraterrestrial systems. These findings will be particularly important for future studies of carbonates on Mars (from meteorites or sample return missions). Martian carbonates can potentially unravel details of the sources and compositions of the fluids responsible for their formation, including Eh – pH conditions and aqueous complexes present in the fluid. As an illustrative example, in the following paragraphs we present specific predictions of the $^{26}Mg/^{24}Mg$ of Martian carbonates using the fractionation factors reported in this study (all assuming equilibrium between magnesite and aqueous $Mg^{2+}$):

***(1) Formation via congruent dissolution of olivine/pyroxene followed by precipitation of magnesite or hydromagnesite:*** The $\delta^{26}$Mg of Bulk Silicate Mars (BSM) is estimated to be −0.27 ± 0.04 ‰ (Magna et al., 2017). Mg-rich carbonates from the martian meteorite ALH84001 have been shown to have formed at a temperature of ~291 K (Halevy et al., 2011) under evaporative conditions. If such magnesites precipitated from a fluid that derived its magnesium content from congruent dissolution of olivine and pyroxene minerals and therefore inherited a fluid $\delta^{26}$Mg similar to BSM, it is predicted to have $\delta^{26}$Mg ~ −2.7 ‰. Conversely, if magnesite was initially deposited as hydromagnesite (a magnesium carbonate phase commonly formed under evaporative conditions) and later converted to magnesite (Mergelsberg et al., 2020; Mavromatis et al., 2021; Scheller et al., 2023; Patel et al., 2024), it is predicted to have $\delta^{26}$Mg ~ +0.8 ‰.

***(2) Formation via alteration of ultramafic minerals:*** On Earth, magnesite is known to be a common end-product of serpentinization and weathering of ultramafic rocks. During such alteration, olivine and pyroxene are typically first converted to hydrated secondary phases such as talc, brucite, and serpentine. These secondary phases preferentially incorporate $^{26}$Mg in their structure (Beinlich et al., 2014; Oskierski et al., 2019; Stamm et al., 2022), leaving the residual fluid depleted in $^{26}$Mg. If magnesite precipitates from such a fluid at a temperature of ~291 K, then it would have Mg isotopic composition lower than scenario 1 (i.e., $\delta^{26}$Mg < −2.7 ‰), with the exact depletion depending upon the extent of secondary phase formation. Such secondary phases have previously been observed in Martian meteorite ALH84001 (Steele et al., 2022).

***(3) Formation via weathering of secondary silicate minerals***: If secondary silicate minerals (formed by alteration of ultramafic lithology) undergo congruent dissolution by interaction with acidic aqueous fluid, the fluid is expected to be enriched in $^{26}$Mg (as it will inherit the $^{26}$Mg–rich signature of the secondary silicate phases). Magnesite forming from such a fluid at ~291 K would be expected to have higher $\delta^{26}$Mg compared to scenario 1 (i.e., $\delta^{26}$Mg > −2.7 ‰), with exact magnitude depending on the $\delta^{26}$Mg of these silicate phases and their relative Mg contribution to the fluid. This scenario represents a simplified version of the Martian carbonate paragenetic model proposed by Melwani Daswani et al. (2016). Secondary silicate minerals have been observed on the surface of Mars via orbital detection (Ehlmann et al., 2011), further bolstering the feasibility of this scenario.

These scenarios provide simple first–order estimates of the $\delta^{26}$Mg of Martian Mg–rich carbonates. Accurate prediction of the $\delta^{26}$Mg of such carbonates would require a detailed study, taking into account various pH conditions, aquatic complexation of Mg, dissolution/precipitation kinetics of the carbonate and silicate minerals involved, the effect of Fe−Ca content of carbonates on mineral−fluid Mg isotope fractionation (Wang et al., 2017; Patron et al., 2025) and any closed–system mineral precipitation resulting in isotopic distillation.

## 5.5 Summary and Conclusions

(1) We modeled structural and vibrational properties of a series of Mg-carbonate minerals (AMC, lansfordite, nesquehonite, hydromagnesite and magnesite) using quantum mechanical methods (DFT). Our results indicate that all carbonate minerals preferentially incorporate $^{13}$C (by ~11.6 - 16.4 ‰, compared to $CO_2$(g)) and $^{18}$O (by ~37.2 - 43.7 ‰ compared to water) in their structure, assuming equilibrium at 273 K. Furthermore, the water molecules incorporated in the structure(s) of the hydrous Mg-carbonate minerals show equilibrium enrichment in $^{18}$O compared to external water by 10.8 - 14.4 ‰ at 273 K.

(2) Two distinct directions of equilibrium $^{26}$Mg/$^{24}$Mg fractionation (relative to aqueous $Mg^{2+}$ ion) are predicted for carbonate minerals. At 273 K, anhydrous carbonate (magnesite) prefers

$^{24}$Mg in its structure (depleted in $^{26}$Mg by –2.6‰) whereas hydrated Mg carbonates prefer $^{26}$Mg (enriched in $^{26}$Mg by 0.6 to 1.3 ‰). Lansfordite is an exception, preferring $^{24}$Mg (depleted in $^{26}$Mg by –1.4 ‰), despite being hydrous. AMC does not preferentially incorporate $^{26}$Mg or $^{24}$Mg in its structure relative to aqueous Mg.

(3) A key factor controlling the $^{13}$C/$^{12}$C and $^{18}$O/$^{16}$O fractionation in this system is the water content of the carbonate mineral, which determines the extent of $CO_3^{2-}$ unit sharing and $Mg^{2+}$ coordination in the lattice. This also correlates with mineral density.

(4) AMC precipitates synthesized in this study are found to be enriched in $^{13}$C and $^{18}$O compared to $CO_2$ and water (by 18.3 ‰ and 37.6 ‰ at 283 K). Both $^{18}$O/$^{16}$O fractionation between AMC and water and the clumped isotopic composition of AMC seem to be relatively invariant across a temperature of 283 - 313 K, which we speculate could be due to post-precipitation isotope exchange or dehydration during storage and/or shipping.

(5) These findings have been used to predict Mg isotopic composition of Martian magnesites, assuming equilibrium formation at ~291 K. If these magnesites formed from a fluid which evidenced congruent dissolution of olivine and pyroxene minerals, they are predicted to have $\delta^{26}$Mg ~ −2.7 ‰. Instead, if they initially formed as hydromagnesite and later converted to magnesite, they are predicted to have $\delta^{26}$Mg ~ +0.8 ‰. If magnesite formed in an event where olivine/pyroxene minerals suffered alteration to produce secondary silicate minerals first, they are expected to have $\delta^{26}$Mg < −2.7 ‰. Conversely, if Mg produced by weathering of secondary silicate minerals is sequestered into Martian magnesites, they are expected to have $\delta^{26}$Mg > −2.7 ‰. Thus, Mg isotopic composition of these magnesites can provide novel insights regarding the source of Mg as well as formation mechanism of these carbonates, which will have potential implications on mobility of liquid water and habitability at Martian conditions.

## Acknowledgements

SB acknowledges Nami Kitchen and Makayla Betts for assistance with isotopic measurements. SB acknowledges Carl Swindle, Ted Present and Emily Cardarelli for helpful discussions. William Palfey and Charles B. Musgrave are acknowledged for their help in resolving computational issues. This study was supported by Simons Foundation grant

(668346). WAG was supported by U.S. National Science Foundation (CBET 2311117). AMC synthesis and characterization at University of Alberta was supported by a Discovery Grant and a Discovery Accelerator Supplement from the Natural Sciences and Engineering Research Council of Canada.

## 5.6 Supplementary Material

### 5.6.1 Hydration and hydroxylation state of the AMC

The hydration and hydroxylation state of the AMC was determined using thermogravimetric analysis (TGA) at University of Alberta. Samples were analyzed on a Nicolet iS50 FTIR Spectrometer (Thermo Fisher) with a diamond crystal and a Discovery TGA (TA Instruments) at the University of Alberta. TGA was run with a gas flow of 20 mL/min from ambient to 1000 °C and a heating rate of 10 °C/min. Structural formula of the AMC has been calculated using (Jensen et al., 2018) formulation.

Table S5.1: Structural formula of the AMC calculated from TGA data.

| **Sample** | **Final Formula** |
|---|---|
| AMC-10C-1 | $MgCO_{2.22}OH_{0.53} \cdot 2.11H_2O$ |
| AMC-10C-2 | $MgCO_{2.17}OH_{0.55} \cdot 2.11H_2O$ |
| AMC-20C-1 | $MgCO_{2.23}OH_{0.51} \cdot 2.04H_2O$ |
| AMC-20C-2 | $MgCO_{2.10}OH_{0.60} \cdot 2.03H_2O$ |
| AMC-30C-1 | $MgCO_{2.17}OH_{0.55} \cdot 1.97H_2O$ |
| AMC-30C-2 | $MgCO_{2.52}OH_{0.32} \cdot 1.97H_2O$ |
| AMC-40C-1 | $MgCO_{2.52}OH_{0.32} \cdot 1.82H_2O$ |
| AMC-40C-2 | $MgCO_{2.38}OH_{0.41} \cdot 1.91H_2O$ |

### 5.6.2 X-Ray diffraction (XRD) analysis of the AMC

X-ray diffraction patterns were collected to confirm the precipitated Mg-carbonate phase was amorphous. Samples were homogenized using an agate mortar and pestle with 100% ethanol, mounted on a zero-diffraction quartz plate and analyzed with a Bruker D8 Advance powder X-ray diffractometer (XRD) with a Co source and a LYNXEYE-XE-T position sensitive detector at University of Alberta. The XRD was operated at 35 kV and 40 mA, using a step size of 0.02° 2θ and a scan speed of 1 s/step between 3–80° 2θ.

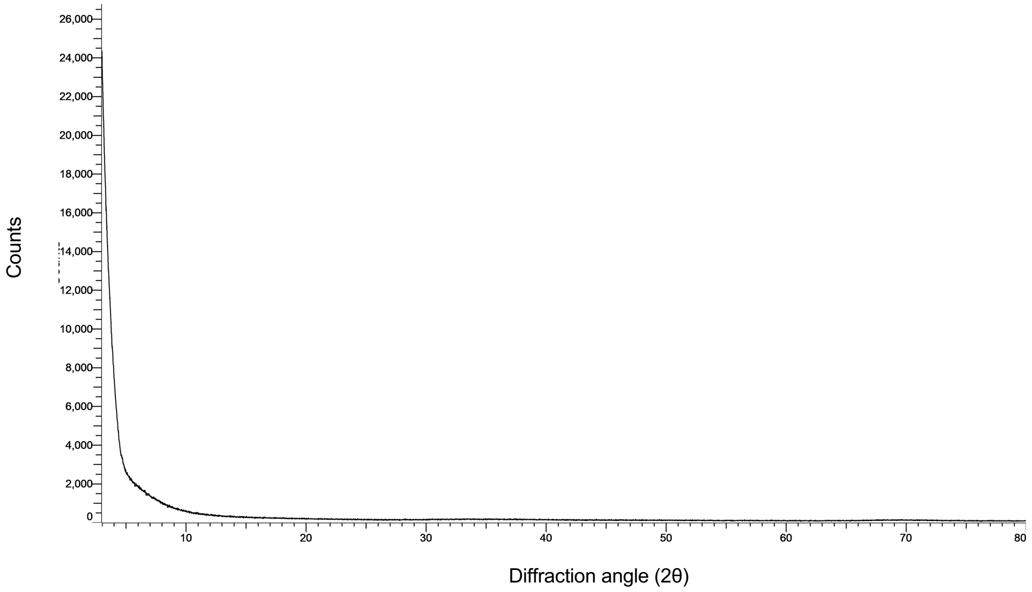

Figure S5.1: Representative XRD pattern of synthetic AMC.

### 5.6.3 Effect of heavy atom substitution strategy on RPFR calculation

The $^{17}O$ and $^{18}O$ RPFRs can be sensitive to the way heavy atoms are substituted in a mineral structure during DFT calculations. We demonstrate this for magnesite. All calculations presented here used identical calculation conditions. While substitution all oxygen atoms at a time in the cell yield the same $^{18}O$ RPFR as substituting one atom at a time, the *k* values changes drastically, yielding implausible *k* - T relationship. If we substitute all three oxygen atoms in one single carbonate unit in a mineral structure at once with heavy isotopes, we get a different $^{18}O$ RPFR and implausible *k* - T relationship. When we substitute all atoms in a structure one by one- a rather time-consuming process, we get $^{18}$O RPFR and $k$ values that agree well with prior calculations of Schauble and Young (2021). Lastly, when we use finite difference/selective dynamics method, we get an identical answer, but computation time is lowered significantly. However, strategy of substitution did not impact $^{13}$C RPFRs.

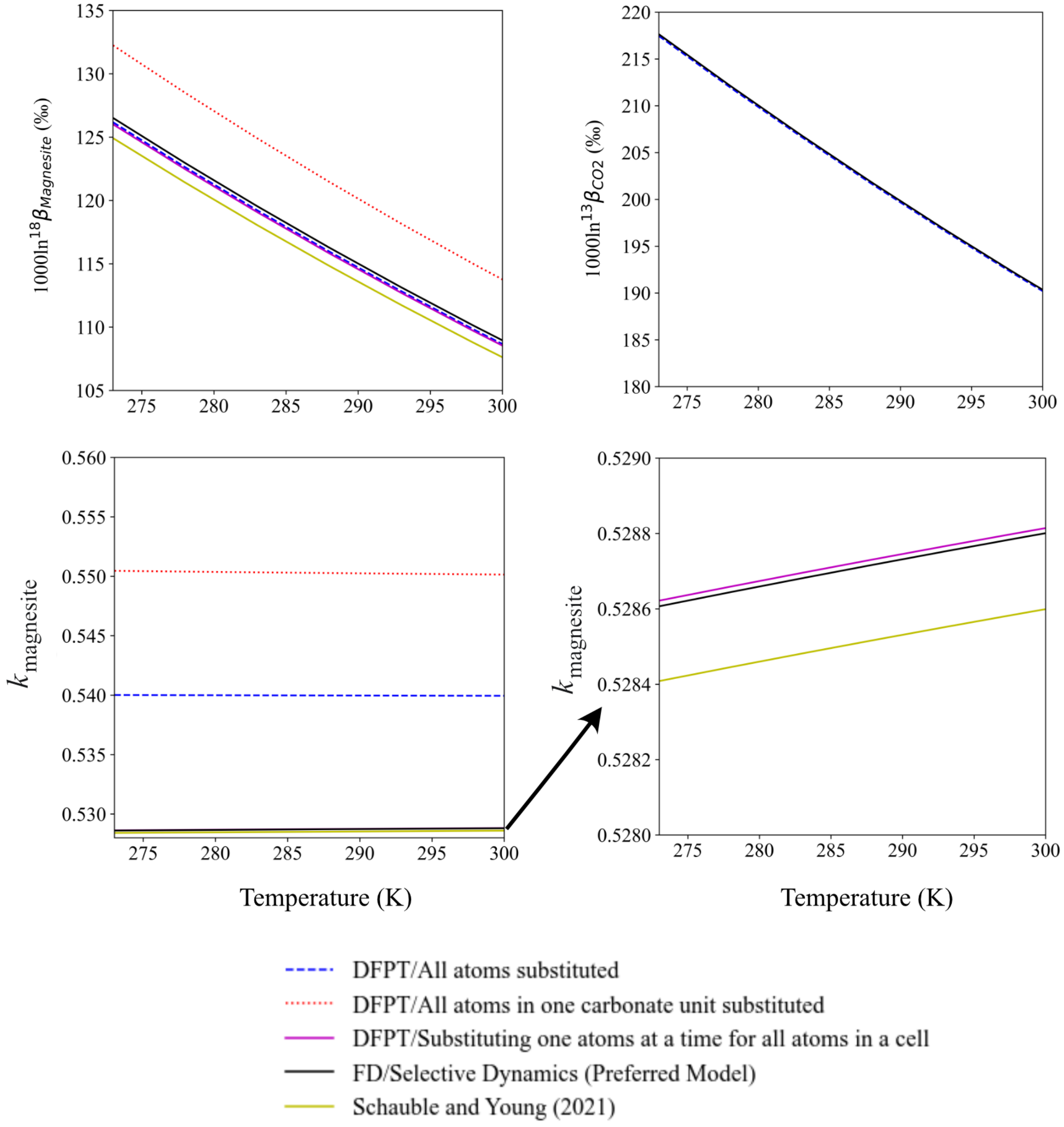

Figure S5.2: Effect of different heavy atom substitution strategies on calculated $^{13}$C, $^{18}$O RPFRs and $k$ value. DFPT = Density Functional Perturbation Theory, FD = Finite Difference.

### 5.6.4 Effect of scaling factor on fractionation factor calculation

The choice of scaling factor is critical in RPFR calculation. We have evaluated how sensitive our reported fractionation factors are with respect to scaling, by performing tests on magnesite-water-$CO_2$ system. At 273 K, the difference between scaled and unscaled $^{18}\alpha$ is 3‰, that for $^{13}\alpha$ is 1.5‰ and that for $^{26}\alpha$ is 0.09‰. The difference between scaled and unscaled $^{18}\alpha_{\text{structural - external water}}$ in ikaite is 1.1‰ at 273 K. Such differences are small and are not expected to impact the Mg isotope interpretation of Martian carbonates presented in this paper. Scaling did not change *k* values, as discussed in (Cao and Liu, 2011).

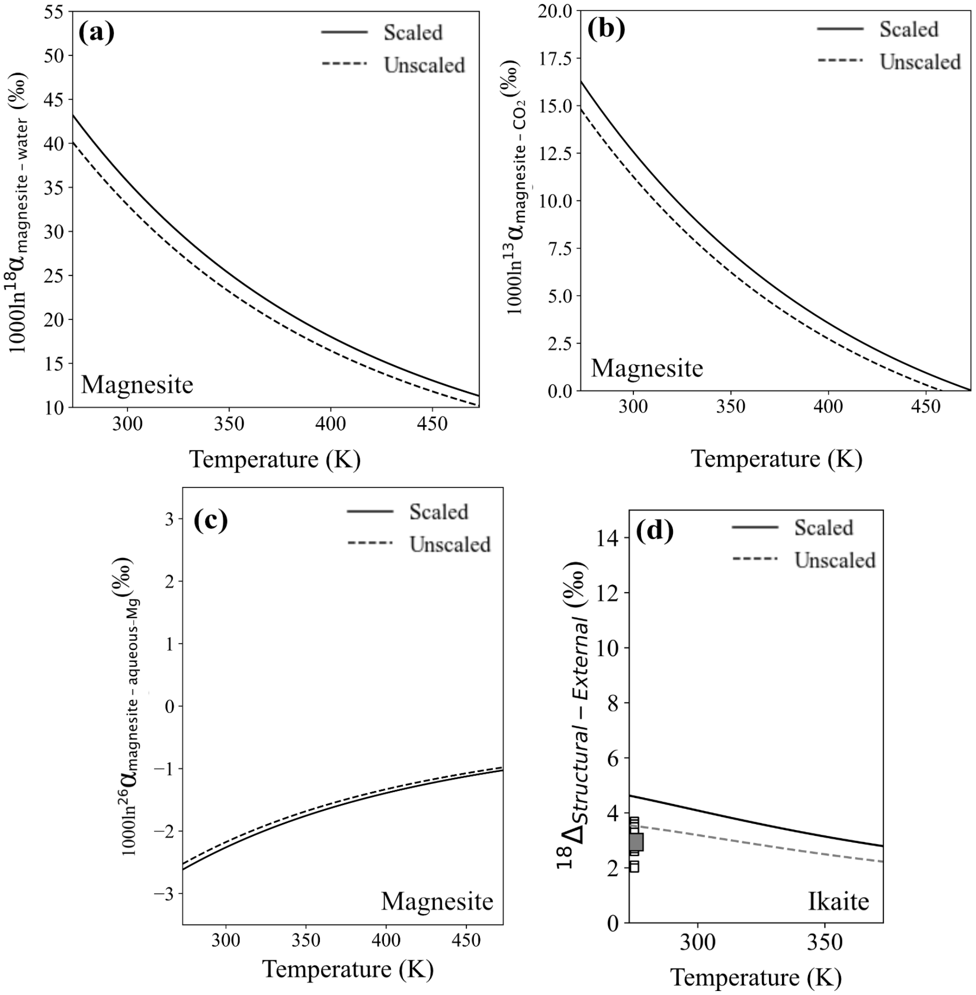

Figure S5.3: Effect of scaling factors on calculated fractionation factors for (a) $^{18}O/^{16}O$, (b) $^{13}C/^{12}C$ and (c) $^{26}Mg/^{24}Mg$ in magnesite and (d) $^{18}O/^{16}O$ fractionation between structural and external water in ikaite.

### 5.6.5 Unscaled fractionation factors

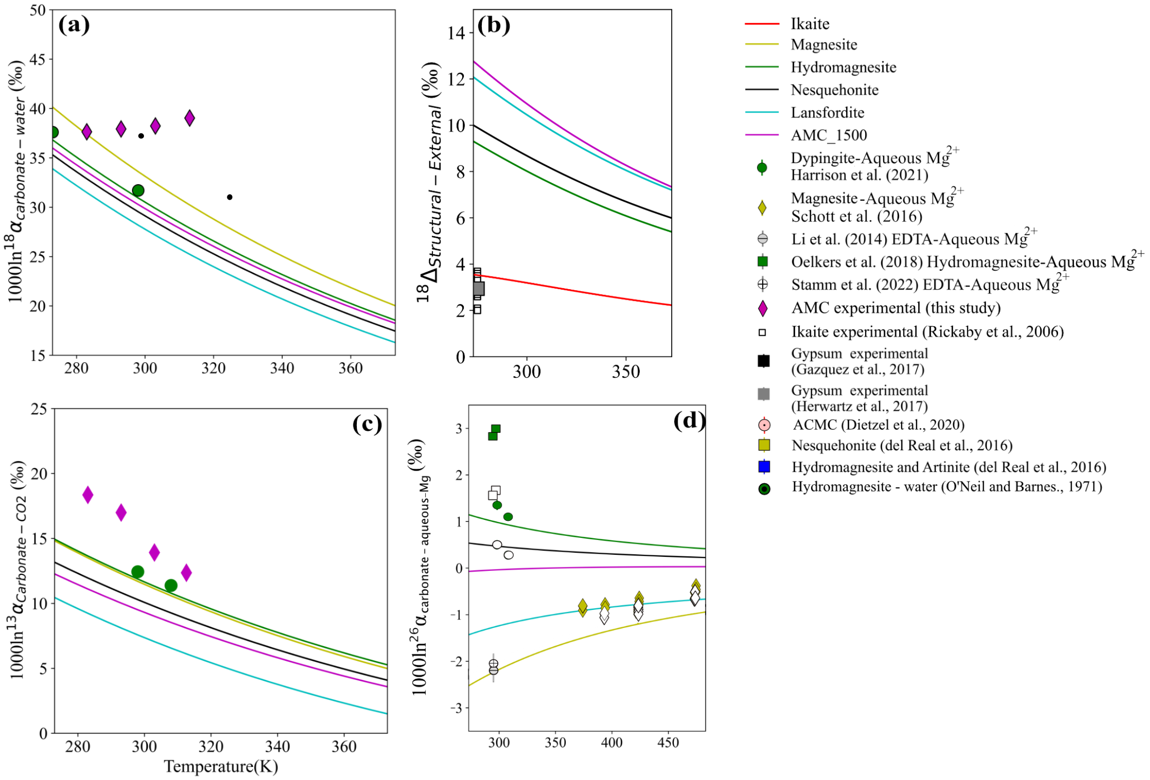

Figure S5.4: Unscaled fractionation factors for (a) Carbonate–water $^{18}O/^{16}O$ fractionation (b) $^{18}O/^{16}O$ fractionation between structurally bound water in hydrous carbonates and water in external environment (c) Carbonate–$CO_2(g)$ $^{13}C/^{12}C$ fractionation (d) $^{26}Mg/^{24}Mg$ fractionation between carbonate minerals and aqueous $Mg^{2+}$.

### 5.6.6 Water clusters used to predict the triple oxygen isotope mass law for vapor pressure isotope effect of water

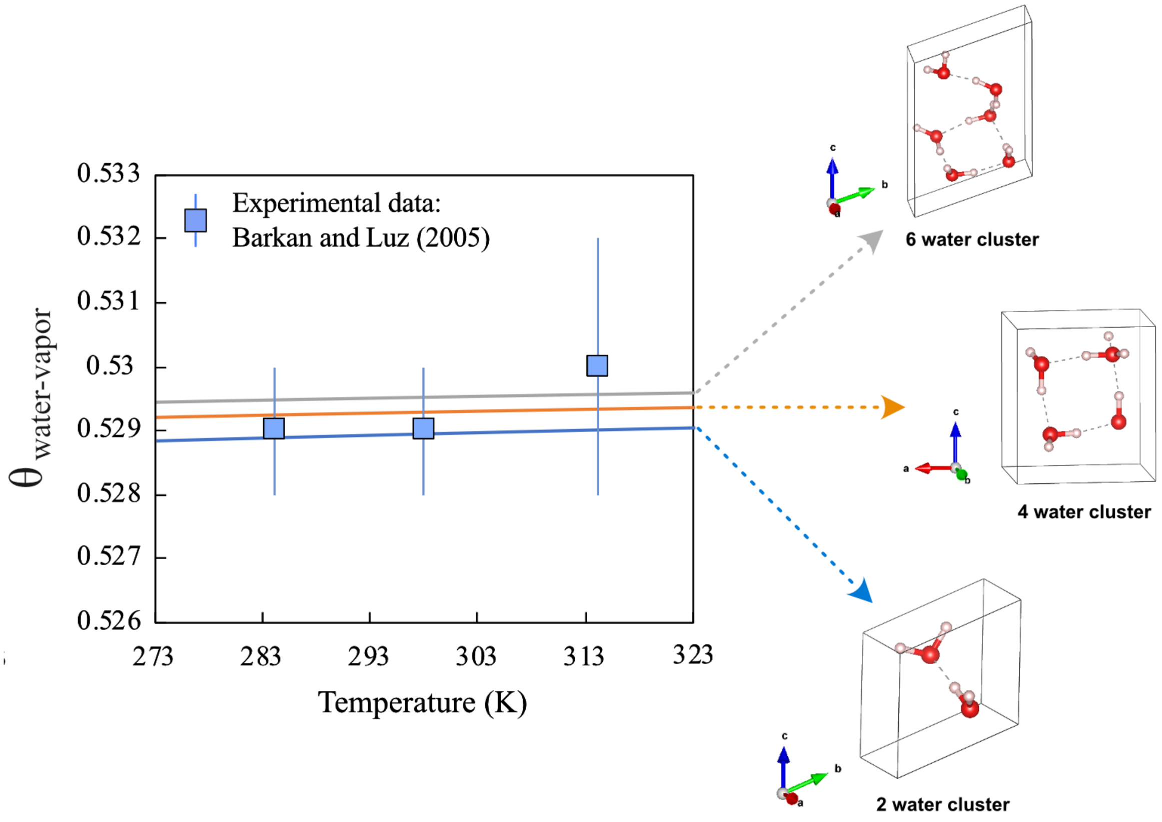

Figure S5.5: Structures of 2-, 4-, and 6-water clusters used to predict the triple oxygen isotope mass law for vapor pressure isotope effect of water, along with their predicted mass laws.

### 5.6.7 Calculation of aqueous $Mg^{2+}$ RPFR

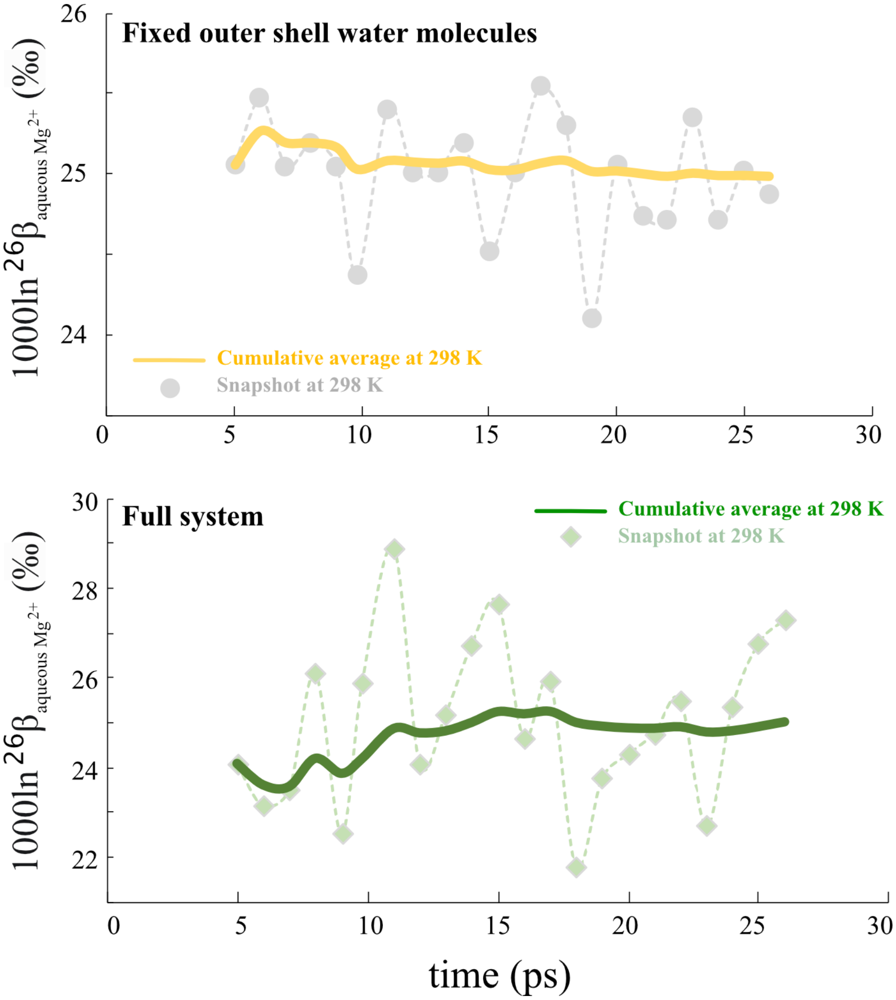

Figure S5.6: Convergence of $\ln^{26}\beta$ (‰) for aqueous $Mg^{2+}$ at 298 K from snapshot method, where vibrational frequencies have been calculated for the entire system (bottom) or with frozen outer hydration shell of $Mg^{2+}$ (top). For both cases, time averaged cumulative RFFRs (thick solid lines) converge to identical values. Symbols indicate $\ln^{26}\beta$ (‰) at each time point.

### 5.6.8 P-T-E variation over DFT–MD simulation timescales

**Aqueous $Mg^{2+}$**

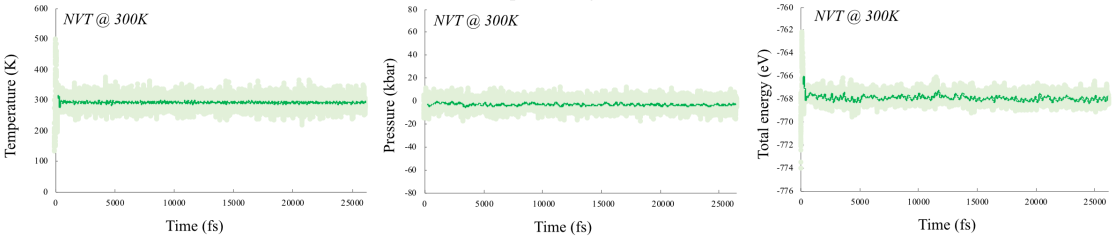

**AMC**

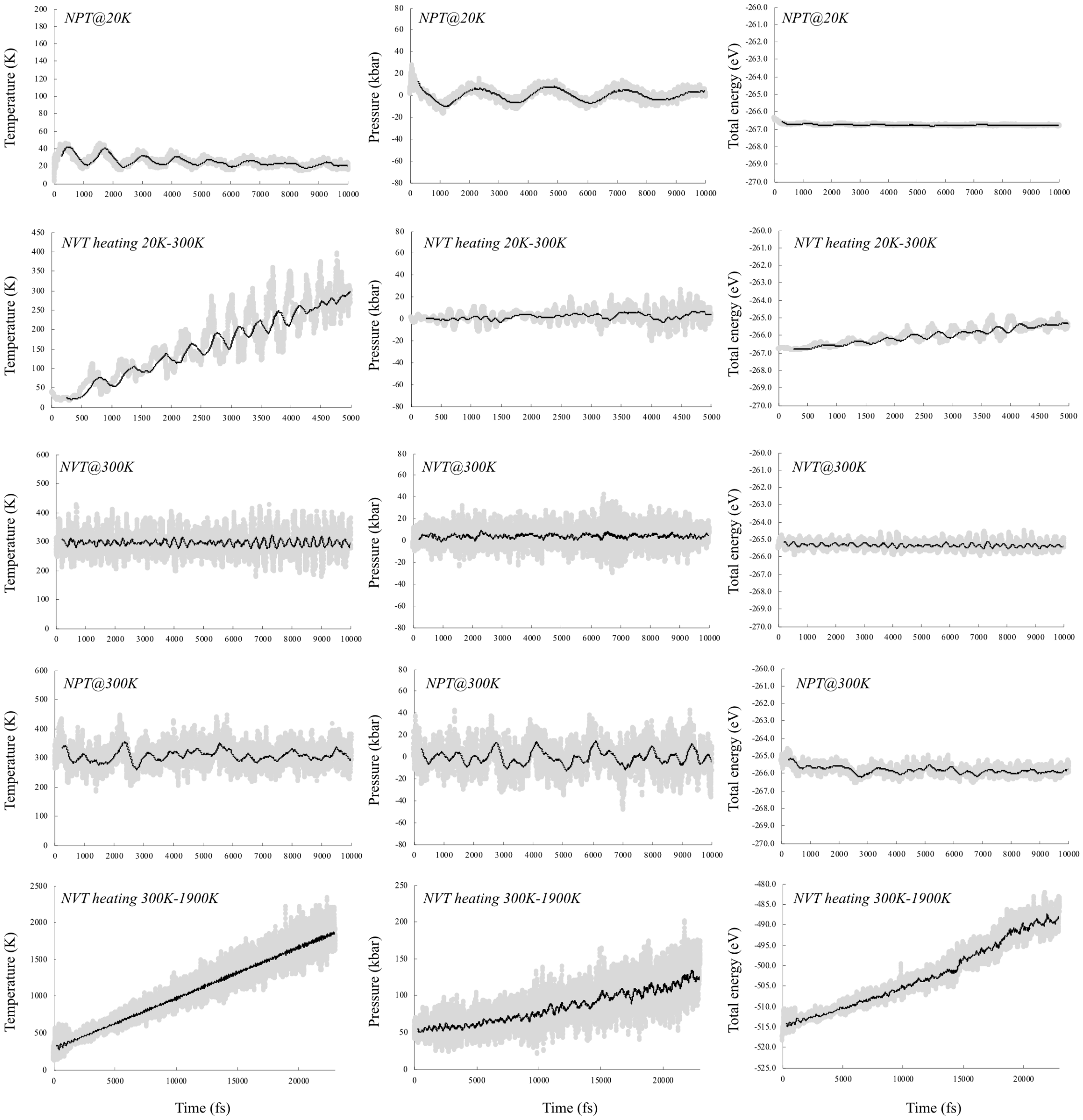

**AMC_1500**

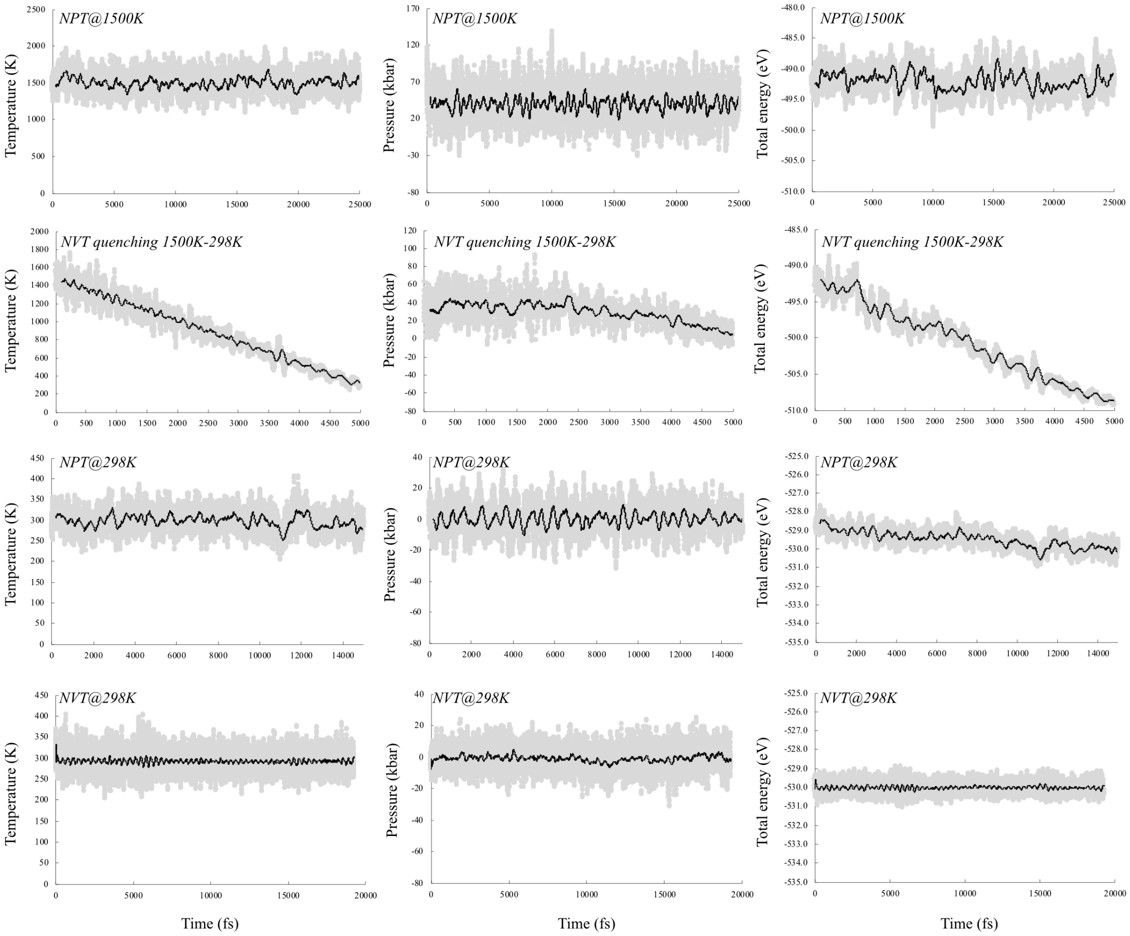
NPT@1500K
Temperature (K)
Pressure (kbar)
Total energy (eV)
NVT quenching 1500K-298K
NPT@298K
NVT@298K
Time (fs)
Time (fs)
Time (fs)

**AMC_1900**

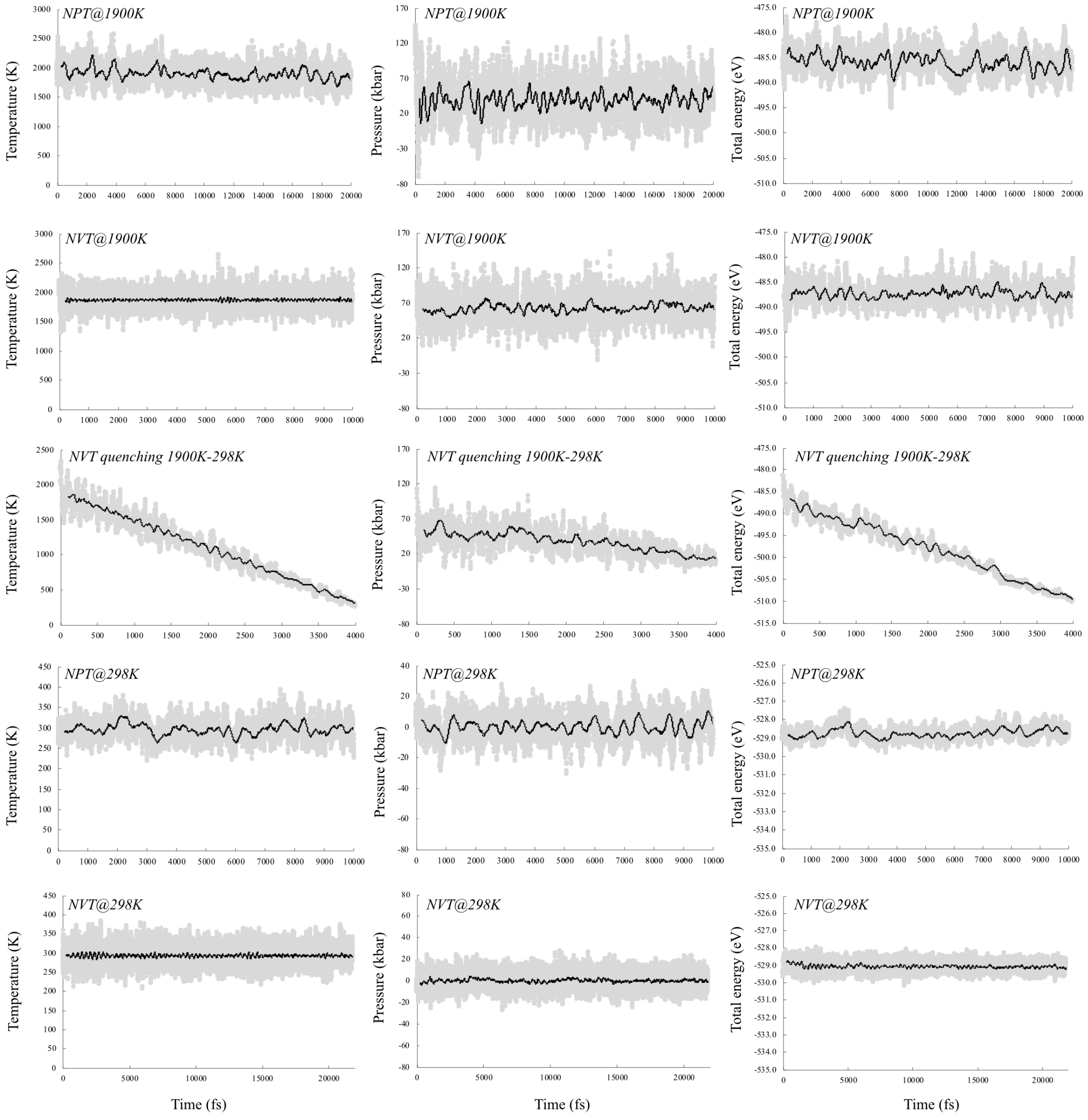

Figure S5.7: Pressure, temperature and total energy variations over all DFT–MD simulation timescales. Each step is indicated by light green (for aqueous $Mg^{2+}$) or gray (for AMC) point. Black or green solid line indicates moving average values.

Table 5.1: Heating schedule for DFT based molecular dynamics simulations followed to derive AMC structures. Where different, numbers in brackets show conditions for simulation of AMC_1900.

| **Step no.** | **Starting Temperature (K)** | **Ending Temperature (K)** | **P(MPa)** | **Starting Structure** | **Calculation Type** | **Duration (ps)** | **End Structure** | **Comments** |
|---|---|---|---|---|---|---|---|---|
| 1 | 0 | 0 | 0 | A | static DFT | — | B | energy minimization |
| 2 | 20 | 20 | 0 | B | MD, NVT | 10 | C | |
| 3 | 20 | 300 | 0 | C | MD, NVT | 5 | D | |
| 4 | 300 | 300 | 0 | D | MD, NVT | 10 | E | |
| 5 | 300 | 300 | 0 | E | MD, NPT | 10 | F | |
| 6 | 0 | 0 | 0 | F | static DFT | — | G | energy minimization |
| Cell size doubled | | | | | | | | |
| 7 | 0 | 0 | 0 | G | static DFT | — | H | energy minimization |
| 8 | 300 | 300 | 0 | H | MD, NVT | 3 | I | velocity initiation, velocities from F |
| 9 | 300 | 1500 (1900) | 400 | I | MD, NVT | 17.2 (23) | J | heating |
| 10 | 1500 (1900) | 1500 (1900) | 400 | J | MD, NPT | 25 (20) | K | equilibration |
| 10a | (1900) | (1900) | 400 | J | MD, NVT | (10) | K | equilibration |
| 11 | 1500 (1900) | 298 | 400 | K | MD, NVT | 5 (4) | L | quenching |
| 12 | 298 | 298 | 0 | L | MD, NPT | 15 (10) | M | equilibrium at room T |
| 13 | 298 | 298 | 0 | M | MD, NVT | 19 (22) | N | trajectory for 2PT analysis |

Table 5.2: Comparison of experimental and modeled unit cell dimensions ($a, b, c$), angles ($\alpha, \beta, \gamma$) and volumes for carbonate minerals considered in this study. The mean absolute deviation (MAD, %) for unit cell parameters is also presented. Sources of experimental unit cell parameters: dolomite = Steinfink and Sans (1959); ikaite = Hesse et al. (1983); magnesite = Ross (1997); hydromagnesite = Akao & Iwai (1977); lansfordite = Liu et al. (1990), nesquehonite = Stephan & MacGillavry (1972).

| ***Mineral*** | **Calculated** | | | | | | |
|---|---|---|---|---|---|---|---|
| | $a$ (Å) | $b$ (Å) | $c$ (Å) | $\alpha$ | $\beta$ | $\gamma$ | unit cell vol (Å$^3$) |
| Dolomite | 4.83 | 4.83 | 15.86 | 90.00 | 90.00 | 120.00 | 321.04 |
| Ikaite | 8.66 | 8.26 | 10.84 | 90.00 | 109.31 | 90.00 | 731.81 |
| Magnesite | 5.64 | 5.64 | 5.64 | 48.72 | 48.73 | 48.72 | 92.97 |
| Hydromagnesite | 10.02 | 9.05 | 8.30 | 90.00 | 114.01 | 90.00 | 687.93 |
| Lansfordite | 7.17 | 7.56 | 12.48 | 90.00 | 102.32 | 90.00 | 660.16 |
| Nesquehonite | 7.61 | 5.40 | 11.76 | 90.00 | 91.73 | 90.00 | 483.27 |
| AMC_1500 | 12.25 | 5.26 | 13.11 | 87.17 | 99.59 | 104.52 | 806.66 |
| AMC_1900 | 11.93 | 5.36 | 13.21 | 89.96 | 90.46 | 110.08 | 792.40 |

| | **Experimental** | | | | | | |
|---|---|---|---|---|---|---|---|
| | $a$ (Å) | $b$ (Å) | $c$ (Å) | $\alpha$ | $\beta$ | $\gamma$ | unit cell vol (Å$^3$) |
| Dolomite | 4.82 | 4.82 | 16.12 | 90.00 | 90.00 | 120.00 | 323.64 |
| Ikaite | 8.79 | 8.31 | 11.02 | 90.00 | 110.53 | 90.00 | 754.07 |
| Magnesite | 5.68 | 5.68 | 5.68 | 48.19 | 48.19 | 48.19 | 93.09 |
| Hydromagnesite | 10.11 | 8.95 | 8.38 | 90.00 | 114.44 | 90.00 | 690.12 |
| Lansfordite | 7.36 | 7.63 | 12.49 | 90.00 | 101.75 | 90.00 | 687.14 |
| Nesquehonite | 7.70 | 5.37 | 12.13 | 90.00 | 90.41 | 90.00 | 501.28 |

| | **Absolute Difference (%)** | | | | | | |
|---|---|---|---|---|---|---|---|
| | $a$ (Å) | $b$ (Å) | $c$ (Å) | $\alpha$ | $\beta$ | $\gamma$ | unit cell vol (Å$^3$) |
| Dolomite | 0.40 | 0.40 | 1.58 | 0.00 | 0.00 | 0.00 | 0.80 |
| Ikaite | 1.50 | 0.64 | 1.60 | 0.00 | 1.10 | 0.00 | 2.95 |
| Magnesite | 0.64 | 0.64 | 0.64 | 1.11 | 1.11 | 1.11 | 0.13 |
| Hydromagnesite | 0.79 | 1.09 | 0.93 | 0.00 | 0.38 | 0.00 | 0.32 |
| Lansfordite | 2.70 | 0.96 | 0.09 | 0.00 | 0.56 | 0.00 | 3.93 |
| Nesquehonite | 1.23 | 0.73 | 2.99 | 0.00 | 1.46 | 0.00 | 3.59 |
| *MAD* | *1.21* | *0.74* | *1.31* | *0.18* | *0.77* | *0.18* | *1.95* |

# BIBLIOGRAPHY

Aharon P. (1988) A stable-isotope study of magnesites from the Rum Jungle Uranium Field, Australia: implications for the origin of strata-bound massive magnesites. *Chemical Geology* **69**, 127–145.

Åhlén M., Cheung O. and Strømme M. (2019) Amorphous mesoporous magnesium carbonate as a functional support for UV-blocking semiconductor nanoparticles for cosmetic applications. *ACS Omega* **4**, 4429–4436.

Akao M. and Iwai S. (1977) The hydrogen bonding of hydromagnesite. *Acta Crystallographica Section B: Structural Crystallography and Crystal Chemistry* **33**, 1273–1275.

Alexander C. M. O., Bowden R., Fogel M. L. and Howard K. T. (2015) Carbonate abundances and isotopic compositions in chondrites. *Meteorit & Planetary Scien* **50**, 810–833.

Azer M. K., Gahlan H. A., Asimow P. D., Mubarak H. S. and Al-Kahtany K. M. (2019) Multiple stages of carbonation and element redistribution during formation of ultramafic-hosted magnesite in Neoproterozoic ophiolites of the Arabian-Nubian Shield, Egypt. *The Journal of Geology* **127**, 81–107.

Barkan E. and Luz B. (2005) High precision measurements of 17O/16O and 18O/16O ratios in H2O. *Rapid Communications in Mass Spectrometry: An International Journal Devoted to the Rapid Dissemination of Up-to-the-Minute Research in Mass Spectrometry* **19**, 3737–3742.

Beinlich A., Mavromatis V., Austrheim H. and Oelkers E. H. (2014) Inter-mineral Mg isotope fractionation during hydrothermal ultramafic rock alteration–Implications for the global Mg-cycle. *Earth and Planetary Science Letters* **392**, 166–176.

Bhattacharjee S. and Eiler J. M. (2025) Constraining oxygen isotope exchange kinetics between organic compounds and water using electrospray ionization Orbitrap mass spectrometry, and implications for the oxygen isotopic compositions of meteoritic organics. *Geochimica et Cosmochimica Acta*.

Bhattacharjee S. and Eiler J. M. (2024) Oxygen isotope equilibria of O-bearing organic compounds based on first principle quantum mechanical models, and implications for their use in the study of extraterrestrial organics. *Geochimica et Cosmochimica Acta* **380**, 96–111.

Bigeleisen J. and Mayer M. G. (1947) Calculation of equilibrium constants for isotopic exchange reactions. *The Journal of Chemical Physics* **15**, 261–267.

Blanchard M., Poitrasson F., Méheut M., Lazzeri M., Mauri F. and Balan E. (2009) Iron isotope fractionation between pyrite (FeS2), hematite (Fe2O3) and siderite (FeCO3): A first-principles density functional theory study. *Geochimica et Cosmochimica Acta* **73**, 6565–6578.

Blöchl P. E. (1994) Projector augmented-wave method. *Phys. Rev. B* **50**, 17953–17979.

Bonal L., Huss G. R., Krot A. N. and Nagashima K. (2010) Chondritic lithic clasts in the CB/CH-like meteorite Isheyevo: Fragments of previously unsampled parent bodies. *Geochimica et Cosmochimica Acta* **74**, 2500–2522.

Bonifacie M., Calmels D., Eiler J. M., Horita J., Chaduteau C., Vasconcelos C., Agrinier P., Katz A., Passey B. H. and Ferry J. M. (2017) Calibration of the dolomite clumped isotope thermometer from 25 to 350 C, and implications for a universal calibration for all (Ca, Mg, Fe) CO3 carbonates. *Geochimica et Cosmochimica Acta* **200**, 255–279.

Bottinga Y. and Craig H. (1968) Oxygen isotope fractionation between CO2 and water, and the isotopic composition of marine atmospheric CO2. *Earth and Planetary Science Letters* **5**, 285–295.

Brenninkmeijer C. A. M., Kraft P. and Mook W. G. (1983) Oxygen isotope fractionation between CO2 and H2O. *Chemical Geology* **41**, 181–190.

Cao X. and Liu Y. (2011) Equilibrium mass-dependent fractionation relationships for triple oxygen isotopes. *Geochimica et Cosmochimica Acta* **75**, 7435–7445.

Chacko T., Cole D. R. and Horita J. (2001) Equilibrium oxygen, hydrogen and carbon isotope fractionation factors applicable to geologic systems. *Reviews in mineralogy and geochemistry* **43**, 1–81.

Chacko T. and Deines P. (2008) Theoretical calculation of oxygen isotope fractionation factors in carbonate systems. *Geochimica et Cosmochimica Acta* **72**, 3642–3660.

Chacko T., Mayeda T. K., Clayton R. N. and Goldsmith J. R. (1991) Oxygen and carbon isotope fractionations between CO2 and calcite. *Geochimica et Cosmochimica Acta* **55**, 2867–2882.

Deines P. (2004) Carbon isotope effects in carbonate systems. *Geochimica et Cosmochimica Acta* **68**, 2659–2679.

Dennis K. J., Affek H. P., Passey B. H., Schrag D. P. and Eiler J. M. (2011) Defining an absolute reference frame for 'clumped'isotope studies of CO2. *Geochimica et Cosmochimica Acta* **75**, 7117–7131.

Devriendt L. S., Watkins J. M. and McGregor H. V. (2017) Oxygen isotope fractionation in the CaCO3-DIC-H2O system. *Geochimica et Cosmochimica Acta* **214**, 115–142.

Dietzel M., Purgstaller B., Kluge T., Leis A. and Mavromatis V. (2020) Oxygen and clumped isotope fractionation during the formation of Mg calcite via an amorphous precursor. *Geochimica et Cosmochimica Acta* **276**, 258–273.

Domagal-Goldman S. D. and Kubicki J. D. (2008) Density functional theory predictions of equilibrium isotope fractionation of iron due to redox changes and organic complexation. *Geochimica et Cosmochimica Acta* **72**, 5201–5216.

Downs R. T. and Hall-Wallace M. (2003) The American Mineralogist crystal structure database. *American Mineralogist* **88**, 247–250.

Ehlmann B. L., Mustard J. F., Murchie S. L., Bibring J.-P., Meunier A., Fraeman A. A. and Langevin Y. (2011) Subsurface water and clay mineral formation during the early history of Mars. *Nature* **479**, 53–60.

Ehlmann B. L., Mustard J. F., Murchie S. L., Poulet F., Bishop J. L., Brown A. J., Calvin W. M., Clark R. N., Des Marais D. J. and Milliken R. E. (2008) Orbital identification of carbonate-bearing rocks on Mars. *Science* **322**, 1828–1832.

Eiler J. M., Valley J. W., Graham C. M. and Fournelle J. (2002) Two populations of carbonate in ALH84001: Geochemical evidence for discrimination and genesis. *Geochimica et Cosmochimica Acta* **66**, 1285–1303.

Falk E. S. and Kelemen P. B. (2015) Geochemistry and petrology of listvenite in the Samail ophiolite, Sultanate of Oman: complete carbonation of peridotite during ophiolite emplacement. *Geochimica et Cosmochimica Acta* **160**, 70–90.

Farley K. A., Stack K. M., Shuster D. L., Horgan B. H. N., Hurowitz J. A., Tarnas J. D., Simon J. I., Sun V. Z., Scheller E. L. and Moore K. R. (2022) Aqueously altered igneous rocks sampled on the floor of Jezero crater, Mars. *Science* **377**, eabo2196.

Fujiya W., Sugiura N., Sano Y. and Hiyagon H. (2013) Mn–Cr ages of dolomites in CI chondrites and the Tagish Lake ungrouped carbonaceous chondrite. *Earth and Planetary Science Letters* **362**, 130–142.

Gao C., Cao X., Liu Q., Yang Y., Zhang S., He Y., Tang M. and Liu Y. (2018) Theoretical calculation of equilibrium Mg isotope fractionations between minerals and aqueous solutions. *Chemical Geology* **488**, 62–75.

Gázquez F., Evans N. P. and Hodell D. A. (2017) Precise and accurate isotope fractionation factors (α17O, α18O and αD) for water and CaSO4· 2H2O (gypsum). *Geochimica et Cosmochimica Acta* **198**, 259–270.

Ghosh P., Adkins J., Affek H., Balta B., Guo W., Schauble E. A., Schrag D. and Eiler J. M. (2006) 13C–18O bonds in carbonate minerals: a new kind of paleothermometer. *Geochimica et Cosmochimica Acta* **70**, 1439–1456.

Golyshev S. I., Padalko N. L. and Pechenkin S. A. (1981) Fractionation of stable oxygen and carbon isotopes in carbonate systems. *Geokhimiya* **10**, 1427–1441.

Grady M. M., Verchovsky A. B., Franchi I. A., Wright I. P. and Pillinger C. T. (2002) Light dement geochemistry of the Tagish Lake CI2 chondrite: Comparison with CI1 and CM2 meteorites. *Meteorit & Planetary Scien* **37**, 713–735.

Grimme S., Antony J., Ehrlich S. and Krieg H. (2010) A consistent and accurate ab initio parametrization of density functional dispersion correction (DFT-D) for the 94 elements H-Pu. *The Journal of chemical physics* **132**, 154104.

Guo W. (2008) *Carbonate clumped isotope thermometry: application to carbonaceous chondrites & effects of kinetic isotope fractionation.*, California Institute of Technology.

Guo W., Mosenfelder J. L., Goddard III W. A. and Eiler J. M. (2009) Isotopic fractionations associated with phosphoric acid digestion of carbonate minerals: insights from first-principles theoretical modeling and clumped isotope measurements. *Geochimica et Cosmochimica Acta* **73**, 7203–7225.

Hafner J. (2008) Ab-initio simulations of materials using VASP: Density-functional theory and beyond. *Journal of computational chemistry* **29**, 2044–2078.

Halevy I., Fischer W. W. and Eiler J. M. (2011) Carbonates in the Martian meteorite Allan Hills 84001 formed at 18$\pm$4 C in a near-surface aqueous environment. *Proceedings of the National Academy of Sciences* **108**, 16895–16899.

Harrison A. L., Bénézeth P., Schott J., Oelkers E. H. and Mavromatis V. (2021) Magnesium and carbon isotope fractionation during hydrated Mg-carbonate mineral phase transformations. *Geochimica et Cosmochimica Acta* **293**, 507–524.

Herwartz D., Surma J., Voigt C., Assonov S. and Staubwasser M. (2017) Triple oxygen isotope systematics of structurally bonded water in gypsum. *Geochimica et Cosmochimica Acta* **209**, 254–266.

Hesse K.-F., Küppers H. and Suess E. (1983) Refinement of the structure of Ikaite, CaCO3· 6H2O. *Zeitschrift für Kristallographie-Crystalline Materials* **163**, 227–231.

Hobbs F. W. and Xu H. (2020) Magnesite formation through temperature and pH cycling as a proxy for lagoon and playa paleoenvironments. *Geochimica et Cosmochimica Acta* **269**, 101–116.

Hofmann M. E., Horváth B. and Pack A. (2012) Triple oxygen isotope equilibrium fractionation between carbon dioxide and water. *Earth and Planetary Science Letters* **319**, 159–164.

Hoppe P., MacDougall D. and Lugmair G. W. (2007) High spatial resolution ion microprobe measurements refine chronology of carbonate formation in Orgueil. *Meteorit & Planetary Scien* **42**, 1309–1320.

Horita J. (2014) Oxygen and carbon isotope fractionation in the system dolomite–water–CO2 to elevated temperatures. *Geochimica et Cosmochimica Acta* **129**, 111–124.

Horita J. and Wesolowski D. J. (1994) Liquid-vapor fractionation of oxygen and hydrogen isotopes of water from the freezing to the critical temperature. *Geochimica et Cosmochimica Acta* **58**, 3425–3437.

Huntington K. W., Eiler J. M., Affek H. P., Guo W., Bonifacie M., Yeung L. Y., Thiagarajan N., Passey B., Tripati A. and Daëron M. (2009) Methods and limitations of 'clumped'CO2 isotope (Δ47) analysis by gas-source isotope ratio mass spectrometry. *Journal of Mass Spectrometry* **44**, 1318–1329.

Jensen A. C., Imberti S., Habraken W. J. and Bertinetti L. (2020) Small ionic radius limits magnesium water interaction in amorphous calcium/magnesium carbonates. *The Journal of Physical Chemistry C* **124**, 6141–6144.

Jensen A. C. S., Rodriguez I., Habraken W. J. E. M., Fratzl P. and Bertinetti L. (2018) Mobility of hydrous species in amorphous calcium/magnesium carbonates. *Phys. Chem. Chem. Phys.* **20**, 19682–19688.

Kaplan H. H., Lauretta D. S., Simon A. A., Hamilton V. E., DellaGiustina D. N., Golish D. R., Reuter D. C., Bennett C. A., Burke K. N., Campins H., Connolly H. C., Dworkin J. P., Emery J. P., Glavin D. P., Glotch T. D., Hanna R., Ishimaru K., Jawin E. R., McCoy T. J., Porter N., Sandford S. A., Ferrone S., Clark B. E., Li J.-Y., Zou X.-D., Daly M. G., Barnouin O. S., Seabrook J. A. and Enos H. L. (2020) Bright carbonate veins on asteroid (101955) Bennu: Implications for aqueous alteration history. *Science* **370**, eabc3557.

Kresse G. and Furthmüller J. (1996) Efficient iterative schemes for *ab initio* total-energy calculations using a plane-wave basis set. *Phys. Rev. B* **54**, 11169–11186.

Kresse G. and Joubert D. (1999) From ultrasoft pseudopotentials to the projector augmented-wave method. *Phys. Rev. B* **59**, 1758–1775.

Lee M. R., Lindgren P., Sofe M. R., Alexander C. O. and Wang J. (2012) Extended chronologies of aqueous alteration in the CM2 carbonaceous chondrites: Evidence from carbonates in Queen Alexandra Range 93005. *Geochimica et Cosmochimica Acta* **92**, 148–169.

Leshin L. A., McKeegan K. D., Carpenter P. K. and Harvey R. P. (1998) Oxygen isotopic constraints on the genesis of carbonates from Martian meteorite ALH84001. *Geochimica et Cosmochimica Acta* **62**, 3–13.

Lin S.-T., Blanco M. and Goddard III W. A. (2003) The two-phase model for calculating thermodynamic properties of liquids from molecular dynamics: Validation for the phase diagram of Lennard-Jones fluids. *The Journal of chemical physics* **119**, 11792–11805.

Lin Y., Knapp W. J., Li W., Zheng M., Ye C., She J., Xia Z., Power I. M., Zhao Y. and Tipper E. T. (2023) Magnesium isotope constraints on the Holocene hydromagnesite formation in alkaline Lake Dujiali, central Qinghai-Tibetan Plateau. *Journal of Geophysical Research: Earth Surface* **128**, e2022JF006907.

Lindgren P., Lee M. R., Sofe M. R. and Zolensky M. E. (2013) Clasts in the CM 2 carbonaceous chondrite Lonewolf Nunataks 94101: Evidence for aqueous alteration prior to complex mixing. *Meteorit & Planetary Scien* **48**, 1074–1090.

Liu B. N., Zhou X. T., Cui X. S. and Tang J. G. (1990) Synthesis of lansfordite MgCO3*5H2O and its crystal structure investigation. *Science in China* **B33**, 1350–1356.

Lloyd M. K., Eiler J. M. and Nabelek P. I. (2017) Clumped isotope thermometry of calcite and dolomite in a contact metamorphic environment. *Geochimica et Cosmochimica Acta* **197**, 323–344.

Lucarelli J. K., Purgstaller B., Ulrich R. N., Parvez Z., Leis A., Goetschl K. E., Eagle R. A., Dietzel M. and Tripati A. (2023) Dual clumped (Δ47-Δ48) isotope data for amorphous carbonates and transformation products reveal a novel mechanism for disequilibrium clumped isotope effects. *Geochimica et Cosmochimica Acta* **359**, 119–134.

Magna T., Hu Y., Teng F.-Z. and Mezger K. (2017) Magnesium isotope systematics in Martian meteorites. *Earth and Planetary Science Letters* **474**, 419–426.

Mavromatis V., Power I. M., Harrison A. L., Beinlich A., Dipple G. M. and Bénézeth P. (2021) Mechanisms controlling the Mg isotope composition of hydromagnesite-magnesite playas near Atlin, British Columbia, Canada. *Chemical Geology* **579**, 120325.

Mavromatis V., Purgstaller B., Dietzel M., Buhl D., Immenhauser A. and Schott J. (2017) Impact of amorphous precursor phases on magnesium isotope signatures of Mg-calcite. *Earth and Planetary Science Letters* **464**, 227–236.

Mcsween Jr H. Y. and Harvey R. P. (1998) An evaporation model for formation of carbonates in the ALH84001 Martian meteorite. *International Geology Review* **40**, 774–783.

Méheut M., Lazzeri M., Balan E. and Mauri F. (2007) Equilibrium isotopic fractionation in the kaolinite, quartz, water system: Prediction from first-principles density-functional theory. *Geochimica et Cosmochimica Acta* **71**, 3170–3181.

Méheut M., Lazzeri M., Balan E. and Mauri F. (2009) Structural control over equilibrium silicon and oxygen isotopic fractionation: a first-principles density-functional theory study. *Chemical Geology* **258**, 28–37.

Melwani Daswani M., Schwenzer S. P., Reed M. H., Wright I. P. and Grady M. M. (2016) Alteration minerals, fluids, and gases on early Mars: Predictions from 1-D flow geochemical modeling of mineral assemblages in meteorite ALH 84001. *Meteorit & Planetary Scien* **51**, 2154–2174.

Mergelsberg S. T., Kerisit S. N., Ilton E. S., Qafoku O., Thompson C. J. and Loring J. S. (2020) Low temperature and limited water activity reveal a pathway to magnesite via amorphous magnesium carbonate. *Chem. Commun.* **56**, 12154–12157.

Monkhorst H. J. and Pack J. D. (1976) Special points for Brillouin-zone integrations. *Phys. Rev. B* **13**, 5188–5192.

de Obeso J. C., Santiago Ramos D. P., Higgins J. A. and Kelemen P. B. (2021) A Mg isotopic perspective on the mobility of magnesium during serpentinization and carbonation of the Oman ophiolite. *Journal of Geophysical Research: Solid Earth* **126**, e2020JB020237.

Oelkers E. H., Berninger U.-N., Pérez-Fernàndez A., Chmeleff J. and Mavromatis V. (2018) The temporal evolution of magnesium isotope fractionation during hydromagnesite dissolution, precipitation, and at equilibrium. *Geochimica et cosmochimica acta* **226**, 36–49.

O'Neil J. R. and Barnes I. (1971) C13 and O18 compositions in some fresh-water carbonates associated with ultramafic rocks and serpentinites: western United States. *Geochimica et Cosmochimica Acta* **35**, 687–697.

Oskierski H. C., Beinlich A., Mavromatis V., Altarawneh M. and Dlugogorski B. Z. (2019) Mg isotope fractionation during continental weathering and low temperature carbonation of ultramafic rocks. *Geochimica et cosmochimica acta* **262**, 60–77.

Oskierski H. C., Dlugogorski B. Z. and Jacobsen G. (2013) Sequestration of atmospheric CO2 in a weathering-derived, serpentinite-hosted magnesite deposit: 14C tracing of carbon sources and age constraints for a refined genetic model. *Geochimica et Cosmochimica Acta* **122**, 226–246.

Patel A. S., Raudsepp M. J., Wilson S. and Harrison A. L. (2024) Water Activity Controls the Stability of Amorphous Ca–Mg- and Mg-Carbonates. *Crystal Growth & Design* **24**, 2000–2013.

Patron P., Martinez C., Elena A. M., Blanchard M. and Pinilla C. (2025) Equilibrium isotope fractionation in carbonate minerals: Role of Mg-Ca distribution and thermal effects. *Geochimica et Cosmochimica Acta* **394**, 53–69.

Pearce C. R., Saldi G. D., Schott J. and Oelkers E. H. (2012) Isotopic fractionation during congruent dissolution, precipitation and at equilibrium: Evidence from Mg isotopes. *Geochimica et Cosmochimica Acta* **92**, 170–183.

Perdew J. P., Burke K. and Ernzerhof M. (1996) Generalized gradient approximation made simple. *Physical review letters* **77**, 3865.

Pinilla C., Blanchard M., Balan E., Natarajan S. K., Vuilleumier R. and Mauri F. (2015) Equilibrium magnesium isotope fractionation between aqueous Mg2+ and carbonate minerals: Insights from path integral molecular dynamics. *Geochimica et Cosmochimica Acta* **163**, 126–139.

Power I. M., Harrison A. L., Dipple G. M., Wilson S., Barker S. L. and Fallon S. J. (2019) Magnesite formation in playa environments near Atlin, British Columbia, Canada. *Geochimica et cosmochimica acta* **255**, 1–24.

Power I. M., Kenward P. A., Dipple G. M. and Raudsepp M. (2017) Room Temperature Magnesite Precipitation. *Crystal Growth & Design* **17**, 5652–5659.

Prange M. P., Mergelsberg S. T. and Kerisit S. N. (2023) Structural water in amorphous carbonate minerals: ab initio molecular dynamics simulations of X-ray pair distribution experiments. *Phys. Chem. Chem. Phys.* **25**, 6768–6779.

Purgstaller B., Goetschl K. E., Mavromatis V. and Dietzel M. (2019) Solubility investigations in the amorphous calcium magnesium carbonate system. *CrystEngComm* **21**, 155–164.

Quesnel B., Boulvais P., Gautier P., Cathelineau M., John C. M., Dierick M., Agrinier P. and Drouillet M. (2016) Paired stable isotopes (O, C) and clumped isotope thermometry of magnesite and silica veins in the New Caledonia Peridotite Nappe. *Geochimica et Cosmochimica Acta* **183**, 234–249.

Rabin S., Blanchard M., Pinilla C., Poitrasson F. and Grégoire M. (2023) Iron and silicon isotope fractionation in silicate melts using first-principles molecular dynamics. *Geochimica et Cosmochimica Acta* **343**, 212–233.

Raudsepp M. J., Wilson S. and Morgan B. (2023) Making Salt from Water: The Unique Mineralogy of Alkaline Lakes. *Elements* **19**, 22–29.

Raudsepp M. J., Wilson S., Morgan B., Patel A., Johnston S. G., Gagen E. J. and Fallon S. J. (2022) Non-classical crystallization of very high magnesium calcite and magnesite in the Coorong Lakes, Australia ed. N. Tosca. *Sedimentology* **69**, 2246–2266.

Raudsepp M. J., Wilson S., Zeyen N., Arizaleta M. L. and Power I. M. (2024) Magnesite everywhere: Formation of carbonates in the alkaline lakes and playas of the Cariboo Plateau, British Columbia, Canada. *Chemical Geology* **648**, 121951.

del Real P. G., Maher K., Kluge T., Bird D. K., Brown Jr G. E. and John C. M. (2016) Clumped-isotope thermometry of magnesium carbonates in ultramafic rocks. *Geochimica et Cosmochimica Acta* **193**, 222–250.

Rickaby Rem., Shaw S., Bennitt G., Kennedy H., Zabel M. and Lennie A. (2006) Potential of ikaite to record the evolution of oceanic δ18O. *Geology* **34**, 497–500.

Romanek C. S., Grossman E. L. and Morse J. W. (1992) Carbon isotopic fractionation in synthetic aragonite and calcite: effects of temperature and precipitation rate. *Geochimica et cosmochimica acta* **56**, 419–430.

Rosenbaum J. M. (1997) Gaseous, liquid, and supercritical fluid H2O and CO2: oxygen isotope fractionation behavior. *Geochimica et cosmochimica acta* **61**, 4993–5003.

Ross N. L. (1997) The equation of state and high-pressure behavior of magnesite. *American Mineralogist* **82**, 682–688.

Rustad J. R., Casey W. H., Yin Q.-Z., Bylaska E. J., Felmy A. R., Bogatko S. A., Jackson V. E. and Dixon D. A. (2010) Isotopic fractionation of Mg2+ (aq), Ca2+ (aq), and Fe2+ (aq) with carbonate minerals. *Geochimica et Cosmochimica Acta* **74**, 6301–6323.

Rustad J. R., Nelmes S. L., Jackson V. E. and Dixon D. A. (2008) Quantum-chemical calculations of carbon-isotope fractionation in CO2 (g), aqueous carbonate species, and carbonate minerals. *The Journal of Physical Chemistry A* **112**, 542–555.

Schauble E. A. (2011) First-principles estimates of equilibrium magnesium isotope fractionation in silicate, oxide, carbonate and hexaaquamagnesium (2+) crystals. *Geochimica et Cosmochimica Acta* **75**, 844–869.

Schauble E. A., Ghosh P. and Eiler J. M. (2006a) Preferential formation of 13C–18O bonds in carbonate minerals, estimated using first-principles lattice dynamics. *Geochimica et Cosmochimica Acta* **70**, 2510–2529.

Schauble E. A., Ghosh P. and Eiler J. M. (2006b) Preferential formation of 13C–18O bonds in carbonate minerals, estimated using first-principles lattice dynamics. *Geochimica et Cosmochimica Acta* **70**, 2510–2529.

Schauble E. A. and Young E. D. (2021) Mass dependence of equilibrium oxygen isotope fractionation in carbonate, nitrate, oxide, perchlorate, phosphate, silicate, and sulfate minerals. *Reviews in Mineralogy and Geochemistry* **86**, 137–178.

Scheller E. L., Ingalls M., Eiler J. M., Grotzinger J. P. and Ryb U. (2023) The mechanisms and stable isotope effects of transforming hydrated carbonate into calcite pseudomorphs. *Geochimica et Cosmochimica Acta* **354**, 146–164.

Scheller E. L., Razzell Hollis J., Cardarelli E. L., Steele A., Beegle L. W., Bhartia R., Conrad P., Uckert K., Sharma S. and Ehlmann B. L. (2022) Aqueous alteration processes in Jezero crater, Mars—implications for organic geochemistry. *Science* **378**, 1105–1110.

Scheller E. L., Swindle C., Grotzinger J., Barnhart H., Bhattacharjee S., Ehlmann B. L., Farley K., Fischer W. W., Greenberger R. and Ingalls M. (2021) Formation of Magnesium Carbonates on Earth and Implications for Mars. *Journal of Geophysical Research: Planets* **126**, e2021JE006828.

Schott J., Mavromatis V., Fujii T., Pearce C. R. and Oelkers E. H. (2016) The control of carbonate mineral Mg isotope composition by aqueous speciation: Theoretical and experimental modeling. *Chemical Geology* **445**, 120–134.

Sharma S. D., Patil D. J. and Gopalan K. (2002) Temperature dependence of oxygen isotope fractionation of CO2 from magnesite-phosphoric acid reaction. *Geochimica et Cosmochimica Acta* **66**, 589–593.

Stamm F. M., Méheut M., Zambardi T., Chmeleff J., Schott J. and Oelkers E. H. (2022) Determination of the equilibrium magnesium isotope fractionation factors between brucite and aqueous inorganic and organic species. *Geochimica et Cosmochimica Acta* **336**, 33–49.

Steele A., Benning L. G., Wirth R., Schreiber A., Araki T., McCubbin F. M., Fries M. D., Nittler L. R., Wang J. and Hallis L. J. (2022) Organic synthesis associated with serpentinization and carbonation on early Mars. *Science* **375**, 172–177.

Steinfink H. and Sans F. J. (1959) Refinement of the crystal structure of dolomite*. *American Mineralogist* **44**, 679–682.

Stephan G. W. and MacGillavry C. H. (1972) The crystal structure of nesquehonite, MgCO3. 3H2O. *Acta Crystallographica Section B: Structural Crystallography and Crystal Chemistry* **28**, 1031–1033.

Swindle C., Vasconcelos P., Dalleska N., Cardarelli E., Bhattacharjee S., Dimarco Z., Farley K. A. and Present T. (2025) Trace Element Compositions and Redox Shifts Preserved in Magnesites, Sediments and Soils from the Kunwarara Magnesite Mine. *Applied Geochemistry*, 106494.

Tanaka J.-Y., Kawano J., Nagai T. and Teng H. (2019) Transformation process of amorphous magnesium carbonate in aqueous solution. *Journal of Mineralogical and Petrological Sciences* **114**, 105–109.

Valley J. W., Eiler J. M., Graham C. M., Gibson E. K., Romanek C. S. and Stolper E. M. (1997) Low-temperature carbonate concretions in the Martian meteorite ALH84001: Evidence from stable isotopes and mineralogy. *Science* **275**, 1633–1638.

Vogel J. C., Grootes P. M. and Mook W. G. (1970) Isotopic fractionation between gaseous and dissolved carbon dioxide. *Zeitschrift für Physik A Hadrons and nuclei* **230**, 225–238.

Wang W., Qin T., Zhou C., Huang S., Wu Z. and Huang F. (2017) Concentration effect on equilibrium fractionation of Mg-Ca isotopes in carbonate minerals: Insights from first-principles calculations. *Geochimica et Cosmochimica Acta* **208**, 185–197.

Wang W., Zhou C., Liu Y., Wu Z. and Huang F. (2019) Equilibrium Mg isotope fractionation among aqueous Mg2+, carbonates, brucite and lizardite: Insights from first-principles molecular dynamics simulations. *Geochimica et Cosmochimica Acta* **250**, 117–129.

Warren P. H. (1998) Petrologic evidence for low-temperature, possibly flood evaporitic origin of carbonates in the ALH84001 meteorite. *Journal of Geophysical Research: Planets* **103**, 16759–16773.

White C. E., Henson N. J., Daemen L. L., Hartl M. and Page K. (2014) Uncovering the true atomic structure of disordered materials: the structure of a hydrated amorphous magnesium carbonate (MgCO3· 3D2O). *Chemistry of Materials* **26**, 2693–2702.

Yoshimura T., Araoka D., Naraoka H., Sakai S., Ogawa N. O., Yurimoto H., Morita M., Onose M., Yokoyama T. and Bizzarro M. (2024) Breunnerite grain and magnesium isotope chemistry reveal cation partitioning during aqueous alteration of asteroid Ryugu. *Nature Communications* **15**, 6809.

Zedef V., Russell M. J., Fallick A. E. and Hall A. J. (2000) Genesis of vein stockwork and sedimentary magnesite and hydromagnesite deposits in the ultramafic terranes of southwestern Turkey: a stable isotope study. *Economic Geology* **95**, 429–445.

Zeebe R. E. (2010) A new value for the stable oxygen isotope fractionation between dissolved sulfate ion and water. *Geochimica et Cosmochimica Acta* **74**, 818–828.

Zeebe R. E. and Wolf-Gladrow D. (2001) *$CO_2$ in seawater: equilibrium, kinetics, isotopes*., Gulf Professional Publishing.

Zhang Y. and Liu Y. (2018) The theory of equilibrium isotope fractionations for gaseous molecules under super-cold conditions. *Geochimica et Cosmochimica Acta* **238**, 123–149.

Zheng Y.-F. (1999) Oxygen isotope fractionation in carbonate and sulfate minerals. *Geochemical Journal* **33**, 109–126.

## *Chapter 6*

# *IN SITU* MAGNESIUM ISOTOPE MEASUREMENT OF CARBONATES USING AN ION MICROPROBE

Surjyendu Bhattacharjee[1]*, Theodore M. Present[1], Clara L. Blättler[2], Damanveer S. Grewal[3], Yunbin Guan[1], Chi Ma[1], Maciej G. Sliwinski[4], Paul D. Asimow[1] and John M. Eiler[1]

[1]Division of Geological and Planetary Sciences, California Institute of Technology, Pasadena, CA, USA

[2]Department of the Geophysical Sciences, University of Chicago, Chicago, IL, USA

[3]Department of Earth and Planetary Sciences, Yale University, New Haven, CT, USA

[4]University of Alaska, Fairbanks, AK, USA

*Corresponding Author: sbhattac@caltech.edu

## Abstract

The magnesium isotope ratios of carbonates have found widespread utility as a geochemical tool in terrestrial and extraterrestrial contexts. However, existing bulk digestion techniques are unable to distinguish between different generations of carbonates within a sample, are destructive to samples, and do not reveal any spatial variation in carbonates' Mg isotope ratio at the micrometer scale. Here, we document the development of a suite of carbonate standards to measure Mg isotope ratios of carbonates *in situ* using an ion microprobe (IMS 7f-GEO at Caltech), for domains ranging from 5–20 µm. We found that the matrix effect for Mg isotope measurement behaves consistently across different sessions, correlates with molar Fe+Mn content of carbonates, and ranges from 0–20‰ (relative to stoichiometric magnesite) for carbonates in the magnesite-siderite series and 0–23‰ (relative to stoichiometric dolomite) for those in the dolomite-ankerite series. Analytical precision was 0.2–0.3‰ (1σ internal). Polynomial fits to the instrumental fractionation vs. molar Fe+Mn content of carbonates give a reliable means to correct for matrix effects. We tested the accuracy of this protocol using secondary standards, including an Fe-zoned dolomite sample. Our newly developed method enables future analysis of micron-scale Mg isotopic variability in terrestrial and extraterrestrial carbonates, including those returned from asteroids Ryugu and Bennu and from Mars.

## 6.1 Introduction

Carbonate minerals are key products of the planetary carbon cycle and record environmental conditions where they formed. They are found in a variety of terrestrial environments, including high temperature igneous/hydrothermal environments (Beinlich et al., 2014; de Obeso et al., 2021; Jin et al., 2025); metamorphic environments (Castelli, 1991; Kuznetsov et al., 2021); low temperature aqueous environments such as playas, sabkhas, and lakes (Passey and Ji, 2019; Mavromatis et al., 2021); caves (Kluge et al., 2014); soil and sediments (Cerling, 1984); diagenetic environments (Swart, 2015; Bryant et al., 2022); and biogenic settings including the global ocean (Bosence, 1989; McCorkle et al., 1990; Allwood et al., 2006). Carbonate minerals such as dolomite, calcite, and 'breunnerite' (Fe-magnesite) are widely detected in carbonaceous chondrites, including CM (Guo and Eiler, 2007; Clog et al., 2024), CR (Guo, 2008; Jilly-Rehak et al., 2018), CI (Johnson and Prinz, 1993; Zito et al., 1998; Guo, 2008; Fujiya et al., 2013; Garvie and Wittmann, 2025; Gattacceca et al., 2025), and ungrouped (Fujiya et al., 2013; Bischoff et al., 2021) chondrites. They are also detected in Martian meteorites (Gyollai et al., 1993; Bridges and Grady, 1999; Farquhar and Thiemens, 2000; Eiler et al., 2002; Piercy et al., 2022) and observed on the Martian surface using orbital spectroscopy (Ehlmann et al., 2008) or rover instrumentation (Niles et al., 2013; Tosca et al., 2025). Lastly, they have been detected in abundance in samples returned from asteroids such as Ryugu (Fujiya et al., 2023; McCain et al., 2023; Kita et al., 2024) and Bennu (Kaplan et al., 2020; Lauretta et al., 2024).

In this work, we demonstrate a new method for analyzing the isotope ratio of magnesium in carbonates. More broadly, the ratios of stable isotopes of carbon, oxygen and cations (principally Mg, Ca, and Fe) in carbonate minerals each record different aspects of the sources, formation conditions, or post-formation modifications of the specimens. While carbon and oxygen isotope ratios are mostly controlled by temperature of formation and isotope ratios of source fluids, the cation isotope ratios—particularly those of magnesium—are particularly sensitive to the nature of the water-rock reactions that formed the carbonates. Hence carbonate minerals and their isotope ratios provide a variety of tools for understanding water-rock cycles on a variety of planetary bodies, which in turn is valuable because water-rock interactions are understood to modulate planetary climate, carbon cycle, and habitability (Walker et al., 1981; Wordsworth, 2016; Winnick and Maher, 2018; Moore et al., 2025; Adams et al., 2025). Water-rock cycling can occur via weathering, serpentinization, and/or a combination of these processes. These processes fractionate Mg isotopes differently (depending on temperature and the formation of secondary minerals), resulting in fluids with distinct Mg isotope ratios. Carbonates track the Mg isotope ratios of the fluids they grow from and therefore constitute a record that can distinguish among these processes (Oskierski et al., 2019; de Obeso et al., 2021; Qu et al., 2025; Luo et al., 2025). For this reason, the Mg isotope ratios of carbonates have recently been widely applied to the problem of tracking carbonate genesis (e.g., Teng, 2017; Bryant et al., 2022).

The Mg isotopic ratio ($^{26}$Mg/$^{24}$Mg) of carbonates is conventionally measured via bulk acid digestion techniques (e.g., Fantle and Higgins, 2014; Blättler et al., 2015; Blättler and Higgins, 2017; Bryant et al., 2022). There are at least four limitations of such bulk methods: (1) They are destructive to the sample. For cases where sample availability is limited, this is a problem. (2) They do not produce phase-resolved Mg isotope data, and average different carbonates present in the sample. For a sample that contains different types of carbonates of different generations and different Mg isotope composition, this is a potential problem. (3) Bulk digestion techniques cannot generate texturally resolved isotope data. Hence, they cannot capture the variation of a particular type of carbonate with different cation chemistry/texture. (4) For samples where carbonates are mixed with phyllosilicates, the Mg isotope ratio of the carbonate can be contaminated by Mg released from phyllosilicates during digestion, which can compromise data quality.

An ion microprobe-based $^{26}$Mg/$^{24}$Mg measurement method can overcome all of the above challenges and render texture and phase-resolved Mg isotope ratios, which can capture the evolution of the Mg isotopes in carbonates over the precipitation timescale. Although there are well-established methods for carbonate carbon and oxygen isotope measurements using the ion microprobe (Eiler et al., 1997; Rollion-Bard and Marin-Carbonne, 2011; Śliwiński et al., 2016a, b, 2018; Xu et al., 2022; Kita et al., 2024), their Mg isotopes have not yet been measured using ion microprobes. Here, we report a method that can measure $^{26}Mg/^{24}Mg$ of carbonates using an ion microprobe, with a full investigation of instrumental matrix effects across different compositional spaces and assessment of the accuracy and precision of the method. Since this study aims to develop standards that can be used to measure intermediate Ca-Mg-Fe carbonates from Martian meteorite ALH84001, we synthesized compositionally matched standards to verify the accuracy of our matrix effect correction protocol.

## 6.2 Materials and methods

### 6.2.1 Natural carbonates

Natural carbonates, including calcite and solid solutions across the dolomite-ankerite and magnesite-siderite series, were acquired from the mineral collection of the Division of Geological and Planetary Sciences, Caltech.

### 6.2.2 Synthetic carbonates

We used knowledge of the phase relations of mixed carbonates (Franzolin et al., 2011; Shatskiy et al., 2018) to synthesize, at elevated pressure and temperature, standards that match the major cation chemistry of carbonates from the Martian meteorite ALH84001, using a piston cylinder apparatus at the California Institute of Technology. Briefly, calcite, magnesite and siderite were ground, dried and mixed in requisite proportions to match composition of ALH84001 carbonates. Before the experiment, starting mixes were stored in a desiccator. We performed experiments at 3 GPa and 1188–1413 K in Au capsules for 48-72 hours, following protocols of previous studies (*3–6*). All of these experimental carbonates showed equilibrium textures and a very close compositional match with ALH84001 carbonates (Fig. 6.1a–d). Experimental conditions are given in Table 6.1.

### 6.2.3 Scanning Electron Microscope - Energy Dispersive Spectroscopy (SEM-EDS)

SEM-EDS was done at California Institute of Technology, on a Zeiss 1550 VP field emission SEM, equipped with an Oxford X-Max Si-Drift Detector EDS system for compositional analysis. We used an acceleration voltage of 15 kV and a working distance of 4.7 mm for both imaging and spectral acquisition.

### 6.2.4 Electron Probe Microanalysis (EPMA)

Major cation chemistry of carbonates was determined using a field-emission electron microprobe (JEOL JXA-iHP200F "Hyperprobe") in wavelength-dispersive spectroscopy mode at California Institute of Technology. Analytical conditions were 15 kV accelerating voltage, 10 nA beam current and 10 μm defocused beam. Natural carbonate standards (Calcite, Dolomite, Siderite, Strontianite and Rhodochrosite) were used as standards to quantify Ca, Mg, Fe, Mn and Sr content in carbonates.

### 6.2.5 Mass spectrometry

#### 6.2.5.1 True Mg isotopic composition of standards

$^{26}$Mg/$^{24}$Mg ratio of standards was measured at University of Chicago, using a Thermo Neptune XT multi-collector inductively-coupled plasma mass spectrometer (MC-ICP-MS), following a well-established protocol described previously (Bryant et al., 2022). Samples were dissolved overnight in excess 5% $HNO_3$ in a sonicated water bath set at 65 °C. These samples were then diluted in de-ionized water. 25 μL aliquots from this diluted sample were processed via a Thermo/Dionex ion chromatography system (IC), using 30 mM methanesulfonic acid eluent (25 mM for seawater) to separate Mg and/or Ca from matrix elements, and fraction collected in eluent windows. The resultant solution was transferred to Teflon vials, dried down on a hot plate at 150 °C, treated with 200 μL 20 N nitric acid for 30 minutes to oxidize organics, and dried down again. Adequate 2% nitric acid was then added to each vial to have ~150 ppb Mg solution for mass spectrometry.

The guard column in the IC removed iron from samples having less than 13 mol% siderite. Above this threshold, Fe started eluting and elution times of Mg-Ca peaks started to shift. Therefore, samples with more that 13 mol% siderite were considered high Fe samples and were pre-processed to remove Fe using offline ion-exchange resin. These samples were digested overnight in Teflon vials on a hot plate set at 115 °C. Subsequently, they were dried down and refluxed in 200 μL 16N $HNO_3$ overnight three times (drying down between steps), to ensure all Fe was oxidized to $Fe^{3+}$. Afterwards, they were refluxed with 200 μL 6N HCl overnight thrice (drying down between steps) to ensure all Fe dissolved in HCl. In the final step, they were reconstituted in 1 mL 6N HCl for preparatory column chemistry. Using a BioRad AG1-X8 resin (100-200 mesh) following a protocol described before (Schoenberg and von Blanckenburg, 2005), we removed Fe from all Fe bearing carbonates. The efficacy of this method was tested on a subset of samples by measuring their major cation composition before and after Fe removal. These measurements were done using an Agilent 8800 Triple Quadrupole ICP-MS at the Resnick Water and Environment Lab, California Institute of Technology. Samples were introduced in 5% $HNO_3$. Isotopes $^{24}Mg$ (in no gas mode), $^{43}Ca$, $^{56}Fe$ (in He mode) were monitored to make calibration curves and concentration calculations. We achieved near-complete Fe removal from samples while Mg recovery was 92% or better (Table 6.2). After this step, the samples were again passed through the Thermo/Dionex ion chromatography system to separate Mg from Ca, as described in previous paragraph, to finally obtain ~150 ppb Mg solution for mass spectrometry.

For Mg isotopic analysis, samples were introduced using a dual-path glass cyclonic spray chamber into a Thermo Neptune XT MC-ICP-MS. Low resolution mode was used for measuring $^{24}Mg$, $^{25}Mg$ and $^{26}Mg$. The effect of [Mg] on $\delta^{26}Mg$ was established using a 5-point calibration. Sample-standard bracketing was used and IHD, RUB, and seawater standards were used to convert the measured $^{26}Mg/^{24}Mg$ to the DSM-3 scale:

$$\delta^{26}Mg_{DSM\text{-}3} = \left[ \frac{\left( {}^{26}Mg / {}^{24}Mg \right)_{sample}}{\left( {}^{26}Mg / {}^{24}Mg \right)_{DSM\text{-}3}} - 1 \right] * 1000 \quad (1)$$

Mg three isotope plots ($^{26}Mg/^{24}Mg$ vs $^{25}Mg/^{24}Mg$) were constructed and applied to ensure that all measured data conformed to mass-dependent fractionation laws.

### 6.2.5.2 Secondary Ion Mass Spectrometry (SIMS)

Mg isotope ratios of standard and unknown carbonates were measured using an ion microprobe (Cameca 7f-GEO) at the California Institute of Technology Microanalysis Center. Samples were coated with Au and the measurements were made over 3 analytical sessions. The analytical conditions are listed in Table 6.3. After analysis, pits were investigated using SEM-EDS. Any pit found to have missed the target area was discarded. About 5 points were measured per sample to assess sample heterogeneity and analytical uncertainties (internal and external) were propagated in quadrature.

Synthetic and natural carbonate standards were used to investigate the matrix effects, which are characterized as variation in instrumental mass fractionation (IMF) with carbonate cation chemistry, defined as:

$$\mathrm{IMF} = \left[ \frac{\left({}^{26}\mathrm{Mg}/{}^{24}\mathrm{Mg}\right)_{\mathrm{SIMS}}}{\left({}^{26}\mathrm{Mg}/{}^{24}\mathrm{Mg}\right)_{\mathrm{True}}} - 1 \right] * 1000 \quad (2)$$

IMF of a mineral relative to an anchor mineral A is expressed as:

$$\mathrm{IMF\ (relative\ to\ A)} = \mathrm{IMF} - \mathrm{IMF(A)} \quad (3)$$

Instrumental drift was monitored and corrected for by measuring a standard pure magnesite (2123) and pure dolomite (7920) across analytical sessions. For the dolomite-ankerite and magnesite-siderite series, IMF is expressed relative to 12700 dolomite and 2123 magnesite, respectively. For synthetic standards, IMF is expressed relative to 2123 magnesite.

## 6.3 Results

### 6.3.1 Textures and compositions of carbonates

The natural carbonate minerals were crystalline and mostly free of inclusions of secondary phases. One natural magnesite sample (LW57) was polycrystalline and massive in appearance. We characterized 11 standards across the dolomite-ankerite join, with molar Fe+Mn content ranging from 0–0.36 and molar Ca content 0.49–0.52 (Fig. 6.1d). Similarly, we characterized 9 standards across the magnesite-siderite series, with molar Fe+Mn content from 0–0.79 and molar Ca content from 0–0.03 (Fig. 6.1d).

Synthetic standards were texturally and compositionally homogeneous (Fig. 6.1 a–c). Since these are sub-solvus experiments, they contained magnesite (major phase) and dolomite (minor phase). High Fe magnesite standards (Run3 and Run5) also had magnetite in them, which is an oxidation product of siderite used in the starting mix (Franzolin et al., 2011; Shatskiy et al., 2018). The magnetite, however, was Mg-free. These high-Fe magnesites represent an important part of carbonate composition space for subsequent studies because they are close to the composition of carbonates from Martian meteorite ALH84001. The magnesites covered a range of 0.04–0.13 for their molar Ca content and 0–0.33 in their molar Fe+Mn content.

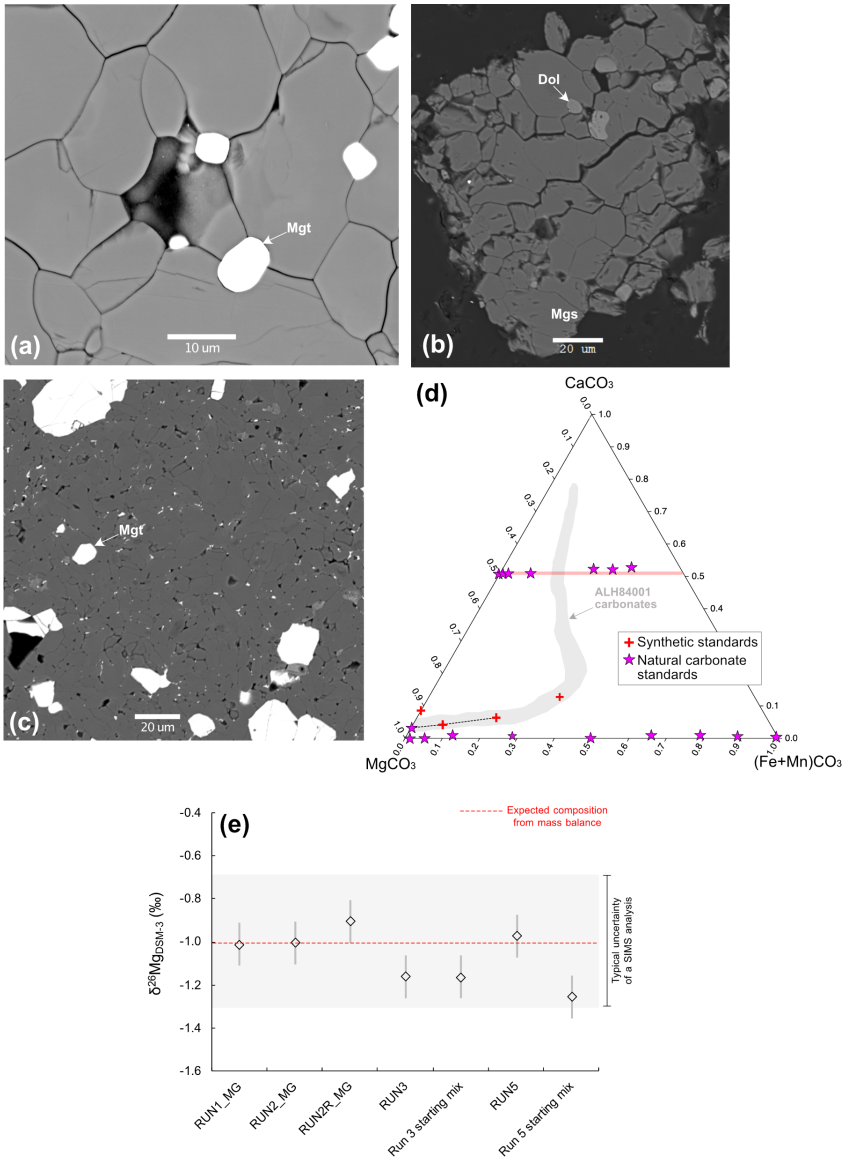

Figure 6.1: Texture, cation chemistry and Mg isotopic composition of synthetic standards. (a-c) Representative equilibrium textures of Fe-Ca rich magnesites after experiment. (d) Major cation chemistry of synthetic carbonates and natural standards, with composition of ALH84001 carbonates shown as shaded region. (e) Mg isotopic compositions of standards and their starting mixes measured by MC-ICP-MS. The red dotted line indicates composition

expected from mass balance calculations. Within typical SIMS uncertainty, these experimental products are statistically indistinguishable from their starting mixes and mass balance calculations.

The $\delta^{26}Mg_{DSM\text{-}3}$ of experimental products was measured using MC-ICP-MS. Within typical SIMS uncertainty (1σ~0.4‰), $\delta^{26}Mg_{DSM\text{-}3}$ of experimental products is indistinguishable from the $\delta^{26}Mg_{DSM\text{-}3}$ of the starting materials used in the experiments (Fig. 6.1e). This agreement suggests that the experiments behaved as a closed system with respect to Mg. The natural carbonates covered a ~3.5‰ range in $\delta^{26}Mg_{DSM\text{-}3}$ (from –2.82‰ to 0.54‰, Table 6.4).

### 6.3.2 Matrix effects across the Magnesite-Siderite series

Matrix effects in carbonates from the magnesite-siderite series were evaluated in analytical sessions 1 and 2, with different analytical conditions (Table 6.3). In both cases, the IMF relative to 2123 magnesite increased non-linearly from 0‰ to 20‰ (Fig. 6.2b) with increasing molar Fe+Mn content. The rise was consistent in both sessions, and agrees with prior findings (Śliwiński et al., 2016b, a). However, due to drastically different analytical conditions, calibrations from sessions 1 and 2 looked different. Second-order polynomials were fit to the data, which yielded calibrations for sessions 1 and 2 with residuals (mean absolute deviations, MAD) of 0.46‰ and 0.8‰, respectively, where respective average residuals were 0±0.24‰ (1SE) and 0±0.42‰ (1SE).

### 6.3.3 Matrix effects across the Dolomite-Ankerite series

Matrix effects of carbonates from dolomite-ankerite series were evaluated in analytical sessions 1 and 3, with different analytical conditions (Table 6.3). In both cases, the IMF relative to 12700 dolomite increased non-linearly from 0‰ to 23‰ (Fig. 6.2b) with increasing molar Fe+Mn content. The rise was consistent in both sessions, and consistent with previous findings (Śliwiński et al., 2018). Second-order polynomials were fit to the data, which yielded calibrations for sessions 1 and 3 with residuals (mean absolute deviations, MAD) of 0.72‰ and 0.58‰, respectively, where respective average residuals were 0±0.32‰ (1SE) and 0±0.31‰ (1SE).

### 6.3.4 Matrix effects for Calcite

Matrix effects were also evaluated for a calcite that had 0.43 mol% $MgCO_3$ in it. This development was aimed at measuring Mg-calcites. 22 spots were measured on a grain. The calcite had an IMF of –49.1±0.1‰ (1SE) (Fig. 6.2f). Because we used different instrumental conditions to analyze the calcite (larger beam current, longer counting time), this IMF was not anchored to dolomite or magnesite.

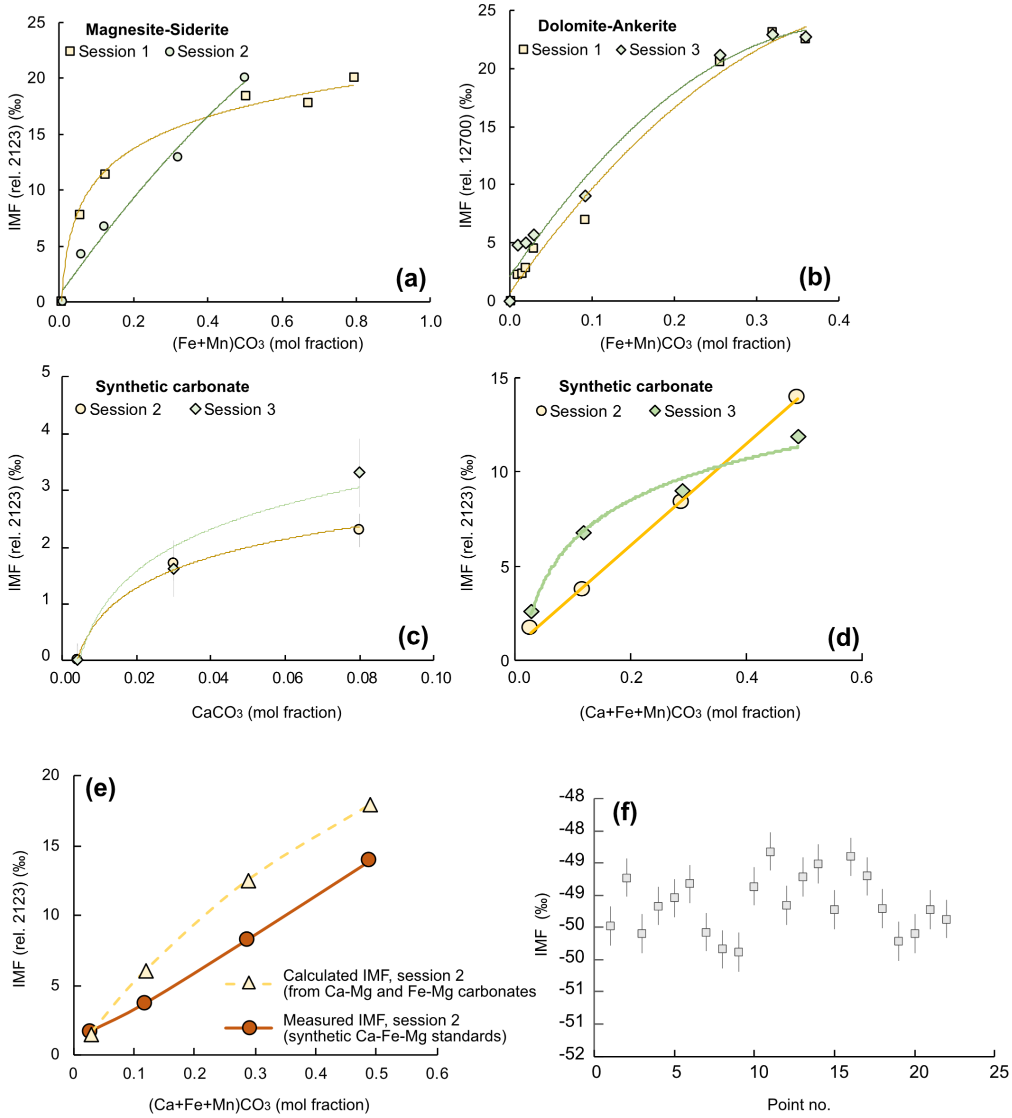

Figure 6.2: SIMS matrix effects for natural and synthetic carbonates from (a) magnesite-siderite, (b) dolomite-ankerite, (c) Fe-free Ca-magnesite, and (d) synthetic carbonate. Panel (e) shows the accuracy of a two-step IMF correction (see text). Panel (f) shows the reproducibility of the IMF for calcite.

### 6.3.5 Matrix effects for synthetic carbonates

Synthetic carbonates were analyzed in sessions 2 and 3. Two series of calibrations were constructed:

(1) One using 2123, LW57 and Run1 (all Fe-free) to evaluate the dependence of IMF on molar Ca content of carbonates (Fig. 6.2c).

(2) One with LW57, Run2R1, Run3 and Run5, a series whose compositions vary along the zoning trend of carbonate concretions in ALH84001 (dotted line in Fig. 6.1d), to evaluate the effect of co-varying molar Ca+Fe+Mn content of IMF (Fig. 6.2d).

IMF (relative to 2123) increased non-linearly from 0‰ to 3.5‰ (for the Fe-free first case) and from 2‰ to 14‰ (for the Fe-bearing second case) with increasing Ca or Ca+Fe+Mn content. The rise was consistent in both sessions. This demonstrates that IMF strongly depends on both molar Ca and Fe+Mn content and is more sensitive to the latter. None of our tests indicated any resolved difference between the effects of Fe and of Mn.

## 6.4 Discussion

### 6.4.1 Matrix effect estimation for mixed carbonates

This study is motivated by measuring the Mg isotopic composition of ~3.94 Ga carbonates in Martian meteorite ALH84001. These carbonates have mixed Ca-Mg-Fe-rich compositions (Fig. 6.1d) that are terrestrially metastable. Finding suitable natural standards for them is difficult. Because ALH84001 carbonates contain significant Ca (up to 15 mol% $CaCO_3$), implementing a correction solely based on Fe+Mn content of carbonates is problematic, as such treatment would neglect the contribution of Ca towards matrix effect. For these carbonates, there are two approaches to estimate the matrix effect as a function of carbonate cation composition:

a) A one-step correction based on the variation of IMF vs Ca+Fe+Mn content of synthetic standards. Given that our synthetic standards cover the composition range of ALH84001 concretion carbonates (dotted line, Fig. 6.1d), this approach provides a direct way for matrix effect correction without any of the assumptions involved in interpolating from separate Ca and Fe+Mn corrections.

b) A two-step correction based on the matrix effect of end-member carbonates. Here, the effects of molar Ca content and of molar Fe+Mn content are estimated separately and then added together. This is a common approach that previous SIMS studies employed for C and O isotopic measurements (Valley et al., 1997). A two-point linear IMF correction for Ca is traditionally constructed using Fe-free magnesite and dolomite (since intermediate compositions are rare due to the dolomite-magnesite solvus).

We have tested the accuracy of each correction scheme. Our measured IMF on synthetic carbonates in session 2 (Fig. 6.2e) accurately represents the matrix effects on mixed carbonates. We improved on the usual two-point linear estimate of the influence of Ca on IMF; our natural and synthetic Fe-free carbonate standards enable instead a non-linear three-point calibration over a slightly smaller compositional range (mol fraction $CaCO_3$ ~ 0–0.9). Following our calibrations of IMF vs. molar Ca content of Ca-magnesites (Fe-free) (Fig. 6.2c) and IMF vs. Fe+Mn content of magnesite-siderite (Fig. 6.2a), we calculated IMF for synthetic ternary carbonates by adding the calculated IMF from Ca and Fe+Mn separately, expressed relative to 2123. This two-step correction overestimates the IMF by 2.3–4.1‰ in the compositional range of interest (Fig. 6.2e). This inaccuracy is significantly larger than the analytical uncertainty (propagated $1\sigma$~0.4‰). Hence, a two-step correction for ion-microprobe $^{26}Mg/^{24}Mg$ measurements that assumes independent and additive effects of Ca and of Fe+Mn is inaccurate for ternary carbonates and should be avoided.

### 6.4.2 Accuracy of protocol

We tested the accuracy of our SIMS $^{26}Mg/^{24}Mg$ measurement protocol and matrix effect correction scheme using secondary standards of end-member dolomite and magnesite and an Fe–Mn zoned dolomite. The zoned dolomite (Fig. 6.3a,b) has domains that have major cation composition close to ALH84001 Fe-dolomites (Fig. 6.3c). Along a traverse from point A to point C in the grain (Fig. 6.3a), the molar Fe+Mn fraction increases from 0.05 to 0.15 (Fig. 6.3a). This sample has $\delta^{26}Mg_{DSM\text{-}3}$ = –0.5‰ based on analysis of two aliquots of bulk powder in MC-ICP-MS. Multiple spots spanning the Fe-Mn gradient in two different grains of this sample were measured $^{26}Mg/^{24}Mg$ by SIMS (Fig. S3a). The matrix effect was corrected to a compositionally closest dolomite (15086) standard as well as an Fe-free dolomite standard (12700), using the calibration curve of dolomite-ankerite series (Fig. 6.2b, session 1), and then the corrected ratio was converted to DSM-3 scale.

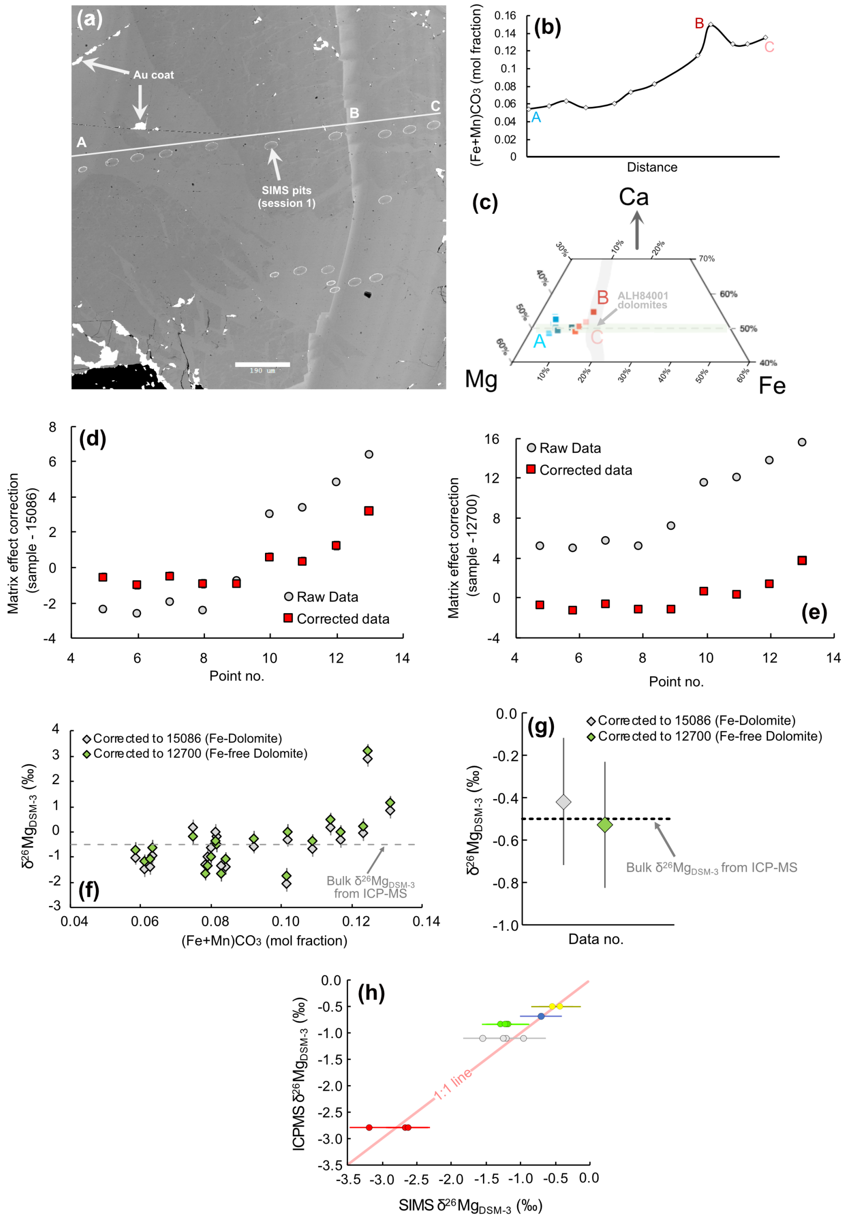

Figure 6.3: Accuracy test of SIMS method using secondary standards. (a) BSE image of a Fe-Mn zoned ankerite, where bright bands indicate Fe-Mn rich areas. (b) Variation of Fe+Mn content of carbonate across a transect. (c) Major cation chemistry of carbonates across a transect. (d) Data before and after matrix correction to compositionally closest dolomite (15086). (e) Data before and after matrix correction to Fe-free dolomite (12700).

(f) Variation of $\delta^{26}$Mg of zoned ankerite as a function of their Fe+Mn content, for both matrix effect correction schemes. (g) Comparison of grain average $\delta^{26}$Mg from SIMS and ICPMS. (h) Agreement of SIMS and ICPMS measured $\delta^{26}$Mg of magnesite and dolomite samples used as secondary standards.

The raw and matrix corrected data for both cases are shown is Fig. 6.3d,e, indicating the extent of matrix effect. In both cases, the corrected data ended up having statistically indistinguishable values from each other, and grain average $\delta^{26}Mg_{DSM-3}$ measured by SIMS in both cases were statistically indistinguishable from the bulk value measured by MC-ICP-MS (Fig. 6.3f,g; Table 6.5). This demonstrates the reproducibility and accuracy of our protocol, even with large matrix effect corrections. Intriguingly, it reveals variation of $\delta^{26}Mg_{DSM-3}$ with carbonates' molar Fe+Mn content (Fig. 6.3f), which bulk techniques are unable to observe.

Additionally, we tested the accuracy of this method on several end-member dolomite and magnesite specimens. We found that SIMS-measured $\delta^{26}$Mg agrees well with that from ICPMS (Fig. 6.3h), further validating our protocol.

### 6.4.3 Potential applications

To our knowledge, this is the first study to report a protocol for accurate, in-situ $^{26}Mg/^{24}Mg$ measurement of carbonates and to establish an accurate matrix effect correction scheme for mixed Ca-Mg-Fe carbonates. Our method would facilitate future Mg isotopic studies of complex terrestrial and extraterrestrial carbonates, such as samples from asteroids Bennu and Ryugu, or those returned from Mars.

Terrestrial carbonates—depending on their origin—can show considerable textural and paragenetic complexity. One such example is Mg-carbonates found in low-temperature serpentinisation environments, where multiple generations of meteoric fluid percolation and magmatic volatile flux weather and serpentinize igneous rocks, form different carbonates in different episodes, recrystallize earlier carbonates, and precipitate chert. The extensive overprinting forms multiple generations of carbonates with complex textural relationships. One such example is shown from the Gumigil mine, Great Serpentinite Belt, Australia. In Fig. 6.4, we can see a magnesite-silica-dolomite-magnesite assemblage. The magnesites included in chert (top figures) and dolomite included in massive magnesite (bottom left) are of different generations and both are needed to constrain the alteration history of rocks from that region. Bulk digestion measurements cannot distinguish between these carbonates, but our ion-microprobe method can render accurate *in situ*, phase-resolved measurements of these carbonates to constrain their alteration history.

Another potential application lies in measurement of extraterrestrial carbonates such as those from carbonaceous chondrites, asteroids like Ryugu and Bennu, and Martian meteorites. Mg isotope geochemistry of these carbonates is unexplored to date but has the potential to reveal their aqueous alteration histories. For example, bulk measurement of $^{26}$Mg/$^{24}$Mg of dolomite and breunnerite from asteroid Ryugu reveals that carbonates are products of serpentinization. Such an implication comes with a tantalizing possibility of potential prebiotic chemistry via Sabatier of Fischer-Tropsch reactions on the asteroid (McCollom and Seewald, 2007).

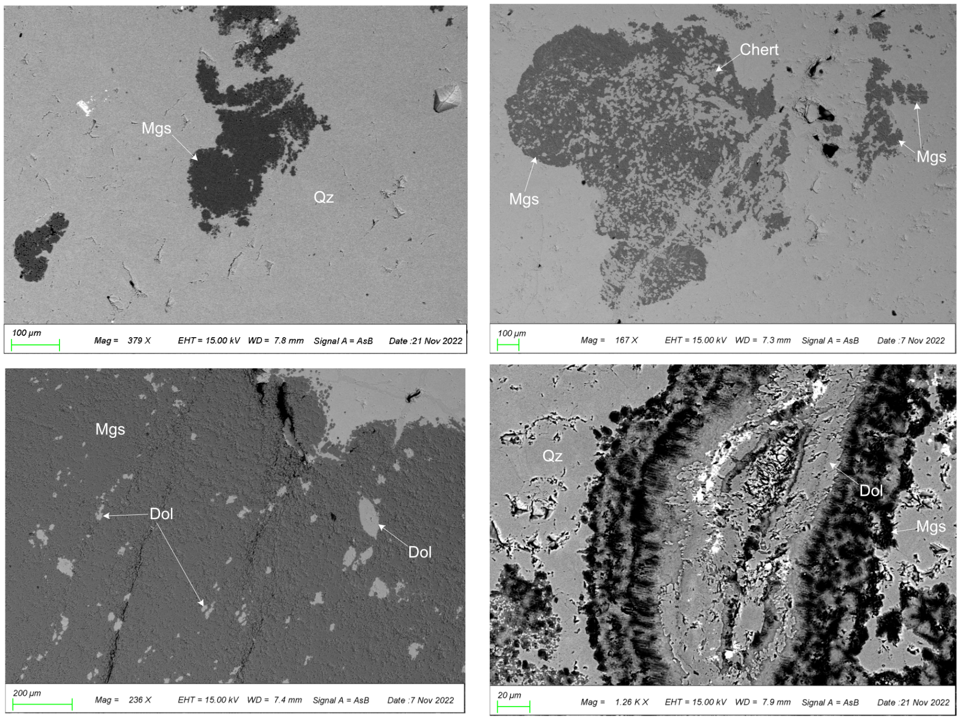

Figure 6.4: Complex magnesite-silica-dolomite-magnesite assemblage from weathered and serpentinized rocks from Gumigil mine, Great Serpentinite Belt, Australia.

For extraterrestrial samples, bulk analysis is challenging due to contributions from phyllosilicate-bound Mg during acid digestion, which dilutes the carbonate signal, and a series of tedious extractions are required to alleviate this issue (Yoshimura et al., 2024). The same is true for younger Martian meteorites, where sideritic carbonate is intermixed with serpentine minerals like iddingsite and hisingerite (Gyollai et al., 1993; Bridges and Grady, 1999; Hicks et al., 2014; Lee et al., 2015; Piercy et al., 2022). Our protocol can measure $^{26}$Mg/$^{24}$Mg of these carbonates conveniently, opening up a new avenue of research. However, these carbonates are often more Mn-rich than terrestrial standards. Any study aimed at analyzing these carbonates should assess the effect of excess Mn on the IMF first; our study considered only Fe+Mn as a combined total.

## 6.5 Conclusion

For the first time, we report a protocol to measure $^{26}$Mg/$^{24}$Mg of carbonates *in situ* using an ion microprobe. We find that IMF increases non-linearrly with molar Fe+Mn content of natural carbonates along both the dolomite-ankerite and magnesite-siderite series. The most (Fe+Mn)-rich members of each series show IMF values 23‰ and 20‰ higher than pure magnesite and dolomite, respectively. IMF also varies non-linearly with molar Ca content of Fe-free Ca-magnesite (up to 9 mol% $CaCO_3$), reaching values as high as 3.5‰ relative to pure magnesite. For synthetic Ca-Fe-Mn magnesites, the IMF increases non-linearly as a function of the molar Ca+Fe+Mn content of carbonates relative to pure magnesite.

We find that a direct matrix effect correction based on compositionally matched standards is more accurate than performing a two-step correction based on separate relationships between IMF vs. molar Ca content and molar Fe+Mn content, respectively. This protocol measured $^{26}$Mg/$^{24}$Mg of secondary standards accurately within analytical error.

Our method will enable future Mg isotopic studies of complex terrestrial and extraterrestrial carbonates, such as samples from asteroids Bennu and Ryugu, or those returned from Mars.

Table 6.1: Experimental conditions used to prepare synthetic carbonates using piston-cylinder apparatus.

| **Name** | **Starting Mix (wt %)** | | | **Pressure (GPa)** | **Temperature (K)** | **Time (hours)** |
|---|---|---|---|---|---|---|
| | Cc (mg) | Mgs (mg) | Sid (mg) | | | |
| Run1 | 11.0 | 89.0 | 0.0 | 3 | 1413 | 44 |
| Run2 | 15.0 | 74.5 | 10.5 | 3 | 1288 | 46 |
| Run2R1 | 15.0 | 74.5 | 10.5 | 3 | 1188 | 74 |
| Run3 | 12.9 | 51.0 | 36.1 | 3 | 1188 | 71 |
| Run5 | 19.9 | 26.5 | 53.6 | 3 | 1373 | 72 |

**Phase 1: Magnesite**

| | $MgCO_3$ | $CaCO_3$ | $FeCO_3$ | $MnCO_3$ |
|---|---|---|---|---|
| Run1 | 0.92 | 0.08 | 0.00 | 0.00 |
| Run2 | 0.84 | 0.08 | 0.08 | 0.00 |
| Run2R1 | 0.89 | 0.04 | 0.08 | 0.00 |
| Run3 | 0.72 | 0.06 | 0.21 | 0.02 |
| Run5 | 0.51 | 0.13 | 0.33 | 0.03 |

**Phase 2: Dolomite**

| | $MgCO_3$ | $CaCO_3$ | $FeCO_3$ | $MnCO_3$ |
|---|---|---|---|---|
| Run1 | 0.53 | 0.46 | 0.00 | 0.00 |
| Run2 | 0.48 | 0.47 | 0.05 | 0.00 |
| Run2R1 | 0.47 | 0.48 | 0.04 | 0.00 |
| Run3 | 0.40 | 0.48 | 0.11 | 0.01 |
| Run5 | 0.28 | 0.48 | 0.21 | 0.02 |

Table 6.2: Fe removal and Mg-recovery yield of samples after cation exchange resin column chemistry.

| **Name** | **Bulk solution** | | **Mg yield during digestion (%)** | **Mg cut after Fe-removal** | | | | **Mg Recovery from column (%)** |
|---|---|---|---|---|---|---|---|---|
| | Expected [Mg] (ppm) | Measured [Mg] (ppm) | | Expected [Mg] (ppm) | Measured [Mg] (ppm) | Expected [Fe] (ppm) | Measured [Fe] (ppm) | |
| Pulaski | 3.46 | 3.58 | 103 | 6.83 | 6.72 | 0 | <0.000 | 98 |
| 16459 | 2.61 | 2.41 | 93 | 4.61 | 4.24 | 0 | <0.000 | 92 |
| 14102 | 1.98 | 2.03 | 102 | 3.87 | 3.77 | 0 | <0.000 | 97 |
| SMS8 | 15.68 | 14.76 | 94 | 28.20 | 28.08 | 0 | <0.000 | 100 |
| SMS9 | 10.64 | 8.65 | 81 | 16.52 | 18.56 | 0 | <0.000 | 112 |
| 9157 | 8.42 | 8.27 | 98 | 15.81 | 15.58 | 0 | <0.000 | 99 |
| 3247 | 5.37 | 5.17 | 96 | 9.88 | 9.91 | 0 | <0.000 | 100 |
| 10778 | 4.01 | 3.24 | 81 | 7.67 | 7.41 | 0 | <0.000 | 97 |
| Run3 | 10.21 | 10.11 | 99 | 19.31 | 20.51 | 0 | <0.000 | 106 |
| Run5 | 5.46 | 5.12 | 94 | 9.77 | 9.58 | 0 | <0.000 | 98 |

Table 6.3: Analytical conditions used in this study.

| | **Session 1** | **Session 2** | **Session 3** |
|---|---|---|---|
| Spot size | 20 µm | 7 µm | 5 µm |
| Beam current | 10 nA | 250 pA | 60 pA |
| Beam | $O^-$ | $O^-$ | $O^-$ |
| Sample voltage | 8.5 kV | 8.5 kV | 8.5 kV |
| Ion source | -13.5 kV | -13.5 kV | -13.5 kV |
| Field aperture | 300 µm | 300 µm | 300 µm |
| MRP | 2000 | 2282 | 2282 |
| Entrance slit | 218 µm | 163 µm | 163 µm |
| Energy slit | 47 µm | 47 µm | 47 µm |
| Pre-Sputter | 120 s | 360 s | 360 s |
| Raster (Pre-sputter) | 8 µm | 5 µm | 5 µm |
| Raster (Analysis) | 5 µm | 2 µm | 2 µm |
| Total time | 7 min | 15 min | 20 min |

Table 6.4: Major cation chemistry and Mg-isotope composition of all standards.

| Name | $MgCO_3$ | $CaCO_3$ | $FeCO_3$ | $MnCO_3$ | $\delta^{26}Mg_{DSM-3}$ (‰) |
|---|---|---|---|---|---|
| ***Natural carbonates*** | | | | | |
| *Dolomite-Ankerite* | | | | | |
| 12700 | 0.50 | 0.51 | 0.00 | 0.00 | –0.88 |
| 7920 | 0.49 | 0.50 | 0.01 | 0.00 | –0.90 |
| 6773 | 0.48 | 0.50 | 0.01 | 0.00 | –1.29 |
| RK7 | 0.48 | 0.50 | 0.02 | 0.00 | –0.87 |
| RK9 | 0.47 | 0.50 | 0.02 | 0.01 | –1.05 |
| 15086 | 0.40 | 0.50 | 0.09 | 0.00 | –0.53 |
| H884 | 0.36 | 0.50 | 0.10 | 0.02 | –0.50 |
| Pulaski | 0.23 | 0.51 | 0.24 | 0.01 | –0.60 |
| 16459 | 0.18 | 0.51 | 0.29 | 0.02 | 0.54 |
| 14102 | 0.13 | 0.52 | 0.34 | 0.02 | –1.05 |
| RK-1 dol | 0.47 | 0.49 | 0.01 | 0.00 | –0.72 |
| *Magnesite-siderite* | | | | | |
| MRR 1077 | 1.00 | 0.00 | 0.00 | 0.00 | –1.14 |
| 2123 | 1.00 | 0.00 | 0.01 | 0.00 | –1.02 |
| RK-6 | 0.94 | 0.00 | 0.05 | 0.01 | –0.86 |
| SMS8 | 0.87 | 0.01 | 0.12 | 0.01 | –0.61 |
| SMS9 | 0.68 | 0.01 | 0.27 | 0.05 | –1.31 |
| 9157 | 0.50 | 0.00 | 0.49 | 0.01 | –0.47 |
| 3247 | 0.33 | 0.01 | 0.64 | 0.03 | –1.18 |
| 10778 | 0.20 | 0.01 | 0.76 | 0.03 | –0.36 |
| LW57 | 0.97 | 0.03 | 0.00 | 0.00 | –2.82 |
| ***Synthetic carbonates*** | | | | | |
| Run1 | 0.92 | 0.08 | 0.00 | 0.00 | –1.01 |
| Run2 | 0.84 | 0.08 | 0.08 | 0.00 | –1.00 |
| Run2R | 0.89 | 0.04 | 0.08 | 0.00 | –0.90 |
| Run3 | 0.72 | 0.06 | 0.21 | 0.02 | –1.16 |
| Run5 | 0.51 | 0.13 | 0.33 | 0.03 | –0.97 |

Table 6.5: Major cation chemistry and Mg isotopic composition of Fe-zoned dolomite used to test the accuracy of our method.

| **Name** | **$MgCO_3$** | **$CaCO_3$** | **$FeCO_3$** | **$MnCO_3$** | **Corrected to 12700** | | **Corrected to 15086** | |
|---|---|---|---|---|---|---|---|---|
| | | | | | $\delta^{26}Mg_{DSM-3}$ (‰) | 1σ | $\delta^{26}Mg_{DSM-3}$ (‰) | 1σ |
| G1-1 | 0.36 | 0.52 | 0.07 | 0.02 | –0.27 | 0.4 | –0.57 | 0.4 |
| G1-2 | 0.36 | 0.51 | 0.08 | 0.02 | 0.00 | 0.4 | –0.30 | 0.4 |
| G1-3 | 0.36 | 0.51 | 0.08 | 0.02 | –1.76 | 0.4 | –2.06 | 0.4 |
| G1-4 | 0.35 | 0.50 | 0.10 | 0.02 | –0.02 | 0.4 | –0.32 | 0.4 |
| G1-5 | 0.42 | 0.49 | 0.04 | 0.01 | –0.71 | 0.4 | –1.01 | 0.4 |
| G1-6 | 0.43 | 0.48 | 0.05 | 0.02 | –1.18 | 0.4 | –1.48 | 0.4 |
| G1-7 | 0.41 | 0.49 | 0.05 | 0.02 | –0.64 | 0.4 | –0.94 | 0.4 |
| G1-8 | 0.41 | 0.49 | 0.05 | 0.02 | –1.10 | 0.4 | –1.40 | 0.4 |
| G1-9 | 0.42 | 0.47 | 0.07 | 0.02 | –1.09 | 0.4 | –1.39 | 0.4 |
| G1-10 | 0.38 | 0.48 | 0.09 | 0.02 | 0.48 | 0.4 | 0.18 | 0.4 |
| G1-11 | 0.37 | 0.47 | 0.10 | 0.02 | 0.23 | 0.4 | –0.07 | 0.4 |
| G1-12 | 0.36 | 0.48 | 0.11 | 0.02 | 1.14 | 0.4 | 0.84 | 0.4 |
| G1-13 | 0.35 | 0.49 | 0.11 | 0.01 | 3.20 | 0.3 | 2.90 | 0.3 |
| G1-14 | 0.36 | 0.51 | 0.09 | 0.02 | –0.38 | 0.4 | –0.68 | 0.4 |
| | | | | | | | | |
| G2-1 | 0.38 | 0.51 | 0.07 | 0.02 | –1.68 | 0.4 | –1.33 | 0.4 |
| G2-2 | 0.38 | 0.51 | 0.06 | 0.02 | –0.98 | 0.4 | –0.63 | 0.4 |
| G2-3 | 0.38 | 0.51 | 0.06 | 0.02 | –1.35 | 0.4 | –1.00 | 0.4 |
| G2-4 | 0.38 | 0.51 | 0.06 | 0.02 | –1.64 | 0.4 | –1.29 | 0.4 |
| G2-5 | 0.38 | 0.51 | 0.06 | 0.02 | –0.52 | 0.4 | –0.16 | 0.4 |
| G2-6 | 0.38 | 0.51 | 0.06 | 0.02 | –0.36 | 0.4 | –0.01 | 0.4 |
| G2-7 | 0.38 | 0.51 | 0.06 | 0.02 | –0.19 | 0.4 | 0.16 | 0.4 |
| | | | | | | | | |
| *Average* | | | | | *–0.42* | *0.4* | *–0.50* | *0.4* |

# BIBLIOGRAPHY

Adams D., Scheucher M., Hu R., Ehlmann B. L., Thomas T. B., Wordsworth R., Scheller E., Lillis R., Smith K., Rauer H. and Yung Y. L. (2025) Episodic warm climates on early Mars primed by crustal hydration. *Nat. Geosci.* **18**, 133–139.

Allwood A. C., Walter M. R., Kamber B. S., Marshall C. P. and Burch I. W. (2006) Stromatolite reef from the Early Archaean era of Australia. *Nature* **441**, 714–718.

Beinlich A., Mavromatis V., Austrheim H. and Oelkers E. H. (2014) Inter-mineral Mg isotope fractionation during hydrothermal ultramafic rock alteration–Implications for the global Mg-cycle. *Earth and Planetary Science Letters* **392**, 166–176.

Bischoff A., Alexander C. M., Barrat J.-A., Burkhardt C., Busemann H., Degering D., Di Rocco T., Fischer M., Fockenberg T. and Foustoukos D. I. (2021) The old, unique C1 chondrite Flensburg–insight into the first processes of aqueous alteration, brecciation, and the diversity of water-bearing parent bodies and lithologies. *Geochimica et Cosmochimica Acta* **293**, 142–186.

Blättler C. L. and Higgins J. A. (2017) Testing Urey's carbonate–silicate cycle using the calcium isotopic composition of sedimentary carbonates. *Earth and Planetary Science Letters* **479**, 241–251.

Blättler C. L., Miller N. R. and Higgins J. A. (2015) Mg and Ca isotope signatures of authigenic dolomite in siliceous deep-sea sediments. *Earth and Planetary Science Letters* **419**, 32–42.

Bosence D. (1989) Biogenic carbonate production in Florida Bay. *Bulletin of Marine Science* **44**, 419–433.

Bridges J. C. and Grady M. M. (1999) A halite-siderite-anhydrite-chlorapatite assemblage in Nakhla: Mineralogical evidence for evaporites on Mars. *Meteorit & Planetary Scien* **34**, 407–415.

Bryant R. N., Present T. M., Ahm A.-S. C., McClelland H.-L. O., Razionale D. and Blättler C. L. (2022) Early diagenetic constraints on Permian seawater chemistry from the Capitan Reef. *Geochimica et Cosmochimica Acta* **328**, 1–18.

Castelli D. (1991) Eclogitic metamorphism in carbonate rocks: the example of impure marbles from the Sesia-Lanzo Zone, Italian Western Alps[1]. *Journal Metamorphic Geology* **9**, 61–77.

Cerling T. E. (1984) The stable isotopic composition of modern soil carbonate and its relationship to climate. *Earth and Planetary science letters* **71**, 229–240.

Clog M., Lindgren P., Modestou S., McDonald A., Tait A., Donnelly T., Mark D. and Lee M. (2024) Clumped isotope and Δ17O measurements of carbonates in CM carbonaceous chondrites: New insights into parent body thermal and fluid evolution. *Geochimica et Cosmochimica Acta* **369**, 1–16.

Ehlmann B. L., Mustard J. F., Murchie S. L., Poulet F., Bishop J. L., Brown A. J., Calvin W. M., Clark R. N., Des Marais D. J. and Milliken R. E. (2008) Orbital identification of carbonate-bearing rocks on Mars. *Science* **322**, 1828–1832.

Eiler J. M., Graham C. and Valley J. W. (1997) SIMS analysis of oxygen isotopes: matrix effects in complex minerals and glasses. *Chemical Geology* **138**, 221–244.

Eiler J. M., Valley J. W., Graham C. M. and Fournelle J. (2002) Two populations of carbonate in ALH84001: Geochemical evidence for discrimination and genesis. *Geochimica et Cosmochimica Acta* **66**, 1285–1303.

Fantle M. S. and Higgins J. (2014) The effects of diagenesis and dolomitization on Ca and Mg isotopes in marine platform carbonates: Implications for the geochemical cycles of Ca and Mg. *Geochimica et Cosmochimica Acta* **142**, 458–481.

Farquhar J. and Thiemens M. H. (2000) Oxygen cycle of the Martian atmosphere-regolith system: $\Delta^{17}$O of secondary phases in Nakhla and Lafayette. *J. Geophys. Res.* **105**, 11991–11997.

Franzolin E., Schmidt M. W. and Poli S. (2011) Ternary Ca–Fe–Mg carbonates: subsolidus phase relations at 3.5 GPa and a thermodynamic solid solution model including order/disorder. *Contributions to Mineralogy and Petrology* **161**, 213–227.

Fujiya W., Kawasaki N., Nagashima K., Sakamoto N., O'D. Alexander C. M., Kita N. T., Kitajima K., Abe Y., Aléon J. and Amari S. (2023) Carbonate record of temporal change in oxygen fugacity and gaseous species in asteroid Ryugu. *Nature Geoscience* **16**, 675–682.

Fujiya W., Sugiura N., Sano Y. and Hiyagon H. (2013) Mn–Cr ages of dolomites in CI chondrites and the Tagish Lake ungrouped carbonaceous chondrite. *Earth and Planetary Science Letters* **362**, 130–142.

Garvie L. A. J. and Wittmann A. (2025) MINERALOGICAL OBSERVATIONS OF THE OUED CHEBEIKA 002 (CI1) METEORITE. In LPSC. p. 1802.

Gattacceca J., Gounelle M., Devouard B., Barrat J. -A., Bonal L., King A. J., Maurel C., Beck P., Roskosz M., Viennet J. -C., Mukherjee D., Dauphas N., Heck P. R., Yokoyama T., López García K., Poch O., Grauby O., Harrison C. S., Vinogradoff V., Vernazza P., Tikoo S., Vidal V., Rochette P., AuYang D., Borschneck D., Juraszek J. and Clark B. (2025) Oued Chebeika 002: A new CI1 meteorite linked to outer solar system bodies. *Meteorit & Planetary Scien*, maps.14359.

Guo W. (2008) *Carbonate clumped isotope thermometry: application to carbonaceous chondrites & effects of kinetic isotope fractionation.*, California Institute of Technology.

Guo W. and Eiler J. M. (2007) Temperatures of aqueous alteration and evidence for methane generation on the parent bodies of the CM chondrites. *Geochimica et Cosmochimica Acta* **71**, 5565–5575.

Gyollai I., Chatzitheodoridis E. and Kereszturi Á. (1993) Secondary minerals of Nakhla, Lafayette and Governador Valadares meteorites–implications of hydrothermal processes on Mars. *Nature* **365**, 715–721.

Hicks L. J., Bridges J. C. and Gurman S. J. (2014) Ferric saponite and serpentine in the nakhlite martian meteorites. *Geochimica et Cosmochimica Acta* **136**, 194–210.

Jilly-Rehak C. E., Huss G. R., Nagashima K. and Schrader D. L. (2018) Low-temperature aqueous alteration on the CR chondrite parent body: Implications from in situ oxygen-isotope analyses. *Geochimica et Cosmochimica Acta* **222**, 230–252.

Jin C., Zhang Z. and Cheng Z. (2025) Carbonatites and related mineralization: an overview. *SP* **551**, 335–367.

Johnson C. A. and Prinz M. (1993) Carbonate compositions in CM and CI chondrites and implications for aqueous alteration. *Geochimica et Cosmochimica Acta* **57**, 2843–2852.

Kaplan H. H., Lauretta D. S., Simon A. A., Hamilton V. E., DellaGiustina D. N., Golish D. R., Reuter D. C., Bennett C. A., Burke K. N., Campins H., Connolly H. C., Dworkin J. P., Emery J. P., Glavin D. P., Glotch T. D., Hanna R., Ishimaru K., Jawin E. R., McCoy T. J., Porter N., Sandford S. A., Ferrone S., Clark B. E., Li J.-Y., Zou X.-D., Daly M. G., Barnouin O. S., Seabrook J. A. and Enos H. L. (2020) Bright carbonate veins on asteroid (101955) Bennu: Implications for aqueous alteration history. *Science* **370**, eabc3557.

Kita N. T., Kitajima K., Nagashima K., Kawasaki N., Sakamoto N., Fujiya W., Abe Y., Aléon J., Alexander C. M. O., Amari S., Amelin Y., Bajo K., Bizzarro M., Bouvier A., Carlson R. W., Chaussidon M., Choi B., Dauphas N., Davis A. M., Di Rocco T., Fukai R., Gautam I., Haba M. K., Hibiya Y., Hidaka H., Homma H., Hoppe P., Huss G. R., Ichida K., Iizuka T., Ireland T. R., Ishikawa A., Itoh S., Kleine T., Komatani S., Krot A. N., Liu M., Masuda Y., McKeegan K. D., Morita M., Motomura K., Moynier F., Nakai I., Nguyen A., Nittler L., Onose M., Pack A., Park C., Piani L., Qin L., Russell S. S., Schönbächler M., Tafla L., Tang H., Terada K., Terada Y., Usui T., Wada S., Wadhwa M., Walker R. J., Yamashita K., Yin Q., Yokoyama T., Yoneda S., Young E. D., Yui H., Zhang A., Nakamura T., Naraoka H., Noguchi T., Okazaki R., Sakamoto K., Yabuta H., Abe M., Miyazaki A., Nakato A., Nishimura M., Okada T., Yada T., Yogata K., Nakazawa S., Saiki T., Tanaka S., Terui F., Tsuda

Y., Watanabe S., Yoshikawa M., Tachibana S. and Yurimoto H. (2024) Disequilibrium oxygen isotope distribution among aqueously altered minerals in Ryugu asteroid returned samples. *Meteorit & Planetary Scien* **59**, 2097–2116.

Kluge T., Affek H. P., Zhang Y. G., Dublyansky Y., Spötl C., Immenhauser A. and Richter D. K. (2014) Clumped isotope thermometry of cryogenic cave carbonates. *Geochimica et Cosmochimica Acta* **126**, 541–554.

Kuznetsov A. B., Gorokhov I. M., Azimov P. Ya. and Dubinina E. O. (2021) Sr- and C-Chemostratigraphy Potential of the Paleoproterozoic Sedimentary Carbonates under Medium-Temperature Metamorphism: the Ruskeala Marble, Karelia. *Petrology* **29**, 175–194.

Lauretta D. S., Connolly H. C., Aebersold J. E., Alexander C. M. O., Ballouz R., Barnes J. J., Bates H. C., Bennett C. A., Blanche L., Blumenfeld E. H., Clemett S. J., Cody G. D., DellaGiustina D. N., Dworkin J. P., Eckley S. A., Foustoukos D. I., Franchi I. A., Glavin D. P., Greenwood R. C., Haenecour P., Hamilton V. E., Hill D. H., Hiroi T., Ishimaru K., Jourdan F., Kaplan H. H., Keller L. P., King A. J., Koefoed P., Kontogiannis M. K., Le L., Macke R. J., McCoy T. J., Milliken R. E., Najorka J., Nguyen A. N., Pajola M., Polit A. T., Righter K., Roper H. L., Russell S. S., Ryan A. J., Sandford S. A., Schofield P. F., Schultz C. D., Seifert L. B., Tachibana S., Thomas-Keprta K. L., Thompson M. S., Tu V., Tusberti F., Wang K., Zega T. J., Wolner C. W. V., and the OSIRIS-REx Sample Analysis Team (2024) Asteroid (101955) Bennu in the laboratory: Properties of the sample collected by OSIRIS - REx. *Meteorit & Planetary Scien* **59**, 2453–2486.

Lee M. R., Tomkinson T., Hallis L. J. and Mark D. F. (2015) Formation of iddingsite veins in the martian crust by centripetal replacement of olivine: Evidence from the nakhlite meteorite Lafayette. *Geochimica et Cosmochimica Acta* **154**, 49–65.

Luo K., Ma J., Teng F., Wei G., Zhu G., Zeng T. and Wang Z. (2025) Magnesium Isotope Fractionation During Basalt Weathering: An Index of Weathering Fluxes and $CO_2$ Consumption. *JGR Earth Surface* **130**, e2024JF007774.

Mavromatis V., Power I. M., Harrison A. L., Beinlich A., Dipple G. M. and Bénézeth P. (2021) Mechanisms controlling the Mg isotope composition of hydromagnesite-magnesite playas near Atlin, British Columbia, Canada. *Chemical Geology* **579**, 120325.

McCain K. A., Matsuda N., Liu M.-C., McKeegan K. D., Yamaguchi A., Kimura M., Tomioka N., Ito M., Imae N. and Uesugi M. (2023) Early fluid activity on Ryugu inferred by isotopic analyses of carbonates and magnetite. *Nature Astronomy* **7**, 309–317.

McCollom T. M. and Seewald J. S. (2007) Abiotic Synthesis of Organic Compounds in Deep-Sea Hydrothermal Environments. *Chem. Rev.* **107**, 382–401.

McCorkle D. C., Keigwin L. D., Corliss B. H. and Emerson S. R. (1990) The influence of microhabitats on the carbon isotopic composition of deep-sea benthic foraminifera. *Paleoceanography* **5**, 161–185.

Moore R. D., Goudge T. A., Klidaras A., Horgan B. H., Broz A., Wordsworth R. and Farrand W. H. (2025) Deep chemical weathering on ancient Mars landscapes driven by erosional and climatic patterns. *Nature Astronomy*, 1–9.

Niles P. B., Catling D. C., Berger G., Chassefière E., Ehlmann B. L., Michalski J. R., Morris R., Ruff S. W. and Sutter B. (2013) Geochemistry of Carbonates on Mars: Implications for Climate History and Nature of Aqueous Environments. *Space Sci Rev* **174**, 301–328.

de Obeso J. C., Santiago Ramos D. P., Higgins J. A. and Kelemen P. B. (2021) A Mg isotopic perspective on the mobility of magnesium during serpentinization and carbonation of the Oman ophiolite. *Journal of Geophysical Research: Solid Earth* **126**, e2020JB020237.

Oskierski H. C., Beinlich A., Mavromatis V., Altarawneh M. and Dlugogorski B. Z. (2019) Mg isotope fractionation during continental weathering and low temperature carbonation of ultramafic rocks. *Geochimica et cosmochimica acta* **262**, 60–77.

Passey B. H. and Ji H. (2019) Triple oxygen isotope signatures of evaporation in lake waters and carbonates: A case study from the western United States. *Earth and Planetary Science Letters* **518**, 1–12.

Piercy J. D., Bridges J. C. and Hicks L. J. (2022) Carbonate dissolution and replacement by odinite and saponite in the Lafayette nakhlite: Part of the CO2-CH4 cycle on Mars? *Geochimica et Cosmochimica Acta* **326**, 97–118.

Qu Y.-R., Liu S.-A. and Gamaleldien H. (2025) Insights Into Subduction-Zone Fluid-Rock Interactions and Carbon Cycling From Magnesium Isotopes of Subducted Ophiolitic Mélanges in the Arabian-Nubian Shield. *Geochemistry, Geophysics, Geosystems* **26**, e2024GC011918.

Rollion-Bard C. and Marin-Carbonne J. (2011) Determination of SIMS matrix effects on oxygen isotopic compositions in carbonates. *Journal of Analytical Atomic Spectrometry* **26**, 1285–1289.

Schoenberg R. and von Blanckenburg F. (2005) An assessment of the accuracy of stable Fe isotope ratio measurements on samples with organic and inorganic matrices by high-resolution multicollector ICP-MS. *International Journal of Mass Spectrometry* **242**, 257–272.

Shatskiy A., Podborodnikov I. V., Arefiev A. V., Minin D. A., Chanyshev A. D. and Litasov K. D. (2018) Revision of the CaCO3–MgCO3 phase diagram at 3 and 6 GPa. *American Mineralogist* **103**, 441–452.

Śliwiński M. G., Kitajima K., Kozdon R., Spicuzza M. J., Fournelle J. H., Denny A. and Valley J. W. (2016a) Secondary Ion Mass Spectrometry Bias on Isotope Ratios in Dolomite–Ankerite, Part I: $\delta^{18}$ O Matrix Effects. *Geostandard Geoanalytic Res* **40**, 157–172.

Śliwiński M. G., Kitajima K., Kozdon R., Spicuzza M. J., Fournelle J. H., Denny A. and Valley J. W. (2016b) Secondary Ion Mass Spectrometry Bias on Isotope Ratios in Dolomite–Ankerite, Part II : $\delta^{13}$ C Matrix Effects. *Geostandard Geoanalytic Res* **40**, 173–184.

Śliwiński M. G., Kitajima K., Spicuzza M. J., Orland I. J., Ishida A., Fournelle J. H. and Valley J. W. (2018) SIMS Bias on Isotope Ratios in Ca-Mg-Fe Carbonates (Part III): δ18O and δ13C Matrix Effects Along the Magnesite–Siderite Solid-Solution Series. *Geostandards and Geoanalytical Research* **42**, 49–76.

Swart P. K. (2015) The geochemistry of carbonate diagenesis: The past, present and future. *Sedimentology* **62**, 1233–1304.

Teng F.-Z. (2017) Magnesium isotope geochemistry. *Reviews in Mineralogy and Geochemistry* **82**, 219–287.

Tosca N. J., Tice M. M., Hurowitz J. A., Pedersen D. A. K., Henneke J., Mandon L., McCubbin F. M., Ross O., Tung P.-Y., Harrison R. J., Li A., Schmidt M. E., Kizovski T. V., Liu Y., Mayhew L., Jones M. W. M., Labrie J., Davidoff S., Allwood A. C., Beyssac O., Brown A., Cable M., Comellas J., Clark B. C., Galvin A. E., Horgan B., Heirwegh C. M., Nemere P., Orenstein B. J., Quantin-Nataf C., Royer C., Treiman A., Wade L. A., Wiens R. and Wright A. P. (2025) In situ evidence for serpentinization within the Máaz formation, Jezero crater, Mars. *Science Advances* **11**, eadr8793.

Valley J. W., Eiler J. M., Graham C. M., Gibson E. K., Romanek C. S. and Stolper E. M. (1997) Low-temperature carbonate concretions in the Martian meteorite ALH84001: Evidence from stable isotopes and mineralogy. *Science* **275**, 1633–1638.

Walker J. C. G., Hays P. B. and Kasting J. F. (1981) A negative feedback mechanism for the long-term stabilization of Earth's surface temperature. *J. Geophys. Res* **86**, 9776–9782.

Winnick M. J. and Maher K. (2018) Relationships between CO2, thermodynamic limits on silicate weathering, and the strength of the silicate weathering feedback. *Earth and Planetary Science Letters* **485**, 111–120.

Wordsworth R. D. (2016) The Climate of Early Mars. *Annu. Rev. Earth Planet. Sci.* **44**, 381–408.

Xu J.-Y., Li Q.-L., Tang G.-Q., Lu K., Liu Y., Feng L.-J. and Melgarejo J. C. (2022) Accurate and Efficient SIMS Oxygen Isotope Analysis of Composition-Variable Minerals: Online Matrix Effect Calibration for Dolomite. *Anal. Chem.* **94**, 7944–7951.

Yoshimura T., Araoka D., Naraoka H., Sakai S., Ogawa N. O., Yurimoto H., Morita M., Onose M., Yokoyama T. and Bizzarro M. (2024) Breunnerite grain and magnesium isotope chemistry reveal cation partitioning during aqueous alteration of asteroid Ryugu. *Nature Communications* **15**, 6809.

Young E. D., Tonui E., Manning C. E., Schauble E. and Macris C. A. (2009) Spinel–olivine magnesium isotope thermometry in the mantle and implications for the Mg isotopic composition of Earth. *Earth and Planetary Science Letters* **288**, 524–533.

Zito K. L., McKeegan K. D., Kerridge J. F., Hutcheon I. D. and Leshin L. A. (1998) Aqueous alteration on the CI parent body: Evidence from oxygen and carbon isotopic studies of single carbonate grains from Orgueil. *Meteoritics & Planetary Science, vol. 33, p. A171* **33**, A171.

## *Chapter 7*

# ISOTOPIC EVIDENCE THAT ADVANCED SILICATE WEATHERING MODULATED EARLY MARS' CARBON CYCLE

Surjyendu Bhattacharjee[1]*, Theodore M. Present[1], Clara L. Blättler[2], Damanveer S. Grewal[3], Abdallah Zaki[4], Yunbin Guan[1], Chi Ma[1], Carl R. Swindle[5], Maciej G. Sliwinski[6], Paul D. Asimow[1], John W. Valley[7] and John M. Eiler[1]

[1]Division of Geological and Planetary Sciences, California Institute of Technology, Pasadena, CA, USA

[2]Department of the Geophysical Sciences, University of Chicago, Chicago, IL, USA

[3]Department of Earth and Planetary Sciences, Yale University, New Haven, CT, USA

[4]Jackson School of Geosciences, University of Texas at Austin, Austin, TX, USA

[5]B. John Garrick Institute for the Risk Sciences, University of California, Los Angeles, CA, USA

[6]University of Alaska, Fairbanks, AK, USA

[7]Department of Geoscience, University of Wisconsin, Madison, WI, USA

*Corresponding Author: sbhattac@caltech.edu

**Abstract**

The interaction of water with crustal rocks has influenced the chemistry, mineralogy, and geomorphology of Mars throughout its history. This interaction involved an unknown combination of silicate weathering (producing and evolving clays) and serpentinization of mafic rocks, each imparting distinct magnesium isotope signatures ($^{26}$Mg/$^{24}$Mg) to their products and bearing substantial influences on Martian habitability. We distinguish these pathways by measuring in situ $^{26}$Mg/$^{24}$Mg in carbonate concretions from the 4.1-Ga meteorite ALH84001. Concretions are enriched in $^{26}$Mg relative to the Martian mantle and display a core-to-rim decline in $^{26}$Mg/$^{24}$Mg. This indicates precipitation as hydrous Mg-carbonates under evaporative, near-surface conditions. Mineralogy and isotope-fractionation constraints indicate that carbonate-forming fluids derived from weathering of pre-existing high $^{26}$Mg/$^{24}$Mg clays from serpentinized igneous rocks and surface deposits —establishing advanced crustal weathering on early (~3.94 billion years) Mars. This connection between the Martian carbon cycle and silicate weathering reveals their potential to modulate Martian climate and habitability, where episodic warm, aqueous conditions and subsurface niches remained conducive to prebiotic chemistry for much longer than current estimations.

## 6.1 Introduction

Early Mars likely hosted liquid water and at least an episodically temperate climate, making the near-surface environment potentially habitable (Wordsworth, 2016). However, the temporal evolution of its hydrosphere and atmosphere, the stability of its climate, and the feasibility and locations of prebiotic chemistry — all factors controlling habitability — depended on the nature of water–rock interactions on Mars (Cockell et al., 2016). Observations from satellites and landers show that the cycling of water between rock-bound and free (liquid and vapor) reservoirs on Mars was likely dominated by serpentinization and chemical weathering (Moore et al., 2025; Tosca et al., 2025a), each with distinct influences on Martian habitability. Serpentinization is associated with abiotic organic synthesis via Sabatier or Fischer-Tropsch reactions (Steele et al., 2022), which provide one of several possible pathways to the emergence of life. Serpentinization-generated molecular hydrogen, if outgassed at sufficiently high rates, can sustain a warm, habitable climate (Adams et al., 2025). Chemical weathering, on the other hand, serves to regulate long-term climate via $CO_2$ drawdown, leading to a negative feedback between surface temperature and the intensity of chemical weathering (Walker et al., 1981).

While there exists strong evidence for serpentinization on Mars, chemical weathering remains relatively unexplored. The mineral products of serpentinization on Mars have been detected by the Mars 2020 Perseverance rover in the igneous Máaz formation on the Jezero Crater floor (Tosca et al., 2025a) and from orbit in terranes like Claritas Rise and the Nili Fossae (Ehlmann et al., 2010). The organic-phyllosilicate-carbonate assemblages in several of the Martian meteorites have also been interpreted as serpentinization products (*4*,*5*). Evidence for chemical weathering, by contrast, is limited to the orbital observation of various clay deposits on Martian terranes. The spectral observation of Fe-Mg clays overlain by Al-clays in these deposits suggests their production followed by chemical evolution through advanced chemical weathering (Ye and Michalski, 2022; Moore et al., 2025). However, while meteoritic studies confirm serpentinization, chemical weathering signatures have not been identified in any Martian meteorite.

Carbonate minerals are common products of both processes. The mechanisms and thermodynamic conditions between the two processes are different, which imparts distinct geochemistry to their respective carbonate products. Serpentinization can form carbonates (usually at high temperatures) in crustal rocks, either directly from olivine or via intermediate serpentine minerals by carbonation with commonly magmatic $CO_2$. Chemical weathering at (or near) the planetary surface mobilizes cations into solutions that then migrate and react with dissolved $CO_2$ drawn from the atmosphere to form carbonates at near-surface temperatures. Nevertheless, the temperature of carbonate formation by itself is not diagnostic of the water-rock cycle, i.e., a low-temperature carbonate formation does not, by default, indicate a weathering origin. Serpentinization-generated, cation-rich fluids can also migrate to the near-surface from deeper crust and precipitate carbonate at low temperature. Although carbonates and are reported from Mars via orbital detection (Ehlmann et al., 2008), rover identification (Tutolo et al., 2025), or found in meteorites (Gyollai et al., 1993; Treiman et al., 1993; Mcsween Jr and Harvey, 1998; Bridges and Grady, 1999, 2000; Niles et al., 2013a), orbital spectroscopy and rover-based instruments are unable to distinguish between carbonates with these different origins. Hence, a detailed laboratory study of the geochemistry of carbonates in Martian meteorites provides the only pathway to distinguish their origin.

The unique meteorite Allan Hills 84001 (ALH84001) is 4.1 billion years (Ga) old and provides our only sample of early (Noachian) Mars (Lapen et al., 2010), the period considered most likely to have been habitable. In addition to its primary igneous assemblage of orthopyroxene with minor chromite, maskelynite, pyrite, magnetite, and apatite, this sample contains ~3.94 Ga old secondary carbonate concretions of low temperature origin (Borg et al., 1999), included in host orthopyroxene ($Mg_{0.70}Fe_{0.27}Ca_{0.03}SiO_3$). These concretions are zoned, having three distinct compositional domains (Fig. 1a): a Ca, Fe-rich core (~50–60 μm diameter) of composition $Mg_{0.52}Fe_{0.35}Ca_{0.13}CO_3$, surrounded by a ~8 μm thick Ca-poor mantle of composition $Mg_{0.70}Fe_{0.25}Ca_{0.05}CO_3$, surrounded in turn by an ~8-10 μm thick rim of nearly pure magnesite ($Mg_{0.97}Ca_{0.03}CO_3$). Layers comprised of magnetite and sulfide separate the magnesite layer from the Ca-poor mantle and host orthopyroxene (Fig. 1) (Moyano-Cambero et al., 2017). Larger (100-300 μm) domains of Fe-dolomite ($Mg_{0.32}Fe_{0.13}Ca_{0.49}Mn_{0.06}CO_3$) (Fig. S5), also found in this meteorite, have been interpreted to be products of high-temperature processes (Scott et al., 1997; Eiler et al., 2002b). Although this meteorite suffered at least two shock events (Treiman, 1995), the carbonate concretions do not seem to have been recrystallized by shock (Halevy et al., 2011), holding pristine information regarding their origin.

Prior studies on the isotope ratios of C and O from carbonate concretions and their clumping into doubly-substituted carbonate groups suggest low-temperature (291 K) precipitation from an evaporating shallow subsurface aquifer, with carbon sourced from the atmosphere (Valley et al., 1997; Eiler et al., 2002b). However, this evidence does not clarify how different forms of water-rock reaction supplied the cations to form these carbonates. The unexplored isotope ratios of Mg (de Obeso et al., 2021; Yoshimura et al., 2024) in these carbonates are sensitive to water-rock reaction mechanisms and can differentiate between serpentinization vs. advanced chemical weathering as the process that supplied these cations. Here, we report the magnesium isotope ratios of carbonate concretions (and Fe-dolomite, see SI) from a thin section of ALH84001 (Eiler et al., 2002b).

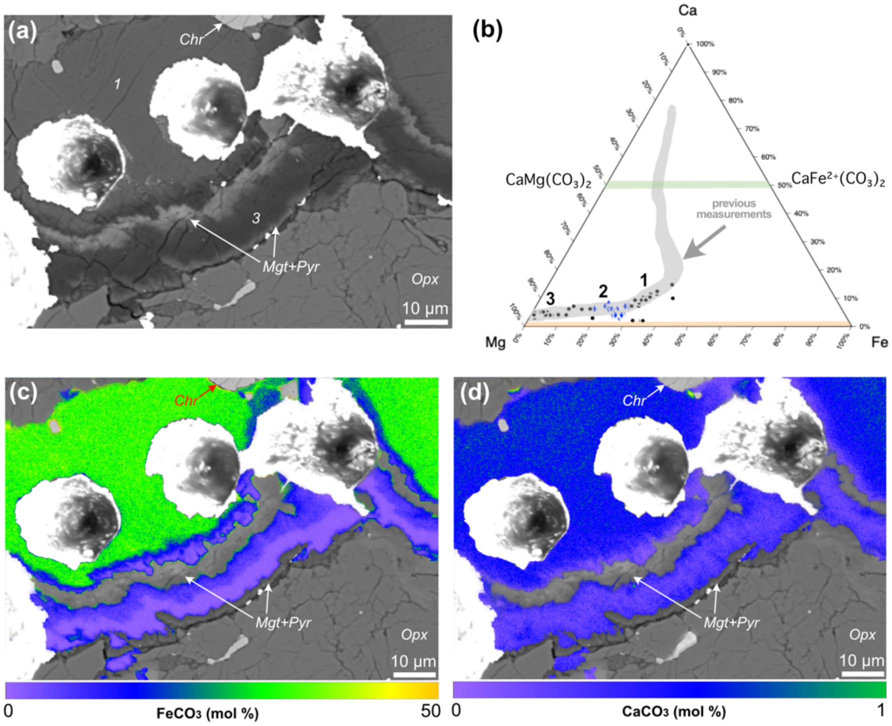

Figure 7.1: Textural relationships between ALH84001 carbonate and silicate phases and their compositions. (a) Backscattered electron image (BSE) of a carbonate concretion surrounded by orthopyroxene (Opx). Three distinct compositional zones are usually observed (1: Ca, Fe core; 2: Mg–Fe mantle, not seen in this particular concretion; 3: Mg-rich rim). The carbonate concretion includes a magnetite and pyrite (Mgt+Pyr) rich layer, typically in between zones

2 and 3. The three bright pits across the field of view are ion-microprobe pits from a previous study (Eiler et al., 2002b). (b) Major cation chemistry of carbonate concretions measured by electron probe. Composition of carbonates in the concretion cores (number 1), along with mantles and rims are Mg-rich (numbers 2, 3) are shown. These compositions are in good agreement with those measured in previous studies (Eiler et al., 2002b). Green line indicates dolomite-ankerite join. (c, d) Quantitative $FeCO_3$ and $CaCO_3$ content (mol%) map of carbonates, showing distinct Fe-Ca zonation. Non-carbonate phases are shown with grayscale BSE contrast.

The relative abundance of the rare Mg isotope $^{26}$Mg—reported as $^{26}$Mg/$^{24}$Mg in δ notation on the DSM-3 reference scale—can be used to unveil the nature of the water-rock reactions that supplied Mg to ALH84001 carbonates. Congruent chemical weathering of basalt leaches Mg from their igneous silicates, generating a fluid with $^{26}$Mg/$^{24}$Mg similar to the parent rocks (Magna et al., 2017; Přikryl et al., 2018). Magnesite — a carbonate commonly associated with basalt weathering — would inherit this signature with fractionation of $^{26}$Mg/$^{24}$Mg relative to dissolved Mg in its parental waters (fractionation factor, $^{26}\alpha_{\text{magnesite-fluid}}$=0.9976 at 291 K). Both serpentinization (de Obeso et al., 2021; Qu et al., 2025) and incongruent basalt weathering (Luo et al., 2025) first form hydrated secondary phyllosilicates that preferentially incorporate $^{26}$Mg (Oskierski et al., 2019; Wang et al., 2019), leaving the fluid depleted in $^{26}$Mg/$^{24}$Mg. Common carbonates forming from that fluid are expected to inherit this signature with similar isotopic fractionation, i.e., they should be even lower $^{26}$Mg/$^{24}$Mg than carbonates that precipitate from solutions produced by congruent basalt weathering. Relative to their unaltered host rock, phyllosilicates in terrestrial serpentinization environments show distinctly higher $^{26}$Mg/$^{24}$Mg enrichment (up to +1.5‰, (*34*)) than weathering-derived phyllosilicates (up to +0.7‰, (*31*)). Since residual fluids should be complementarily depleted in $^{26}$Mg/$^{24}$Mg by mass balance, serpentinization-derived carbonates should have a lower $^{26}$Mg/$^{24}$Mg than those from incongruent basalt weathering.
However, if advanced silicate weathering (i.e., continued reaction between water and the initial products of weathering or serpentinization) follows a first stage of serpentinization incongruent basalt weathering, then the cations leached out of the secondary hydrous phyllosilicates by the weathering fluid would create a high $^{26}$Mg/$^{24}$Mg rich fluid from which, carbonates with $^{26}$Mg/$^{24}$Mg *higher* than that from congruent basalt weathering fluid would

precipitate. Furthermore, Mg isotope fractionation is sensitive to the identity of the precipitated carbonate phase: hydrous Mg-carbonates (nesquehonite, hydromagnesite) fractionate heavier Mg isotopes in their structure (${}^{26}\alpha_{\text{carbonate-fluid}}$ up to 1.0012 at 291 K), whereas anhydrous Mg-carbonates (dolomite, magnesite) fractionate lighter ones (${}^{26}\alpha_{\text{carbonate-fluid}}$ down to 0.9976 at 291 K). Thus, ${}^{26}$Mg/${}^{24}$Mg of carbonates tracks several aspects of the water-rock interaction that led to carbonate precipitation and is particularly useful when combined with other information (carbonate chemistry, texture, and C-O isotopes) to resolve ambiguities regarding the drivers of ${}^{26}$Mg/${}^{24}$Mg variations.

## 6.2 Materials and methods

### 6.2.1 Material

A petrographic section (1" round) of ALH84001 (ALH84001,311) was acquired from National Aeronautics and Space Administration (NASA) for this study. This section has previously been characterized for mineralogy and oxygen isotopic composition (Eiler et al., 2002b). Most of our Mg isotopic measurements are from this section. Another ALH84001 mount, also characterized before (Valley et al., 1997), was acquired and studied for textural relationships and mineralogical compositions.

### 6.2.2 Scanning Electron Microscope - Energy Dispersive Spectroscopy (SEM-EDS)

SEM-EDS was done at California Institute of Technology, on a Zeiss 1550 VP field emission SEM, equipped with Oxford X-Max SDD X-ray Energy Dispersive Spectrometer (EDS) system, with acceleration voltage of 15 kV and a working distance of 4.7 mm for both imaging and spectral acquisition.

### 6.2.3 Electron Probe Microanalysis (EPMA)

Major cation chemistry of carbonates was determined using a field-emission electron microprobe (JEOL JXA-iHP200F "Hyperprobe") in wavelength dispersive spectroscopy (WDS) mode at California Institute of Technology. Analytical conditions were 15 kV accelerating voltage, 10 nA beam current and 10 μm defocused beam. Natural carbonate standards (Calcite, Dolomite, Siderite, Strontianite and Rhodochrosite) were used as standards to quantify Ca, Mg, Fe, Mn and Sr content in carbonates. Both point data and WDS maps were acquired, and data processing was done using Probe for EPMA software. Using same conditions, we prepared WDS maps of different carbonate regions. These were converted to quantitative WDS maps using Probe for EPMA software. The chemical compositions of some Secondary Ion Mass Spectrometer (SIMS, also called ion microprobe) spots were retrieved from these maps using ArcMap software.

### 6.2.4 Mass spectrometry

Since bulk digestion measurements mix Mg from different carbonate components and are destructive to the meteorite, we measured $^{26}Mg/^{24}Mg$ of carbonates as small as 5 µm *in-situ* using SIMS.

We standardized our ion-microprobe measurements using synthetic carbonates and one natural magnesite, described in Chapter 6. We made 23 analyte measurements spread over two analytical sessions, comprising 19 measurements of carbonate concretions and 4 measurements of Fe-dolomite domains. The composition of each spot was determined from quantitative electron-microprobe X–ray mapping of cation concentrations, to apply a matrix effect correction based on carbonates' molar Ca+Fe+Mn content. Corrected $^{26}Mg/^{24}Mg$ of ALH84001 carbonates measured in the same regions in both sessions were statistically indistinguishable. These are the first reported $^{26}Mg/^{24}Mg$ measurements of any carbonate mineral using SIMS. Analytical conditions are reported in Table 6.3 (sessions 2,3), and matrix effect calibration is shown in Fig. 6.2d.

### 6.2.5 Fluid $^{26}Mg/^{24}Mg$ calculation

Bulk Mg isotopic composition of carbonate precipitating fluid depends on proportions of different $Mg^{2+}$ complexes in the fluid and their $^{26}Mg/^{24}Mg$. Constraining the bulk fluid is critical to fingerprint the Mg source of the fluid. To examine the aqueous speciation of Mg during precipitation of hydromagnesite in ALH84001, we constructed a geochemical model simulates the batch evaporation of hypothetical Martian groundwater in connection with a $CO_2$-rich atmosphere, modified from a similar analysis by Catling (Catling, 1999a). Calculations were made using PHREEQC v. 3 (Parkhurst and Appelo, 2013) with the *llnl.dat* thermodynamic database. The Truesdell-Jones (Truesdell and Jones, 1974) extension of the Debye-Hückel equation was used to estimate the activity of aqueous species at high ionic strength, although ionic strengths required to precipitate magnesite far exceed its empirical validity.

The initial composition of Martian groundwater that interacted with ALH84001 is uncertain. We considered the evolution of a model fluid derived from surficial carbonic acid weathering of orthopyroxenite, modified from Catling's (Catling, 1999b) estimate of Martian ultramafic-sourced groundwater. As no calcite is observed in ALH84001 and orthopyroxene is Ca-poor compared other ultramafic rocks, a lower initial Ca concentration of 0.25 mmol/kg was used than Catling (Catling, 1999b). Similarly, as ALH84001 is a more Mg-rich orthopyroxenite than average Martian meteorites, a lower initial Mg/Fe ratio of 1:0.04 mmol/mmol matching the composition of ALH84001 was used (Mittlefehldt, 1994; Catling, 1999b). The concentration of initial $HCO_3^-$ was decreased in a 2:1 ratio for both Ca and Fe, under the assumption that both ions derive from carbonic acid weathering. The initial solution composition is shown in Table S6.

Evaporation was simulated at 298 K and 0.6 bar $pCO_2$. Amorphous silica, crystalline siderite, ordered dolomite, hydromagnesite, and gypsum were permitted to precipitate and remain in equilibrium with the solution as it evolved. Although Catling (Catling, 1999b) modelled calcite equilibration, dolomite was modelled as the Ca-rich carbonate phase to better match the observed ankerite compositions in ALH84004. Considerable uncertainty exists in the saturation state at which these minerals precipitated, the temperature, the ability for fluids to equilibrate with martian atmospheric $CO_2$, and the solubility product constants for the siderite-ankerite and magnesite-magnesiosiderite solid solutions observed.

In the simulation, hydromagnesite precipitation starts at an evaporation factor of $10^{2.55}$, by which pH has risen to 7.1 (Figure S4A). Mg is speciated predominately as the $Mg^{2+}$-aquo complex (53%), with 34% as $MgHCO_3^+$ and 11% $MgSO_4^0$ (**Error! Reference source not found.**B, Table S7). As hydromagnesite continues to precipitate, the importance of the $MgSO4^0$ and $MgCl^+$ complexes increase in predominance. Hydromagnesite has largely precipitated by an evaporation factor of $10^{3.5}$, after which point these are the dominant complexes, Mg is 62% complexed, and pH has fallen to 6.9. Only about 135 μmol of hydromagnesite per kg of initial solution, or 0.0135% of the initial Mg, precipitates; this is limited by the activity of free $Mg^{2+}$, and of free $HCO_3^-$ and $CO_3^{2-}$, which is largely complexed to Mg or Na (Figure S4B,C,D). Given that previous studies have convincingly provided evidence for a near-complete evaporation and mineral precipitation (Halevy et al., 2011), it seems that our simple model failed to predict the extent of Mg precipitated, possibly because we simply modelled hydromagnesite precipitation, as equilibrium constants for Ca,Fe,Mg-rich carbonates like those seen in ALH84001 are lacking in the database.

Once the relative proportions of Mg-anion complexes in aqueous fluid is determined, the next step is to calculate the bulk $^{26}$Mg/$^{24}$Mg of the fluid. Hydrous carbonates prefer to incorporate $^{26}$Mg in their structure relative to aqueous $Mg^{2+}$. Previous studies reported that $^{26}$Mg/$^{24}$Mg fractionation between aqueous $Mg^{2+}$ and anhydrous Mg-Ca carbonate minerals depend on their Mg/(Mg+Ca) ratio (Wang et al., 2017; Patron et al., 2025). While a similar effect is expected for variation of Fe/(Fe+Mg) ratio of hydrous carbonates, the exact magnitude of this correction has not been quantified. Assuming substitution by $Fe^{2+}$ impacts this fractionation similar to $Ca^{2+}$ (given their ionic radii are similar), we estimated this fractionation factor as a function of Mg/(Mg+Ca) ratio of our analyte carbonates (Wang et al., 2017) at 291 K. We then calculated the fluid $^{26}$Mg/$^{24}$Mg with both the corrected fractionation factors (a function of Mg/(Mg+Ca) of carbonates) and a constant hydromagnesite-water fractionation factor ($^{26}\alpha_{\text{hydromagnesite-fluid}} = 1.0012$). The extent of this concentration effect was found to be highest for concretion cores (~0.7–1.7‰), and negligible for mantle or rim compositions (~0.1–0.3‰). The ~5‰ range observed in measured $\delta^{26}\text{Mg}_{\text{carbonates}}$ suggests that the entire data cannot be simply explained by a concentration effect. However, the corrected and uncorrected data are statistically indistinguishable within analytical uncertainty (0.8‰, 2σ), and the correction neither changed the trend in Fig. 2a, nor our interpretations (Fig. S7). Using equilibrium fractionation factors previously reported (Li et al., 2011; Gao et al., 2018), we calculated $^{26}$Mg/$^{24}$Mg of different Mg-bearing aqueous complexes in equilibrium with aqueous $Mg^{2+}$. Finally, $^{26}$Mg/$^{24}$Mg of bulk fluid is the weighted average $^{26}$Mg/$^{24}$Mg of all Mg-bearing aqueous complexes present in fluid, weighted by their relative proportions in fluid (Table S7).

## 6.3 Results and discussion

### 6.3.1 Mg isotope evidence for hydrous carbonates

We measured $^{26}$Mg/$^{24}$Mg of ALH84001 carbonates *in situ*, in domains ranging in diameter from 5-7.5 μm, using an ion microprobe (or Secondary Ion Mass Spectrometer, SIMS). The accuracy of SIMS-based isotope ratio measurements in carbonates is sensitive to their cation composition (i.e., due to instrumental matrix effects), and compositionally similar standards are required to correct for instrumental fractionations. The rarity of suitable terrestrial carbonates poses a serious challenge for the standardization of our measurements. To mitigate this problem, we used knowledge of the phase relations of mixed carbonates (Franzolin et al., 2011; Shatskiy et al., 2018) to synthesize, at elevated pressure and temperature, standards that match the major cation chemistry of each layer of the ALH84001 concretions. The synthesized material is texturally and compositionally homogeneous and showed consistent instrumental mass fractionation behavior over two analytical sessions (see SI). We standardized our ion-microprobe measurements using these carbonates and one natural magnesite. We made 23 measurements over two analytical sessions, comprising 19 from carbonate concretions and 4 from Fe-dolomite domains. The cation composition of each spot was determined from quantitative electron-microprobe X–ray mapping of cation concentrations, to apply a matrix effect correction (see SI). Corrected $^{26}Mg/^{24}Mg$ of ALH84001 carbonates measured in the same regions in both sessions were statistically indistinguishable. These are the first reported $^{26}Mg/^{24}Mg$ measurements of any carbonate mineral using SIMS.

Two measurements of the (Ca, Fe)-rich cores of the concretions (Fig. 2a; Table S9) yield $\delta^{26}Mg$ of 3.3±0.8‰ and 4.7±0.8‰—the highest among all phases, and distinctly high compared to terrestrial carbonates ($-5.6‰<\delta^{26}Mg<-0.4‰$; (*34*)). The Fe-rich mantles have a more restricted range of 1.7–3.1‰ in $\delta^{26}Mg$. The outermost mantle of nearly pure magnesite has the lowest Mg isotope ratios of all (–2.4 to 1.3‰). Other carbonate globules have intermediate $\delta^{26}Mg$ values (–0.7 to 2.0‰), depending on their composition. The Mg isotope ratios of the concretion carbonates are positively correlated with the mole fraction of $FeCO_3$ in them (Fig. 2a), showing a core-to-rim decrease in $\delta^{26}Mg$.

Prior studies have established that these concretions precipitated from core to rim in a single event (Golden et al., 2000; Niles et al., 2009; Halevy et al., 2011). If these carbonates precipitated as magnesite ($^{26}\alpha_{\text{magnesite-fluid}}=0.9976$, *42*), then the initial fluid that precipitated their cores would need to have $\delta^{26}Mg \sim 7‰$. We know of no process or source capable of generating such a Mg isotope ratio in the fluid (highest $\delta^{26}Mg$ from terrestrial reservoir

~1.75‰, *39*). Moreover, since magnesite fractionates lighter Mg isotopes relative to fluid, continuous magnesite precipitation would lead to an isotopic distillation where the last precipitates (rims) should have heavier $\delta^{26}$Mg than earlier precipitates (cores) (Fig. S6) — opposite to what we observe.

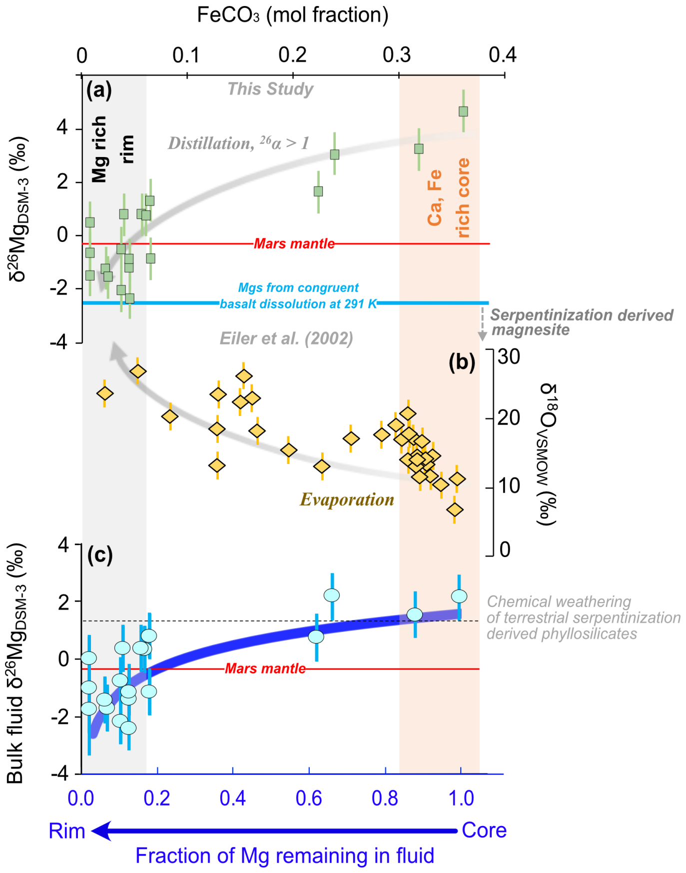

Figure 7.2: (a) Mg and (b) previously published O isotopic composition of carbonates from ALH84001, as a function of their $FeCO_3$ content (all error bars are 2σ propagated). Compositions Ca, Fe-rich carbonate cores and Mg rich rims are shown as shaded orange and gray bars, respectively. Gray arrow in (a) represents precipitation of $^{26}$Mg rich hydrous carbonates (see SI), while yellow arrow in (b) indicates evaporation trend. Arrows are schematic and only to guide the eye. (c) Evolution of calculated Mg isotopic composition of bulk carbonate precipitating fluid, as a function of carbonates' $FeCO_3$ content. Dissolution of terrestrial serpentinization produced phyllosilicates (gray dotted line) explains the fluid Mg isotopic composition of concretion cores. Blue curve shoes modelled Mg isotopic distillation of such a fluid, by continuous hydromagnesite precipitation, as a function of the remaining Mg in the fluid (against blue horizontal axis in the bottom). This scenario explains the calculated fluid Mg isotope range as well as trend in this space.

Instead, both the elevated $\delta^{26}$Mg in the cores and the core-to-rim decrease in $\delta^{26}$Mg suggest carbonate initially precipitated as a phase that fractionates heavier Mg isotopes in its structure relative to aqueous fluid ($^{26}\alpha_{\text{carbonate-fluid}}>1$), resulting in isotopic distillation towards lower $\delta^{26}$Mg values as the carbonate precipitation proceeded. Hydrous Mg-carbonates (hydromagnesite, nesquehonite) are the only carbonate solids known to preferentially incorporate $^{26}$Mg compared to aqueous $Mg^{2+}$ ions. In alkaline fluid (Niles et al., 2009), hydromagnesite is the more stable of these two minerals, suggesting that the concretions initially precipitated as hydromagnesite (or similar hydrous phase) near the Martian surface, and subsequently transformed to anhydrous Fe-Mg-Ca carbonates. Moreover, a core-to-rim increase in $^{18}O/^{16}O$ of carbonates (Fig. 2b) reflects the evaporative enrichment in $^{18}O/^{16}O$ in the fluid during precipitation (Eiler et al., 2002b; Halevy et al., 2011). This suggests that hydromagnesite precipitated on Mars under evaporative conditions ~3.94 billion years ago. This aligns with hydromagnesite formation on Earth under similar conditions (Mavromatis et al., 2021; Eva L. Scheller et al., 2021), where anhydrous carbonates resist precipitation due to a kinetic $Mg^{2+}$ dehydration barrier (Power et al., 2017). Initial precipitation of the concretions as hydrous carbonate also explains their trace deuterium-rich hydrous component (Eiler et al., 2002a) with D/H confirming their Martian origin (Sugiura and Hoshino, 2000; Boctor et al., 2003) and may also help understand their $^{17}$O-rich nature, as only hydrous carbonates can exchange oxygen with $^{17}$O-rich atmospheric compounds via their waters of hydration (*40*).

### 6.3.2 Clay-derived Mg in ALH 84001 carbonates

Previous constraints on the pH and major cation composition of the carbonate-forming fluids (Catling, 1999a) allow us to calculate their speciation. Using the known isotopic fractionation factors between hydromagnesite and aqueous species (see SI; *37*), we calculated the $\delta^{26}$Mg of the bulk fluid at each stage of concretion growth. Fluids precipitating the (Ca, Fe-rich) cores were $^{26}$Mg-rich ($\delta^{26}Mg = 1.8\pm0.8‰$), while the magnesite rims grew from relatively $^{26}$Mg-poor fluid ($\delta^{26}Mg = -2.5$ to $0.6‰$); a decrease consistent with modelled fluid isotopic distillation by continuous hydromagnesite precipitation (Fig. 2c). Such high initial $\delta^{26}$Mg of the fluid cannot be derived by congruent dissolution of igneous silicates in

Martian basalts ($\delta^{26}Mg_{\text{Bulk Silicate Mars}}$ = –0.27±0.04‰; *31*) or of the orthopyroxene in ALH84001 ($\delta^{26}Mg_{\text{opx}}$ = –0.19±0.08‰; *31*) and also cannot result from serpentinization or incongruent basalt weathering of igneous rocks ($\delta^{26}Mg_{\text{fluid}}$ < –0.19±0.08‰). Moreover, if fluid derived its cations by altering basalts, they should be enriched $Mn^{2+}$ (a significant component in primary minerals), and any carbonate precipitating from such a fluid should have high $Mn^{2+}$ content, as they are easily incorporated in Mg-Fe carbonates (Tutolo et al., 2025). The absence of $Mn^{2+}$ in concretion carbonates suggests that basalt is not the source of carbonate-forming cations. Alternatively, a fluid can evolve to high $\delta^{26}Mg$ values if it dissolves/precipitates secondary minerals during its flow path before the ALH84001 host rock. Based on limited observational and experimental constraints, such a dissolution-precipitation aided fluid evolution seems unlikely (see SI). Phyllosilicate from serpentinization/incongruent weathering constitute a sufficiently high $\delta^{26}Mg$ reservoir on Earth. If observed Martian phyllosilicates (e.g., smectites, (Ye and Michalski, 2022)) have comparable $\delta^{26}Mg$, their dissolution by weathering, i.e., by advanced chemical weathering that progresses beyond initial phyllosilicate formation, can only parsimoniously explain the carbonate forming fluids. Such a scenario satisfies all prior constraints and geological observations, and is supported by the susceptibility of smectites to weathering (by acids or oxidants, which were abundant on a $CO_2$- and $SO_2$-rich early Mars (Gaudin et al., 2011)).

We require a Martian phyllosilicate that is 2.0±0.8‰ heavier in $\delta^{26}Mg$ than host Martian mafic rocks to explain the concretion core. Because $\delta^{26}Mg$ values in Martian phyllosilicates are unknown, we resort to terrestrial observations, as mechanisms of phyllosilicate generation are expected to be similar on Earth and Mars. Dissolution of phyllosilicates from incongruent terrestrial weathering—with $\delta^{26}Mg$ up to +0.7‰ heavier than igneous hosts (Luo et al., 2025)—cannot explain the 2.0±0.8‰ enrichment. However, terrestrial serpentinization-derived phyllosilicates can be up to +1.5‰ heavier in $\delta^{26}Mg$ than their host rocks (de Obeso et al., 2021). If Martian phyllosilicates are likewise enriched in $\delta^{26}Mg$ via serpentinization, then their near-complete chemical weathering can yield the high $\delta^{26}Mg$ solution required to form concretion cores. If so, concretions and their source phyllosilicates should have a comparable Fe/Mg ratio. The Fe/Mg ratio of concretion carbonates is consistent with derivation from an Mg-rich clay, possibly serpentinization-generated (see SI). This reveals that serpentinization and silicate weathering operated on Mars in tandem.

### 6.3.3 Si isotopic composition of chert grain in ALH84001

To strengthen our interpretations, we measured Si isotopic composition of one silica path included in orthopyroxene in ALH84001. Phyllosilicates favor $^{28}Si$ in their structure (Kleine et al., 2018), and their dissolution produces $^{28}Si$ rich fluid. As conditions become alkaline, this silica eventually precipitates as chert earlier than carbonates (Hobbs and Xu, 2020). This likely happened elsewhere before the fluid reached orthopyroxenite host rock. Major chert precipitation enriched the residual fluid in $^{28}Si$ as chert preferentially incorporates $^{30}Si$ in its structure (Kleine et al., 2018). Rarely, silica precipitated in ALH84001 host rock concurrent with carbonate precipitation. We made SIMS Si isotope measurements of such a small silica domain associated with the carbonate concretions. The silica grain is found to be highly $^{28}Si$-rich ($\delta^{30}Si = –8.5±0.4‰$) compared to bulk Mars ($\delta^{30}Si = –0.49±0.03‰$; *36*). Such extreme values are not observed on Earth and only testify to near-complete chert precipitation upstream. The initial chert precipitating fluid likely was $^{28}Si$-rich via chemical weathering of clays.

### 6.3.4 Mg isotopic composition of Fe-dolomite in ALH84001

ALH84001 has large (100-300 μm) domains of dolomites ($Mg_{0.13}Fe_{0.32}Ca_{0.49}Mn_{0.06}CO_3$) texturally intermixed with feldspathic glass (Eiler et al., 2002b) (Fig. S5a–c). These Fe-dolomites are previously thought of having a high temperature origin, possibly products of shock melting of pre-existing carbonate-pyroxene assemblage. We measured the $\delta^{26}Mg$ of 4 Fe-dolomite grains, and coupled them to their $\delta^{18}O$ measurements (Eiler et al., 2002b). These dolomites have lighter Mg isotopic composition (average $\delta^{26}Mg = –0.9±0.5‰$) relative to the concretions. Using known $\delta^{18}O$ (Eiler et al., 2002b) and $\delta^{26}Mg$ (Magna et al., 2017) of orthopyroxenes from ALH84001 and Mg-O isotopic fractionation factors between pyroxene and dolomite (Schauble, 2011; Schauble and Young, 2021), we predicted $\delta^{26}Mg$ and $\delta^{18}O$ of dolomite in equilibrium with ALH84001 orthopyroxene at 373–973 K. The average ALH84001 dolomite composition conforms to equilibrium with orthopyroxene at high temperature (Fig. S5d, Table S8). The isotopic equilibrium temperature is in fact close to a shock event temperature recorded by the cation composition of orthopyroxenes (Domeneghetti et al., 2007).

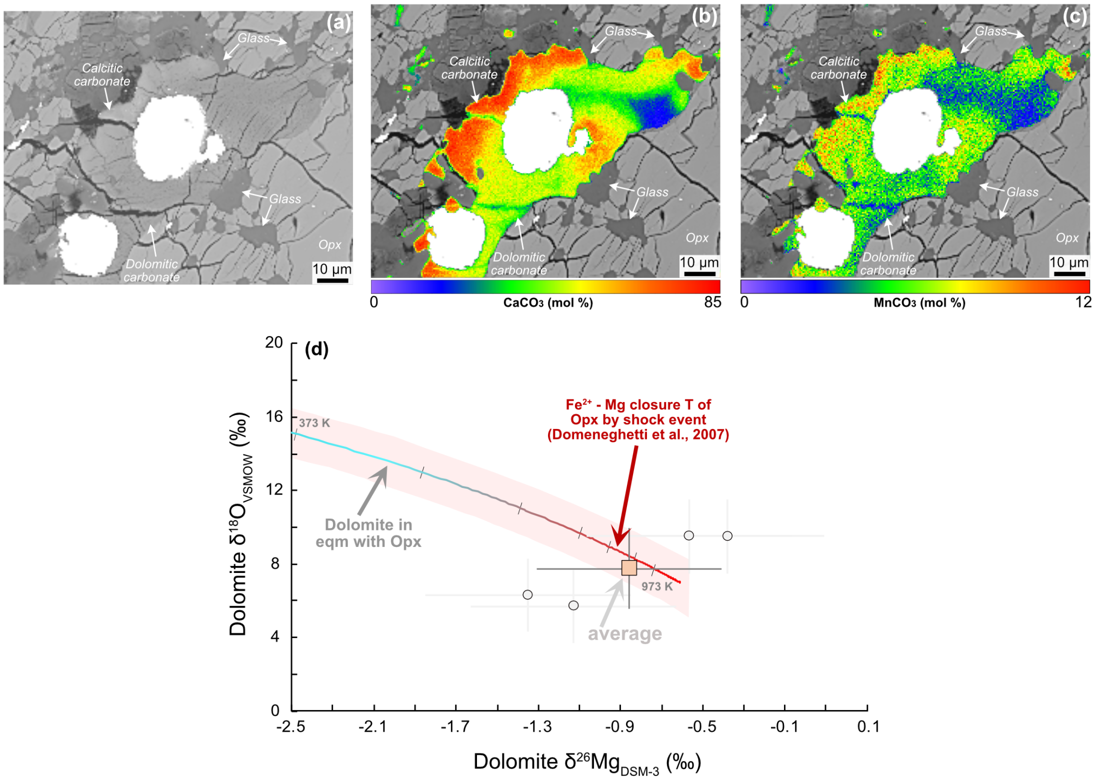

Figure 7.3: Texture and composition of Fe-dolomite from ALH84001. (a) BSE image of dolomites, Ca-carbonate, Opx and glass. (b,c) Quantitative $CaCO_3$ and $MnCO_3$ content map of dolomites. (d) Mg-O isotopic composition of the dolomites (circles), and their average (square). Oxygen isotope data from (Eiler et al., 2002b). Gradient colored line with shaded area shows calculated isotopic composition of dolomite in equilibrium with ALH84001 Opx (Valley et al., 1997; Eiler et al., 2002b; Magna et al., 2017) at 373 K - 973 K, with fractionation factors from (Schauble, 2011; Schauble and Young, 2021). Average dolomite is in isotopic equilibrium with Opx at ~873 K, which is close to shock resetting temperature of Opx (Domeneghetti et al., 2007).

## 6.4 Implications

### 6.4.1 Silicate weathering on early Mars and impact on its climate and habitability

Our findings suggest a geological scenario for the development of carbonate concretions in an orthopyroxenite rock on early Mars, as a simple two-stage process. First, alteration (likely serpentinization, see SI) of mafic or ultramafic rocks developed a reservoir of high

$\delta^{26}$Mg phyllosilicates (Oskierski et al., 2019; Qu et al., 2025). From mass balance, a complementary reservoir of isotopically light Mg (sink of low $\delta^{26}$Mg residual fluids) should exist elsewhere on the Martian crust; perhaps sampled by secondary phases in other Martian meteorites or those in evaporite deposits (Bridges and Grady, 1999; Ye and Michalski, 2022). Second, these phyllosilicate-bearing rocks became exposed near the Martian surface, and chemical weathering leached out their base cations (Fe, Mg, Ca) into solution (presumably leaving behind Al-rich clays) (Ye and Michalski, 2022; Moore et al., 2025). These solutions, carrying their elevated $\delta^{26}$Mg signature, flowed into the regolith and precipitated carbonates as the fluids evaporated from an unconfined subsurface aquifer under arid conditions (Fig. 3). Such a process is consistent with inferences about early Martian watersheds. Numerous impact craters serve as active Martian watersheds due to their topographic relief, exposing altered mafic rocks in crater rims upstream of igneous assemblages on the crater floors (Farley et al., 2022). Phyllosilicates like Fe-Mg smectite, formed by alteration of basalts or ultramafic rocks, are observed in such crater rims (Ehlmann et al., 2013), often capped by Al-rich clays that indicate extensive leaching of base cations from the smectite (Ye and Michalski, 2022). Such weathering, possibly intermittent in nature (*49*) and occurring alongside or after the aqueous alteration of the Martian crust (E. L. Scheller et al., 2021), was likely prevalent on early Mars (Moore et al., 2025). Occasional warm and wet episodes of early Noachian climate may have allowed episodic snowmelt from higher altitudes in the southern highlands (Christensen, 2003; Kite, 2019; Kite and Conway, 2024), generating aqueous fluids that could facilitate this episodic weathering.

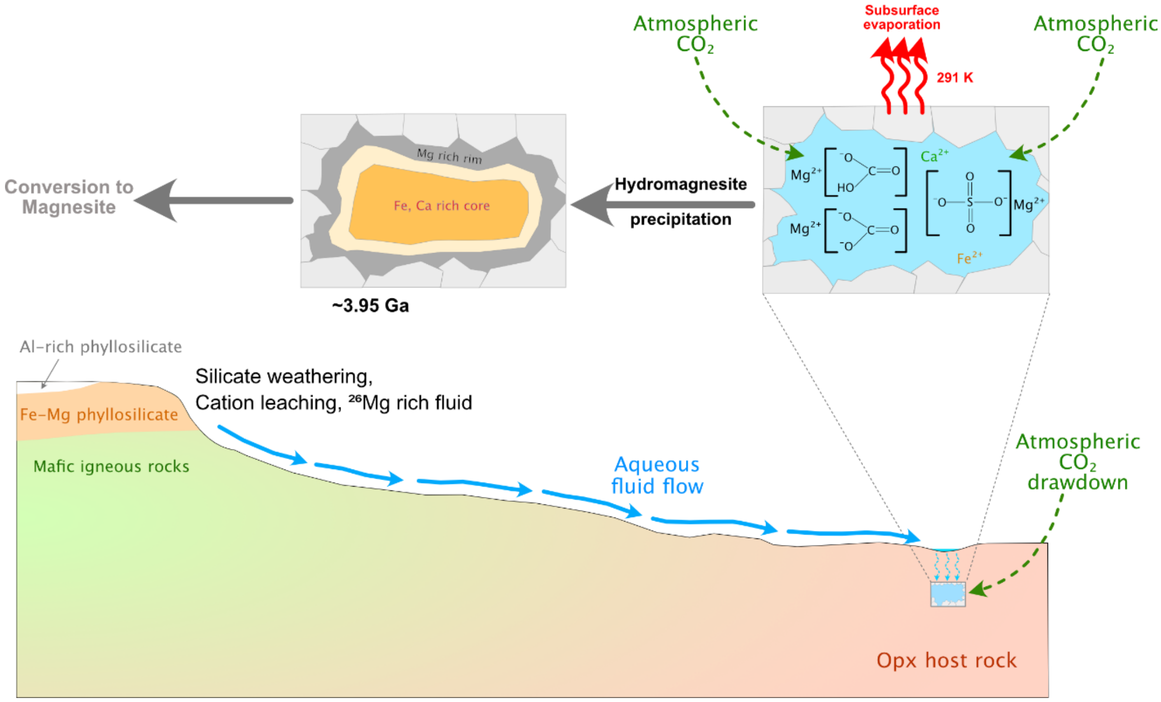

Figure 7.4: Geological model for water-rock cycles on early Mars.

Our proposed geological scenario reveals a holistic Martian carbon cycle—cations sourced from smectite weathering combined with carbon from the Martian atmosphere (Niles et al., 2005; Halevy et al., 2011; Shaheen et al., 2015) to form carbonates. Carbonate concretions in ALH84001 may represent a more widespread authigenic carbonate reservoir that closes the Noachian Martian carbon cycle (Moore et al., 2025; Tutolo et al., 2025). It is possible that the majority of near-surface Martian carbonates formed, like ALH84001 concretions, in subsurface evaporative environments, explaining why they are rarely observed on the surface by orbital or rover-based observations.

An intriguing consequence of ALH84001 carbonates being connected to weathering is silicate weathering feedback, where continuous carbonate formation and atmospheric $CO_2$ drawdown could lead to global cooling, the extent of which depends on the surface exposure of weatherable clays, availability of liquid water, and emission of counterbalancing volcanogenic $CO_2$ (Moore et al., 2025; Tutolo et al., 2025). Silicate weathering feedback is understood to regulate terrestrial climate and maintain habitable conditions that sustain liquid water near the Earth's surface (Walker et al., 1981; Sleep and Zahnle, 2001). If such a mechanism operated on Mars, it would be expected to have a similar influence on the Martian climate. Global ancient Martian surface evaporative sequences are estimated to store up to 36 mbar atmospheric $CO_2$ equivalent as carbonates, which is large compared to the present Martian atmosphere of ~6 mbar $CO_2$ (Tutolo et al., 2025). Additional major subsurface carbonate formation—resembling ALH84001 concretions—would imply that even more Martian atmospheric $CO_2$ can be stored geologically (Stanley et al., 2011; Lammer et al., 2013) than currently estimated, possibly facilitating climatic shifts. As such, our findings support the existence of an active Martian silicate weathering feedback (Moore et al., 2025; Tutolo et al., 2025).

ALH84001 carbonate concretions represent episodes of warm and humid conditions, during which liquid water and products of Martian crustal alteration (Fe-Mg smectites) were available (Moore et al., 2025; Adams et al., 2025), gradually giving way to arid and cooler conditions, resulting in strong evaporation. These transitions, perhaps modulated by silicate weathering feedback and likewise mechanisms (Wordsworth, 2016; Rapin et al., 2023; Kite and Conway, 2024), may have been a part of the 'wet-dry' cyclic climatic transitions predicted to have happened on early Mars (Rapin et al., 2023). These transitions possibly promoted the availability of near-surface liquid water that participated in chemical weathering. Martian weathering sequences witnessed tens of millions of years of aqueous activity (Ye and Michalski, 2022). Such long-term availability of liquid water near the Martian surface—unlike a mere short-term presence—fulfills a key criterion for the proliferation of life. As such, these transitions were critical in modulating the spatial and temporal distribution of environments favorable for the emergence of life. While previous rover observations from Gale crater indicate that wet–dry cycling began around 3.8–3.6 Ga (Rapin et al., 2023), our findings suggest that it was active even as early as ~4 Ga. Thus, influenced by a weathering-driven climate feedback, Martian habitability likely persisted for longer than currently estimated, episodically sustaining climate and subsurface conditions favorable for prebiotic chemistry (Sasselov et al., 2020; Rapin et al., 2023). The detection of organics in the near-surface environments of Jezero Crater (Hurowitz et al., 2025) underscores the role of water-rock cycling in shaping these environments, and future laboratory studies of returned Martian samples are required to unveil the global water-rock cycle and biopotential of Mars.

## 6.5 Conclusion

We conclude that ALH84001 carbonate concretions initially precipitated as hydromagnesite and sampled shallow crustal fluids that were products of advanced aqueous weathering of phyllosilicates previously formed by crustal serpentinization. If these carbonates are representative of early Noachian near-surface environments and processes, they would indicate active carbon and water cycles modulated by silicate weathering and carbonate precipitation, with the potential to drive climate feedbacks and thus environmental transitions on an early habitable Mars.

## Acknowledgements

SB acknowledges Morteza Safari, Arka Pratim Chatterjee, Noriko Kita, Bethany Ehlmann, Ken Farley, John Grotzinger for helpful discussions. This study was supported by Simons Foundation Life Science Project Award 668346 awarded to JPG and 3CPE funding awarded to SB and TMP.

## 6.6 Supplementary Material

### 6.6.1 Alternate mechanisms to generate $^{26}$Mg rich fluid on Mars

Our findings suggest that Mg in ALH84001 carbonates is sourced from phyllosilicate weathering. Alternative hypotheses avoiding silicate weathering must be tested, where a congruent basalt weathering or serpentinization-derived fluid can evolve to substantially $^{26}$Mg rich composition such as those needed to explain concretion cores. This can happen if fluid evolves via by secondary mineral dissolution/precipitation before concretion formation. The two Mg-bearing minerals that can precipitate under these conditions and are observed on Mars are anhydrous Mg-carbonate or Mg-sulfate (epsomite). Since these minerals are not seen in this meteorite, such precipitations would have to have happened elsewhere before the fluid percolated ALH84001 host rock. Cation and sulfate-rich fluid can potentially precipitate epsomite, where the residual fluid is left with cations (if sulfate-limited) or sulfate (if cation-limited). However, epsomite precipitation requires extreme aridity, to the extent that the aqueous fluids would completely evaporate before reaching the ALH84001 host rock. Even if a small fraction of fluid escapes evaporation, such fluid would be completely Mg, Ca-free, if cation limited. Such a fluid cannot precipitate Ca-Mg-Fe rich ALH84001 carbonates. If sulfate-limited, this fluid will have residual base cations after epsomite precipitation. But epsomite prefers $^{26}$Mg in its structure (Li et al., 2011). If we continually precipitate Mg-sulfate from a mantle-like or serpentinization-derived fluid, the residual fluids become $^{26}$Mg depleted, exactly opposite of that needed to explain ALH84001 carbonate cores. Hence, a fluid that has evolved by epsomite precipitation cannot explain the composition of ALH84001 carbonates. Mg-sulfate dissolution can make $^{26}$Mg rich fluid. Epsomite precipitated from Mantle like fluid at 291 K would have $\delta^{26}$Mg ~ +0.3‰ (Li et al., 2011), and that from serpentinization-derived fluid will have $\delta^{26}$Mg ~ <0.3‰. Their dissolution alone should generate fluid with $\delta^{26}$Mg up to +0.3‰—much lighter than needed to precipitate concretion cores.

Anhydrous Mg-carbonates like dolomite and magnesite remove lighter Mg isotopes from fluids ($^{26}\alpha_{\text{carbonate-fluid}}$ <1). One plausible idea is that congruent basalt dissolution creates a fluid with mantle-like $\delta^{26}$Mg, which then loses Mg through anhydrous Mg-carbonate precipitation along its flow path before reaching ALH84001. To match the fluid $\delta^{26}$Mg (~2.0‰) seen in concretion cores, 60–65% of the fluid's Mg would need to precipitate as anhydrous carbonates at the Martian surface. However, dolomite and magnesite are very rare on Mars; most surface carbonates are Fe–Mg-rich and often described as products of serpentinization of colocated olivine (Hicks et al., 2014; Tosca et al., 2025b). To our knowledge, dolomite hasn't been detected on Mars yet, except dolomite in ALH84001 which is genetically unrelated to the concretions. These suggest against fluid distillation via dolomite precipitation.

The idea that magnesite precipitation explains the isotopic record has two main problems. First, under near-surface Martian conditions, magnesite is unlikely to form because aqueous $Mg^{2+}$ dehydration is kinetically inhibited. Instead, hydrous Mg-carbonates are more likely to precipitate—and these have indeed been detected on Mars (Ehlmann et al., 2008; Niles et al., 2013b; Ehlmann and Edwards, 2014). However, their prior precipitation would drive the fluid toward lighter $\delta^{26}$Mg values (Fig. S6). Given the finding that ALH84001 concretion carbonates initially precipitated as hydromagnesite, it is difficult to comprehend a prior magnesite precipitation under similar conditions. Second, for magnesite to form, the fluid must already be depleted in calcium, and its precipitation would also remove $Fe^{2+}$. This would leave a residual fluid lacking both Ca and Fe, and therefore possibly unable to supply the necessary elements to form the Ca–Fe–rich ALH84001 carbonate concretions. One can argue that such Ca, Fe poor fluid dissolved secondary phases later to enhance its cation inventory, but that wouldn't have the high $\delta^{26}$Mg required to explain concretions cores.

Anhydrous Mg-carbonates may have formed in the Martian subsurface—similar to the ALH84001 concretions—and gone undetected by orbiters or rovers. However, evidence indicates that the carbonate-forming fluids in ALH84001 were initially linked to the atmosphere, not to long-term subsurface water–rock reactions (Halevy et al., 2011). If anhydrous carbonates had precipitated earlier under evaporative subsurface conditions, the resulting $\delta^{13}$C–$\delta^{18}$O evolution of the fluids would not explain that recorded in the concretions. These evidences suggest that a prior anhydrous Mg-carbonate precipitation is very unlikely. However, these are relatively loose constraints, and remain to be verified by further studies on returned samples.

Anhydrous carbonate dissolution makes $^{24}$Mg rich fluid—opposite of that needed to explain concretion cores. Hence, these events seem implausible. Since Martian Fe-Mg clay deposits are expected to preferentially incorporate heavier Mg isotopes, a complimentary reservoir of lighter Mg isotopes ($\delta^{26}$Mg<–0.3‰) is expected to exist on the Martian crust, possibly secondary minerals observed on the surface or evaporite deposits. Dissolution of minerals constituting this lighter Mg isotope reservoir would not explain that required for cocretion cores.

One can argue that the carbonate rims precipitated first, followed by the core. This is very unlikely, considering orders of magnitude higher compatibility of Ca, Fe than Mg in carbonates (Rimstidt et al., 1998), and directly contradicts previous petrographic, experimental, modelling or analog-study findings (Catling, 1999a; Golden et al., 2000; Steele et al., 2007; Niles et al., 2009; Moyano-Cambero et al., 2017). Moreover, precipitation of magnesite rim first cannot explain the trend observed in the carbonate and fluid $\delta^{26}$Mg space (Fig S6). Thus, starting from mantle-like or serpentinization fluids, no known processes can produce the $^{26}$Mg-rich fluids needed to explain ALH84001 carbonates, except with subsequent phyllosilicate weathering.

### 6.6.2 Origin of clays that weathered to supply cations for ALH84001 concretions

Diverse types of clays have been detected on the Martian surface, and there is considerable uncertainty about their origin (Ehlmann et al., 2013; Ye and Michalski, 2022). It is difficult to be certain of the origin of clays that acted as the source of cations for ALH84001 carbonates. Serpentinization and weathering forms clays under different redox conditions, and their Fe/Mg content is sensitive to the process (Michalski et al., 2015). The Fe/Mg ratio of different Martian clays suggests two major formation pathways: formation in an oxic environment with elevated Fe/Mg than igneous rocks (likely weathering), and formation in a reducing environment with Fe/Mg like Martian igneous rocks (likely serpentinization). The former are Fe-rich clays, where the latter are Mg-rich (Michalski et al., 2015).

Fe-serpentine minerals (e.g., hisingerite, characteristic product of Fe-rich igneous rocks on Earth, *50*)) and smectites have been identified in Nakhlites (Treiman et al., 1993; Changela and Bridges, 2010; Hicks et al., 2014; Lee et al., 2015; Pignatelli et al., 2025). Fe/Mg ratio of Nakhlitic smectite-rich phyllosilicates (1.2–3.2) (Changela and Bridges, 2010; Hicks et al., 2014) overlaps with that of their host olivine–pyroxene (0.7–5) (Lee et al., 2013). Rover-based observation and geochemical investigation found in-situ evidence for serpentinization in igneous rocks of Máaz formation, where Fe-Mg content of olivine overlaps with that of the product Fe-serpentine assemblage (Tosca et al., 2025b). These observations validate the utility of Fe-Mg content of host rocks and alteration products as a possible indicator of serpentinization.

With the premise that Martian phyllosilicates (e.g., smectites) completely leached its cations to weathering fluid that maintained its pristine cation content until ALH84001 carbonates precipitated, the average Fe/Mg ratio of concretions can be diagnostic of the type of clay that weathered to supply its cations. Forming Mg-rich concretions (Fe/Mg<0.4) requires chemical weathering of Mg-rich (Fe/Mg<0.5) clays. Such a clay Fe/Mg ratio overlaps with that of igneous protoliths (Michalski et al., 2015). This suggests a process of clay formation that did not segregate Fe from Mg, possibly via water limiter and/or reducing conditions of Martian subsurface—conditions consistent with serpentinization (Ehlmann et al., 2011; Meunier et al., 2012).

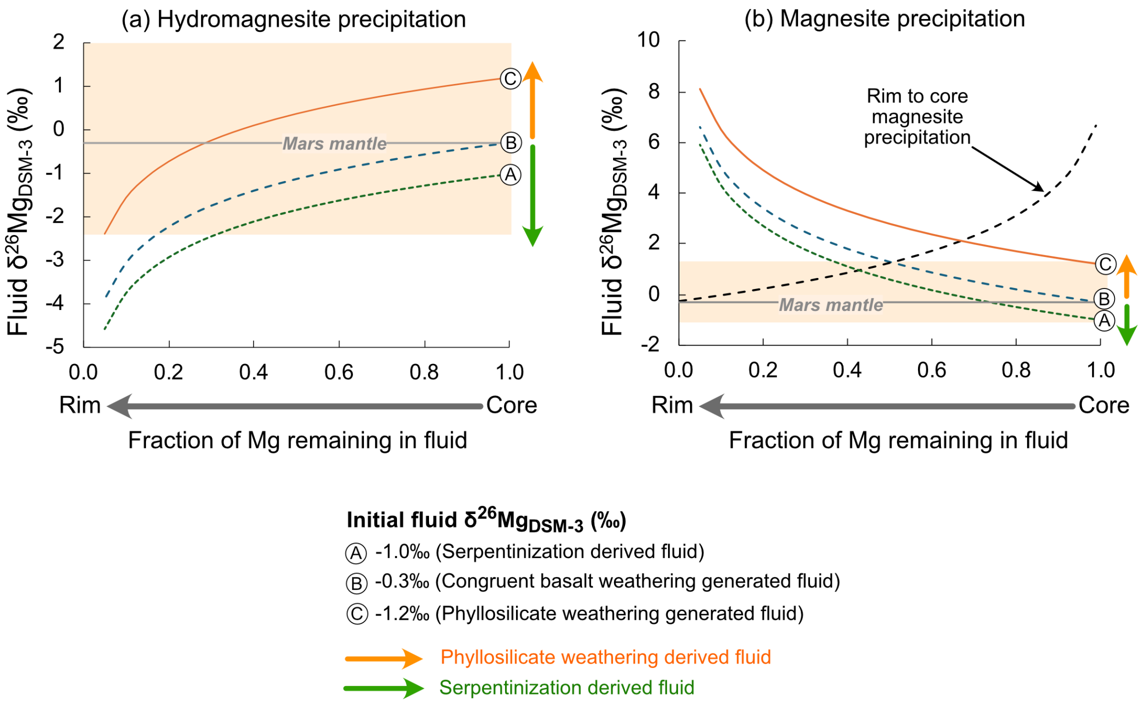

Figure S7.1: Evolution of fluid $\delta^{26}$Mg via continuous closed-system precipitation of (a) hydromagnesite ($^{26}\alpha_{\text{hydromagnesite-fluid}} = 1.0012$) and (b) magnesite ($^{26}\alpha_{\text{magnesite-fluid}} = 0.9977$), as a function of fraction of Mg remaining in the fluid. Fractionation factors from Chapter 5. Green and orange arrows indicate the evolution of initial fluid by serpentinisation and phyllosilicate weathering, respectively. Pale orange field shows the range of calculated fluid $\delta^{26}$Mg. A magnesite precipitation cannot explain the trend in observed core to rim isotopic evolution of fluid (Fig. 2), whereas a hydromagnesite precipitation explains both the range in fluid $\delta^{26}$Mg and their core to rim trend.

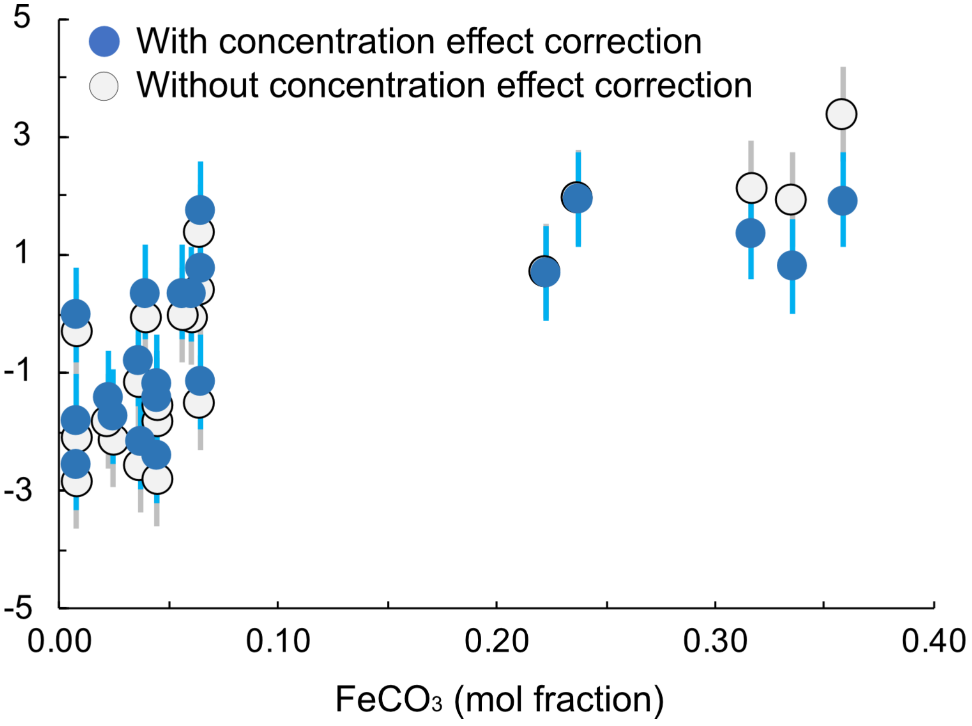

Figure S7.2: Calculated fluid $\delta^{26}$Mg with and without the 'concentration effect' correction (variation of $^{26}\alpha_{\text{hydromagnesite-fluid}}$ with its Fe content), according to the previously reported relationship between $^{26}\alpha_{\text{carbonate-fluid}}$ and mol% $MgCO_3$ in carbonates (Wang et al., 2017). This correction is highest for the most Ca-rich inner core data (~1.7‰ difference between corrected and uncorrected data). However, all the corrected and uncorrected data are statistically indistinguishable within propagated analytical uncertainty (2σ).

Table 7.1: Initial groundwater composition used for evaporation model, derived from Catling (1999b) with modified $Fe^{2+}$, $Ca^{2+}$, and $HCO_3^-$ (see supplemental text). Concentration units are mmol/kg of water.

| | **$H_4SiO_4^0$** | **$Fe^{2+}$** | **$Mg^{2+}$** | **$Ca^{2+}$** | **$Na^+$** | **$K^+$** | **$Cl^-$** | **$HCO_3^-$** | **$SO_4^{2-}$** |
|---|---|---|---|---|---|---|---|---|---|
| Catling's (Catling, 1999b) average Martian ultramafic groundwater | 1.0 | 0.8 | 1.0 | 0.5 | 0.8 | 0.07 | 0.65 | 4.49 | 0.18 |
| Modified Martian opx groundwater (this study) | 1.0 | 0.4 | 1.0 | 0.25 | 0.8 | 0.07 | 0.65 | 3.19 | 0.18 |

Table 7.2: Speciation of Mg at onset and after most hydromagnesite precipitation. Concentration units are mmol/kg of water.

| **Evaporation factor** | **$\Sigma Mg_{(aq)}$** | **$Mg^{2+}$** | **$MgSO4^0$** | **$MgCl^+$** | **$MgHCO_3^+$** | **$MgCO_3^0$** | **$MgOH^+$** | **pH** |
|---|---|---|---|---|---|---|---|---|
| $10^{2.2}$ | 0.1381 | 7.306E-2 | 1.524E-2 | 1.829E-3 | 4.636E-2 | 1.634E-3 | 8.195E-7 | 7.10 |
| $10^{3.5}$ | 0.6424 | 2.426E-1 | 2.408E-1 | 7.860E-2 | 7.867E-2 | 1.766E-3 | 1.265E-6 | 6.90 |

Table 7.3: Cation chemistry and Mg isotopic composition of ALH84001 concretion carbonates and bulk fluid.

| Point | $CaCO_3$ | $MgCO_3$ | $FeCO_3$ | $SrCO_3$ | $MnCO_3$ | $\delta^{26}Mg_{DSM-3}$ (‰) | 1σ | Bulk fluid $\delta^{26}Mg_{DSM-3}$ (‰) | 1σ |
|---|---|---|---|---|---|---|---|---|---|
| Mag-1 | 0.05 | 0.91 | 0.04 | 0.00 | 0.00 | –1.2 | 0.4 | –1.4 | 0.4 |
| Mag-2 | 0.14 | 0.50 | 0.36 | 0.00 | 0.01 | 4.7 | 0.4 | 2.1 | 0.4 |
| Mag-3 | 0.03 | 0.97 | 0.01 | 0.00 | 0.00 | 0.5 | 0.4 | 0.0 | 0.4 |
| Mag-4 | 0.11 | 0.54 | 0.32 | 0.00 | 0.01 | 3.3 | 0.4 | 1.5 | 0.4 |
| Mag-5 | 0.05 | 0.70 | 0.24 | 0.00 | 0.00 | 3.1 | 0.4 | 2.2 | 0.4 |
| Mag-6 | 0.03 | 0.90 | 0.06 | 0.00 | 0.00 | 0.8 | 0.4 | 0.3 | 0.4 |
| Mag-7 | 0.03 | 0.94 | 0.04 | 0.00 | 0.00 | –2.1 | 0.4 | –2.2 | 0.4 |
| Mag-8 | 0.03 | 0.91 | 0.02 | 0.00 | 0.00 | –1.6 | 0.4 | –1.7 | 0.4 |
| Mag-9 | 0.04 | 0.92 | 0.04 | 0.00 | 0.00 | –0.5 | 0.4 | –0.8 | 0.4 |
| Mag-10 | 0.03 | 0.97 | 0.01 | 0.00 | 0.00 | –1.5 | 0.4 | –1.8 | 0.4 |
| Mag-11 | 0.03 | 0.97 | 0.01 | 0.00 | 0.00 | –0.7 | 0.4 | –1.0 | 0.4 |
| Mag-12 | 0.04 | 0.92 | 0.04 | 0.00 | 0.00 | 0.8 | 0.4 | 0.4 | 0.4 |
| Mag-13 | 0.04 | 0.92 | 0.06 | 0.00 | 0.00 | 0.8 | 0.4 | 0.4 | 0.4 |
| Mag-14 | 0.06 | 0.70 | 0.22 | 0.00 | 0.00 | 1.7 | 0.4 | 0.7 | 0.4 |
| Mag-15 | 0.05 | 0.89 | 0.06 | 0.00 | 0.00 | –0.9 | 0.4 | –1.1 | 0.4 |
| Mag-16 | 0.05 | 0.89 | 0.06 | 0.00 | 0.00 | 1.3 | 0.4 | 0.8 | 0.4 |
| Mag-17 | 0.04 | 0.90 | 0.04 | 0.00 | 0.00 | –0.9 | 0.4 | –1.2 | 0.4 |
| Mag-18 | 0.04 | 0.92 | 0.02 | 0.00 | 0.00 | –1.2 | 0.4 | –1.4 | 0.4 |
| Mag-19 | 0.05 | 0.91 | 0.04 | 0.00 | 0.00 | –2.3 | 0.4 | –2.4 | 0.4 |

Table 7.4: Cation chemistry and Mg isotopic composition of Fe-dolomite from ALH84001.

| Point | $CaCO_3$ | $MgCO_3$ | $FeCO_3$ | $SrCO_3$ | $MnCO_3$ | $\delta^{26}Mg_{DSM-3}$ (‰) | 1σ |
|---|---|---|---|---|---|---|---|
| Dol-1 | 0.48 | 0.32 | 0.15 | 0.00 | 0.06 | –1.1 | 0.4 |
| Dol-2 | 0.49 | 0.30 | 0.09 | 0.00 | 0.06 | –0.4 | 0.4 |
| Dol-3 | 0.48 | 0.31 | 0.14 | 0.00 | 0.06 | –0.6 | 0.4 |
| Dol-4 | 0.47 | 0.31 | 0.14 | 0.00 | 0.06 | –1.3 | 0.4 |

# BIBLIOGRAPHY

Adams D., Scheucher M., Hu R., Ehlmann B. L., Thomas T. B., Wordsworth R., Scheller E., Lillis R., Smith K., Rauer H. and Yung Y. L. (2025) Episodic warm climates on early Mars primed by crustal hydration. *Nat. Geosci.* **18**, 133–139.

Bhattacharjee S., Patel A. S., Cheng J., Raudsepp M. J., Wilson S., Goddard III W. A., Asimow P. D. and Eiler J. M. (2025) Equilibrium carbon, magnesium and position-specific oxygen isotope fractionations in the magnesium carbonate – water – carbon dioxide system based on quantum mechanical calculations and laboratory precipitation experiments. *Geochimica et Cosmochimica Acta*.

Boctor N. Z., Alexander C. O., Wang J. and Hauri E. (2003) The sources of water in Martian meteorites: Clues from hydrogen isotopes. *Geochimica et Cosmochimica Acta* **67**, 3971–3989.

Borg L. E., Connelly J. N., Nyquist L. E., Shih C.-Y., Wiesmann H. and Reese Y. (1999) The Age of the Carbonates in Martian Meteorite ALH84001. *Science* **286**, 90–94.

Bridges J. C. and Grady M. M. (1999) A halite-siderite-anhydrite-chlorapatite assemblage in Nakhla: Mineralogical evidence for evaporites on Mars. *Meteorit & Planetary Scien* **34**, 407–415.

Bridges J. C. and Grady M. M. (2000) Evaporite mineral assemblages in the nakhlite (martian) meteorites. *Earth and Planetary Science Letters* **176**, 267–279.

Catling D. C. (1999a) A chemical model for evaporites on early Mars: Possible sedimentary tracers of the early climate and implications for exploration. *J. Geophys. Res.* **104**, 16453–16469.

Catling D. C. (1999b) A chemical model for evaporites on early Mars: Possible sedimentary tracers of the early climate and implications for exploration. *Journal of Geophysical Research: Planets* **104**, 16453–16469.

Changela H. G. and Bridges J. C. (2010) Alteration assemblages in the nakhlites: Variation with depth on Mars: Alteration assemblages in the nakhlites. *Meteoritics & Planetary Science* **45**, 1847–1867.

Christensen P. R. (2003) Formation of recent Martian gullies through melting of extensive water-rich snow deposits. *Nature* **422**, 45–48.

Cockell C. S., Bush T., Bryce C., Direito S., Fox-Powell M., Harrison J. P., Lammer H., Landenmark H., Martin-Torres J., Nicholson N., Noack L., O'Malley-James J., Payler S. J., Rushby A., Samuels T., Schwendner P., Wadsworth J. and Zorzano M. P. (2016) Habitability: A Review. *Astrobiology* **16**, 89–117.

Domeneghetti M. C., Fioretti A. M., Cámara F., Molin G. and Tazzoli V. (2007) Thermal history of ALH 84001 meteorite by $Fe^{2+}$ -Mg ordering in orthopyroxene. *Meteorit & Planetary Scien* **42**, 1703–1710.

Ehlmann B. L., Berger G., Mangold N., Michalski J. R., Catling D. C., Ruff S. W., Chassefière E., Niles P. B., Chevrier V. and Poulet F. (2013) Geochemical Consequences of Widespread Clay Mineral Formation in Mars' Ancient Crust. *Space Sci Rev* **174**, 329–364.

Ehlmann B. L. and Edwards C. S. (2014) Mineralogy of the Martian Surface. *Annu. Rev. Earth Planet. Sci.* **42**, 291–315.

Ehlmann B. L., Mustard J. F. and Murchie S. L. (2010) Geologic setting of serpentine deposits on Mars. *Geophysical Research Letters* **37**, 2010GL042596.

Ehlmann B. L., Mustard J. F., Murchie S. L., Bibring J.-P., Meunier A., Fraeman A. A. and Langevin Y. (2011) Subsurface water and clay mineral formation during the early history of Mars. *Nature* **479**, 53–60.

Ehlmann B. L., Mustard J. F., Murchie S. L., Poulet F., Bishop J. L., Brown A. J., Calvin W. M., Clark R. N., Des Marais D. J. and Milliken R. E. (2008) Orbital identification of carbonate-bearing rocks on Mars. *Science* **322**, 1828–1832.

Eiler J. M., Kitchen N., Leshin L. and Strausberg M. (2002a) Hosts of hydrogen in Allan Hills 84001: Evidence for hydrous martian salts in the oldest martian meteorite? *Meteorit & Planetary Scien* **37**, 395–405.

Eiler J. M., Valley J. W., Graham C. M. and Fournelle J. (2002b) Two populations of carbonate in ALH84001: Geochemical evidence for discrimination and genesis. *Geochimica et Cosmochimica Acta* **66**, 1285–1303.

Farley K. A., Stack K. M., Shuster D. L., Horgan B. H. N., Hurowitz J. A., Tarnas J. D., Simon J. I., Sun V. Z., Scheller E. L. and Moore K. R. (2022) Aqueously altered igneous rocks sampled on the floor of Jezero crater, Mars. *Science* **377**, eabo2196.

Franzolin E., Schmidt M. W. and Poli S. (2011) Ternary Ca–Fe–Mg carbonates: subsolidus phase relations at 3.5 GPa and a thermodynamic solid solution model including order/disorder. *Contributions to Mineralogy and Petrology* **161**, 213–227.

Gao C., Cao X., Liu Q., Yang Y., Zhang S., He Y., Tang M. and Liu Y. (2018) Theoretical calculation of equilibrium Mg isotope fractionations between minerals and aqueous solutions. *Chemical Geology* **488**, 62–75.

Gaudin A., Dehouck E. and Mangold N. (2011) Evidence for weathering on early Mars from a comparison with terrestrial weathering profiles. *Icarus* **216**, 257–268.

Golden D. C., Ming D. W., Schwandt C. S., Morris R. V., Yang S. V. and Lofgren G. E. (2000) An experimental study on kinetically-driven precipitation of calcium-magnesium-iron carbonates from solution: Implications for the low-temperature formation of carbonates in martian meteorite Allan Hills 84001. *Meteorit & Planetary Scien* **35**, 457–465.

Gyollai I., Chatzitheodoridis E. and Kereszturi Á. (1993) Secondary minerals of Nakhla, Lafayette and Governador Valadares meteorites–implications of hydrothermal processes on Mars. *Nature* **365**, 715–721.

Halevy I., Fischer W. W. and Eiler J. M. (2011) Carbonates in the Martian meteorite Allan Hills 84001 formed at 18$\pm$4 C in a near-surface aqueous environment. *Proceedings of the National Academy of Sciences* **108**, 16895–16899.

Hicks L. J., Bridges J. C. and Gurman S. J. (2014) Ferric saponite and serpentine in the nakhlite martian meteorites. *Geochimica et Cosmochimica Acta* **136**, 194–210.

Hobbs F. W. and Xu H. (2020) Magnesite formation through temperature and pH cycling as a proxy for lagoon and playa paleoenvironments. *Geochimica et Cosmochimica Acta* **269**, 101–116.

Hurowitz J. A., Tice M. M., Allwood A. C., Cable M. L., Hand K. P., Murphy A. E., Uckert K., Bell III J. F., Bosak T. and Broz A. P. (2025) Redox-driven mineral and organic associations in Jezero Crater, Mars. *Nature* **645**, 332–340.

Kite E. S. (2019) Geologic Constraints on Early Mars Climate. *Space Sci Rev* **215**.

Kite E. S. and Conway S. (2024) Geological evidence for multiple climate transitions on Early Mars. *Nature Geoscience* **17**, 10–19.

Kleine B. I., Stefansson A., Halldórsson S. A., Whitehouse M. J. and Jónasson K. (2018) Silicon and oxygen isotopes unravel quartz formation processes in the Icelandic crust. *Geochemical Perspectives Letters* **7**, 5–11.

Lammer H., Chassefière E., Karatekin Ö., Morschhauser A., Niles P. B., Mousis O., Odert P., Möstl U. V., Breuer D., Dehant V., Grott M., Gröller H., Hauber E. and Pham L. B. S. (2013) Outgassing History and Escape of the Martian Atmosphere and Water Inventory. *Space Sci Rev* **174**, 113–154.

Lapen T. J., Righter M., Brandon A. D., Debaille V., Beard B. L., Shafer J. T. and Peslier A. H. (2010) A Younger Age for ALH84001 and Its Geochemical Link to Shergottite Sources in Mars. *Science* **328**, 347–351.

Lee M. R., Tomkinson T., Hallis L. J. and Mark D. F. (2015) Formation of iddingsite veins in the martian crust by centripetal replacement of olivine: Evidence from the nakhlite meteorite Lafayette. *Geochimica et Cosmochimica Acta* **154**, 49–65.

Lee M. R., Tomkinson T., Mark D. F., Stuart F. M. and Smith C. L. (2013) Evidence for silicate dissolution on Mars from the Nakhla meteorite. *Meteorit & Planetary Scien* **48**, 224–240.

Li W., Beard B. L. and Johnson C. M. (2011) Exchange and fractionation of Mg isotopes between epsomite and saturated MgSO4 solution. *Geochimica et Cosmochimica Acta* **75**, 1814–1828.

Luo K., Ma J., Teng F., Wei G., Zhu G., Zeng T. and Wang Z. (2025) Magnesium Isotope Fractionation During Basalt Weathering: An Index of Weathering Fluxes and $CO_2$ Consumption. *JGR Earth Surface* **130**, e2024JF007774.

Magna T., Hu Y., Teng F.-Z. and Mezger K. (2017) Magnesium isotope systematics in Martian meteorites. *Earth and Planetary Science Letters* **474**, 419–426.

Mavromatis V., Power I. M., Harrison A. L., Beinlich A., Dipple G. M. and Bénézeth P. (2021) Mechanisms controlling the Mg isotope composition of hydromagnesite-magnesite playas near Atlin, British Columbia, Canada. *Chemical Geology* **579**, 120325.

Mcsween Jr H. Y. and Harvey R. P. (1998) An evaporation model for formation of carbonates in the ALH84001 Martian meteorite. *International Geology Review* **40**, 774–783.

Meunier A., Petit S., Ehlmann B. L., Dudoignon P., Westall F., Mas A., El Albani A. and Ferrage E. (2012) Magmatic precipitation as a possible origin of Noachian clays on Mars. *Nature Geoscience* **5**, 739–743.

Michalski J. R., Cuadros J., Bishop J. L., Darby Dyar M., Dekov V. and Fiore S. (2015) Constraints on the crystal-chemistry of Fe/Mg-rich smectitic clays on Mars and links to global alteration trends. *Earth and Planetary Science Letters* **427**, 215–225.

Mittlefehldt D. W. (1994) ALH84001, a cumulate orthopyroxenite member of the martian meteorite clan. *Meteoritics* **29**, 214–221.

Moore R. D., Goudge T. A., Klidaras A., Horgan B. H., Broz A., Wordsworth R. and Farrand W. H. (2025) Deep chemical weathering on ancient Mars landscapes driven by erosional and climatic patterns. *Nature Astronomy*, 1–9.

Moyano-Cambero C. E., Trigo-Rodríguez J. M., Benito M. I., Alonso-Azcárate J., Lee M. R., Mestres N., Martínez-Jiménez M., Martín-Torres F. J. and Fraxedas J. (2017) Petrographic and geochemical evidence for multiphase formation of carbonates in the Martian orthopyroxenite Allan Hills 84001. *Meteorit & Planetary Scien* **52**, 1030–1047.

Niles P. B., Catling D. C., Berger G., Chassefière E., Ehlmann B. L., Michalski J. R., Morris R., Ruff S. W. and Sutter B. (2013a) Geochemistry of Carbonates on Mars: Implications for Climate History and Nature of Aqueous Environments. *Space Sci Rev* **174**, 301–328.

Niles P. B., Catling D. C., Berger G., Chassefière E., Ehlmann B. L., Michalski J. R., Morris R., Ruff S. W. and Sutter B. (2013b) Geochemistry of Carbonates on Mars: Implications for Climate History and Nature of Aqueous Environments. *Space Sci Rev* **174**, 301–328.

Niles P. B., Leshin L. A. and Guan Y. (2005) Microscale carbon isotope variability in ALH84001 carbonates and a discussion of possible formation environments. *Geochimica et Cosmochimica Acta* **69**, 2931–2944.

Niles P. B., Zolotov M. Y. and Leshin L. A. (2009) Insights into the formation of Fe-and Mg-rich aqueous solutions on early Mars provided by the ALH 84001 carbonates. *Earth and Planetary Science Letters* **286**, 122–130.

de Obeso J. C., Santiago Ramos D. P., Higgins J. A. and Kelemen P. B. (2021) A Mg isotopic perspective on the mobility of magnesium during serpentinization and carbonation of the Oman ophiolite. *Journal of Geophysical Research: Solid Earth* **126**, e2020JB020237.

Oskierski H. C., Beinlich A., Mavromatis V., Altarawneh M. and Dlugogorski B. Z. (2019) Mg isotope fractionation during continental weathering and low temperature carbonation of ultramafic rocks. *Geochimica et cosmochimica acta* **262**, 60–77.

Parkhurst D. L. and Appelo C. A. J. (2013) Description of Input and Examples for PHREEQC Version 3—A Computer Program for Speciation, Batch-Reaction, One-Dimensional Transport, and Inverse Geochemical Calculations. In U.S. Geological Survey Techniques and Methods. U.S. Geological Survey, Reston, Virginia. p. 497.

Patron P., Martinez C., Elena A. M., Blanchard M. and Pinilla C. (2025) Equilibrium isotope fractionation in carbonate minerals: Role of Mg-Ca distribution and thermal effects. *Geochimica et Cosmochimica Acta* **394**, 53–69.

Pignatelli I., Mugnaioli E., Marrocchi Y. and Folco L. (2025) Constraints on the fluid alteration of Nakhla meteorite inferred from Fe-rich phyllosilicate characterization. *Meteorit & Planetary Scien*, maps.70031.

Power I. M., Kenward P. A., Dipple G. M. and Raudsepp M. (2017) Room Temperature Magnesite Precipitation. *Crystal Growth & Design* **17**, 5652–5659.

Přikryl J., Stefánsson A. and Pearce C. R. (2018) Tracing olivine carbonation and serpentinization in CO2-rich fluids via magnesium exchange and isotopic fractionation. *Geochimica et Cosmochimica Acta* **243**, 133–148.

Qu Y.-R., Liu S.-A. and Gamaleldien H. (2025) Insights Into Subduction-Zone Fluid-Rock Interactions and Carbon Cycling From Magnesium Isotopes of Subducted Ophiolitic Mélanges in the Arabian-Nubian Shield. *Geochemistry, Geophysics, Geosystems* **26**, e2024GC011918.

Rapin W., Dromart G., Clark B. C., Schieber J., Kite E. S., Kah L. C., Thompson L. M., Gasnault O., Lasue J. and Meslin P.-Y. (2023) Sustained wet–dry cycling on early Mars. *Nature* **620**, 299–302.

Rimstidt J. D., Balog A. and Webb J. (1998) Distribution of trace elements between carbonate minerals and aqueous solutions. *Geochimica et Cosmochimica Acta* **62**, 1851–1863.

Sasselov D. D., Grotzinger J. P. and Sutherland J. D. (2020) The origin of life as a planetary phenomenon. *Sci. Adv.* **6**, eaax3419.

Schauble E. A. (2011) First-principles estimates of equilibrium magnesium isotope fractionation in silicate, oxide, carbonate and hexaaquamagnesium (2+) crystals. *Geochimica et Cosmochimica Acta* **75**, 844–869.

Schauble E. A. and Young E. D. (2021) Mass dependence of equilibrium oxygen isotope fractionation in carbonate, nitrate, oxide, perchlorate, phosphate, silicate, and sulfate minerals. *Reviews in Mineralogy and Geochemistry* **86**, 137–178.

Scheller E. L., Ehlmann B. L., Hu R., Adams D. J. and Yung Y. L. (2021) Long-term drying of Mars by sequestration of ocean-scale volumes of water in the crust. *Science* **372**, 56–62.

Scheller Eva L., Swindle C., Grotzinger J., Barnhart H., Bhattacharjee S., Ehlmann B. L., Farley K., Fischer W. W., Greenberger R. and Ingalls M. (2021) Formation of Magnesium Carbonates on Earth and Implications for Mars. *Journal of Geophysical Research: Planets* **126**, e2021JE006828.

Scott E. R., Yamaguchi A. and Krot A. N. (1997) Petrological evidence for shock melting of carbonates in the Martian meteorite ALH84001. *Nature* **387**, 377–379.

Shaheen R., Abramian A., Horn J., Dominguez G., Sullivan R. and Thiemens M. H. (2010) Detection of oxygen isotopic anomaly in terrestrial atmospheric carbonates and its implications to Mars. *Proc. Natl. Acad. Sci. U.S.A.* **107**, 20213–20218.

Shaheen R., Niles P. B., Chong K., Corrigan C. M. and Thiemens M. H. (2015) Carbonate formation events in ALH 84001 trace the evolution of the Martian atmosphere. *Proc. Natl. Acad. Sci. U.S.A.* **112**, 336–341.

Shatskiy A., Podborodnikov I. V., Arefiev A. V., Minin D. A., Chanyshev A. D. and Litasov K. D. (2018) Revision of the CaCO3–MgCO3 phase diagram at 3 and 6 GPa. *American Mineralogist* **103**, 441–452.

Sleep N. H. and Zahnle K. (2001) Carbon dioxide cycling and implications for climate on ancient Earth. *J. Geophys. Res.* **106**, 1373–1399.

Stanley B. D., Hirschmann M. M. and Withers A. C. (2011) CO2 solubility in Martian basalts and Martian atmospheric evolution. *Geochimica et Cosmochimica Acta* **75**, 5987–6003.

Steele A., Benning L. G., Wirth R., Schreiber A., Araki T., McCubbin F. M., Fries M. D., Nittler L. R., Wang J. and Hallis L. J. (2022) Organic synthesis associated with serpentinization and carbonation on early Mars. *Science* **375**, 172–177.

Steele A., Fries M. D., Amundsen H. E. F., Mysen B. O., Fogel M. L., Schweizer M. and Boctor N. Z. (2007) Comprehensive imaging and Raman spectroscopy of carbonate globules from Martian meteorite ALH 84001 and a terrestrial analogue from Svalbard. *Meteorit & Planetary Scien* **42**, 1549–1566.

Sugiura N. and Hoshino H. (2000) Hydrogen-isotopic compositions in Allan Hills 84001 and the evolution of the martian atmosphere. *Meteorit & Planetary Scien* **35**, 373–380.

Tosca N. J., Tice M. M., Hurowitz J. A., Pedersen D. A. K., Henneke J., Mandon L., McCubbin F. M., Ross O., Tung P.-Y., Harrison R. J., Li A., Schmidt M. E., Kizovski T. V., Liu Y., Mayhew L., Jones M. W. M., Labrie J., Davidoff S., Allwood A. C., Beyssac O., Brown A., Cable M., Comellas J., Clark B. C., Galvin A. E., Horgan B., Heirwegh C. M., Nemere P., Orenstein B. J., Quantin-Nataf C., Royer C., Treiman A., Wade L. A., Wiens R. and Wright A. P. (2025a) In situ evidence for serpentinization within the Máaz formation, Jezero crater, Mars. *Sci. Adv.* **11**, eadr8793.

Tosca N. J., Tice M. M., Hurowitz J. A., Pedersen D. A. K., Henneke J., Mandon L., McCubbin F. M., Ross O., Tung P.-Y., Harrison R. J., Li A., Schmidt M. E., Kizovski T. V., Liu Y., Mayhew L., Jones M. W. M., Labrie J., Davidoff S., Allwood A. C., Beyssac O., Brown A., Cable M., Comellas J., Clark B. C., Galvin A. E., Horgan B., Heirwegh C. M., Nemere P., Orenstein B. J., Quantin-Nataf C., Royer C., Treiman A., Wade L. A., Wiens R. and Wright A. P. (2025b) In situ evidence for serpentinization within the Máaz formation, Jezero crater, Mars. *Science Advances* **11**, eadr8793.

Treiman A. H. (1995) A petrographic history of martian meteorite ALH84001: Two shocks and an ancient age. *Meteoritics* **30**, 294–302.

Treiman A. H., Barrett R. A. and Gooding J. L. (1993) Preterrestrial aqueous alteration of the Lafayette (SNC) meteorite. *Meteoritics* **28**, 86–97.

Truesdell A. H. and Jones B. F. (1974) WATEQ, a computer program for calculating chemical equilibria of natural waters. *Journal of Research of the U.S. Geological Survey* **2**, 233–248.

Tutolo B. M., Hausrath E. M., Kite E. S., Rampe E. B., Bristow T. F., Downs R. T., Treiman A., Peretyazhko T. S., Thorpe M. T., Grotzinger J. P., Roberts A. L., Archer P. D., Des Marais D. J., Blake D. F., Vaniman D. T., Morrison S. M., Chipera S., Hazen R. M., Morris R. V., Tu V. M., Simpson S. L., Pandey A., Yen A., Larter S. R., Craig P., Castle N., Ming D. W., Meusburger J. M., Fraeman A. A., Burtt D. G., Franz H. B., Sutter B., Clark J. V., Rapin W., Bridges J. C., Loche M., Gasda P., Frydenvang J. and Vasavada A. R. (2025) Carbonates identified by the Curiosity rover indicate a carbon cycle operated on ancient Mars. *Science* **388**, 292–297.

Tutolo B. M. and Tosca N. J. (2023) Observational constraints on the process and products of Martian serpentinization. *Sci. Adv.* **9**, eadd8472.

Valley J. W., Eiler J. M., Graham C. M., Gibson E. K., Romanek C. S. and Stolper E. M. (1997) Low-temperature carbonate concretions in the Martian meteorite ALH84001: Evidence from stable isotopes and mineralogy. *Science* **275**, 1633–1638.

Walker J. C. G., Hays P. B. and Kasting J. F. (1981) A negative feedback mechanism for the long-term stabilization of Earth's surface temperature. *J. Geophys. Res* **86**, 9776–9782.

Wang W., Qin T., Zhou C., Huang S., Wu Z. and Huang F. (2017) Concentration effect on equilibrium fractionation of Mg-Ca isotopes in carbonate minerals: Insights from first-principles calculations. *Geochimica et Cosmochimica Acta* **208**, 185–197.

Wang W., Zhou C., Liu Y., Wu Z. and Huang F. (2019) Equilibrium Mg isotope fractionation among aqueous Mg2+, carbonates, brucite and lizardite: Insights from first-principles molecular dynamics simulations. *Geochimica et Cosmochimica Acta* **250**, 117–129.

Wordsworth R. D. (2016) The Climate of Early Mars. *Annu. Rev. Earth Planet. Sci.* **44**, 381–408.

Ye B. and Michalski J. R. (2022) Chemical weathering over hundreds of millions of years of greenhouse conditions on Mars. *Communications Earth & Environment* **3**, 266.

Yoshimura T., Araoka D., Naraoka H., Sakai S., Ogawa N. O., Yurimoto H., Morita M., Onose M., Yokoyama T. and Bizzarro M. (2024) Breunnerite grain and magnesium isotope chemistry reveal cation partitioning during aqueous alteration of asteroid Ryugu. *Nature Communications* **15**, 6809.

Zambardi T., Poitrasson F., Corgne A., Méheut M., Quitté G. and Anand M. (2013) Silicon isotope variations in the inner solar system: Implications for planetary formation, differentiation and composition. *Geochimica et Cosmochimica Acta* **121**, 67–83.